UNIVERSITY OF CALIFORNIA,
IRVINE

Multi-Axis Solutions for MEMS Inertial Sensors

DISSERTATION

submitted in partial satisfaction of the requirements
for the degree of

DOCTOR OF PHILOSOPHY

in Mechanical and Aerospace Engineering

by

Alexandra Efimovskaya

Dissertation Committee:
Professor Andrei M. Shkel, Chair
Professor Faryar Jabbari
Professor Lorenzo Valdevit

2017

DEDICATION

To my family and friends.

TABLE OF CONTENTS

LIST OF FIGURES

LIST OF TABLES

LIST OF SYMBOLS

Symbol	Description
x, y, z	Roll, pitch, and yaw axes in body reference frame
X, Y, Z	Axes of coordinate frame oriented along the gyroscope's intended axes of symmetry X and Y
α, β	Anisoelasticity angles, angles between the actual and intended axes of elasticity of the gyroscope's mechanical element
Ω	Angular rate applied to the gyroscope
Center freq. (f)	Mean frequency of the two primary modes of the resonator
Q-factor	Ratio of stored energy to energy loss per vibration cycle ($Q = \tau\pi f$)
Δf	Frequency split between primary modes in Hz ($\Delta f = f_x - f_y$)
$\Delta\omega$	Frequency split between primary modes in rad/s ($\Delta\omega = \omega_x - \omega_y$)
$\Delta\tau^{-1}$	Measure of anisodamping in the gyroscope ($\Delta\tau^{-1} = \lvert\tau_x^{-1} - \tau_y^{-1}\rvert$)
k_g	Gyroscope's angular gain factor
A	Dynamic amplification factor, ration between the amplitudes of vibration of two coupled proof-masses in a dual-mass system
n = 1 mode	A 2-node degenerate mode pair of a wineglass or ring/disk system
n = 2 mode	A 4-node degenerate mode pair of a wineglass or ring/disk system
n = 3 mode	A 6-node degenerate mode pair of a wineglass or ring/disk system
K	Transimpedance amplifier gain
c	Damping coefficient in transfer function of the electro-mechanical resonator system
k	Stiffness coefficient in transfer function of the electro-mechanical resonator system
χ_1 and χ_2	In transfer function of the electro-mechanical resonator system, coefficients for conversion from the input signal to mechanical force and for the mechanical displacement to motion induced current
I_{mot}	Motion-induced current of the sensor
I_p	Parasitic feed-through current of the sensor

ACKNOWLEDGMENTS

I would like to express my deepest gratitude and appreciation to my advisor Professor Andrei M. Shkel, whose guidance, support, and continuous encouragement made this dissertation possible. I am also deeply grateful to my dissertation committee, Professor Faryar Jabbari and Professor Lorenzo Valdevit, for taking the time to review this work and provide valuable comments.

I would like to acknowledge the Defense Advanced Research Projects Agency (DARPA) and U.S. Navy for generous financial support granted through the Micro-Technology for Positioning, Navigation and Timing (Micro-PNT) program (DARPA grant N66001-13-1-4021 & DARPA grant 66001-16-1-4021). I am especially deeply grateful to Dr. Robert Lutwak for his invaluable guidance and support of my research under this program.

I am very thankful to my colleagues and friends at UCI MicroSystems Laboratory for their help and support through my Ph.D. studies. In particular, I would like to thank my colleagues Yu-Wei Lin, Dr. Doruk Senkal, Dr. Joan Giner de Haro, Danmeng Wang, Mohammad Asadian Ardakani, Yusheng Wang, and Sina Askari for numerous technical discussions and insightful suggestions. I also would like to thank Prof. Mohammed J. Ahamed, Dr. Alexander Trusov, Dr. Montgomery Rivers, Dr. Sergei Zotov, Dr. Gunjana Sharma, and Dr. Brenton R. Simon for their help and support through the early years of my Ph.D.

I am grateful to Professor Thomas W. Kenny and his group at Stanford University, especially Dr. Yushi Yang, Dr. Eldwin Ng, Dr. Yunhan Chen, Dr. Ian Flader, Dr. Chae Hyuck Ahn, and Dr. Vu Hong, for the great collaboration opportunity on epitaxially-encapsulated sensors.

In addition, I would like to thank UCI Integrated Nanosystems Research Facility staff Jake Hes and Dr. Mo Kebaili for their help and valuable suggestions on fabrication aspects of the project.

Finally, I am deeply thankful to my family for the inspiration and support that helped me to complete this work.

CURRICULUM VITAE

Alexandra Efimovskaya

EDUCATION

Doctor of Philosophy in Mechanical and Aerospace Eng. **2017**
University of California, Irvine *Irvine, California*

Master of Science in Mechanical and Aerospace Eng. **2015**
University of California, Irvine *Irvine, California*

Diploma (with excellence), Mechanical and Aerospace Eng. **2009**
Saint-Petersburg State University of Aerospace Instrumentation *Saint-Petersburg, Russia*

RESEARCH EXPERIENCE

Graduate Research Assistant **2012–2017**
University of California, Irvine *Irvine, California*

SELECTED FELLOWSHIPS, HONORS AND AWARDS

Outstanding Paper Award (Lecture Track) **2017**
IEEE/ASME Int. Symposium on Inertial Sensors and Systems, 2017

Amelia Earhart Fellowship **2015-2016**
Zonta International

DARPA Raising Star Award **2015**
Defense Advanced Research Projects Agency

Outstanding Paper Award (Lecture Track) **2015**
18th Int. Conf. on Solid-State Sensors, Actuators and Microsystems
Transducers'2015

Holmes Endowed Engineering Fellowship **2012-2013**

The Henry Samueli School of Engineering, UCI

Fulbright Fellowship **2011-2012**
Visiting Student Researcher, UCI

REFEREED JOURNAL PUBLICATIONS

A. Efimovskaya, D. Wang, Y. Lin, and A. M. Shkel, *Electrostatic Compensation of Structural Imperfections in Dynamically Amplified Dual-Mass Gyroscope*, submitted for publication at Sensors and Actuators Journal, 2017.

A. Efimovskaya, Y. Lin, and A. M. Shkel, *Double-Sided Process for MEMS SOI Sensors Co-fabricated with Deep Vertical Thru-Wafer Interconnects*, submitted for publication at IEEE/ASME Journal Microelectromech. Syst., (2017).

A. Efimovskaya, Y. Lin, and A. M. Shkel, *Origami-Like 3-D Folded MEMS Approach for Miniature Inertial Measurement Unit*, IEEE/ASME Journal Microelectromech. Syst., Vol. 26, Issue 5, pp. 1030-1039, (2017).

REFEREED CONFERENCE PUBLICATIONS

A. Efimovskaya, Y. Yang, E. Ng, Y. Chen, I. Flader, T. W. Kenny, and A. M. Shkel, *Ultra-Compact Roll-Pitch-Yaw Gyroscope Implemented in Wafer-level Epitaxial Silicon Encapsulation Process*, IEEE/ASME International Symposium on Inertial Sensors and Systems, Kauai, HI, USA, March 27-30, 2017.

A. Efimovskaya, Y. Lin, D. Wang, and A. M. Shkel, *Electrostatic Compensation of Structural Imperfections in Dynamically Amplified Dual-Mass Gyroscope*, IEEE/ASME International Symposium on Inertial Sensors and Systems, Kauai, HI, USA, March 27-30, 2017.

D. Wang, M. H. Asadian, A. Efimovskaya, A. M. Shkel, *A Comparative Study of Conventional Single-Mass and Amplitude Amplified Dual-Mass MEMS Vibratory Gyroscopes*, IEEE/ASME International Symposium on Inertial Sensors and Systems, Kauai, HI, USA, March 27-30, 2017.

Y. Lin, A. Efimovskaya, and A. M. Shkel, *Study of Environmental Survivability and Stability of Folded MEMS IMU*, IEEE/ASME International Symposium on Inertial Sensors and Systems, Kauai, HI, USA, March 27-30, 2017.

A. Efimovskaya, Y. Lin, Y. Yang, E. Ng, Y. Chen, I. Flader, C. H. Ahn, V. Hong, T. W. Kenny, and A. M. Shkel, *On Cross-Talk between Gyroscopes Integrated on a Folded MEMS IMU Cube*, IEEE MEMS17 Conference, January 22-26, Las Vegas, NV, USA, (2017).

A. Efimovskaya, D. Wang, Y. Lin, and A. M. Shkel, *On Ordering of Fundamental Wineglass Modes in Toroidal Ring Gyroscope*, IEEE Sensors 2016, Orlando, FL, USA, Oct 30-Nov 2, (2016).

A. Efimovskaya, Y. Lin, A. M. Shkel, *Thru-Wafer Interconnects for Double-Sided (TWIDS) Fabrication of MEMS*, IEEE Inertial Sensors, Laguna Beach, CA, USA, 22-25 February, 2016.

A. Efimovskaya, D. Senkal, and A. M. Shkel, *Miniature Origami-like Folded MEMS TIMU*, IEEE Transducers Conference, Anchorage, Alaska, USA, June 21-25, 2015.

D. Senkal, A. Efimovskaya, and A. M. Shkel, *Dual Foucault Pendulum Gyroscope*, IEEE Transducers Conference, Anchorage, Alaska, USA, June 21-25, 2015.

A. Efimovskaya, D. Senkal, Sina Askari, and A. M. Shkel, *Origami-Like Folded MEMS for Realization of TIMU: Fabrication Technology and Initial Demonstration*, IEEE/ASME International Symposium on Inertial Sensors and Systems, Kohala Coast, Hawaii, USA, March 23-26, 2015.

D. Senkal, A. Efimovskaya, and A. M. Shkel, *Minimal Realization of Dynamically Balanced Lumped Mass WA Gyroscope: Dual Foucault Pendulum*, IEEE/ASME International Symposium on Inertial Sensors and Systems, Kohala Coast, Hawaii, USA, March 23-26, 2015.

A. Efimovskaya and A. M. Shkel, *160 Milli-ohm electrical resistance thru-wafer interconnects with 10:1 aspect ratio*, IMAPS 2014 Conference, October 13-16, San Diego, CA, 2014.

IVENTION DISCLOSURES

A. M. Shkel, A. Efimovskaya, D. Senkal, Y. Lin, *A Low-cost Wafer-level Process for Packaging MEMS 3-D Devices*, UCI Case No.: 2015-807-1 US, 2015.

A. M. Shkel, A. Efimovskaya, *Thru-Wafer Interconnects for MEMS Double-Sided Fabrication Process (TWIDS)*, US Patent 20160167958, 2016.

PROFESSIONAL MEMBERSHIPS

Institute of Electrical and Electronics Engineers (IEEE)

ABSTRACT OF THE DISSERTATION

Multi-Axis Solutions for MEMS Inertial Sensors

By

Alexandra Efimovskaya

Doctor of Philosophy in Mechanical and Aerospace Engineering

University of California, Irvine, 2017

Professor Andrei M. Shkel, Chair

Inertial Measurement Unit (IMU) integrates three-axis gyroscopes and three-axis accelerometers to provide information about position, orientation, and trajectory. For decades, IMUs based on high-end sensors have been widely used for navigation, flight control, and stabilization functions. Inspired by recent improvements in performance of MEMS inertial sensors, this Ph.D. dissertation explores a large-scale integration of discrete inertial sensors in a single micro chip solution, and introduces two approaches for a compact tactical-grade MEMS IMU.

The first approach is based on a silicon "origami-like" MEMS fabrication process, which involves fabrication of a high density array of discrete single-axis inertial sensors and then folding the array into a 3D IMU configuration. The main contribution of this thesis is invention and implementation of a double-sided fabrication process for foldable structures with flexible polymer hinges, integrated high-end MEMS inertial sensors, and integration of thru-wafer interconnects in the fabrication process. Dissimilar materials were explored for fabrication of the "origami-like" structures, expanding our knowledge on the use of polymers and standard bulk and surface micro-machining tools for manufacturing of 3D MEMS devices. In addition, this work investigated two tactical-grade gyroscope designs for potential integration with the introduced fabrication process: Dynamically Amplified Gyroscope

(DAG) and Toroidal Ring Gyroscope (TRG). We designed, modeled, and implemented the control electronics, and experimentally demonstrated the tactical-grade performance of the DAG and TRG gyroscopes. In this dissertation, for the first time, an IMU prototype with all sensors operational was reported, demonstrating feasibility of the Folded MEMS approach for implementation of a compact tactical-grade performance system.

This thesis also explored a MEMS IMU solution, utilizing a single multi-axis sensing element. We demonstrated a 3-axis roll-pitch-yaw gyroscope, a major building block of the miniaturized IMU. The mechanical structure of the gyroscope employed a single vibrational element with a torsional drive mode and a multi-directional sense modes. Experimental characterization of the sensor showed that it is capable of measuring an angular rate around all three orthogonal axes simultaneously with a minimal cross talk between axes of sensitivity and increased immunity to external vibrations.

Chapter 1

Introduction

In this Chapter we present motivation for the research, followed by a literature review of the MEMS-based Inertial Measurement Units (IMUs). Then, objectives of the research are defined. The Chapter is concluded with an outline of the dissertation.

1.1 Motivation

Nowadays, a substantial number of navigation systems, both civil and military, rely heavily on GPS (Global Positioning System) technology for Positioning, Navigation, and Timing (PNT). This reliance on satellite technology creates a critical vulnerability of these systems in environments, where GPS access is unavailable, such as indoors, urban canyons, tunnels, caves, underground, or underwater.

An alternative solution is inertial navigation through dead reckoning, which is completely self-contained and may provide accurate PNT without the need for external signals.

Among the inertial measurement tools, based on high-precision mechanical sensors and op-

tical sensors [4], MEMS (Micro-Electro-Mechanical Systems) hold a special place.

MEMS-based Inertial Measurement Units (IMUs) provide an advantage of small size, low power, and low cost, which resulted in their fast adoption in consumer electronics, such as mobile phones and gaming devices. A scope of applications for consumer MEMS IMUs includes activity detection, virtual and augmented reality, optical and electronic image stabilization, to name a few.

Over the last years, there have been a continuous improvement in performance of MEMS consumer inertial sensors, opening paths for new and intriguing applications.

Present day ultra-compact consumer IMUs can be used for tracing position and orientation for a short duration of time (on the order of few seconds), but not yet applicable for self-contained navigation (from minutes to hours of navigation). Due to fast accumulating errors, such devices are used in a combination with magnetometers, altimeters and other sensors, as a short-term backup system, when GPS or other location sources are temporarily lost or interrupted.

Meanwhile, a number of high performance silicon MEMS sensors have been recently reported in literature, for example a degenerate mode Disk Resonator Gyroscope, [6], or a Quadruple Mass Gyroscope, [7]. Noise characteristics of these devices showed a potential for achieving the navigation grade accuracy.

A technology providing an efficient way to assemble the high-end inertial sensors into a 6-axis IMU configuration, while preserving advantages of a relatively compact size and low cost, may enable a wide range of demanding applications. Some potential applications include uninterrupted personal navigation in presence of jamming/spoofing of RF signals and navigation of small, fast, highly maneuverable unmanned vehicles in GPS-challenged environments, [8].

1.2 Background

The basic concepts of inertial navigation and inertial measurement units are outlined in this Section.

1.2.1 Inertial Navigation

Inertial navigation is a technique in which measurements provided by the Inertial Measurement Unit (IMU) are used to track the absolute position and orientation of a body. Unlike many other types of navigation system, inertial systems are entirely self-contained, in the sense that they are not dependent on the signals from from an external source.

Inertial navigation is used in a wide range of applications, including the navigation of aircrafts, missiles, ships, submarines, and spacecrafts. Recent advances in MEMS fabrication technology have made it possible to manufacture small and low power consumption inertial navigation systems, which have been fast adopted for navigation of miniature platforms, such as small Unmanned Aerial Vehicles (UAV) and small Autonomous Underwater Vehicles (AUV).

Generally, IMU contains, but is not limited to, three gyroscopes and three accelerometers oriented along 3 orthogonal axes to allow for orientation and position data in 3-D space, Fig. 1.1. Gyroscopes provide information about the roll, pitch and yaw rates or angles. Accelerometers provide information about the acceleration along the x, y, and z axes. By processing signals from these devices, it is possible to track the position and orientation of a body.

Fig. 1.2 represents a general case of a strapdown inertial navigation system, where navigation takes place with respect to inertial space. Gyroscopes provide measurements of changes

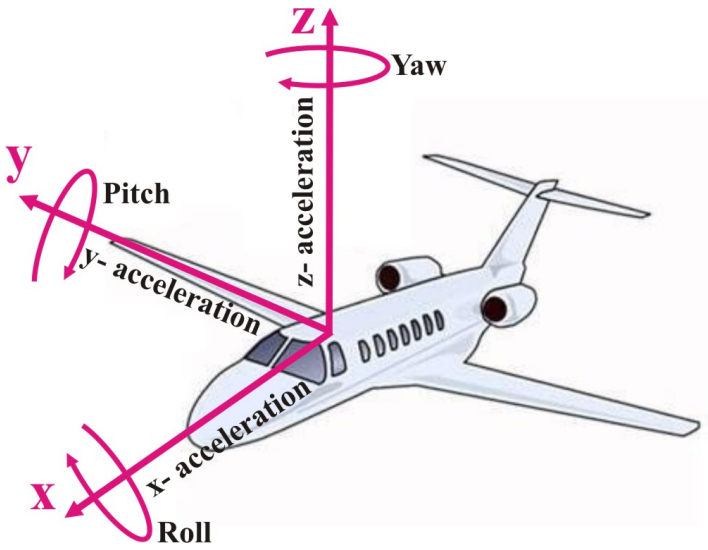

Figure 1.1: Three gyroscopes and three accelerometers oriented along 3 orthogonal axes allow for absolute position and orientation data.

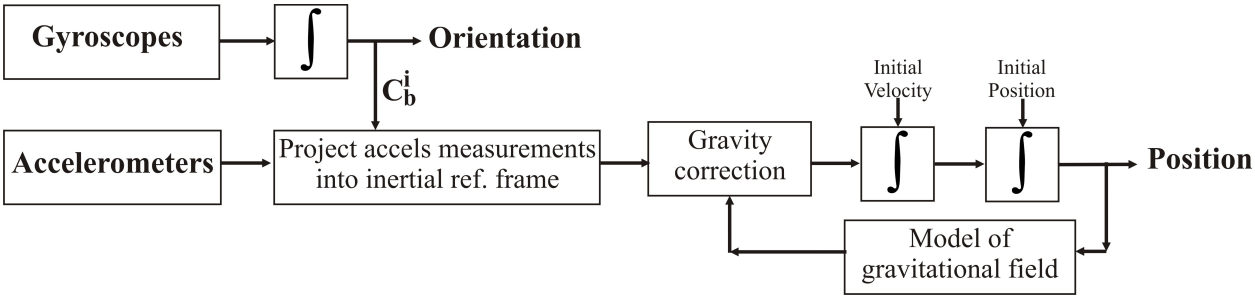

Figure 1.2: Strapdown inertial navigation system, where navigation takes place with respect to inertial space.

in vehicle attitude or its turn rate with respect to inertial space. The measurements provided by the gyroscopes are used to determine the attitude and heading of the body with respect to the reference frame in which it is required to navigate. The attitude of the body with respect to the chosen reference frame, may be defined in a number of different ways, such as, for example, using direction cosines method. The direction cosine matrix C_b^i is used to project the accelerometer measurements into the inertial reference frame. Accelerometers, however, measure the combined total acceleration of the vehicle and the acceleration caused by the presence of a gravitational field. Therefore, the measurements provided by the accelerometers must be combined with knowledge of the gravitational field in order to determine the acceleration of the vehicle with respect to inertial space. The calculated accelerations may

then be integrated twice to obtain the vehicle velocity and position in the defined reference frame.

1.2.2 Inertial Measurement Units

Inertial Measurement Unit (IMU), containing the gyroscopes and accelerometers, is a core of the inertial navigation system. Performance grades of IMUs are distinguished according to the accuracy level of the inertial sensors. Gyroscopes and accelerometers can be roughly divided into performance categories according to the bias stability specifications, with the lowest grade being used for consumer products, and the highest performing grades being used for mission critical strategic applications.

Four performance categories of the gyroscopes can be distinguished:

- Strategic gyros (0.0001 deg/h);
- Navigation-grade gyros (0.005-0.01 deg/h);
- Tactical gyros (0.1-1.5 deg/h);
- Consumer grade gyros (10-1000 deg/h).

Four performance categories of the accelerometers can be distinguished:

- Strategic accelerometers (1 μg);
- Navigation-grade accelerometers (0.01-0.1 mg);
- Tactical accelerometers (0.1-1 mg);
- Consumer grade accelerometers (>1 mg).

Performance, cost and applications of IMUs of different categories are summarized in Fig. 1.3. The strategic-grade or marine-grade IMUs are the highest grade systems that are commercially available. These systems are used for strategic navigation of ships and submarines, strategic missile navigation, and on spacecrafts for attitude control and orbit correction. A high-end marine-grade INS provide position errors that are less than 1.8 km per day. These

	Position Error	Cost	Technology	Application
Consumer Grade	50 m in 10 sec	**$1**	• MEMS	• navigation of ships and submarines, • strategic missile navigation, • spacecrafts attitude and orbit control
Tactical Grade	5 m per min	**$1 k**	• Mechanical • Optical • Quartz MEMS, MEMS	• mid-course missiles guidance • AHRS • UAVs
Navigation Grade	1.5 km per hour	**$100 k**	• Ring Laser Gyros • FOGs	• commercial and military aircrafts
Strategic/Marine Grade	1.8 km per day	**$1 M**	• HRG • FOGs	• navigation of ships and submarines, • strategic missile navigation, • spacecrafts attitude and orbit control

Figure 1.3: Performance, cost and applications of different performance grade IMU.

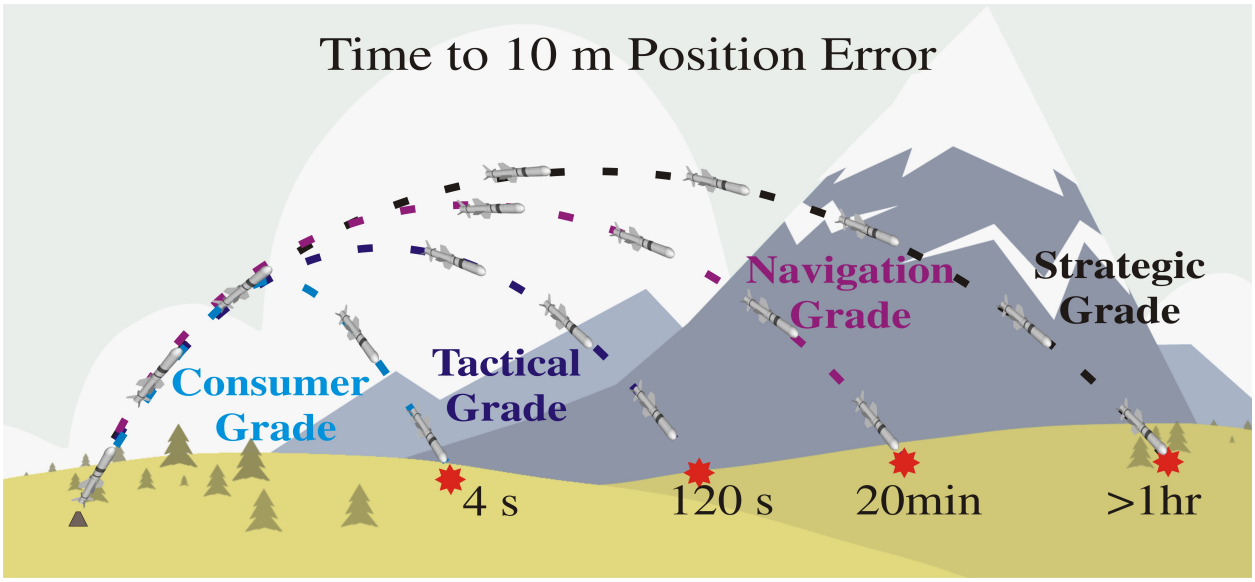

Figure 1.4: The lower the performance grade of the IMU, the shorter the time it can be used for self-contained un-aided navigation.

systems can cost over 1 million US dollars. An example of the strategic-grade IMU is the IMU based on the triads of the ultra-high precision Hemispherical Resonator Gyroscopes (HRG), [1]. Another example is a Fiber Optic Gyro CIRUS-A IMU, available from L3 Space & Navigation, [3].

Navigation-grade systems have slightly lower performance than the marine systems and are typically used on commercial and military aircrafts. The drifts of the navigation-grade systems are typically less than 1.5 km per hour. The cost of these systems is around 100,000

US dollars. An example of a navigation-grade IMU is the Honeywell HG9900 IMU, [2], which includes a triad of the Ring Laser Gyroscopes and a triad of quartz accelerometers.

Tactical-grade systems are used for mid-course missiles guidance, for Attitude and Heading Reference Systems (AHRS), Unmanned Aerial Vehicles (UAVs). The drifts of the tactical-grade systems are typically around 5 m per minute. The cost of these systems is around 1,000 US dollars. One example of a tactical-grade IMU is the Northrop Grumman LN-200, which contains three solid-state fiber-optic gyros and three solid-state silicon MEMS accelerometers, [4]. Another example is the SDI500 MEMS Quartz MEMS IMU from Systron Donner, [12]. Recently, a tactical-grade performance MEMS IMU ADIS16490 was introduced by Analog Devices, [5].

The lowest grade of IMUs is often referred to as consumer-grade. These sensors accumulate a position error of more than 10 m in just several seconds and they are not accurate enough to be used for self-contained inertial navigation. However, they are widely used in smart-phones and tablets, gaming platforms, image stabilization systems, and activity detection devices. Examples of MEMS compact consumer-grade IMUs are the ST Microelectronics LSM330DLC, [21], and InvenSense ICM-20601, [24].

The lower the performance grade of the IMU, the shorter the time it be used for self-contained un-aided navigation, Fig. 1.4. Typically, the consumer-grade IMU achieve a 10 m position error in several seconds, while the navigation and strategic/marine-grade IMUs are capable of maintaining the GPS-level position accuracy ($<$ 10m position error) for minutes and hours of un-aided navigation.

1.3 Literature Review

This Section reviews the currently commercially available MEMS IMUs and reports the status of laboratory research prototypes of compact tactical-grade performance MEMS IMUs.

1.3.1 MEMS IMUs Market

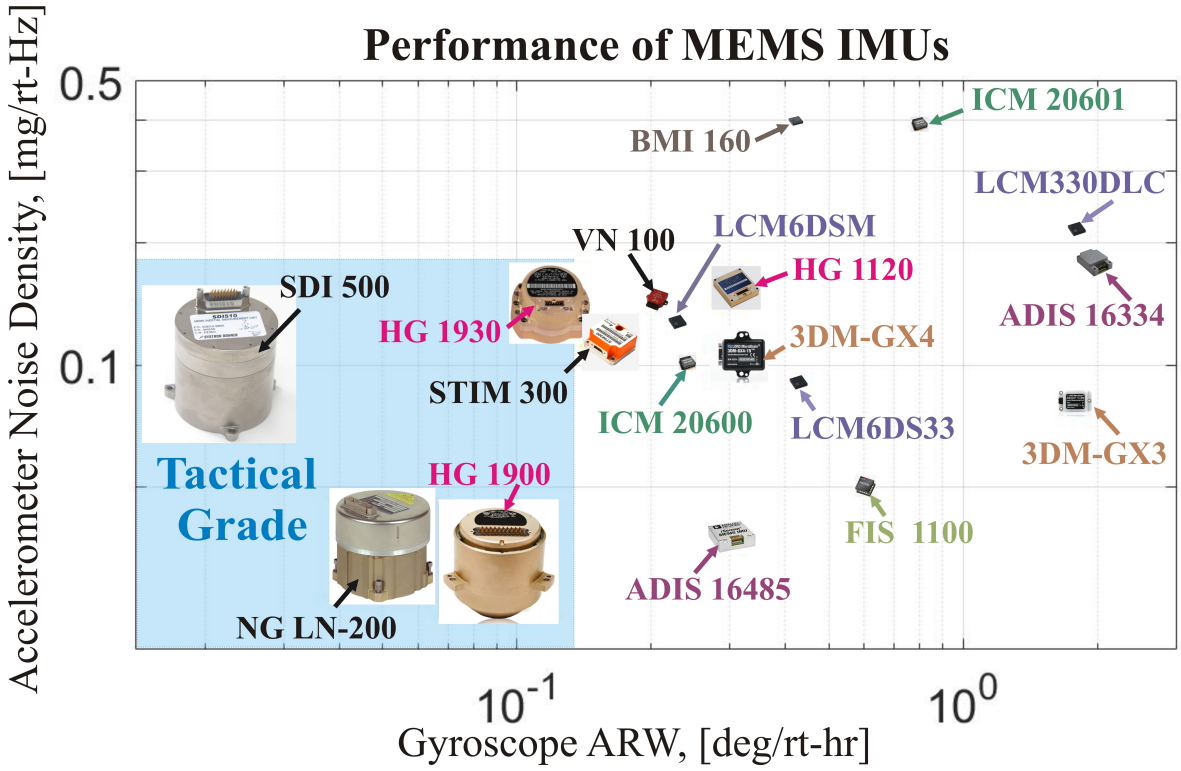

Figure 1.5: Current status of the commercially available MEMS IMUs. For size comparison, the area occupied by the unit image is proportional to the unit volume.

.

Current status of the commercially available MEMS IMUs is shown in Fig. 1.5. Tactical-grade performance IMUs contain accelerometers with noise density of less than 0.1 $mg/\sqrt{Hz}$ and gyroscopes with Angle Random Walk (ARW) of less than 0.1 $deg/\sqrt{hr}$. Currently, most of the IMUs in the tactical-grade performance class of devices have a large volume (100-470 cm^3) and high cost (several thousand \$), for-example, Systron Donner SDI-500 IMU, [12],

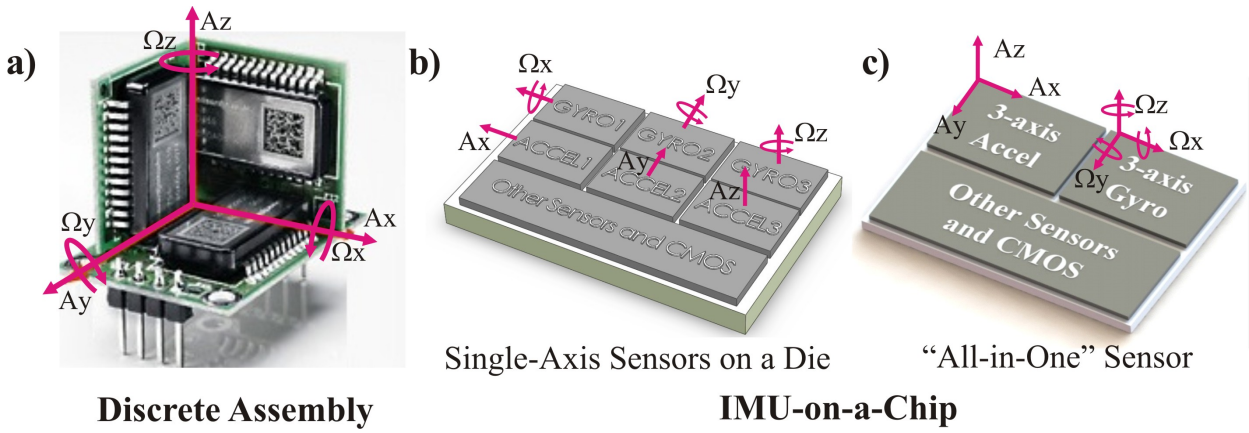

Figure 1.6: Conventional approaches for IMU implementation.

and Honeywell HG1900, [10]. On the other hand, consumer IMUs are available in <10 mm^3 volume for the cost of less than $5, for-example, ST Microelectronics LSM330DLC, [21], and InvenSense ICM-20601, [24]. The tactical-grade performance in a small volume and relatively low cost still remains to be a challenge.

Most conventional methods to implement a MEMS IMU fall into two general categories: discrete assembly of 6 individual sensors and IMU on-a-chip, Fig. 1.6.

Discrete Assembly of Sensors

A discrete assembly of 6 individual sensors is the most common approach for a high-performance IMU. Using this method, off-the-shelf single-axis sensors are assembled manually into a 3D IMU configuration, [9]-[14]. Single-axis sensors are typically optimized to reject off-axis inputs, allowing for improved IMU performance. However, this approach generally results in increased size and weight of the IMU, since it requires an assembly of 6 separate Printed Circuit Boards (PCB), each carrying a single sensor. For example, utilizing the discrete assembly approach, an ultra-low noise quartz MEMS IMU in 311 cm^3 volume has been demonstrated by Systron Donner, [12], a tactical grade MEMS IMUs in 278 cm^3 volume, [10], and in 82 cm^3 volume, [9], have been demonstrated by Honeywell, and a near-tactical

grade IMU in 35 cm^3 volume has been reported by Sensonor, [14].

IMU-on-a-Chip

Another method, a so-called single-chip approach, is based on fabrication of multi-axes or single-axis sensors on-a-single-chip. Utilizing a single chip approach, very small volume (<10 mm^3) consumer IMUs have been reported, such as a miniature multi-axis IMU in 10.9 mm^3 volume by Fairchild, [27], iNEMO inertial module in 6.2 mm^3 volume by ST Micro, [19], a 6-axis Motion Tracking device in 6.75 mm^3 volume by InvenSense, [24], and a 6-axis IMU by Bosch in 6 mm^3 volume, [33]. IMUs fabricated using a single-chip approach can be divided into two general categories: multiple single-axis sensors on a single substrate or multi-axis "all-in-one" sensors.

1. Single-Axis Sensors On-a-Chip

Single-chip implementation of multiple single-axis devices involves fabrication of the in-plane and out-of-plane sensors on the same substrate or placing them alongside, Fig. 1.6(b). This solution is significantly more compact than the discrete assembly approach. However, in such implementation, different devices would generally pursue self-contradicting objectives, and a compromise in performance must be ultimately made. For example, implemented alongside of the Z-axis sensor, the X- and Y-axis gyroscopes with the out-of-plane detection mode often suffer from large quadrature errors, [38]. In addition, high signal-to-noise ratio sensors, like degenerate mode gyroscopes in [6] and [39], are typically designed only for in-plane operation (for measuring rotation around the Z axis). Due to a lack of symmetry in XZ and YZ planes of SOI devices, a single-chip implementation of such sensors for all three axes of sensitivity is challenging.

2. "All-In-One-Sensors"

In "all-in-one-sensor" implementation, Fig. 1.6(c), a single mechanical element is used for measuring rotation and/or acceleration in multiple directions. For-example, ST Microelectronics' 3-axis gyroscope utilizes a single driving structure design ("beating heart") and multi-directional sense for tracking rotation around three orthogonal axes, [22]. Other examples of a single driving structure multi-axis sensors are the InvenSense 3-axis gyroscope, [25], and Fairchild 3-axis gyroscope, [27].

To provide 6-DOF position and orientation data, 3-axis gyroscopes are usually placed alongside with 3-axis accelerometers, such as in ST Microelectronics' LSM330DLC iNEMO Inertial Module, [21], Fairchild FIS-1100 IMU, [27], Bosch BMI055 6-axis inertial sensor, [32].

"All-in-one-sensor" approach delivers an advantage of extremely small volume (<10 mm^3). However, when a single structural element is used for measuring rotation or acceleration in multiple directions, a cross-talk between axes of sensitivity is a potential challenge.

1.3.2 Alternative Solutions

In recent years, a number of new approaches and fabrication processes has been demonstrated in research laboratories.

A MEMS IMU approach utilizing a multi-layer vertically stacked fused silica microsystem was developed by a research group at University of Michigan, [34]. The technique is based on a vertical stack bonding of multiple layers of inertial sensors and electronic components. This approach allows for the reduced IMU footprint, however mechanical, electrical, and thermal cross-talk, reliability of bonding, and implementation of interconnects remain to be a challenge, [34].

Research group at Georgia Institute of Technology, Atlanta, GA, USA explored a single-chip IMU approach, which evolves fabrication of 3-axis Bulk Acoustic Wave (BAW) gyroscopes

and 3-axis accelerometers on a single substrate using a modified version of the HARPSS process, [35]. Recently, the group presented a design of a pitch/roll gyroscope with the slanted electrodes for quadrature tuning. The sensor is designed for integration within a high-performance monolithic inertial measurement unit, [36].

A tri-fold IMU fabricated using a batch-mode 3D assembly process was reported by Evigia Systems Inc., [37]. The single-axis inertial sensors are fabricated separately before the final integration step. A silicon mounting cavity wafer with embedded vacuum channels is then utilized to assemble the individual sensors into a 3D IMU. The described approach allows for wafer-level assembly and packaging of the IMU devices, while enabling precision alignment of the sensors along the cavity sidewalls in the assembly process.

1.3.3 Folded IMU Approach

Folded MEMS fabrication process is another alternative solution for a high-performance micro-IMU. Patent US 8368154 describes a method to implement a 6-axis 3D IMU using conventional 2D micro-fabrication technology, [51]. The approach, first demonstrated by the

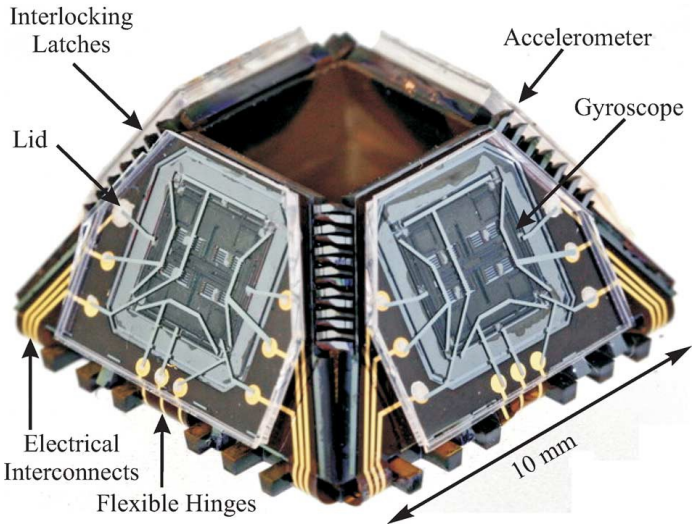

Figure 1.7: MEMS single-sided Folded IMU, [52].

research group at UC Irvine [52], utilizes a 3-D foldable silicon-on-insulator (SOI) structure with in-situ fabricated inertial sensors, Fig. 1.7. Planar Si structures, with polymer hinges interconnecting the panels, are fabricated on wafer-level and subsequently folded in a pyramidal shape, forming a compact IMU. The inter-locking latches located along the edges of each sidewall of a pyramid were used to lock the panels in a 3D structure. The sidewalls were then fused together to maintain the alignment of sensors and improve the IMU structural rigidity.

In the single-sided fabrication process, high-aspect ratio sensors and polyimide hinges were fabricated on the front side of the SOI wafer. Electrical interconnects were formed on the same side of the wafer and served to transmit signals from the sidewall to the base of the structure. In this approach, metal interconnects enabled the interface between sensors and external signal conditioning electronics.

In the first step of the fabrication process the flexible hinges are formed. Photo-definable polyimide is deposited onto a substrate and then a pattern is photo-lithographically defined. Once the polyimide is cured, the metal traces are formed on top of polyimide using the e-beam evaporation process and lift-off technique. Next, individual SOI sensors are defined on the same side of the SOI wafer and etched using DRIE process. Backside etching through the entire thickness of the SOI wafer is then performed to separate the Si panels and define the shape of the foldable IMU structures.

Along with all advantages of the single-sided Folded IMU approach [52], including a relatively simple 4-mask fabrication process, a small size of IMU, structural rigidity, and compatibility with the wafer-level packaging process, several challenges emerged during the initial studies. First, the thick layer of polyimide on the device side of a wafer limited the accuracy of lithography resulting in reduced performance of inertial sensors. Second, placing sensors and metal traces on the same side of the wafer introduced challenges associated with cleaning of devices at the end of the fabrication. This significantly decreased the yield of the overall

process, and fabrication runs did not result in fully operational IMUs. Additionally, the electrical connections between the front and the handle side of the wafer were not available as a part of the process. As a result, in the previously reported approach, the inner volume of the folded structure could not be used, for example, for integration with signal processing electronics.

Therefore, it is desired to develop an alternative double-sided Origami IMU approach, providing the following advantages: improved sensor performance, increased process yield, and wafer-level integration with signal processing electronics.

1.4 Research Objective

The main objective of this thesis is to identify the MEMS inertial sensors suitable for tactical-grade performance applications and to explore two different approaches for a compact 6-axis MEMS IMU: 1) "Origami-like" Folded MEMS IMU and 2) IMU utilizing a multi-axis sensing element.

We explored two different designs of a single-axis gyroscope for potential integration within a compact tactical-grade IMU. This includes a Dynamically Amplified Gyroscope (DAG) and a miniature Toroidal Ring Gyroscope (TRG).

A novel double-sided Folded IMU process is investigated in this dissertation, [53], [54]. The approach is based on a wafer-level fabrication of double-sided flat foldable structures, where inertial sensors are created on the device side of the wafer, while metal interconnects and polymer flexible hinges are formed on the handle side of the wafer. Two sides of the wafer are electrically connected by means of the through-wafer vertical interconnects. Different materials for flexible hinges were explored, including photo-definable polyimide and parylene-C.

In addition, this dissertation investigates a single-chip roll-pitch-yaw gyroscope, as a basic design for an ultra-compact multi-axis IMU, implemented using an "all-in-one-sensor" approach. The solution allows for extreme miniaturization, potentially at the cost of some possible sacrifice in performance. We considered an architecture of a three-axis gyroscope, which employs a single vibrational element with a torsional drive mode and a multi-directional sense modes. The sensor is designed for improved vibrational stability and reduced cross-talk between the operational modes.

1.5 Dissertation Outline

This dissertation is divided into six chapters and four supporting appendices.

The motivation of the research and the basic concepts of inertial navigation and inertial measurement units are outlined in Chapter 1. This Chapter also contains the prior art of the commercially available and laboratory prototypes of MEMS IMUs. Two different designs of inertial sensors, suitable for implementation within a miniature tactical-grade IMU, are explored in Chapter 2. "Origami-like" Folded MEMS approach for a compact IMU is presented in Chapter 3. In Chapter 4, IMU integration with electronics, enabled by the vertical electrical interconnects, is discussed. An approach for packaging of Folded 3D IMU devices is also presented in Chapter 4. Chapter 5 describes a compact IMU solution utilizing a multi-axis sensing element. Finally, the thesis is concluded in Chapter 6 with a summary of results and future research directions.

Chapter 2

Discrete Inertial Sensors for Miniature IMU

This Chapter explores two designs of Silicon-on-Insulator (SOI) gyroscopes for potential implementation within a miniature tactical-grade IMU device: Dynamically Amplified Gyroscope (DAG) and Toroidal Ring Gyroscope (TRG).

2.1 Dynamically Amplified Gyroscope

This Section presents a study on dynamics of a dual-mass MEMS vibratory gyroscope in presence of fabrication imperfections and reports a method for precision electrostatic frequency tuning of the operational modes. A number of multi-mass MEMS gyroscopes have emerged in recent years, pursuing different goals, such as dynamic balance, increased bandwidth, and dynamic amplification. Along with many of perceived advantages, several challenges associated with mode-matching in a system with increased number of Degrees-of-Freedom (DOF) have to be considered. This study shows that it is possible to apply the DC tuning

techniques, similar to tuning a conventional single-mass gyroscope, for precision tuning in a dual-mass sensor without loosing advantages of increased DOF of the system. The presented frequency trimming technique is based on assessing the modes mismatch and cross-coupling by means of fitting the experimental frequency response curves to the analytical solutions of the dual-mass system in presence of imperfections. The tuning algorithm involves, first, identification of the stiffness mismatch along the two axes and the anisoelasticity angles α and β, then choosing the tuning DC voltages for modification of the diagonal, off-diagonal, and coupling terms in the stiffness matrix. The method of electrostatic tuning was validated through the experimental characterization of a dual-mass dynamically amplified gyroscope, where the coupling between the two operational modes was eliminated and frequency split was reduced from 26 Hz down to 50 mHz, resulting in 17.5X increase in the gyroscope scale factor and significantly improved noise characteristics.

2.1.1 Introduction

Conceptually, a single-axis gyroscope requires a single proof-mass for measuring the Coriolis acceleration induced angular rate signal. In recent years, however, a variety of multi-mass solutions emerged, offering advantages, such as dynamic balance, Fig. 2.1(a), increased bandwidth, Fig. 2.1(b), and dynamic amplification, Fig. 2.1(c).

Dynamically balanced systems, Fig. 2.1(a), such as, for example, the Dual Foucault Pendulum (DFP) gyroscope, [58], utilize two, four or more dynamically equivalent, mechanically coupled proof masses, oscillating in the anti-phase motion, for improved vibration immunity and anchor loss mitigation, resulting in the ultra-high quality factor. The concept of dynamic balance for anchor loss mitigation and a common-mode rejection of shock and vibration is employed in the design of the Tuning Fork (TF) Gyroscope, [59], where two dynamically equivalent, mechanically coupled proof masses are utilized. A similar principle is employed

in the design of a Quadruple Mass Gyroscope (QMG), [60] , where the structural element is formed by the four mechanically coupled proof masses, and thus enabling dynamic balance of forces and moments in drive and sense modes, as opposed to a dynamic balance of forces in a single-axis TF architecture.

In [61] C. Acar et al. demonstrated an increased bandwidth inherently robust dual-mass gyroscope. The mechanical element was comprised of a two degree-of-freedom (DOF) sense-mode oscillator, formed by two interconnected masses, Fig. 2.1(b). The device was operated in the flat region of the sense-mode response curve, where the amplitude and phase of the response are insensitive to environmental fluctuations.

Another example of a multi-mass solutions is a dual-mass dynamically amplified system, Fig. 2.1.(c), where an increased number of degree-of-freedom (DOF) results in dynamic amplification of motion and improved sensitivity of the device, [62]-[63].

Along with many advantages of the dual-mass systems, the structural symmetry is a challenge. The symmetric mechanical element is necessary for the mode-matched devices, and a method of compensation for fabrication imperfections is required.

Most methods of matching the operational modes of the gyroscope can be divided in two general categories: passive techniques, such as post-processing mechanical trimming methods, [64]-[68], and active techniques, such as electrothermal, [69], feedback control, [70]-[72], and electrostatic tuning, [73]-[85].

Mechanical trimming methods are based on a permanent modification of the structure by means of selective adding/removing material to/from the vibrational element. Such trimming can employ, for example, laser ablation, [64]-[65], focused ion beam, [66], and selective deposition, [67]-[68]. The main advantage of this technique is a permanent change of the sensor structure, enabling minimization of voltages necessary for subsequent electrostatic tuning. Passive tuning method, however, is mainly limited to off-line calibration in a labo-

ratory environment.

In contrast to the mechanical trimming, active tuning techniques do not introduce a permanent defect to the structure, do not require an expensive precision trimming equipment, and can be implemented in real-time after the sensor is packaged, including during an on-line in-field calibration. A method of active thermal tuning for microresonators using resistive heaters to generate localized thermal stresses in the structure is described in [69]. A number of active tuning approaches using feedback control for quadrature signal compensation, [70], and precision mode matching, [71]-[72], were reported in literature.

Electrostatic tuning, which employs electrostatic force gradients to selectively modify the effective stiffness of a certain operational mode, is a common active technique for the gyroscope mode-matching. The method has been extensively studied by different research groups. Active electrostatic "trimming" utilizing non-linearity of capacitive parallel-plate actuators was applied for frequency tuning and reduction of modes coupling in rate integrating gyroscopes, [73]. An approach for electrostatic tuning of the wineglass modes in MEMS ring gyroscopes was described in [74] and [97]. In these publications, the 16 tuning electrodes surrounding the ring structure were used to independently modify the diagonal and off-diagonal terms of the structural stiffness matrix and to achieve a reduction of the frequency split between the modes. Electrostatic tuning has been successfully used for many other different types of planar, [139], [75]-[80], and three-dimensional structures, [81]-[85].

In this Section, we first introduce a concept of a Dynamically Amplified Gyroscope (DAG), then present a method for precision electrostatic tuning of the operational modes in a gyroscope with a dual-mass structural element. Most of the electrostatic tuning methods, previously described in the literature, consider a 2-degrees-of-freedom system with a 2x2 stiffness matrix, [73]-[97]. However, increasing the number of proof-masses in a gyroscope results in a more complex form of the system stiffness matrix. Hence, new algorithms have to be developed for precision electrostatic tuning. In this Section, we study the dynamics of

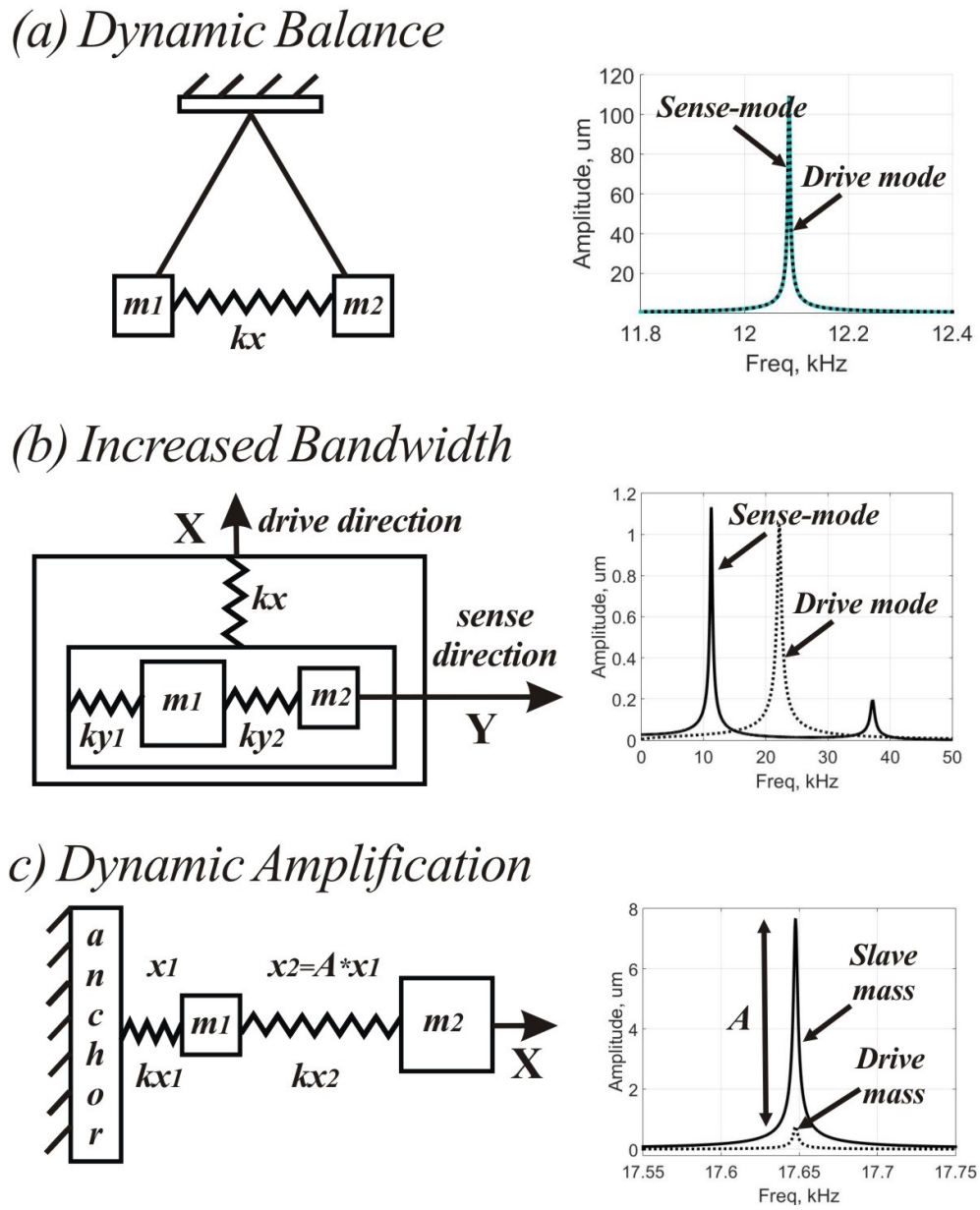

Figure 2.1: Examples of multi-mass gyroscopes: (a) dynamically balanced two-mass system, (b) dual-mass system with 2-DOF sense-mode oscillator; (c) dynamically amplified system.

an imperfect dual-mass system, using as an example a dynamically amplified MEMS gyroscope. A method of electrostatic frequency tuning in such multi-degree of freedom system is described and experimental verification of the proposed approach is presented.

Our report of research results of a MEMS Dynamically Amplified Gyroscope is organized as follows. We will first introduce the dynamic amplification concept, Section 3.2.2. We will

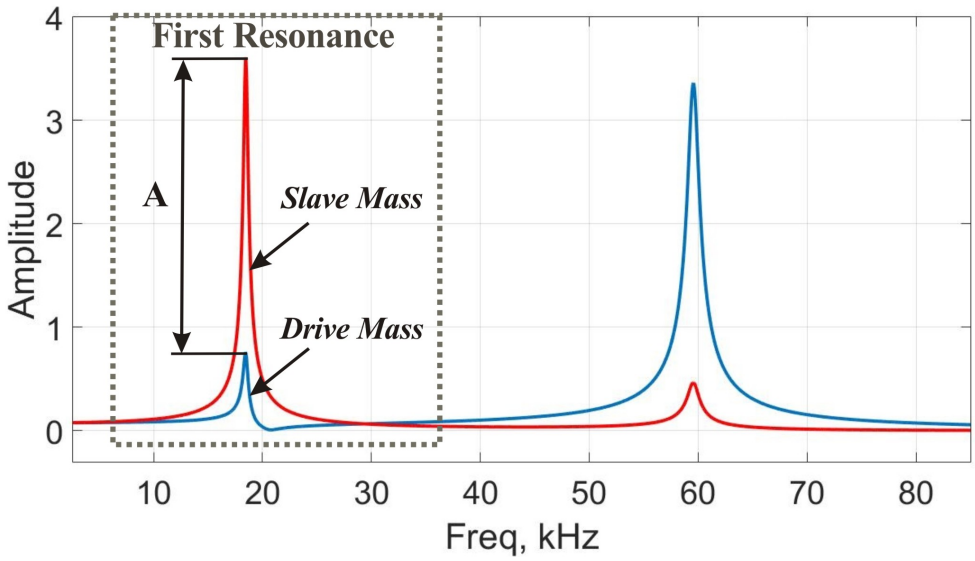

Figure 2.2: Dynamic amplification at the first resonant frequency of the coupled dual-mass system.

then present the design of a dynamically amplified gyroscope, which is used for illustration of the frequency tuning algorithm, Section 3.2.3. In the same Section 3.2.3, we will also derive dynamic equations of a dual-mass system and report results of experimental characterization of the fabricated prototypes, demonstrating the amplitude amplification phenomenon. In Section 3.2.4, we will describe an algorithm for the precision electrostatic tuning of a dual-mass dynamically amplified gyroscope and provide experimental verification of the proposed approach. Introduction of the tuning algorithm will be followed by comparison of the sensor performance, before and after electrostatic tuning, in Section 3.2.5. Section 3.2.6 concludes the paper with a discussion on applicability of the presented electrostatic compensation technique.

2.1.2 Dynamic Amplification Concept

A dual mass-spring model of a simple dynamically amplified system is shown in Fig. 2.1(c). The system is comprised of two mechanically coupled proof-masses: drive mass m_1 and slave mass m_2. Here, k_{x1} is the spring constant of coupling between the mass m_1 and the anchor,

k_{x2} is the spring constant of coupling between the two proof-masses. The dynamic equations of motion for this system can be expressed as:

$$\begin{aligned} m_1\ddot{x}_1 + c_1\dot{x}_1 + (k_{x1} + k_{x2})x_1 - k_{x2}x_2 = F_{x1}; \\ m_2\ddot{x}_2 + c_2\dot{x}_2 + k_{x2}x_2 - k_{x2}x_1 = 0, \end{aligned} \tag{2.1}$$

where c_1 and c_2 are the damping coefficients of the drive and the slave masses, respectively. F_{x1} is the external force applied to the drive mass.

The system of equations (2.1) can be solved with respect to the ratio between the amplitudes of the drive and slave masses, [62]:

$$A = \frac{X_2}{X_1} = \frac{k_{x2}}{k_{x2} + c_2(i\omega) - m_2\omega^2}, \tag{2.2}$$

where ω is the frequency of an external force applied to the drive mass. The frequency of the driving force is the first resonant frequency of the coupled dual-mass system (Fig. 2.2), where the dynamic amplification condition (A>1) is satisfied and high deflections of the slave mass can be achieved:

$$\omega = \frac{1}{2}\left[\frac{k_{x1} + k_{x2}}{m_1} + \frac{k_{x2}}{m_2} - \sqrt{\frac{(k_{x1} + k_{x2})^2}{m_1^2} + \frac{k_{x2}^2}{m_2^2} - \frac{2k_{x2}(k_{x1} - k_{x2})}{m_1 m_2}}\right]. \tag{2.3}$$

From equations (2.2) and (2.3), it can be concluded that in order to maximize the dynamic amplification factor A, the spring constant k_{x2}, the damping coefficient c_2 and mass m_1 have to be reduced, while the spring constant k_{x1}, and mass m_2 have to be increased.

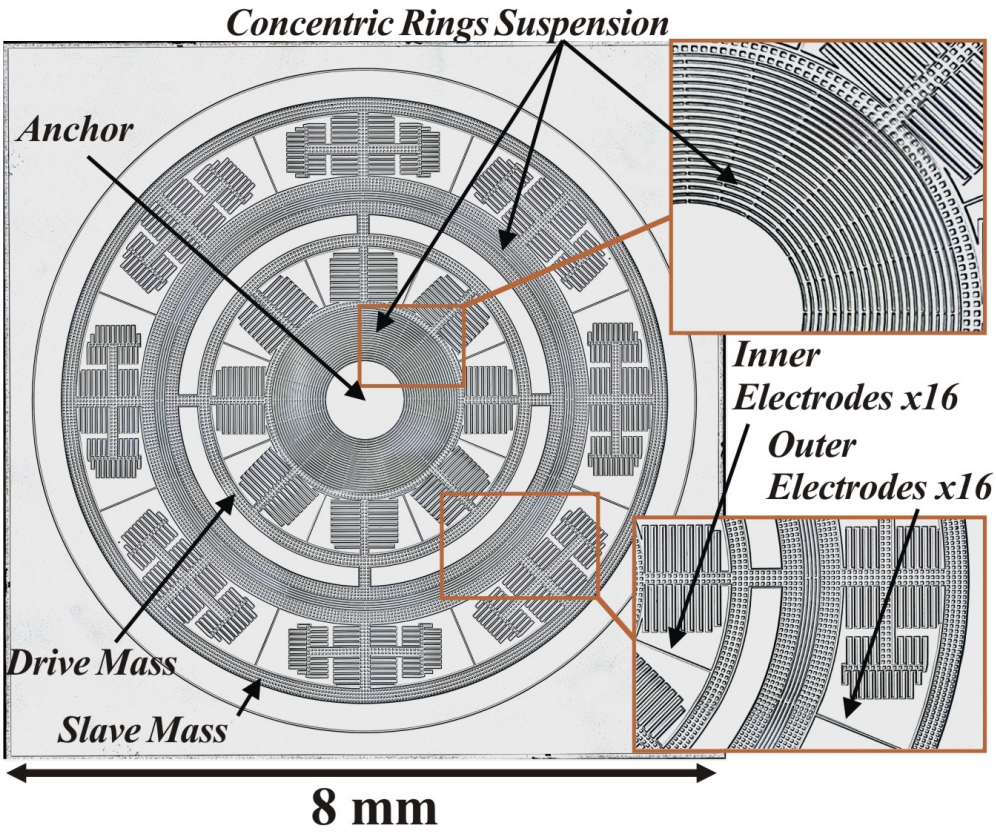

Figure 2.3: Micro-photograph of a fabricated prototype of the dynamically amplified dual-mass gyroscope.

2.1.3 Dynamically Amplified Gyroscope Implementation

Design and Fabrication

The dynamic amplification concept can be applied in design of a MEMS gyroscope with a dual-mass architecture, Fig. 2.3, where the increase in structural degrees of freedom is used to improve sensitivity, linearity, and to reduce drift, [62], [63]. In a dynamically amplified gyroscope, the first "drive mass" is actively driven to oscillate at a small amplitude of motion, in a linear operation regime. Meanwhile, the mechanically coupled "slave mass" is used for sensing the Coriolis signal. The amplitude of motion of the "slave mass" is dynamically amplified resulting in an increased scale factor of the gyroscope.

The implemented gyroscope prototypes have a footprint of 7.4x7.4 mm^2. The design param-

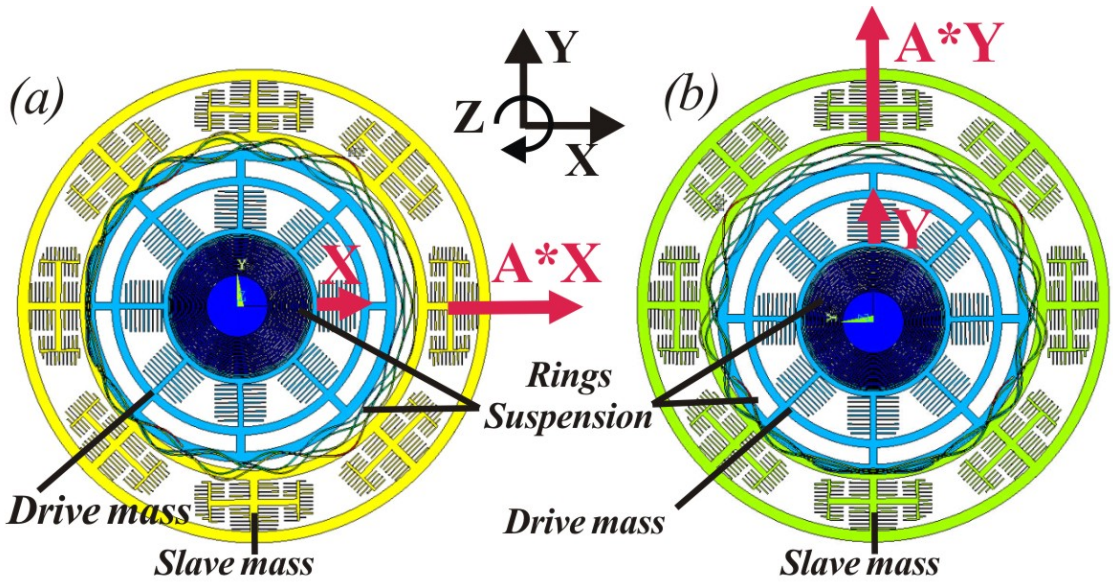

Figure 2.4: FEA model, showing characteristic motion of "drive mass" and in-phase amplified motion of "slave" mass in (a) drive-mode direction; (b) sense-mode direction.

eters are summarized in Table 2.1. In order to investigate the dependance of the sensor's dynamic amplification factor on structural imperfections in the system, two designs of the gyroscope were studied, providing the dynamic amplification of 5X (Design I) and 10X (Design II). The sensor is comprised of an inner, "drive mass", and an outer, "slave mass", mechanically connected by means of the concentric rings suspension. The outer suspension is formed by 18 μm thick concentric rings between the two masses. The inner suspension is formed by 18 μm thick concentric rings, connecting the inner mass to the center anchor. Each proof-mass is surrounded by 16 electrodes with parallel plates for drive, pick-off, and electrostatic tuning. The nominal capacitive gap between the parallel plates is 5 μm.

The two proof-masses are driven to oscillate in the in-phase motion, Fig. 2.4. Devices were designed to operate at the resonant frequency of 17.5 kHz.

The axisymmetric dynamically amplified gyroscope can operate in a rate or an angle measuring mode, Fig. 2.5. In the rate measuring mode of operation, the drive and sense modes consist of the translational motion of the driving mass, and dynamically amplified in-phase translational motion of the "slave mass" along the X and Y axes, correspondingly, Fig. 2.5(a).

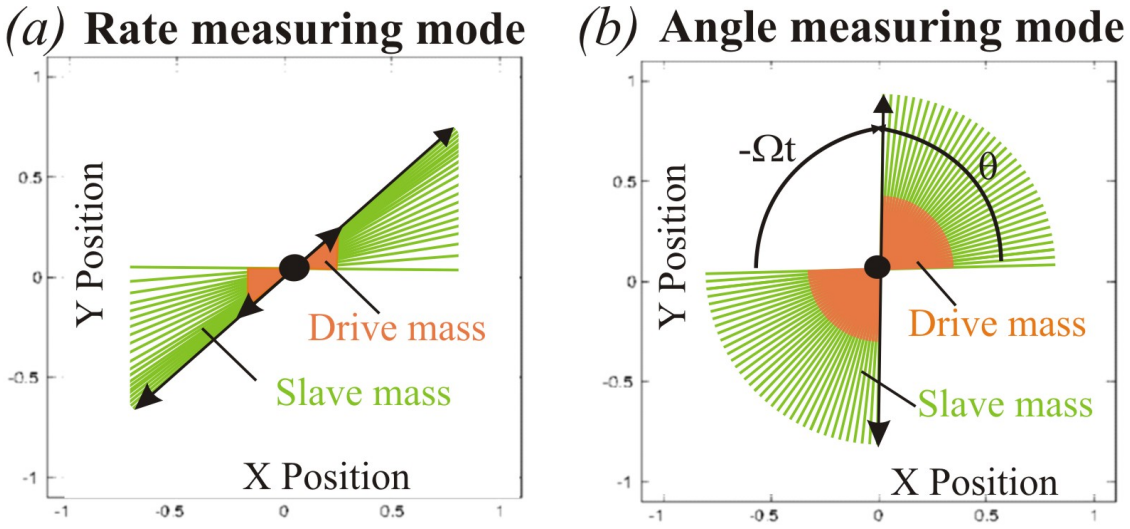

Figure 2.5: (a) In rate measuring mode, sense deflection (Y-axis) is proportional to the input angular rate; (b) In angle measuring mode, angle of precession follows the negative angle of rotation (or, equivalently, preserves its orientation of vibration in the absolute-inertial coordinate frame).

Table 2.1: Design Parameters of the Dynamically Amplified Gyroscope

	Design I	**Design II**
Dynamic Amplification	5 X	10 X
Footprint, mm^2	7.4x7.4	7.4x7.4
Drive mass, kg	1.23e-6	1.23e-6
Slave mass, kg	2.07e-6	2.07e-6
Frequency, kHz	17.5	19.0
Number of rings in inner suspension	22	7
Number of rings in outer suspension	4	4
Width of rings in suspension, μ**m**	18	18
Stiffness k_1**, kN/m**	84.9	166.8
Stiffness k_2**, kN/m**	43.4	43.4
Capacitive gap, μ**m**	5	5
Total cap. of inner electrodes, pF	7.21	7.21
Total cap. of outer electrodes, pF	16.5	16.5

The mechanical element is driven to oscillate in drive mode along the X direction. The sense mode oscillations (along the Y direction) are induced by the Coriolis force due to inertial rotation. The amplitude of the slave mass deflection along the Y axis is proportional to the input angular rate, [98]:

$$A^{y}_{slave} = 2k_g \Omega A^{x}_{slave} \frac{Q_y}{\omega_y \sqrt{1 + (2Q_y \Delta\omega/\omega_y)^2}}, \tag{2.4}$$

where A^{x}_{slave} is the amplitude of oscillations of the dynamically amplified "slave" mass along the X direction, k_g is the sensor's angular gain factor, Ω is the applied angular rate, ω_y and Q_y are the sense mode natural frequency and quality factor, respectively, $\Delta\omega$ is the frequency mismatch between the modes.

In the rate integrating mode of operation, the in-phase translational motion of the two proof-masses is free and unconstrained, while the motion of the slave mass is dynamically amplified. Generally, the trajectory of free oscillations is an elliptical orbit (or a straight line, in an ideal case). When an angular rotation is applied, Fig. 2.5(b), the line of oscillation of the two proof-masses starts precessing in presence of the Coriolis force, following the negative angle of the applied rotation, [98]:

$$\theta = -k_g \int \Omega(\tau) d\tau, \tag{2.5}$$

where k_g is the sensor angular gain factor and Ω is the applied angular rotation. For the rate integrating mode of operation, the angular rate drift of the gyroscope can be expressed as [88]:

$$\dot{\theta} \leq \frac{1}{2} \left| \Delta(\frac{1}{\tau}) \right| + \frac{q}{A_{slave}} \left| \Delta\omega \right|, \tag{2.6}$$

where $\left|\Delta(\frac{1}{\tau})\right|$ is the difference in damping coefficients along the two principle directions of vibration, $|\Delta\omega|$ is the frequency split between the two modes of vibration, A_{slave} is the amplitude of oscillation along the major diagonal of the elliptical orbit, q is the amplitude of oscillation along the minor diagonal of the elliptical orbit.

From equations (2.4) and (2.6), it can be concluded that dynamic amplification is beneficial for both the angular rate and the angle measuring modes of operation since it allows for improved scale factor and reduced drift of the gyroscope.

Prototypes of the dynamically amplified gyroscope, Fig. 2.3, were fabricated on a wafer-level using a single-mask SOI fabrication process with a 100 μm thick device layer and using a 1.5 μm thick thermal oxide layer as a hard mask for the Deep Reactive Ion Etching (DRIE) of silicon. The SPTS APS PM tool, [89], was utilized to etch the oxide layer to create the hard mask, while STS System DRIE, [90], was utilized for etching the silicon device layer. Once fabrication process was complete, the wafers were diced using an ultra-clean stealth dicing method (Disco Hi-Tec America, Inc.). The sensors were then released using a vapor HF process (for 1 hr 15 min at 45 °C temperature) and packaged in ceramic Leadless Chip Carrier (LCC) packages.

Equations of Motion

The dynamics of a dual-mass system is analyzed in the non-inertial coordinate frame associated with the gyroscope (the coordinate frame attached to the outer frame of the die). The equations of motion are derived using a dual mass-spring-damper model. In an "ideal" case (Fig. 2.6(a)), when damping, stiffness mismatch and structural anisoelasticity are ignored, the governing equations of motion of a gyroscope, measuring rotation about the Z-axis, are expressed in a matrix form as:

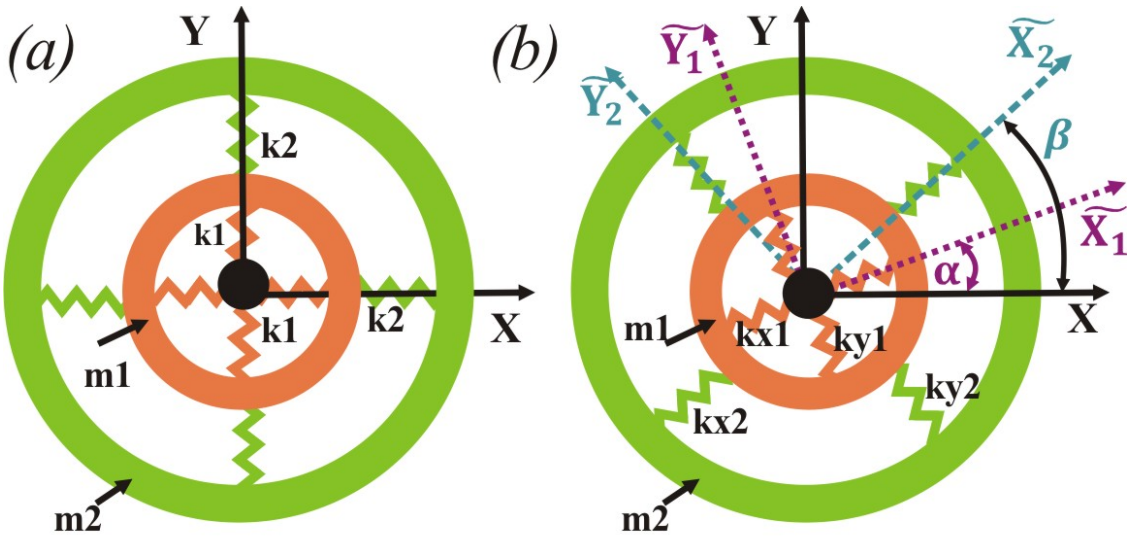

Figure 2.6: (a)"Ideal" dual-mass system, when damping, stiffness mismatch, and structural anisoelasticity are not considered; (b) Imperfections in suspension and mass cause the misalignment of the principle axes of elasticity.

$$[M]\ddot{q} + [C]\dot{q} + [K]q + [R_c]\dot{q} = [F], \tag{2.7}$$

where q is the vector of the generalized coordinates $q = [x_1 y_1 x_2 y_2]^T$. The generalized mass and damping matrices have the structure:

$$M = \begin{bmatrix} m_1 & 0 & 0 & 0 \\ 0 & m_1 & 0 & 0 \\ 0 & 0 & m_2 & 0 \\ 0 & 0 & 0 & m_2 \end{bmatrix}, C = \begin{bmatrix} c_1 & 0 & 0 & 0 \\ 0 & c_1 & 0 & 0 \\ 0 & 0 & c_2 & 0 \\ 0 & 0 & 0 & c_2 \end{bmatrix}$$

The external force vector and the Coriolis force matrix have the structure:

$$F = \begin{bmatrix} F_{x1} \\ F_{y1} \\ 0 \\ 0 \end{bmatrix}, R_c = \begin{bmatrix} 0 & -2m_1\Omega & 0 & 0 \\ 2m_1\Omega & 0 & 0 & 0 \\ 0 & 0 & 0 & -2m_2\Omega \\ 0 & 0 & 2m_2\Omega & 0 \end{bmatrix},$$

where Ω is the angular rate applied around the Z axis.

Finally, the generalized stiffness matrix has the structure:

$$K = \begin{bmatrix} k_1 + k_2 & 0 & -k_2 & 0 \\ 0 & k_1 + k_2 & 0 & -k_2 \\ -k_2 & 0 & k_2 & 0 \\ 0 & -k_2 & 0 & k_2 \end{bmatrix}, \tag{2.8}$$

where k_1 and k_2 are the stiffness coefficients for the inner and the outer mass suspension, correspondingly.

Experimental Demonstration of Dynamic Amplification

Experimental frequency response of the sensor was obtained using electrostatic excitation with 10V DC voltage and 60mV AC voltage, applied to the driving electrodes of the inner mass. Design I devices were designed to operate at the resonant frequency of 17.5 kHz and to provide the dynamic amplification of 5X, Fig. 2.7(a). Characterization of the fabricated Design I prototype revealed the central frequency of 17.44 kHz with the amplification factor of 4.7X and the frequency split (Δf) of 26 Hz, Fig. 2.7(b). Design II devices were designed to operate at the resonant frequency of 19 kHz and to provide the dynamic amplification of 9.2X, Fig. 2.8(a). Characterization of the fabricated Design II prototype revealed the

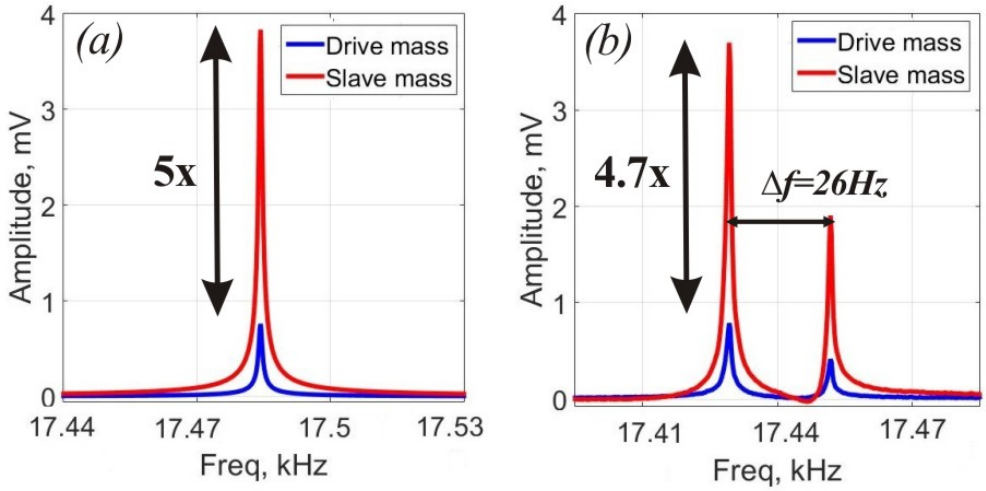

Figure 2.7: Gyroscope Design I: (a) Simulated freq. response with predicted amplification of 5X. (b) Experimental response with coupling of drive and sense modes: Δf=26Hz; amplification 4.7X.

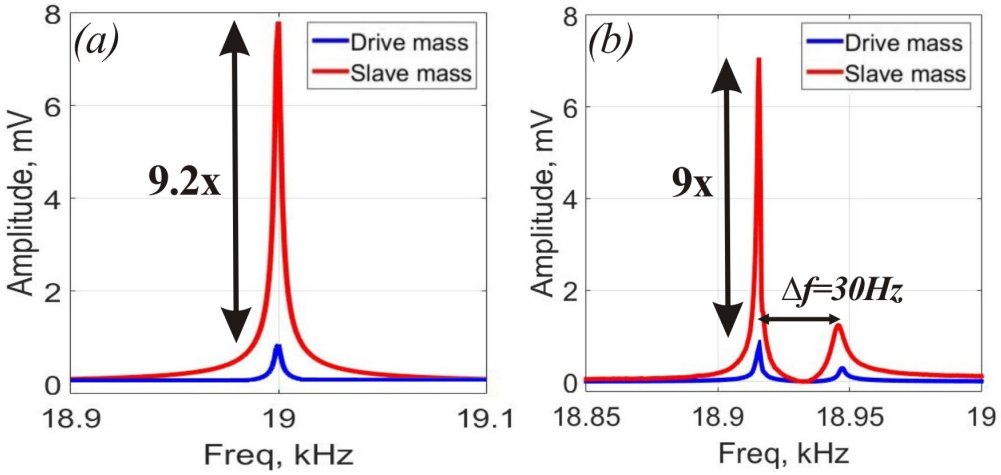

Figure 2.8: Gyroscope Design II:(a) Simulated freq. response with predicted amplification of 9.2X. (b) Experimental response with coupling of drive and sense modes: Δf=30Hz; amplification 9X.

central frequency of 18.93 kHz with the amplification factor of 9X and the frequency split (Δf) of 30 Hz, Fig. 2.7(b).

For the drive and slave masses in Fig. 2.7(b) and Fig. 2.8(b), the first peak on the sense-mode frequency response curves corresponds to the frequency of the sense mode, the second peak corresponds to the frequency of the drive mode and is caused by the coupling of the

drive motion to the sense mode. This coupling leads to the energy distribution between the modes and results in reduced amplitude amplification factor, as compared to the analytically predicted, 4.7X vs 5X, Fig. 2.7, and 9X vs 9.2X, Fig. 2.8. It is important to notice that a stronger coupling between the drive and sense modes of the Design I prototype resulted in higher drop in the amplification factor, as compared to the Design II prototype.

2.1.4 Electrostatic Correction of Structural Imperfections

Experimental frequency characterization of 12 prototypes revealed a frequency split between the modes (Δf) in the range from 25 Hz to 59 Hz, which arises from fabrication-induced asymmetries in the mechanical element. In the following Section, the method of electrostatic correction of structural imperfections will be introduced and utilized to tune the Design I gyroscope prototype, which was shown to have a stronger coupling between the operational modes, Fig. 2.7.

In the case of a dual-mass gyroscope, the structural symmetry is defined by a 4x4 stiffness matrix, Eq. (5.8). Imperfections in suspension and mass cause the misalignment of the principle axes of elasticity [86],[87] of both masses, resulting in non-zero off-diagonal terms of the stiffness matrix and increased coupling between the drive and sense modes, Fig. 2.7(b) and Fig. 2.8(b). Fabrication imperfections of both masses also result in non-equal diagonal terms of the stiffness matrix, leading to frequency splits between the modes. The resulting generalized stiffness matrix for the dual-mass system in presence of imperfections has the structure:

$$K = \begin{bmatrix} k_{11} & k_{12} & k_{13} & k_{14} \\ k_{12} & k_{22} & k_{23} & k_{24} \\ k_{13} & k_{23} & k_{33} & k_{34} \\ k_{14} & k_{24} & k_{34} & k_{44} \end{bmatrix}, \tag{2.9}$$

where the diagonal terms are:

$$k_{11} = cos^2\alpha(k_{x1} + k_{x2}) + sin^2\alpha(k_{y1} + k_{y2}),$$

$$k_{22} = sin^2\alpha(k_{x1} + k_{x2}) + cos^2\alpha(k_{y1} + k_{y2}),$$

$$k_{33} = cos^2\beta * k_{x2} + sin^2\beta * k_{y2},$$

$$k_{44} = sin^2\beta * k_{x2} + cos^2\beta * k_{y2};$$

the off-diagonal terms are:

$$k_{12} = 0.5 * sin2\alpha(k_{x1} + k_{x2} - k_{y1} - k_{y2}),$$

$$k_{34} = 0.5 * sin2\beta(k_{x2} - k_{y2});$$

and the coupling terms are:

$$k_{13} = -k_{x2}cos\beta * cos\alpha - k_{y2}sin\beta * sin\alpha;$$

$$k_{14} = -k_{x2}sin\beta * cos\alpha + k_{y2}cos\beta * sin\alpha;$$

$$k_{23} = -k_{x2}cos\beta * sin\alpha + k_{y2}sin\beta * cos\alpha;$$

$$k_{24} = -k_{x2}sin\beta * sin\alpha - k_{y2}cos\beta * cos\alpha.$$

Here, α and β are the anisoelasticity angles for the inner and outer masses; k_{x1} and k_{x2} are the stiffness coefficients along the X axis for the inner and the outer mass suspension; k_{y1} and k_{y2} are the stiffness coefficients along the Y axis for the inner and the outer mass suspension, Fig. 2.6(b).

Our method for precision electrostatic frequency tuning of the operational modes is based

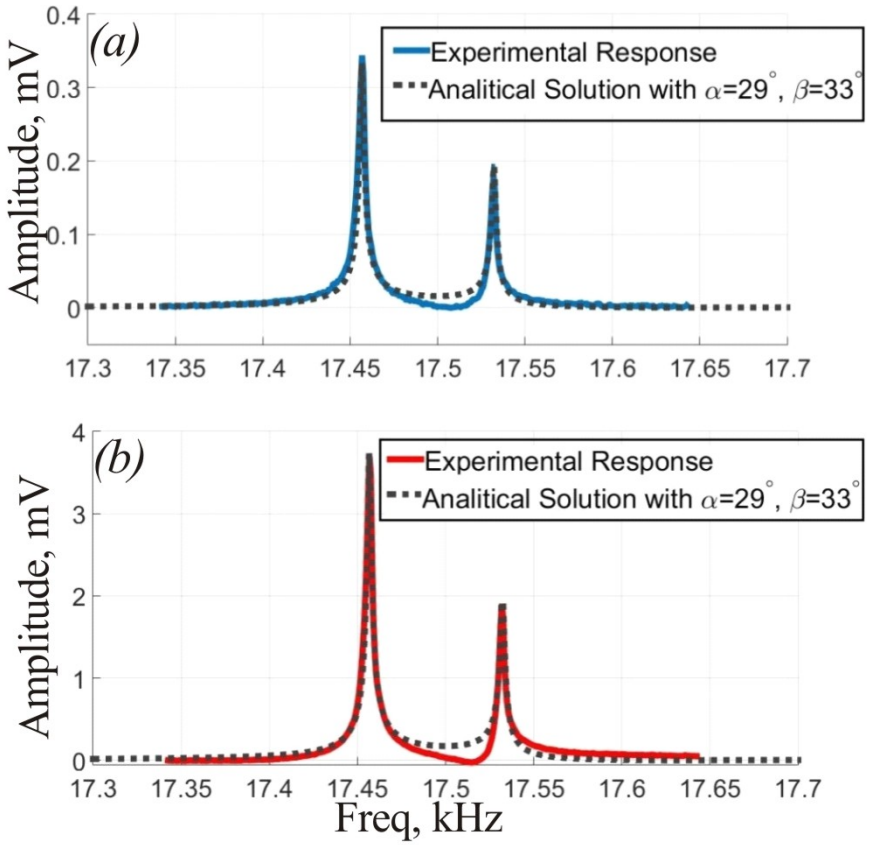

Figure 2.9: Experimental frequency responses of (a) drive and (b) slave masses were fitted to the analytical solutions of the dynamic equations in presence of imperfections.

on estimation of the anisoelasticity angles using the experimental frequency responses of the inner and outer proof-masses, followed by identification of the tuning voltages using an analytical solution of the dynamic equations in presence of imperfections:

$$[M]\ddot{q} + [C]\dot{q} + ([K] - [K_e])q + [R_c]\dot{q} = [F], \tag{2.10}$$

where $([K] - [K_e])$ is the electrostatically modified stiffness matrix.

In order to identify the anisoelasticity and modes mistuning parameters, the experimental frequency responses of the drive and slave masses were fitted to the analytical solutions of the dynamic equations (2.7) for the dual-mass system in presence of imperfections, Fig. 2.9. For the prototype of the dynamically amplified gyroscope (Design I) with a 26 Hz frequency

split (Δf) between the operation mode, the anisoelasticity angles α= 29° and β=26° were found.

Next, using the equation (2.10), the terms of the matrix K_E for tuning the diagonal, off-diagonal and coupling terms of the stiffness matrix were analytically identified and the necessary tuning voltages for the two masses were determined.

Electrostatic tuning matrix has the structure:

$$K_e = \begin{bmatrix} k_{e11} & k_{e12} & 0 & 0 \\ k_{e12} & k_{e22} & 0 & 0 \\ 0 & 0 & k_{e33} & k_{e34} \\ 0 & 0 & k_{e34} & k_{e44} \end{bmatrix}. \tag{2.11}$$

Configuration of the drive, the sense and the tuning electrodes of a dynamically amplified dual-mass gyroscope is shown in Fig. 2.10. Electrodes X1D, X1S and X2D, X2S are used for drive and/or signal pick-off along the X-axis for the mass m_1 and mass m_2, correspondingly. Electrodes Y1D, Y1S and Y2D, Y2S are used for drive and/or signal pick-off along the Y-axis for the mass m_1 and mass m_2, correspondingly. Electrodes TX1A, TX1W, TY1A, and TY1W are used for tuning the off-diagonal stiffness terms corresponding to the mass m_1. Electrodes TX2A, TX2W, TY2A, and TY2W are used for tuning the off-diagonal stiffness terms corresponding to the mass m_2.

The terms of the electrostatic tuning matrix can be represented as:

$$k_{e11} = V_{x1}^2 + (cos(\gamma))^2 T_{1a}^2 + (cos(\gamma)^2 T_{1w}^2;$$

$$k_{e12} = cos(\gamma) sin(\gamma) T_{1a}^2 - cos(\gamma) sin(\gamma) T_{1w}^2;$$

$$k_{e22} = V_{y1}^2 + sin((\gamma))^2 T_{1a}^2 - sin((\gamma))^2 T_{1w}^2;$$

$$k_{e33} = V_{x2}^2 + cos((\gamma))^2 T_{2a}^2 + cos((\gamma))^2 T_{2w}^2;$$

$$k_{e34} = cos(\gamma)sin(\gamma)T_{2a}^2 - cos(\gamma)sin(\gamma)T_{2w}^2;$$

$$k_{e44} = V_{y2}^2 + sin((\gamma))^2 T_{2a}^2 - sin((\gamma))^2 T_{2w}^2,$$

where T_{1a} and T_{2a} are the tuning voltage applied to the mass m_1 and mass m_2 along the A-axis; T_{1w} and T_{2w} are the tuning voltage applied to the mass m_1 and mass m_2 along the W-axis; γ is an angle of the off-diagonal tuning electrodes.

Simulated frequency response curves for different voltages of the off-diagonal and diagonal tuning are shown in Fig. 2.11(a) and Fig. 2.12(a), correspondingly. For sensor excitation,

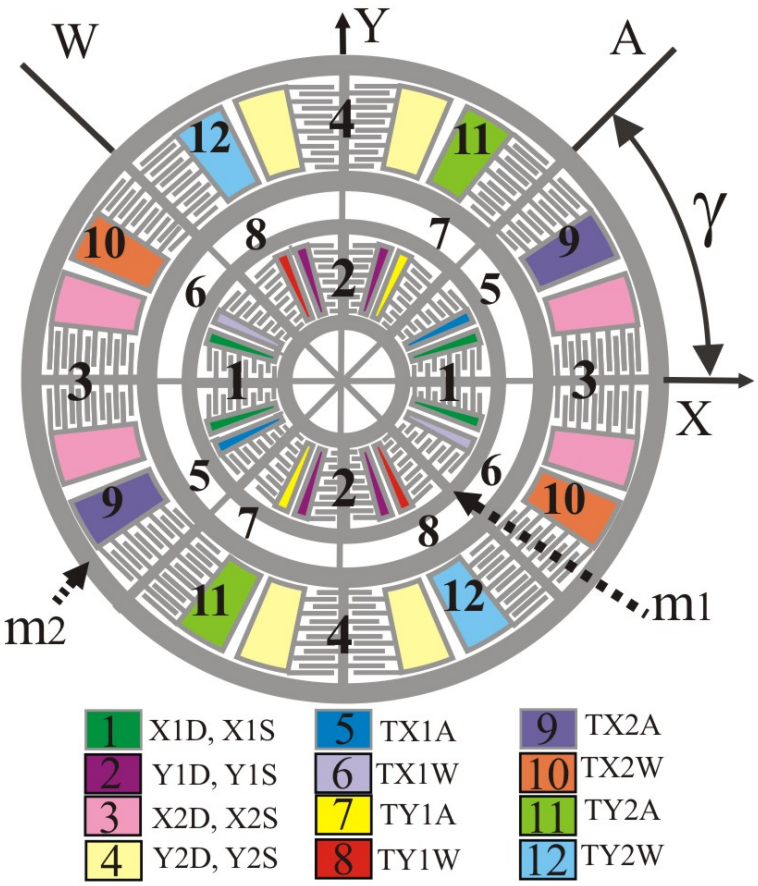

Figure 2.10: Configuration of drive, sense and tuning electrodes of dynamically amplified dual-mass gyroscope.

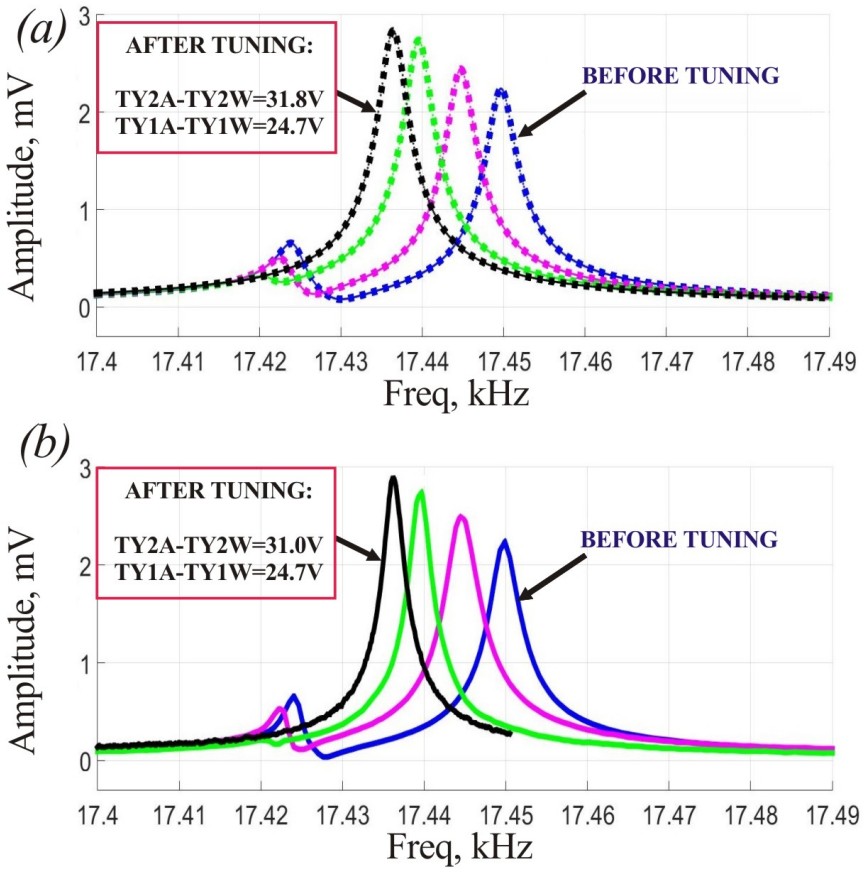

Figure 2.11: Freq. response showing tuning of the off-diagonal terms of stiffness matrix and reduction of coupling between modes: (a) simulated; (b) experimental.

10V DC voltage and 60mV AC voltage were applied to the driving electrodes X1D of the inner mass. The DC voltages were applied to the electrodes (TY2A, TY2W) and (TY1A, TY1W) to modify the off-diagonal terms of the stiffness matrix, Fig. 2.11(b). To compensate for coupling between the modes, the DC voltage of 31 V was applied between the electrodes (TY2A, TY2W), while the DC voltage of 24.7 V was applied between the electrodes (Y1A, TY1W). This result is in good agreement with the analytically predicted values, Fig. 2.11(a).

In addition, the DC voltage of 50.7 V was applied to the electrodes Y2D to modify the diagonal terms of the stiffness matrix, enabling mode matching, Fig. 2.12(b). The predicted value of the DC voltage to be applied to these pair of electrodes was 46.1 V, which is in good agreement with the experiment, Fig. 2.12(a).

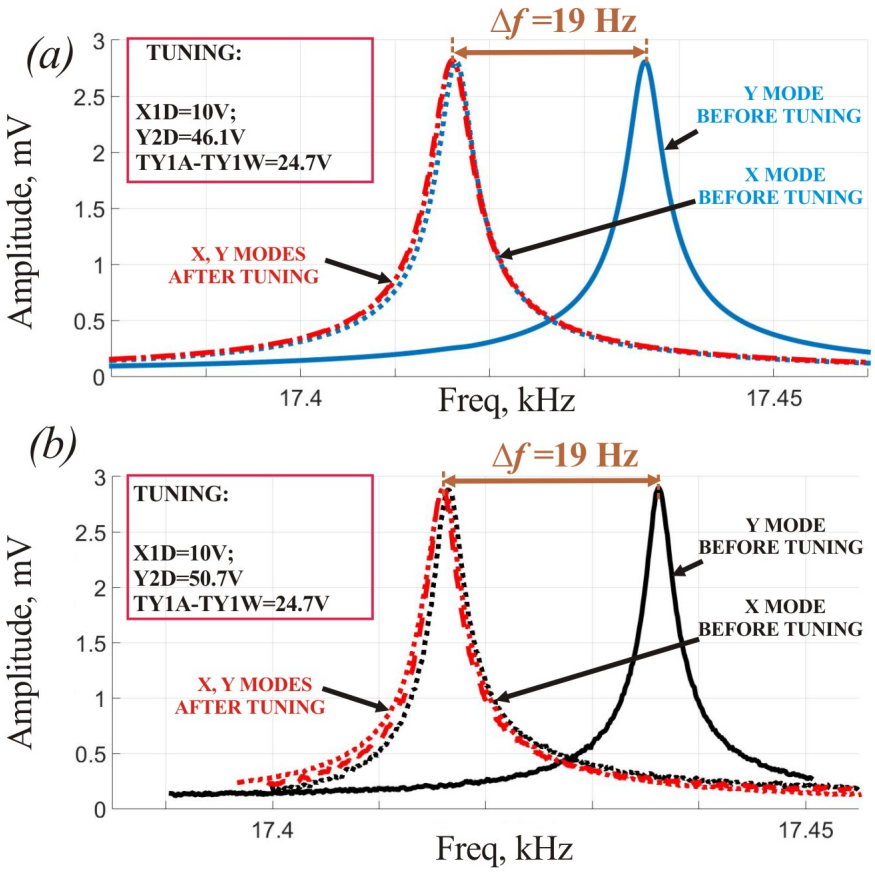

Figure 2.12: Freq. response showing tuning of the diagonal terms of stiffness matrix and reduction of frequency split between modes: (a) simulated; (b) experimental.

The coupling terms of the stiffness matrix, arising from the mechanical coupling of the two masses, are compensated during the simultaneous off-diagonal tuning and diagonal tuning.

During a higher precision tuning, when the resonant peaks of the gyroscope were tracked in the narrow range of frequencies, operational modes were tuned down to 50 mHz using the following DC voltages: TY2A-TY2W=29.6V; TY1A-TY1W=24.7V; Y2D=50.7V, Fig. 2.13.

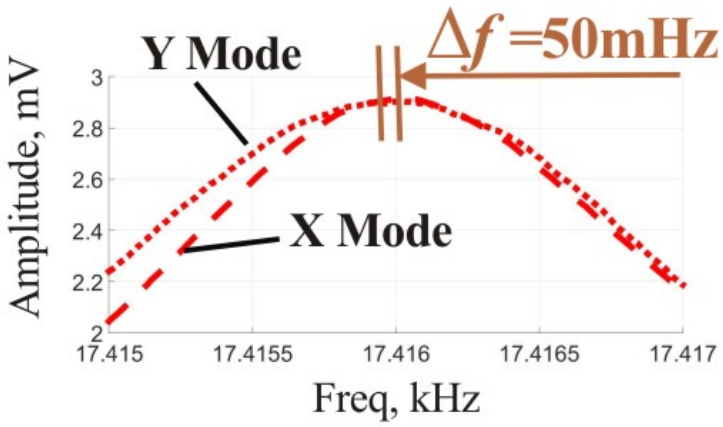

Figure 2.13: Using simultaneous tuning of diagonal, off-diagonal, and coupling terms in stiffness matrix, the frequency split between the operational modes was reduced from 26 Hz down to 50 mHz.

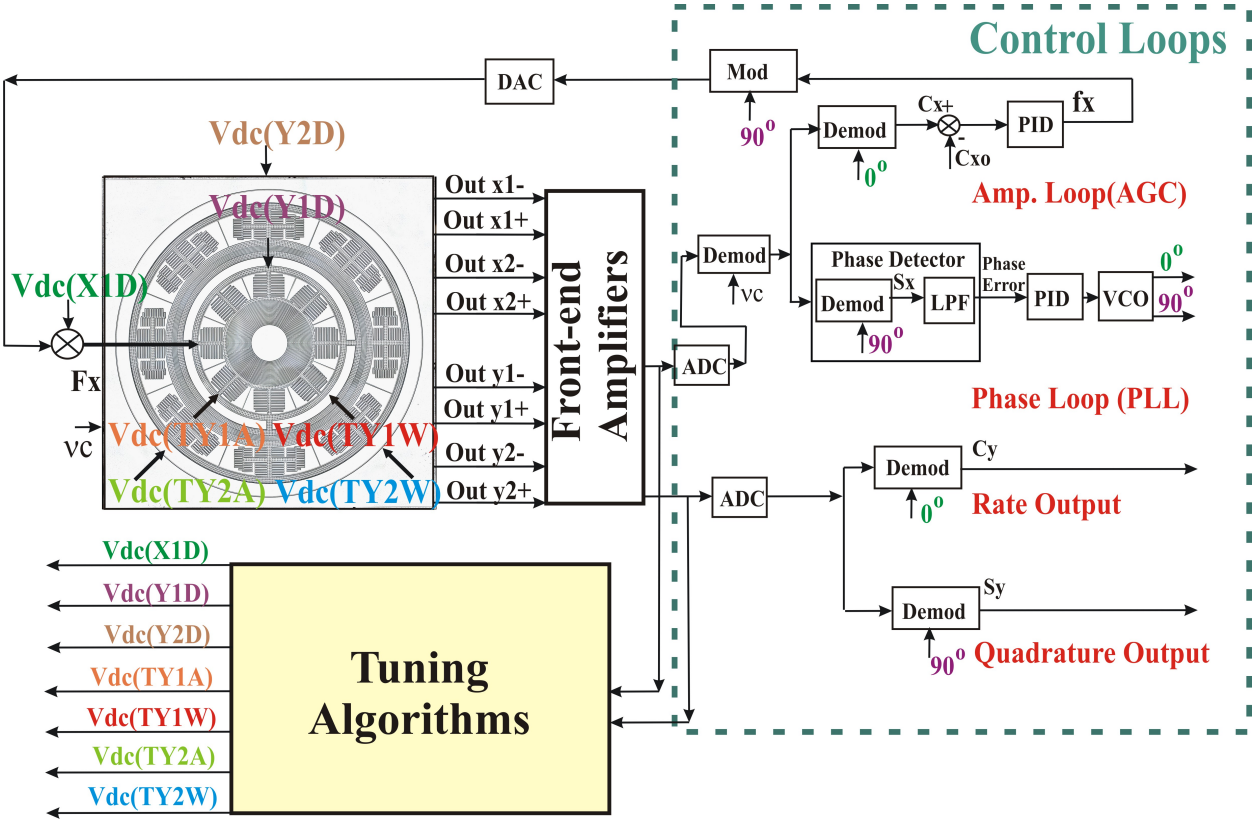

Figure 2.14: System-level schematic of control electronics for gyroscope open-loop operation.

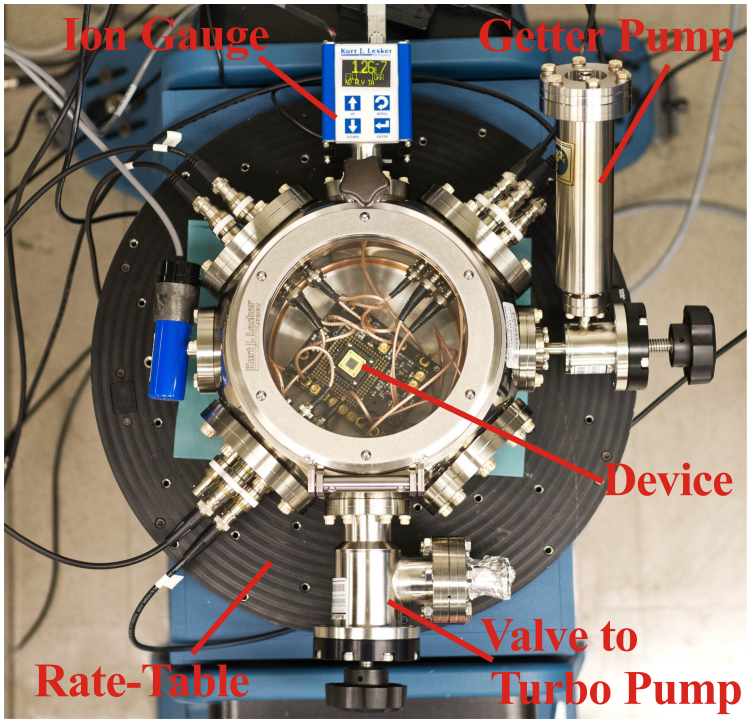

Figure 2.15: The angular rate response was obtained in vacuum at 0.1 μTorr pressure.

2.1.5 Gyroscope Angular Rate Response and Noise Characterization

In order to evaluate the sensor performance, before and after the electrostatic tuning, the dynamic response of the gyroscopes was obtained. To derive the sensor scale factor, the Ideal Aerosmith 2102 Series Two-Axis Position and Rate Table System was used to produce a reference rotation with programmed sinusoidal angular acceleration. The gyroscope was excited with a constant DC voltage and an AC voltage generated by a Phase Locked Loop (PLL), Fig. 2.14. A carrier signal ν_c at the frequency of 100 kHz was applied to the proof-mass, resulting in the amplitude modulation of the sensor output. The output signal was then demodulated to reveal the low frequency changes in capacitance. The amplitude of the drive-mode motion was stabilized using an Automatic Gain Control (AGC), [141]. All loops were realized using a Zurich Instruments HF2LI digital lock-in amplifier.

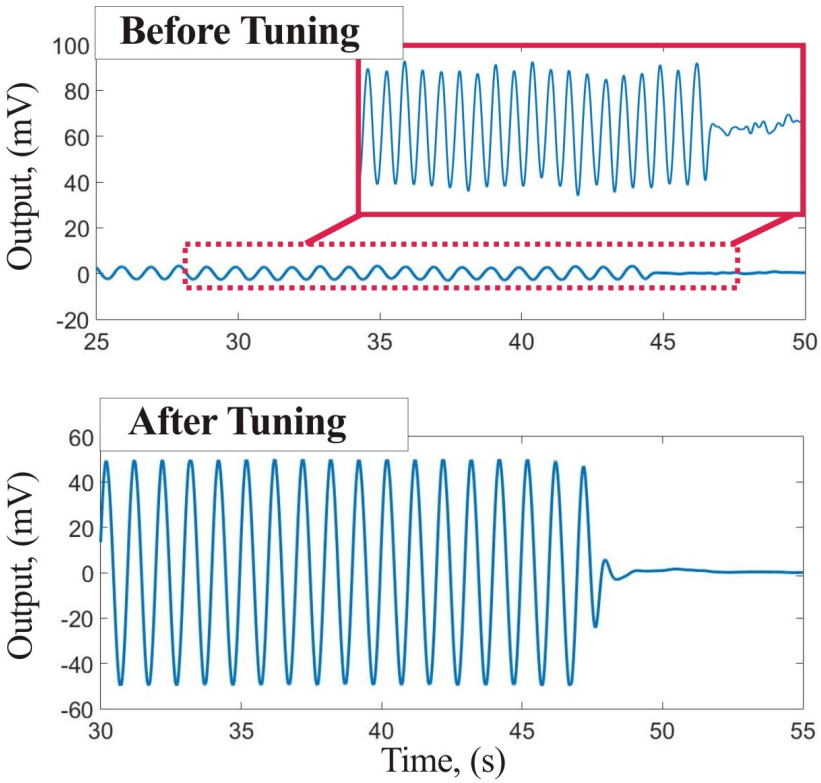

Figure 2.16: Gyroscope response to sinusoidal input of the rate-table, showing 17.5X higher SF and stable amplitude after tuning.

Gyroscope characterization was performed in an open loop configuration. The angular rate response was obtained in vacuum at 0.1 μTorr pressure, Fig. 2.15. The gyroscope response to the sinusoidal input of the rate-table with frequency 1 Hz and 10° amplitude is shown in Fig. 2.16. The rate-table characterization of the sensor before and after electrostatic tuning of the operational modes, showed an increase in scale factor by more than an order of magnitude, from 0.275 mV/deg/s to 4.82 mV/deg/s.

The Root Allan Variance Analysis (r-AVAR) was used to experimentally identify the random noise characteristics of the sensor. Noise analysis of the gyroscope, before and after tuning, revealed the reduction in bias stability, from 25.3 $^\circ/hr$ to 1.72 $^\circ/hr$ and the reduction in ARW, from 1.18 $^\circ/\sqrt{hr}$ to 0.16 $^\circ/\sqrt{hr}$, Fig. 2.17.

Experimental testing of the gyroscope, revealed a increased scale factor, reduced quadra-

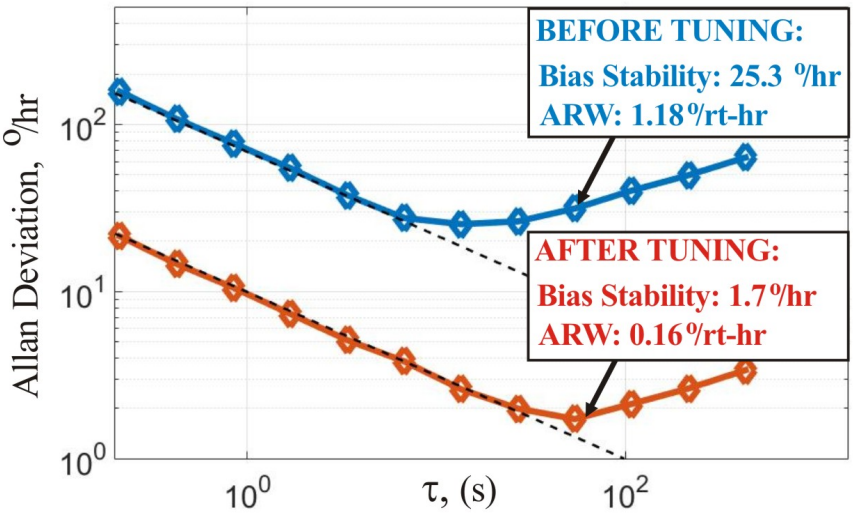

Figure 2.17: Noise analysis of the gyroscope before and after tuning revealed reduction in bias stability, from 25.3 $^\circ/hr$ to 1.7 $^\circ/hr$ and reduction in ARW, from 1.18 $^\circ/\sqrt{hr}$ to 0.16 $^\circ/\sqrt{hr}$.

Table 2.2: Experimentally Tested Parameters of the Design I Gyroscope

Parameter	**Before Tuning**	**After Tuning**
Frequency split (Δf), Hz	26	<0.05
Quadrature error, dps	521	2.59
Scale Factor, mV/dps	0.275	4.82
ARW, $^\circ/\sqrt{hr}$	1.18	0.16
Bias Stability, $^\circ/hr$	25.3	1.72

ture error and improved noise characteristics, after electrostatic compensation for structural imperfections, Table 2.2.

The presented electrostatic compensation method can be used for off-line tuning of the gyroscope in the laboratory environment. Once device is packaged and mounted within the measurement platform, the identified values of tuning DC voltages can be used as a starting point for on-line tuning. However, the packaging stresses often introduce additional frequency splitting and coupling between the operational modes of the sensor. In this case, the described compensation procedure has to be repeated in real time for on-line calibration.

It is important to notice that the presented analytical model accounts for imperfections in gyroscope's suspension, but does not take into consideration the imperfections of the proof masses and damping mismatch between the operational modes. The simplified model was shown to be sufficient for tuning the modes down to 50 mHz. However, an extended dynamical model might be necessary for the ultra-high precision tuning.

2.2 Miniature TRG

In this Section, we introduce the concept of a Toroidal Ring Gyroscope (TRG) and discuss the primary sources of frequency splits in degenerate mode pairs of this device. The isotropic suspension of the gyroscope is formed by a series of concentric rings. We show that operation in the n=3 wineglass mode might be preferable for prioritized device symmetry. We demonstrate, that by means of the structural design optimization, it is possible to achieve a desired order of fundamental wineglass modes, critical for vibration immunity, and potentially for improved performance of miniature devices. It is shown that mode-ordering is enabled by structural anisotropy, which arises from the spokes connecting the adjacent rings in suspension and results in a various levels of stiffening for different pairs of vibratory modes. Our design optimization, using the method of mode-ordering, is confirmed through experimental characterization of 2.8 mm diameter TRG prototypes. The optimization is based on variation of two parameters: the number of rings in suspension and the angle between the spokes connecting the rings.

2.2.1 Introduction

Axisymmetric structures, such as structures with concentric ring suspension, can possess multiple pairs of nominally degenerate modes, in which each pair shows some degree of

Coriolis coupling (the so-called wine- glass modes). Generally, for a simple isotropic ring or an isotropic disk, the lower the order of the fundamental wine-glass mode the lower its natural frequency.

Most of the degenerate wine-glass mode CVGs are designed to operate in the n=2 or the n=3 modes. Generally, for improved environmental performance of a gyroscope it is preferable to selectively soften the frequency of the pair of operational modes, placing them before the rest of the wine-glass modes (undesirable vibration) on a frequency response curve. For a simple isotropic ring, or a disk, such mode ordering, where the higher order modes exhibit lower natural frequencies, is counter-intuitive and is impossible achieve in general case. This work shows that a desired mode-ordering is achievable in the case of a series of concentric rings. We demonstrate that anisotropy introduced by interconnecting spokes between multiple rings in concentric ring suspension enables reordering the fundamental wine-glass modes, placing the desired operational mode before any other pair of degenerate modes.

2.2.2 Toroidal Ring Gyroscope with Concentric Ring Suspension

Coriolis Vibratory Gyroscopes (CVGs) can be divided into two general categorizes based on their principle of operation: rate and angle measuring sensors, [92]. Micromachined degenerate mode gyroscopes is a class of sensors which uses a pair of degenerate vibrational modes to measure the Coriolis signal induced by an inertial rotation. This class of devices have recently gained attention due to many favorable features, such as a high angular rate sensitivity, increased signal-to-noise ratio, a capability for rate and whole-angle modes of operation, and compatibility with advanced self-calibration techniques, [93]. However, mechanical elements with a high level of symmetry and highly isotropic suspension are required to exploit these advantages.

One simple structure that satisfies the isotropy requirement for a degenerate mode gyroscope

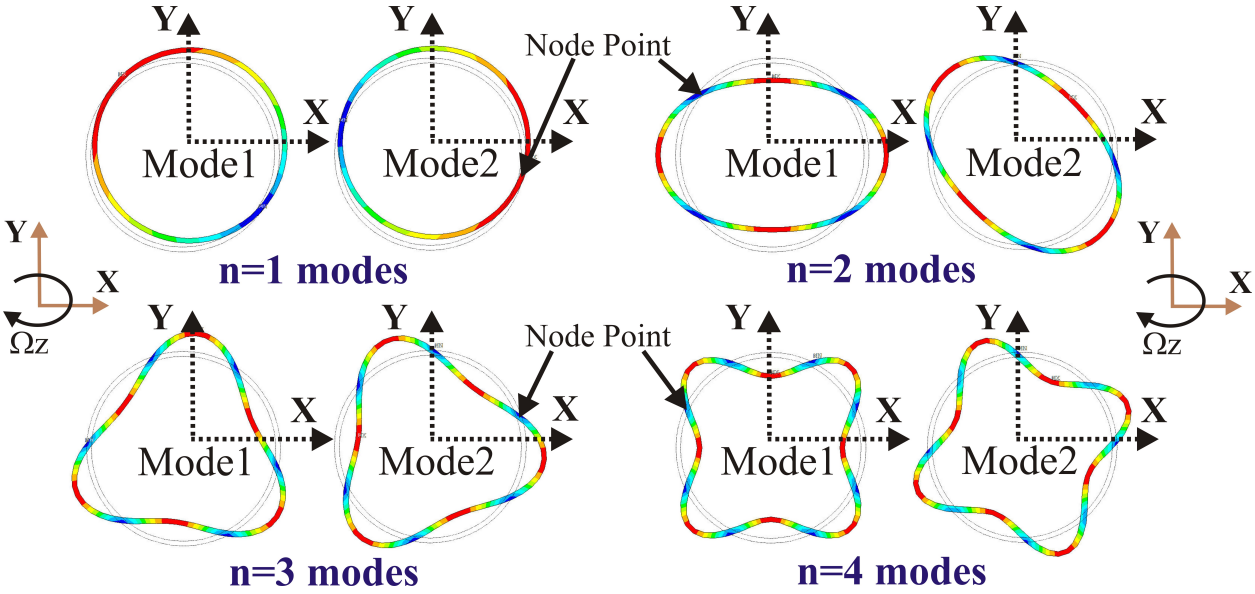

Figure 2.18: First four pairs of degenerate wineglass modes of isotropic ring. Each pair of modes has some degree of Coriolis coupling.

is a single ring. An isotropic ring exhibit an infinite number of in-plane wineglass vibration modes. Each of the degenerate pairs of order n can be used to measure the Coriolis acceleration induced angular rate signal, Fig. 2.18. Here, n represents a number of pairs of stationary nodes in the vibration pattern.

With the goal of achieving a highly-symmetrical degenerate mode gyroscope, many designs with an isotropic concentric ring suspension emerged in recent years. For example, a 100k Q-factor Toroidal Ring Gyroscope (TRG) with distributed suspension system and outer anchor has been reported in [39]. This device at 1.76 mm diameter was implemented in epitaxial silicon encapsulation process, [94], (EpiSeal). Silicon Disk Resonator Gyroscope (DRG) [95] at 8 mm diameter with concentric rings suspension and central support was demonstrated in [6]. A high frequency poly-silicon version of DRG at 0.6 mm diameter was reported in [96].

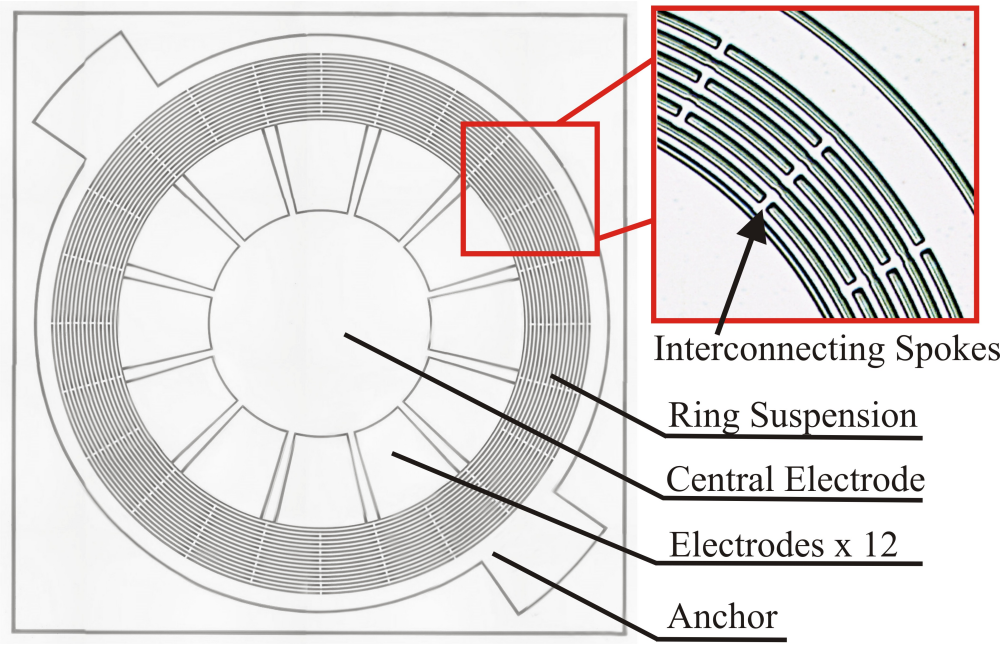

Figure 2.19: Microphotograph of a fabricated Toroidal Ring Gyroscope (TRG) prototype.

Gyroscope Architecture

The idea of concentric ring suspension is utilized in design of a Toroidal Ring Gyroscope (TRG), [39]. The sensor is comprised of an inner electrode assembly, an outer support, and a ring-type suspension, Fig. 2.19. In one possible implementation, the mechanical element is 2.8 mm in diameter, and the suspension system is formed by the 10 μm wide and 100 μm thick concentric rings, each connected by at least four spokes.

The inner electrode assembly consists of radial electrodes that are used as a forcer and as a pick-off, for each of the wineglass modes. Generally, the gyroscope, designed to operate in the n=2 mode, includes 8 radial electrodes; the gyroscope, designed to operate in the n=3 mode, includes 12 radial electrodes. Alternatively, the gyroscope can be designed with 24 electrodes for operation in n=2 or n=3 modes. Additional electrodes can be used for quadrature control, [97]. The central star-shaped electrode acts as a shield by sinking parasitic currents between discrete electrodes, [39].

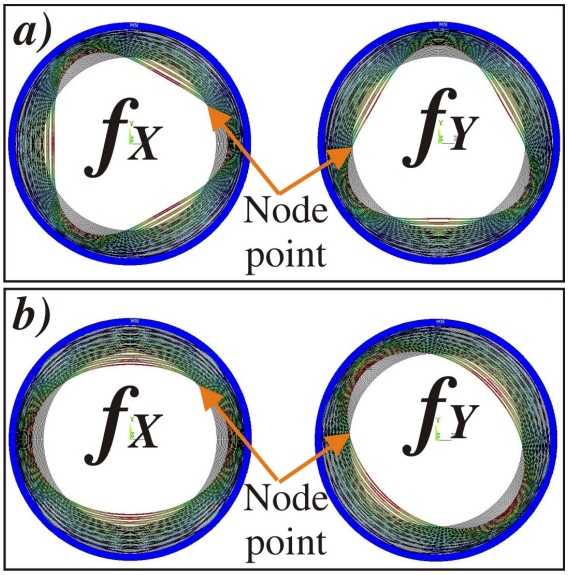

Figure 2.20: TRG mode shapes: sensor can be designed to operate in the n=2 or the n=3 wine-glass modes.

Fundamental Wine-glass Modes

The mechanical element of the gyroscope is a planar resonating structure which has degenerate pairs of in-plane wineglass vibration modes, each of these pairs can be used to measure the Coriolis acceleration-induced angular rate signal. TRG can be designed to operate in the n=2 or the n=3 fundamental wine-glass modes, Fig. 2.20. There is typically a trade-off between these two implementations. While the n=2 mode operation offers an advantage of a higher angular gain [98], the n=3 mode devices are inherently more symmetric. The splitting between stiffnesses in this pair of modes is nearly insensitive to manufacturing errors-induced misalignment in crystalline orientation of the wafer, [99].

In the case of the large-scale devices, above 5 mm, the high angular-gain factor generally determines the choice of operational modes. In contrast, for the smaller diameter gyroscopes (<3 mm) with a limited electrostatic tuning capability, the symmetry and a small as-fabricated Δf have to be often prioritized. For the smaller diameter TRG, the n=3 mode of operation is preferable, [99].

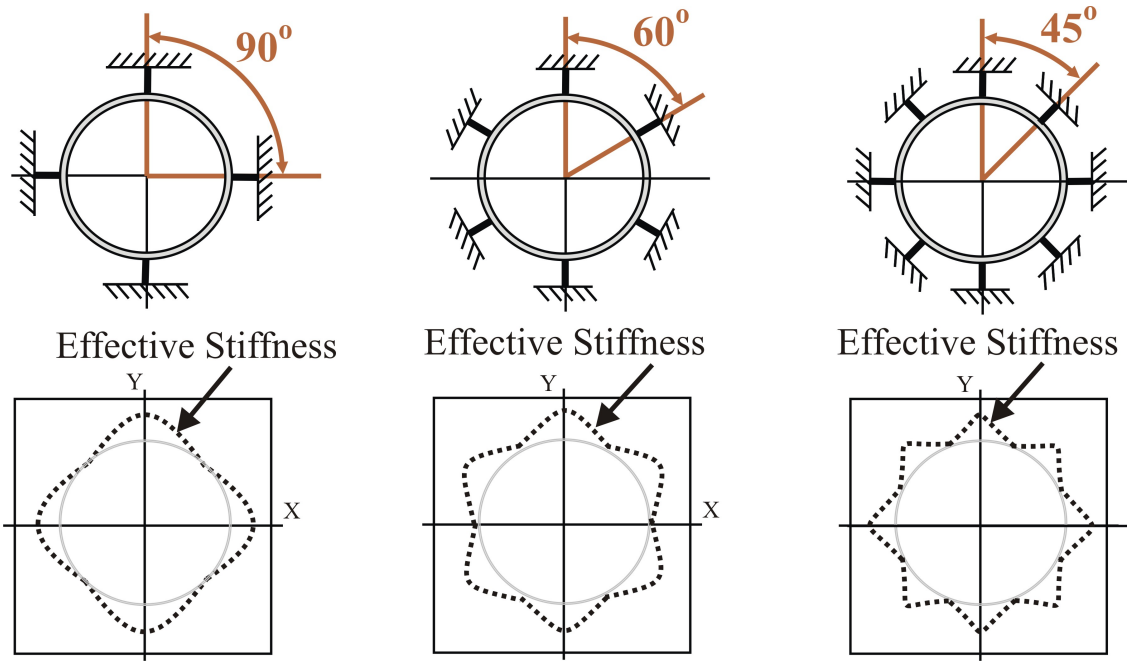

Figure 2.21: Placing structural spokes between the adjacent rings results in direction-dependent effective stiffness curve.

For improved environmental performance of the sensor, it is preferable to selectively stiffen the undesirable modes to reduce the sensitivity to external vibrations, [100]. However, in the case of a single isotropic ring, the lower order vibratory modes are usually lower in frequency and, hence, are most sensitive to external acceleration.

2.2.3 Sources of Anisotropy in a Ring-type Gyroscope

Isotropic ring in Fig. 2.18 is an ideal case. In reality, there are a number of factors introducing an undesirable anisotropy into a system and resulting in frequency splits in a pair of degenerate modes. The three primary sources of frequency splits or asymmetry between the two wineglass modes of a silicon ring include frequency split due to fabrication imperfections Δf_{fab}, frequency split Δf_{Si} induced by anisotropic modulus of elasticity of crystalline silicon, and frequency split Δf_{struct} induced by structural anisotropy:

$$\Delta f = \Delta f_{fab} + \Delta f_{Si} + \Delta f_{struct}.$$

The frequency splits Δf_{fab} due to imperfect fabrication of rings have been studied earlier in [101]. Some fabrication errors that occur in MEMS can be characterized by a few dominant terms in the Fourier expansion of the perturbed geometry. Generally, the effect of geometric imperfections is different for different pairs of degenerate modes, and frequency splitting of each pair of modes depends on the dominant type of perturbations.

For the ring fabricated on a single-crystal silicon wafer, the material anisotropy has to be considered. It has been shown in literature, that in the case of a single circular ring, the orientation of mode shapes relative to the Si(100) anisotropic elastic modulus curve is the same for the n=3 pair of degenerate modes and different for the n=2 pair of modes, [102]. Therefore, the frequency split Δf_{Si} of an ideal n=3 mode ring is zero, while up to a several hundreds Hz splitting can be observed in n=2 pair of modes. On the other hand, for Si(111) elastic modulus is direction-independent in plane; frequency splits of any pair of degenerate modes can be eliminated in an ideal case, [102]. However, even a slight misalignment of the wafer plane from <111> crystalline planes (usually 1-2° due to fabrication imperfections) leads to a significant splitting in n=2 pair of modes, while the n=3 pair of modes is nearly insensitive to misalignment errors relative to the crystalline orientation of the wafer, [99].

In order to use a ring as a mechanical element of the gyroscope it has to be connected to a stationary anchor, usually by means of the interconnecting spokes inside or outside the ring. Placing the spokes results in structural anisotropy arising from the direction-dependent effective stiffness curve, Fig. 2.21. It is important to notice that the shape of the effective stiffness curve or the level of anisotropy varies for different number of spokes or, in other words, for different angles between the spokes.

Similar to the material anisotropy, structural anisotropy may induce splitting of the modes, Δf_{struct}. Splitting occurs when orientations of the ring mode shapes relative to the effective stiffness curve are different for two modes in a degenerate pair. The frequency split Δf_{struct} induced by the misalignment of the mode shapes relative to the spokes orientation can be eliminated by using a proper angle of the spokes connecting the ring to an anchor. For example, in the case of the 45° angle between the spokes, the geometric effective stiffness in Mode 1 and Mode 2 directions of n=2 pair is the same. Similarly, the geometric effective stiffness in Mode 1 and Mode 2 directions of n=3 pair is the same.

The described sources of anisotropy are also present in the case of a TRG silicon device with suspension formed by the series of interconnected rings.

Ordering of Fundamental Wine-glass Modes in TRG

Using Finite Element Analysis (ANSYS), we explored the natural frequencies of the first three pairs of degenerate wineglass modes TRG. Simulation was performed for a number of rings in the gyroscope suspension in the range from 12 to 24 and for an angle of 60°, 45°, and 30° between the interconnecting spokes.

Fig. 2.22 shows that stiffening the suspension by means of reducing the number of rings has a different effect on the different pairs of wineglass modes. The dependance of the wineglass modes frequency on the number of rings in suspension is non-linear. The level of structural anisotropy in the system defines the degree of non-linearity and the rate of change in frequency of a certain pair of modes with reduction in the number of rings. By changing the number of rings in suspension and by changing the angle of spokes orientation, thus effectively controlling the structural anisotropy level, it is possible to selectively stiffen a certain pair of vibratory modes.

Fig. 2.22(a) shows that in the case of 60° angle between the spokes, the lowest frequency

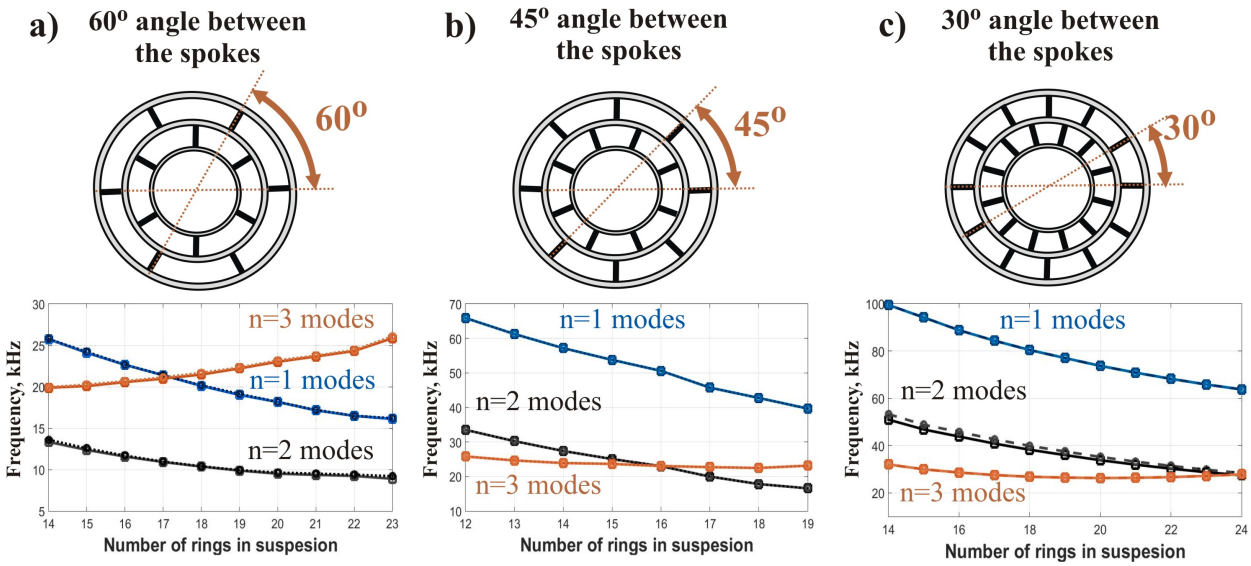

Figure 2.22: Structural anisotropy introduced by interconnecting spokes can be used to selectively stiffen the undesired modes: (a) n=2 wineglass mode pair is the lowest in frequency among all the degenerate modes, (b) as the number of concentric rings in suspension is decreased, the n=2 and the n=3 pairs of modes switch the order, (c) n=3 wineglass mode is the lowest in frequency among all the degenerate modes.

pair of modes is the n=2 pair, but the split between the n=2 and the n=3 degenerate modes decreases with reduction in the number of concentric rings in the suspension. As we decrease the angle between the spokes to 45°, the two pairs of wineglass modes would eventually switch the order, Fig. 2.22(b). As we further decrease the angle between the spokes to 30°, the n=3 pair becomes the lowest frequency pair of modes, 2.22(c).

To experimentally demonstrate the effect of mode-ordering in MEMS TRG, four sensors were designed with a different number of rings in suspension, Table 2.3. According to the results of the Finite Element Modeling (FEM), in Design I gyroscope the central frequency of the n=2 pair of degenerate modes is the lowest among all the wineglass modes, followed by the n=1 pair of modes. In Design II gyroscope the central frequency of the n=2 pair of degenerate modes and the central frequency of the n=3 pair of degenerate modes are closely spaced. In Design III gyroscope the central frequency of the n=3 pair of modes is 7.7 kHz lower than the n=2 pair of modes and it is the lowest among all the wineglass modes.

Finally, in Design IV gyroscope the central frequency of the n=3 pair of modes is 8.2 kHz lower than the n=2 pair of modes and it is also the lowest among all the wineglass modes of the gyroscope.

2.2.4 Experimental Characterization

Prototypes of the Design I-IV gyroscopes were fabricated on a wafer-level using a single-mask SOI fabrication process with a 100 μm thick device layer and using a 1.5 μm thick thermal oxide layer as a hard mask for the Deep Reactive Ion Etching (DRIE) of silicon. In order to reduce the effect of material induced anisotropy, all sensors were fabricated on a single-crystal silicon wafer with orientation <111>. The sensors were then released using a stiction-free vapor HF process (for 50 min at 45 °C temperature) and packaged in ceramic Leadless Chip Carrier (LCC) packages.

There are eight electrodes designated for n=2 modes operation and twelve electrodes des-

Table 2.3: Finite Element Modeling (FEM) and Experimental Analysis of the TRG Natural Frequencies

	Design I	**Design II**	**Design III**	**Design IV**
Angle between the spokes	60°	45°	45°	30°
Number of rings	23	16	12	20
	Finite Element Modeling (FEM)			
Freq. of n=1 modes	16.14 kHz	50.6 kHz	65.9 kHz	73.7 kHz
Freq. of n=2 modes	9.05 kHz	22.97 kHz	33.5 kHz	34.5 kHz
Freq. of n=3 modes	25.97 kHz	23.04 kHz	25.8 kHz	26.26 kHz
	Experimental Characterization			
Freq. of n=2 modes	7.7 kHz Δf=155 Hz	16.48 kHz Δf=37 Hz	21.15 kHz Δf=59 Hz	25.8 kHz Δf=1620 Hz
Freq. of n=3 modes	16.3 kHz Δf=137 Hz	16.35 kHz Δf=19 Hz	15.82 kHz Δf=29 Hz	17.6 kHz Δf=24 Hz

ignated for n=3 modes. The gyroscope can be electrostatically excited to oscillate in n=2 mode using 2 differential electrodes as a forcer in the X direction and 2 differential electrodes as a forcer in the Y direction, Fig. 2.23(a). The corresponding 2 electrodes are used for pick-off in each direction. The gyroscope can be electrostatically excited to oscillate in n=3 mode using 4 differential electrodes as a forcer in the X direction and 4 differential electrodes as a forcer in the Y direction, Fig. 2.23(b). Corresponding 2 electrodes are used for pick-off in each direction.

Fig. 2.24 shows the experimentally identified resonant frequencies of Design III gyroscope, Table 2.3, which was electrostatically excited using (a) n=3 mode electrodes, and (b) n=2 mode electrodes. For the sensor excitation, 9V DC voltage and 150mV AC voltage were applied to the driving electrodes. The carrier demodulation technique was used to eliminate the effect of parasitic currents between the sensor's input and output, [133]. For this purpose, a carrier signal at frequency of 100 kHz and amplitude of 3V was applied to the proof-mass, resulting in the amplitude modulation of the sensor output. The output signal was then demodulated to reveal the low frequency changes in capacitance.

The frequency response in Fig. 2.24(a) was obtained for the sensor electrostatically excited

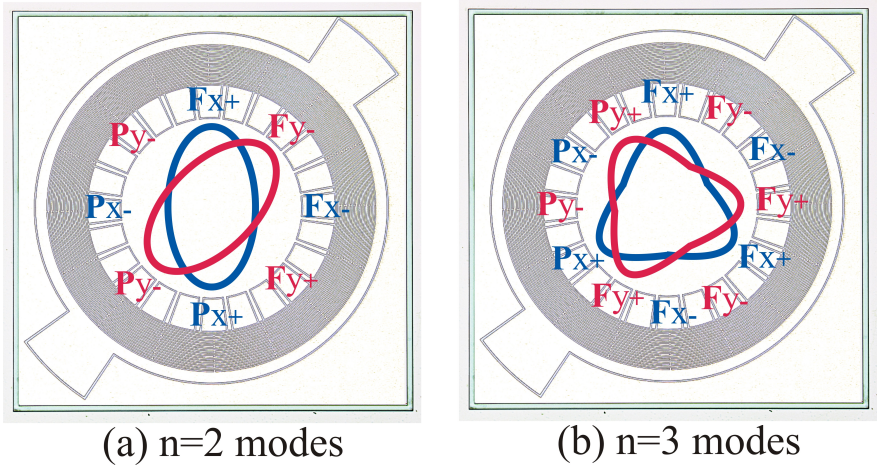

(a) n=2 modes (b) n=3 modes

Figure 2.23: (a) n=2 wineglass modes are excited electrostatically using 4 out of 8 electrodes in the central electrode assembly, (b)n=3 wineglass modes are excited electrostatically using 8 out of 12 electrodes in the central electrode assembly.

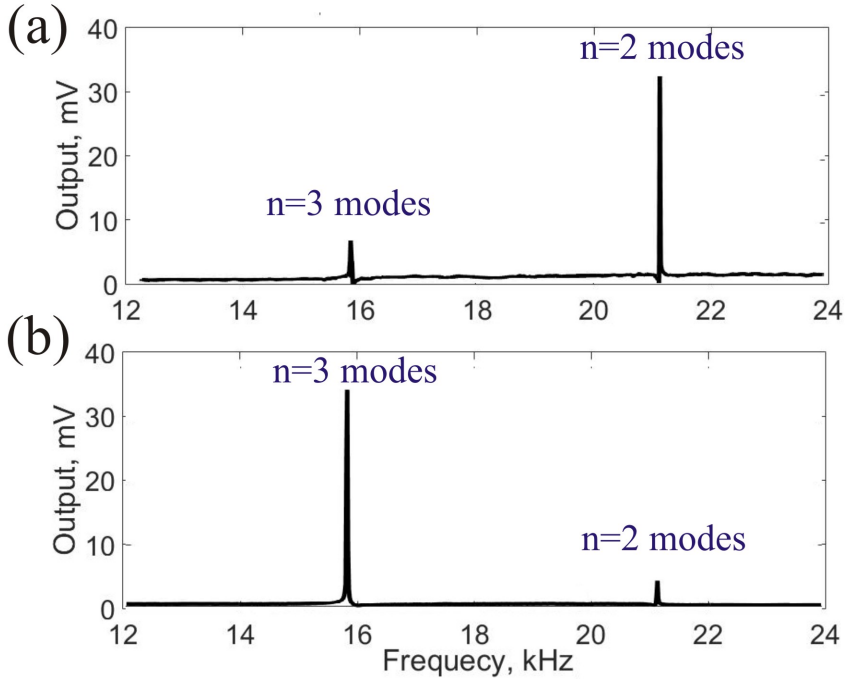

Figure 2.24: Experimentally identified resonant frequencies of Design III gyroscope: (a) n=2 mode electrodes are used for electrostatic excitation, (b) n=3 mode electrodes are used for electrostatic excitation.

using n=2 mode electrodes. The higher in amplitude peak on the response curve corresponds to the n=2 pair of the wineglass mode. The frequency response in Fig. 2.24(b) was obtained for the same sensor electrostatically excited using n=3 mode electrodes, and the higher in amplitude peak corresponds to the n=3 pair of the wineglass mode. This experiment revealed that the mode-ordering was successfully achieved for the Design III gyroscope, placing the resonant frequency of the n=3 pair of modes below the n=2 pair of modes. A similar experiment was performed for the prototypes of the gyroscope from Design I through Design IV in order to identify the order of the fundamental wineglass modes. The results of these experiments are summarized in Table 5.5.

The frequency response curves in Fig. 2.25 were obtained using an excitation with n=3 electrodes. For the Design I gyroscope, we observed two high in amplitude resonant peaks at 16.3 kHz with Δf of 137 Hz, corresponding to the n=3 wineglass modes and two lower in amplitude peaks at 7.7 kHz with Δf of 155 Hz, corresponding to the n=2 modes. The

a) Design I: 60^{o} angle between the spokes; 23 rings

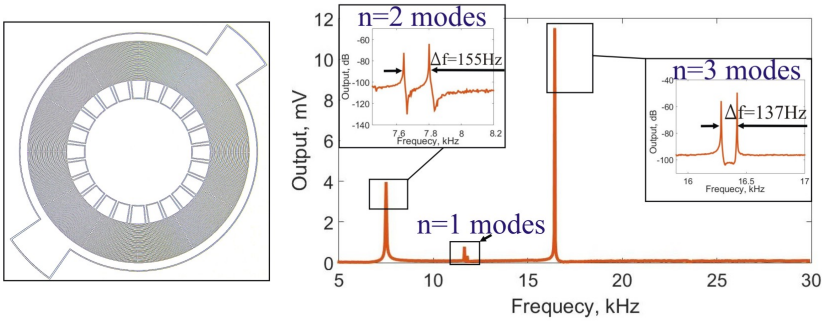

b) Design II: 45^{o} angle between the spokes; 16 rings

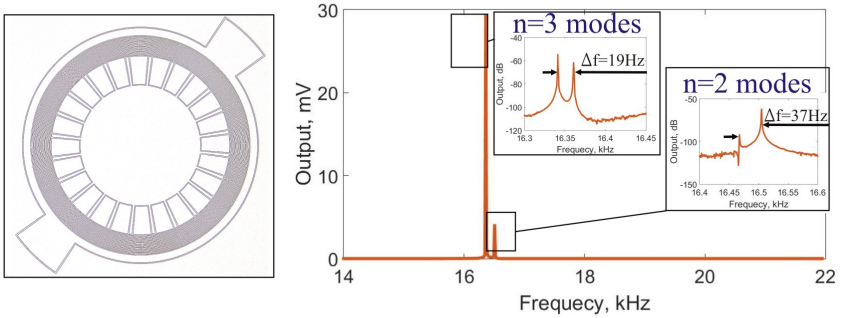

c) Design III: 45^{o} angle between the spokes; 12 rings

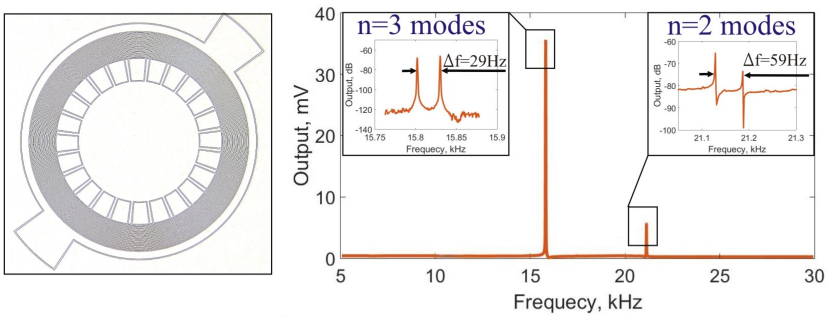

d) Design IV: 30^{o} angle between the spokes; 20 rings

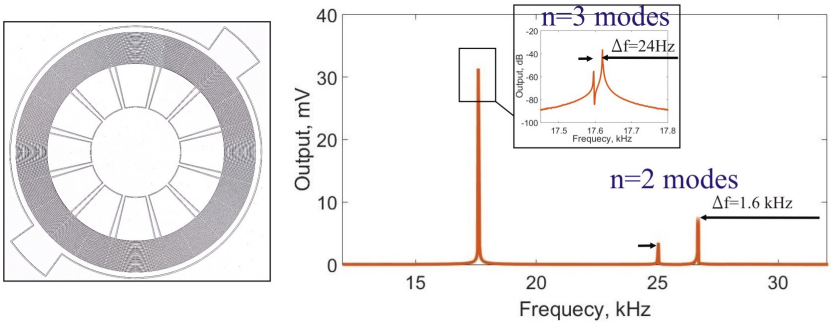

Figure 2.25: Experimental characterization of prototypes: (a) n=2 pair of modes is the lowest in frequency among all the vibrational modes, (b) the n=2 and the n=3 pairs of modes have nearly equal central frequencies, (c) and (d) n=2 pair of wineglass modes is the lowest in frequency among all the vibrational modes.

small peaks at 11.7 kHz frequency corresponded to the n=1 modes. Comparatively large frequency splits in the n=2 and n=3 pairs are due to the combined effect of the fabrication imperfections and a structural anisotropy induced by the interconnecting spokes.

For the Design II gyroscope, we observed two closely spaced pairs of peaks: two high in amplitude resonant peaks at 16.35 kHz with Δf of 19 Hz, corresponding to the n=3 wineglass modes, and two lower in amplitude peaks at 16.48 kHz with Δf of 37 Hz, corresponding to the n=2 modes. The splits between the modes in n=2 and between the modes in n=3 pair are induced by fabrication errors. The larger split between the modes in n=2 pair might be attributed to the additional effect of material anisotropy arising from misalignment of the wafer orientation from the <111> plane.

For the Design III gyroscope, two high in amplitude resonant peaks at 15.82 kHz with Δf of 29 Hz correspond to the n=3 wineglass modes and two lower in amplitude peaks at 21.15 kHz with Δf of 59 Hz correspond to the n=2 modes. As analytically predicted, the n=3 wineglass mode is the lowest in frequency among all the vibrational modes. The separation between the n=2 and n=3 pairs of degenerate modes is 5.3 kHz. Similarly to the Design II gyroscope, the modes in n=3 pair exhibit a lower Δf.

For the Design IV gyroscope, the n=3 mode resonant peaks were observed at 17.6 kHz with Δf of 24 Hz. The central frequency of the n=2 pair of modes is 8.2 kHz higher than the frequency of the n=3 pair of modes. The large frequency split of 1620 Hz between the two modes in the n=2 pair is mainly caused by the structural anisotropy induced by the interconnecting spokes. For the 30° angle between the spokes, the misalignment of the n=2 mode shapes relative to the spokes orientation induces a difference in effective stiffness of the two modes in a pair. In comparison, the n=3 modes are inherently symmetrical.

The experimentally obtained resonant frequencies of the gyroscopes are noticeably lower as compared to the analytically predicted values. The reason behind the reduction in frequen-

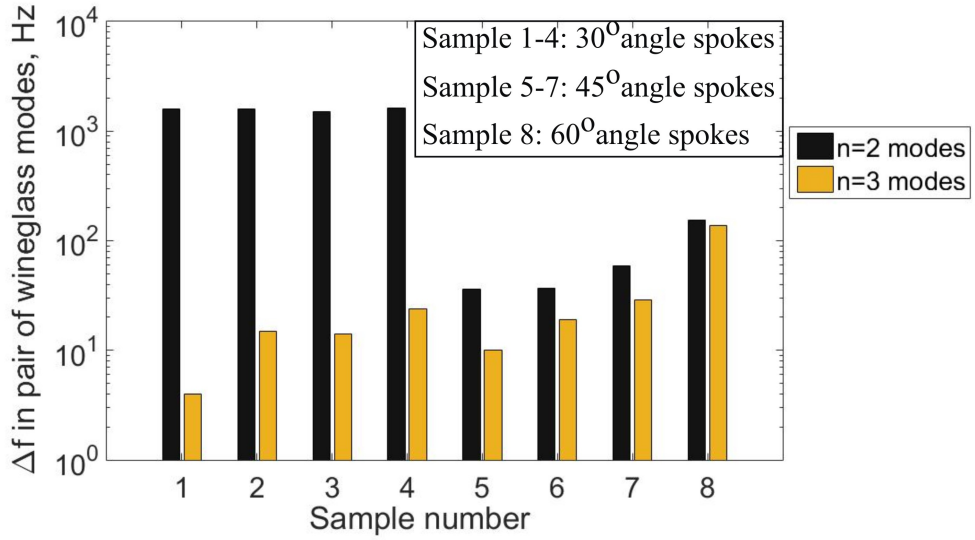

Figure 2.26: Frequency splits between two wineglass modes in n=2 and n=3 pairs for 8 TRG prototypes.

cies is over-etching of the sensors during the DRIE step, which resulted in undercut of the device layer and reduction in the thickness of the rings. However, a frequency reduction happened in all modes of interest and, in terms of placement of wineglass modes on the frequency response curves, for all four designs, there is a good match between the experiment and the FEA.

The frequency splits in n=2 and n=3 pairs of wineglass modes for eight TRG prototypes are summarized in Fig. 2.26. Due to the high level of structural anisotropy in the case of 30° angle between the spokes, the gyroscope samples 1-4 exhibit a significantly higher frequency splits of the n=2 modes. The modes asymmetry due to spokes orientation is eliminated in the case of 45° angle between the spokes. However, due to the fabrication imperfections and material anisotropy, the gyroscope samples 5-7 exhibit a higher frequency split of the n=2 modes. For the 60° angle between the spokes, structural anisotropy contribute into both the n=2 and the n=3 pairs of modes. Hence, the frequency splits of the gyroscope sample 8 are induced by a combined effect of the structural and material anisotropy, as well as the fabrication errors.

2.3 Conclusion

This Chapter investigated two designs of a tactical-grade MEMS gyroscopes for potential integration on sidewalls of a miniature IMU device: dual-mass Dynamically Amplified Gyroscope (DAG) and mode-ordered Toroidal Ring Gyroscope (TRG).

Different designs of multi-mass gyroscopes have been extensively studied in literature. Multi-mass dynamically coupled systems offer advantages, such as dynamic balance, increased bandwidth, and dynamic amplification. However, an increased number of DOF of a mechanical element results in a more complex form of structural stiffness matrix, as compared to a conventional single-mass gyroscope. Hence, more complex techniques have to be considered for electrostatic frequency tuning of operational modes, in case of a non-ideal multi-mass structural element.

In this Chapter, we introduced a design of a Dynamically Amplified Gyroscope with a dual-mass architecture. A DC tuning technique, similar to a method commonly used for tuning a conventional single-mass gyroscope, has been employed for precision mode-matching of an imperfect dual-mass sensor. The analytical model of a dual-mass system in presence of imperfections has been explored and a method of electrostatic frequency trimming in a dual-mass gyroscope has been proposed. The tuning procedure is based on estimation of the modes mismatch and coupling between the modes, utilizing the experimental frequency response data. The analytical model is then used to determine the necessary tuning voltages to permit the removal of anisoelasticity and the mismatch of principle axes of stiffness, thus enabling the gyroscope operational modes to be matched.

Results of simulation were verified using experimental electrostatic frequency tuning of a Dynamically Amplified Gyroscope. The coupling between the drive and sense modes was compensated and the frequency split between the modes was reduced from 26 Hz down to 50 mHz, resulting in 17.5X increase in the scale factor of the gyroscope, the reduction in

bias stability, from 25.3 $^\circ/hr$ to 1.72 $^\circ/hr$ and the reduction in ARW, from 1.18 $^\circ/\sqrt{hr}$ to 0.16 $^\circ/\sqrt{hr}$. The dynamic amplification of motion, in a combination with the precision mode tuning, enable an increased sensitivity, making the DAG a candidate for high-performance applications.

In this Chapter, we also described a design of the Toroidal Ring Gyroscope (TRG) with suspension formed by the series of concentric rings. We reviewed the main sources of frequency splits in degenerate mode TRG with concentric rings suspension. The trade-offs of operation in the n=2 and the n=3 wineglass modes have been discussed. While the n=2 mode offers an advantage of a higher angular gain factor, the n=3 mode devices are inherently more symmetric, resulting in a lower as-fabricated frequency split Δf. It has been shown experimentally, that n=3 mode of operation is preferable for prioritized device symmetry.

Ordering of vibrational modes in a way that the operational mode exhibits the lowest natural frequency is used to improve the environmental performance of the sensor. Sensitivity to external vibrations can be greatly reduced by placing the frequencies of undesired modes outside of the vibration range. We demonstrated that structural anisotropy, which arises from the spokes connecting the adjacent rings in suspension, allows for selective stiffening of certain pairs of wineglass vibrational modes, resulting in changing the modes order. Our method of fundamental wineglass modes ordering was validated through the experimental characterization of the TRG prototypes.

Chapter 3

"Origami-like" Folded MEMS IMU

This Chapter reports on developments of the Folded 3D MEMS technology, introducing a double-sided process for a high-performance miniature Inertial Measurement Unit (IMU). The new method involves fabrication of inertial sensors and metal traces utilizing both sides of the Silicon-on-Insulator (SOI) wafer. This approach aims to overcome the limitations of the single-sided Folded MEMS process, attempted previously, [52], leading to a increased fabrication yield and improved performance of a miniature IMU.

Folded MEMS process is a versatile technological platform, enabling an efficient way to assemble the inertial sensors into a 6-axis IMU configuration. A number of different designs of miniature high-end sensors, including Dynamically Amplified Gyroscope (DAG) and Toroidal Ring Gyroscope (TRG) discussed in Chapter 2, are compatible with the fabrication process.

In the following Sections, we will first introduce the double-sided Folded IMU concept, Section 3.1. We will then present the fabrication sequence and discuss the choice of material for flexible hinges, Section 3.2. This will be followed by experimental characterization of the fabricated prototypes, Section 3.3, demonstrating feasibility of the Folded MEMS process. Section 3.4 concludes this Chapter with a discussion of results.

3.1 Double-Sided Design Concept

Folded MEMS IMU approach is based on a double-sided Silicon-on-Insulator (SOI) process for fabrication of flat foldable MEMS structures, on a wafer-level. In our process, both sides of the SOI wafer are efficiently utilized. Inertial sensors are created on the device side of the wafer (Fig. 3.1(a)), while metal interconnects and polymer flexible hinges are formed on the handle side of the wafer (Fig. 3.1(b)).

The front and the handle side of the SOI wafer are electrically connected using thru-wafer copper interconnects. The technology of Thru-Wafer Interconnects for Double-Sided (TWIDS) realization of sensors on SOI wafers is an integral part of the Folded IMU process, [56]. Based on bottom-up seedless copper electroplating, TWIDS approach enables high aspect-ratio ultra-low resistance vertical electrical connections.

Thru-wafer interconnects provide a path for electrical signals from sensors on the device side of the wafer to the handle side of the wafer. This facilitates IMU integration with electronic components integrated inside the 3D structure. Such efficient utilization of the inner volume results in reduction of the finial product dimensions.

Every IMU device is comprised of at least three single-axis gyroscopes and three single-axis accelerometers. In addition, a clock might be co-integrated with IMU to provide timing information along with position and orientation, or as a reference clock for signal processing. All sensors are designed to have a single axis of sensitivity and are optimized to reject off-axis inputs. We take advantage of a thick device layer of the SOI wafer for improved sensitivity of high aspect-ratio inertial sensors and increased immunity to vibration perpendicular to substrate. Flexible hinges enable folding of a flat device into a 3D configuration.

Devices are usually implemented on the front side of the folded structure to provide an easy access for inspection and probing. Alternatively, to protect the sensors from environment,

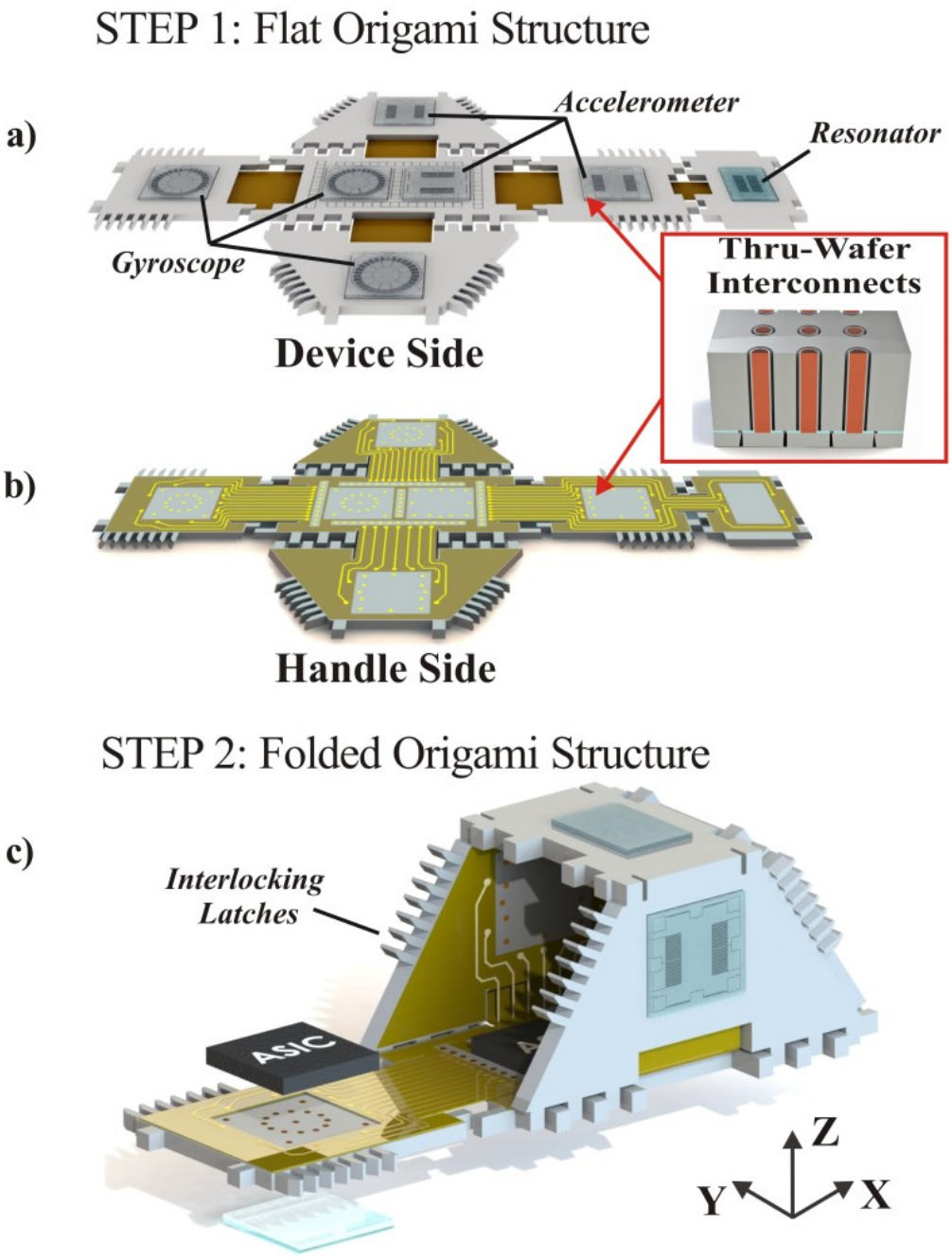

Figure 3.1: Folded MEMS IMU. Double-sided fabrication process and thru-wafer interconnects enable efficient utilization of the IMU inner volume.

Folded IMU can be implemented with sensors on the inner faces of the silicon panels and metal traces on the outer faces. Placing the sensors inside the 3D structure is possible due to the thru-wafer via and does not result in any changes of the fabrication process flow. However, when placing flexible hinges on the outside, the hinge length has to be increased to account for substrate thickness and allow for folding.

Once folded, IMU allows for measurement of 3-DOF orientation, 3-DOF positioning, and timing data (Fig. 3.1(c)). The change in alignment of sensors' axes of sensitivity during operation is the factor contributing to degradation of IMU performance. To maintain the original alignment of sensors (after the calibration) under different environmental conditions, the Folded IMU structures are reinforced by means of epoxy, eutectic soldering, or silicon welding of the interlocking latches located along the silicon panels. It was previously shown in [52] that solder reinforced IMU structures exhibit <0.2 mrad change in sidewall alignment angle during thermal testing in the range of temperatures from 25 °C to 85 °C. The misalignment error due to temperature can be further minimized using silicon welding for reinforcement of IMU structures, [55].

3.2 Fabrication Process

The manufacturing process for double-sided folded TIMU starts with processing the backside of an SOI wafer, Fig. 3.2. In the first step, 500 μm deep blind via holes are patterned on the handle-side of the wafer and etched using Deep Reactive Ion Etching (DRIE), Fig. 3.2(a). This is followed by removal of 5 μm buried oxide layer inside the via holes to permit an electrical contact with the 100 μm device layer. The via holes are then filled with copper using sonic-assisted seedless electroplating method. This approach does not require any additional conductive seed layer deposition, but utilizes a highly doped silicon device layer as a seed for electroplating, Fig. 3.2(b). The technique assures void-free features and allows

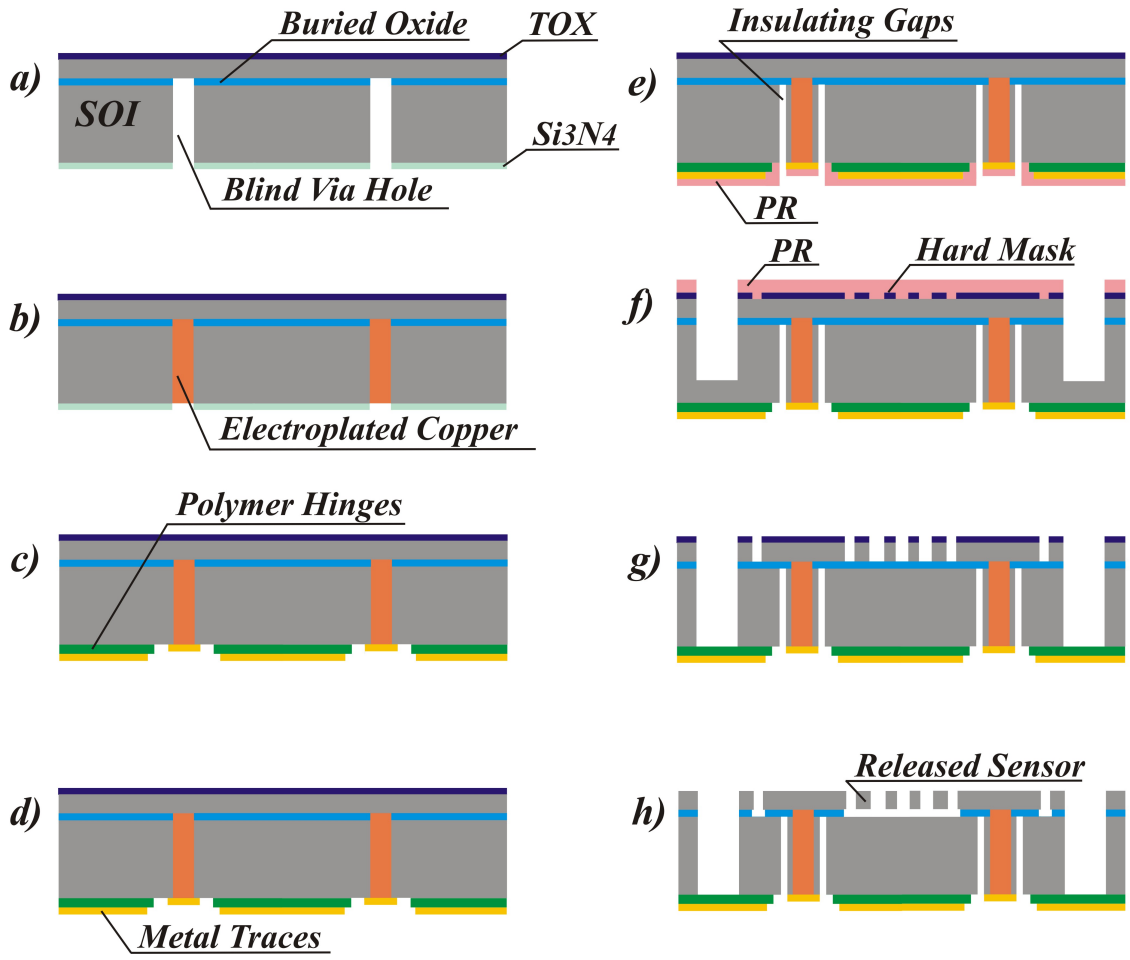

Figure 3.2: 6-Mask wafer-level fabrication process for double-sided IMU with thru-wafer interconnects: a) Deep Reactive-Ion Etching (DRIE) of blind via holes, b) filling the via holes with copper using seedless electroplating method, c) formation of polymer flexible hinges on the handle-side of the wafer, d) formation of metal traces on polymer, e) DRIE of insulating gaps, f) sensors hard mask definition and top-side pre-etch, g) top-side thru-wafer etch, and h) sensors release.

for high density array of ultra-low resistance thru-wafer interconnects, [128]. The aspect ratio of the interconnects varies for different sensor designs and is usually in the range from 6:1 to 10:1 (wafer thickness to copper stem diameter), [56].

Following the fabrication of interconnects, the polymer flexible hinges are defined on the handle-side of the wafer, Fig. 3.2(c). Metal traces are then created on top of the polymer insulating layer, Fig. 3.2(d). Next, the donut-shape insulating gaps are etched around the copper filled vias, completing the handle-side processing, Fig. 3.2(e).

Front-side processing starts with creating a SiO_2 hard mask, Fig. 3.2(f). This is followed by etching of sensor features and the thru-wafer etch, which is necessary for separation of panels for subsequent folding in a 3-D shape, Fig. 3.2(g). The thru-wafer etch is performed by, first, covering the sensors with a layer of photoresist, then DRIE etching of a 100 μm device layer, removing buried oxide, and DRIE etching of a 400 μm handle wafer, Fig. 3.2(f). At this point, the thru-wafer etch is not complete and another 100 μm of the handle wafer needs to be removed. This is done by stripping off the photoresist protective layer to open the sensors features and continuing the etching, using the previously defined SiO_2 hard mask. During this fabrication step, the sensors and the last 100 μm of the handle wafer are etched in parallel, Fig. 3.2(g). The sensors are then released, using vapor HF, Fig. 3.2(h).

Among main advantages of the new approach for double-sided origami IMU with TWIDS, Fig. 3.2 as compared to the single-sided approach reported in [52] are:

1. Including the processing steps for fabrication of thru-wafer interconnects enable electrical interface between devices on the front side of the wafer and electrical components on the back side of the wafer. This approach provides a path for further miniaturization of the IMU integrated with signal processing electronics.

2. In contrast to the single-sided process, in double-sided IMU, a thick layer of polymer hinges is deposited on the backside of the wafer, while the inertial sensors are still patterned on the front-side of the wafer. This allows for increased accuracy of the sensors photo-lithographic pattern and hence the improved performance of the inertial sensors.

3. The sensors etch step is moved to the end of the fabrication process, eliminating the requirement for a photoresist protective layer covering the sensors during the through-wafer etch, Fig. 3.2(g). As a result, the problem of baking the photoresist during the long duration through-wafer etch is eliminated, and no aggressive cleaning of devices

at the end of the fabrication in necessary. This allows for improved yield of the overall process.

3.2.1 Back-side processing: Flexible hinges and metal traces fabrication

Formation of flexible polymer hinges is a critical step in the "Origami" MEMS process. Hinges allow for folding of flat micro-structures to form a three-dimensional IMU device. In addition to the mechanical support of the device panels, the polymer material provides the electrical insulation for the network of metal traces. Therefore, while choosing the material for flexible-hinge fabrication, both electrical and mechanical properties need to be considered.

Photo-definable polyimide is widely used for fabrication of flexible structures. It has garnered much attention as a structural material due to its many favorable features, including low Youngs modulus (3.4 GPa) and excellent electrical properties, such as a low dielectric constant, high volume, and surface resistivity. Polyimide is typically spin-coated and cured at high temperature. Once cured, the polyimide film is resistant to most solvents and chemicals.

The process flow for polyimide flexible-hinge fabrication is shown in Fig. 3.3. The HD-4110 polyimide is first deposited on the substrate by spin-coating, then the pattern is photo-

	Polyimide	**Parylene C**
Tensile Strength (MPa)	200	96
Elongation to Break (%)	45	200
Dielectric Constant at 1kHz	3.2	3.1
Volume Resistivity (Ohm-cm)	3.3×10^{16}	8.8×10^{16}
Maximum Temperature (°C)	1,0,0350	1,0,0290

Table 3.1: Mechanical, electrical, and thermal properties of polyimide and parylene C

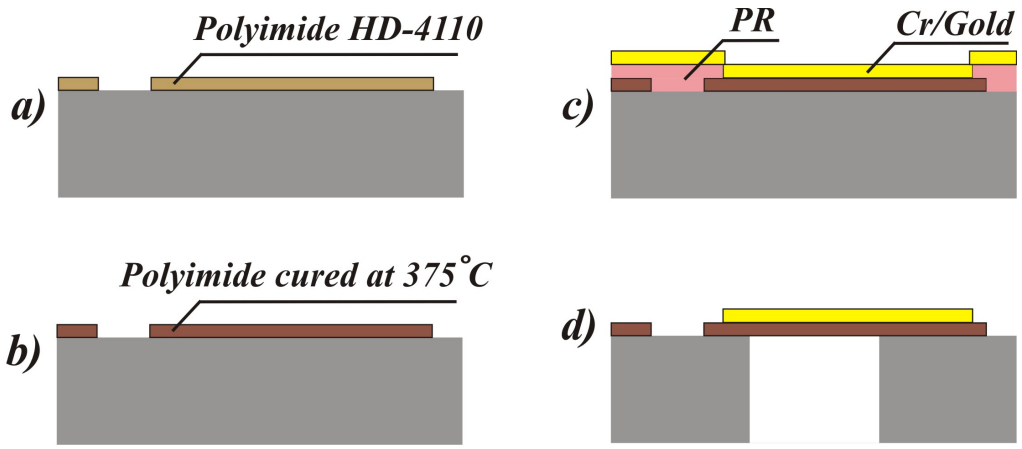

Figure 3.3: Fabrication of polyimide flexible hinges: a) polyimide deposition using spin-coating of substrate, b) curing to enable extensive polymer cross-linking, c) metal traces formation using lift-off process, d) silicon back-side etching.

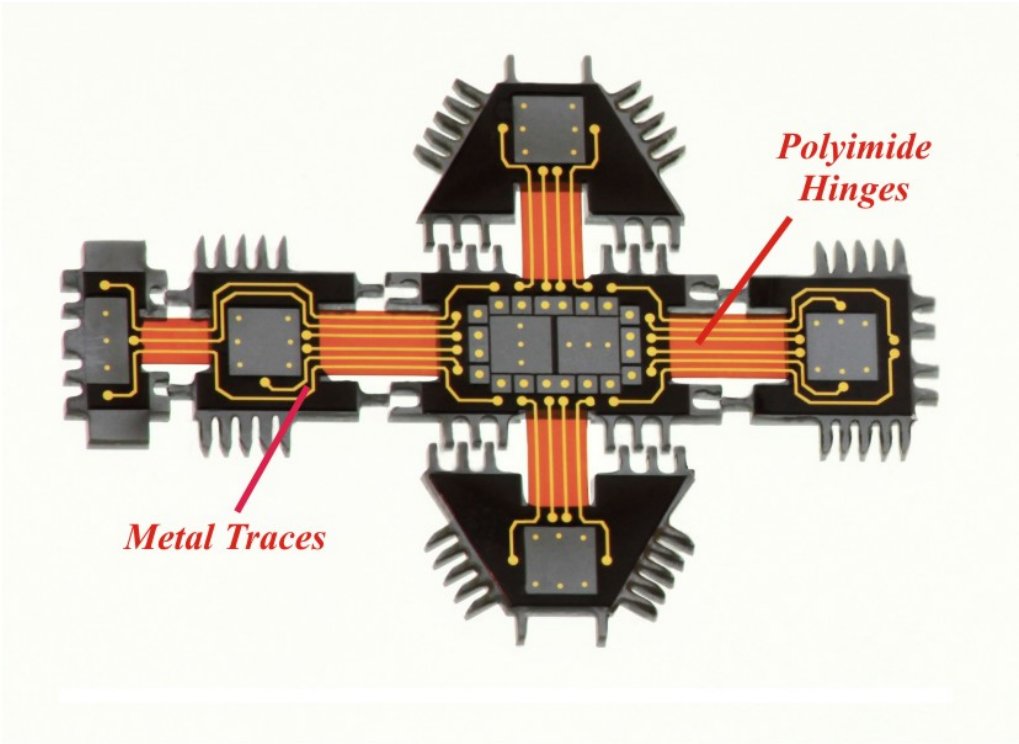

Figure 3.4: Micro-photograph of a fabricated foldable IMU structure with 15 μm thick polyimide flexible hinges and metal traces.

lithographically defined, Fig. 3.3(a). To improve the adhesion of polyimide to the silicon nitride surface the VM-652 adhesion promoter is used, available from HD MicroSystems. The thickness of polyimide layer before curing is 28 μm.

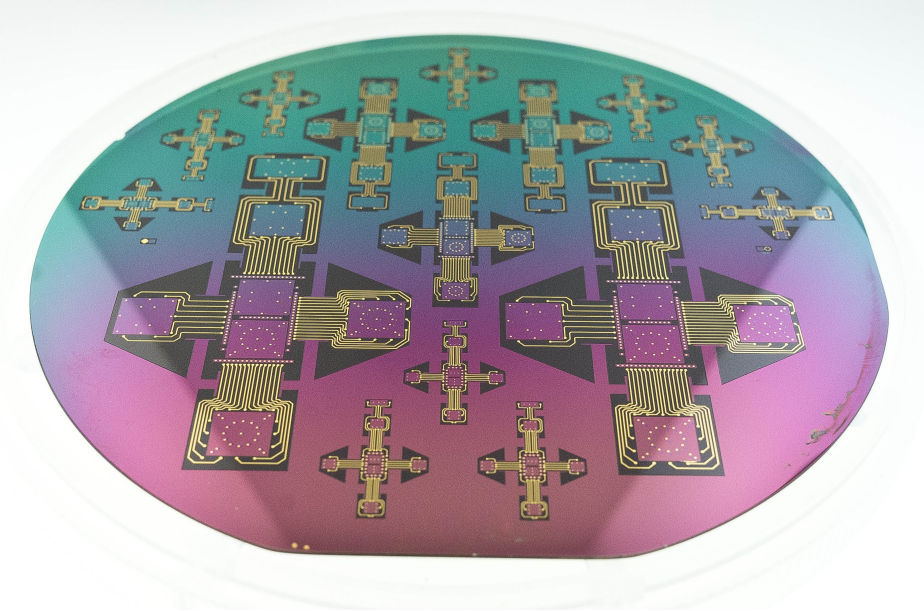

Figure 3.5: Backside of the SOI wafer with patterned flexible polyimide hinges and metal traces on polyimide.

Once the polyimide is deposited and patterned, it is cured at 375 °C in the nitrogen environment, Fig. 3.3(b). One hour of curing enables extensive polymer cross-linking, which provides mechanical and chemical robustness. After polyimide is fully cured, the final film thickness is approximately 15 μm. Following the polyimide deposition, a 0.05 μm thick Cr adhesion layer and a 0.5 μm gold layer are evaporated, Fig. 3.3(c). Lift-off process is utilized to pattern the metal and define the electrical traces and the contact pads features, Fig. 3.3(d). Fig. 3.5 illustrates the backside of the SOI wafer with patterned flexible polyimide hinges and metal traces on polyimide.

Parylene-C is another polymer which has recently gained interest as a structural material for fabrication of 3D foldable structures, and it was also explored in this work. Parylene is a polymer deposited using vapor deposition at a room temperature; it is chemically inert and stable, while having a very high surface and volume resistivity and low Youngs modulus (2-5 GPa). With an elongation-to-break percentage of more than 200%, parylene-C is a preferable material for applications requiring large deflections. Parylene has excellent electrical properties: low dielectric constant and loss with good high-frequency properties; good

dielectric strength; and high bulk and surface resistivities. In addition, parylene is virtually not out-gassing, which is critical for vacuum packaging of IMU devices.

The process flow for fabrication of parylene flexible hinges starts with E-Beam deposition of 50 nm Cr layer, which enables an improved adhesion between the parylene layer and a Si wafer, Fig. 3.6(a). An alternative option to use Silane A-174 as an adhesion promoter was also explored. However, this material was concluded to be not compatible with a subsequent HF release step. Adhesion promoter, Silane A-174, is damaged during prolonged immersion in HF solution, resulting in a loss of adhesion of the parylene film and easy peeling off. A vacuum deposition system (SCS Labcoter 2) is used to deposit a 16 μm thick film of parylene-C. This is followed by evaporation of a 150 nm thick Ti layer, which serves as a mask for parylene etching. The AZ nLOF 2035 photoresist lithography is performed to define the flexible hinges and the Ti mask is etched using Reactive Ion Etching (RIE), Fig. 3.6(b).

Next, we RIE process the parylene and etch the photoresist layers, Fig. 3.6(c). This part of the process completes with immersing the wafer into a 20 % hydrofluoric acid (HF) solution for 1 min to remove the Ti residue redeposited onto the wafer during the RIE etching. Metal traces on top of the parylene are created using E-Beam evaporation of Cr adhesion layer (0.05 μm) and gold layer (0.5 μm), followed by the lithography step and metal lift-off, Fig. 3.6(d). Fig. 3.8 illustrates the backside of the SOI wafer with patterned flexible parylene hinges and metal traces on parylene.

The critical mechanical, electrical and thermal properties of polyimide and parylene C are summarized in Table 3.1. In order to compare advantages of different polymers for flexible hinges, foldable IMU structures with HD-4110 polyimide and with parylene-C hinges were fabricated, Fig. 3.4 and Fig. 3.7 . Using polyimide has an advantage of a simple deposition process, where a wafer is spin-coated with a thick polymer film. Polyimide, however, requires curing. It has been noticed that after the heat treatment at high temperatures (>350 °C) the polyimide film does not allow for easy plastic deformation and is less suitable for folding.

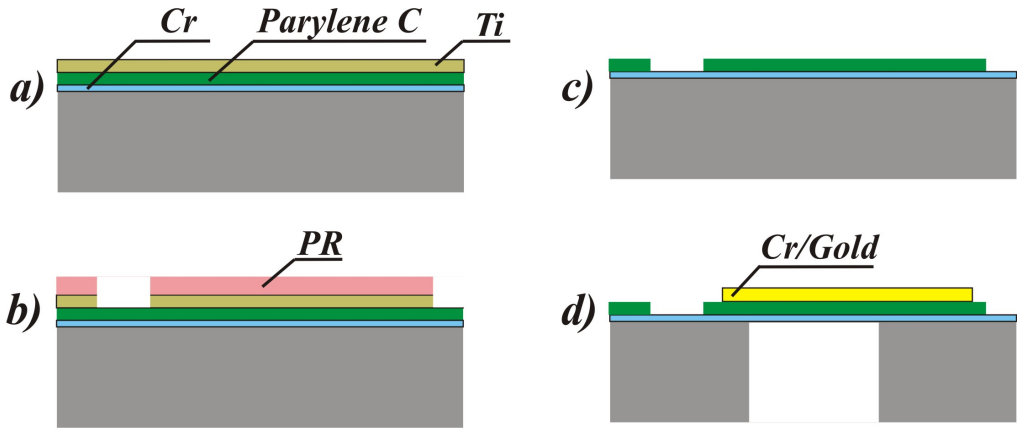

Figure 3.6: Fabrication of parylene flexible hinges: a) Cr adhesion layer and parylene deposition, followed by Ti layer evaporation, b) Ti mask etching, c) parylene etching using RIE, d) metal traces formation and silicon back-side etching.

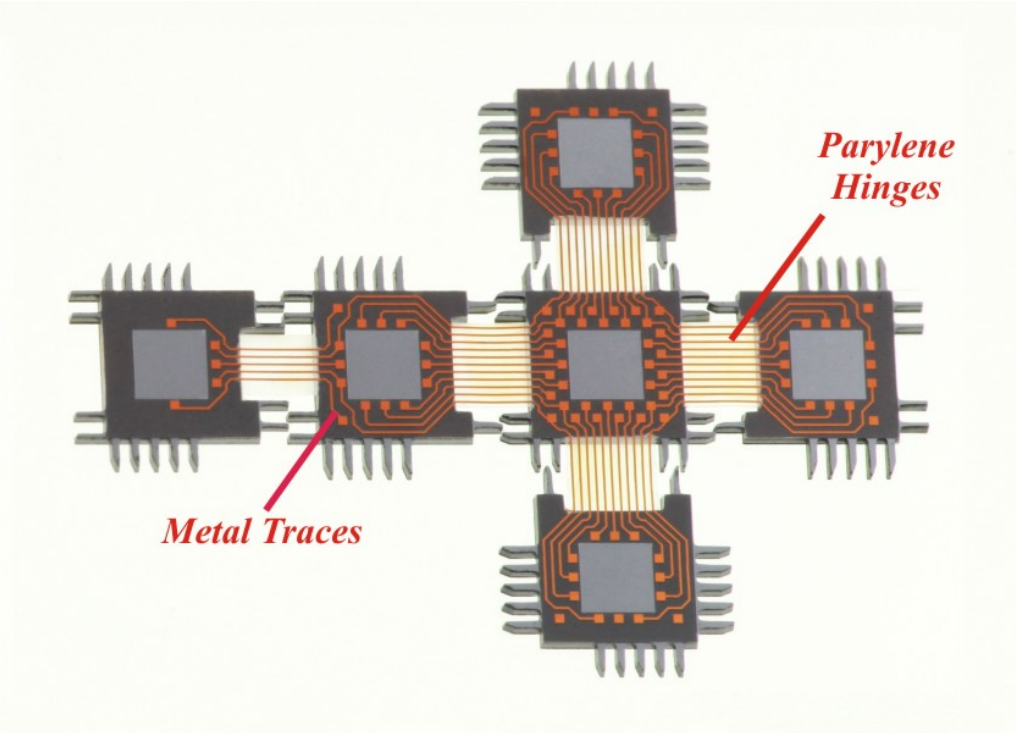

Figure 3.7: Micro-photograph of a foldable IMU structure with 16 μm thick parylene-C flexible hinges and metal traces.

Bending of polyimide hinges from 0 to 120° resulted in forming cracks in the film. For larger plastic deformation, a lower curing temperature has to be considered [41], but the adjustment might potentially lead to degradation in the mechanical, chemical, and dielectric properties of the film. In contrast to polyimide, parylene is deposited using a vacuum vapor deposition

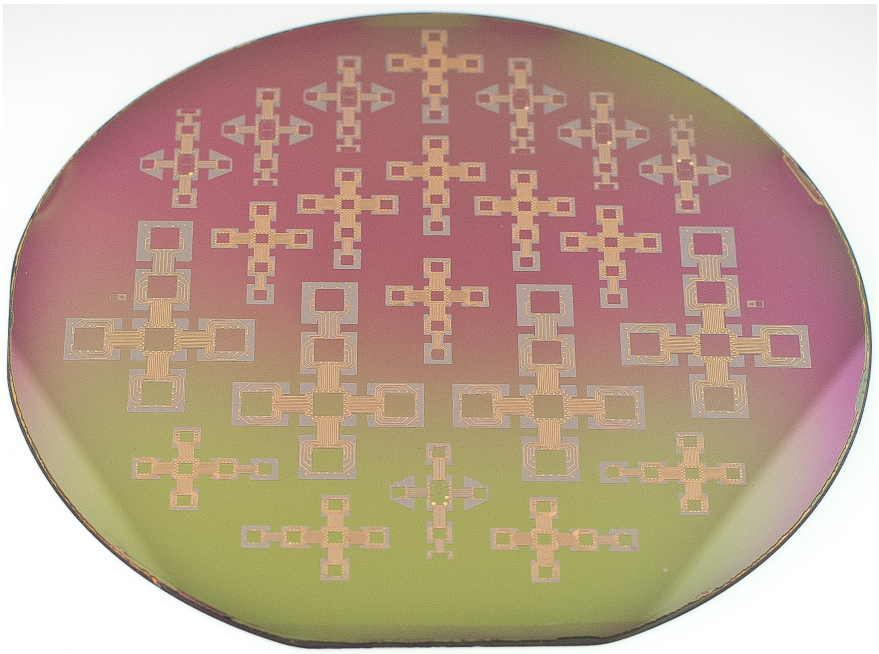

Figure 3.8: Backside of the SOI wafer with patterned flexible parylene hinges and metal traces on parylene.

process, which requires up to 6 hours for a 16 μm thick film. Parylene, however, does not require curing. Fabricated IMU prototypes with parylene hinges showed superior quality of the film after folding: no cracking or traces delamination were observed.

Both polymers were experimentally demonstrated to survive the prolonged temperature treatment at 285 °C for Parylene C and at 350 °C for polyimide HD-4110. This opens a path for wafer-level vacuum packaging and chip-level ceramic packaging of Folded IMU.

However, due to the described advantageous properties of parylene, it was selected as a material for flexible hinges in the most recent folded IMU fabrication runs.

3.2.2 Back-side processing: Contact pads reinforcement with electroplated nickel

Metal traces on polymer serve to provide a path for electrical signals from the sensors integrated on the IMU sidewalls to signal processing electronics. Traces for the sensors on the side panels and a top panel of the 3D structure run through the flexible hinges and terminate at the IMU bottom side. Integration with electronics can be realized using one of the following methods:

- by flip-chip bonding of the gold contact pads on polymer to the adapter board, followed by wirebonding from the adapter board to the package;
- by flipping the 3D structure "bottom-side up" and wirebonding from the gold contact pads on polymer to the adapter board, followed by wirebonding from the adapter board to the package or by direct wirebonding from the gold contact pads on polymer to the package.

The last method is often used for initial characterization of the inertial sensors. First prototypes of the IMU structures were fabricated using the original process for metal traces on polyimide, Fig. 3.3, and gold traces on parylene, Fig. 3.6. However, the flip-chip bonding connections and wirebonding connections (from the electrical contact pads on polymer to the glass adapter board and to the package) were found to be highly unreliable, especially in case of gold pads on parylene. Increasing the gold thickness from 0.5 μm to 2 μm resulted in only slightly better stability of the electrical connections. Therefore, the process in Fig. 3.6 was modified to include the step of reinforcing the electrical contact pads with electroplated nickel.

Foldable Si structures can be fabricated using the process flow in Fig. 3.9 for Ni-reinforced metal traces on parylene, or using the process flow in Fig. 3.10 for Ni-reinforced contact

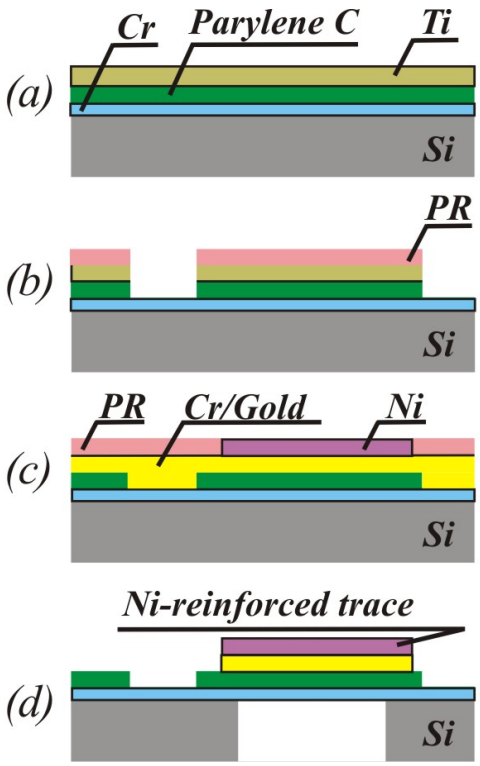

Figure 3.9: Process flow for foldable structures with Ni-reinforced metal traces on parylene.

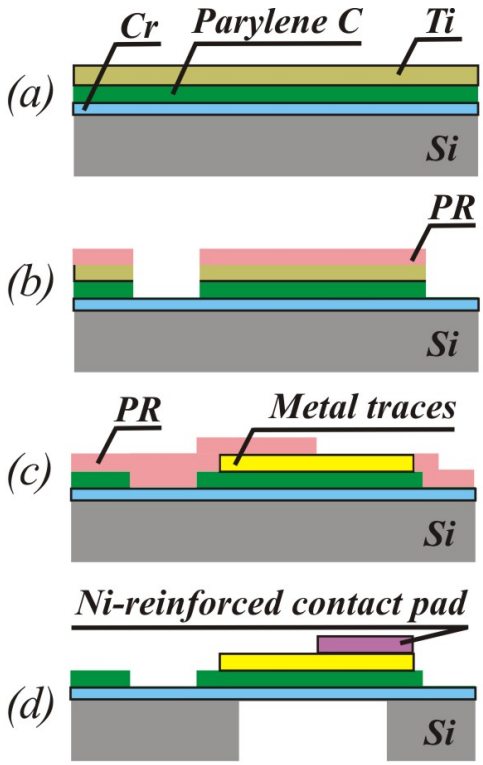

Figure 3.10: Process flow for foldable structures with Ni-reinforced contact pads and gold traces on parylene.

pads and gold traces on parylene. In both cases, the fabrication starts with deposition of a Cr adhesion layer and a 16 μm thick film of parylene-C, Fig. 3.9(a) and Fig. 3.10(a). The flexible hinges are photo-lithographically defined, and the parylene is etched using the RIE process with a Ti mask, Fig. 3.9(b) and Fig. 3.10(b).

Metal traces are created using E-Beam evaporation of the Cr layer (50 nm) and the Au layer (0.5 μm), Fig. 3.9(c). Next, the wafer is spin-coated with a thick layer of photoresist and the metal traces features are defined. A wafer-level electroplating method is then used to cover the areas of the wafer, free of the photoresist, with a 0.7$\div$1 μm thick layer of Ni, Fig. 3.9(c). Nickel electroplating is performed at 54°C temperature, using sulfamate nickel plating solution. The total plating time for 1 μm layer of nickel is approximately 15 min with a current of 8.3 mA (0.3 V). The plating rate was identified, using the Dektak profilometer measurements, Fig. 3.11.

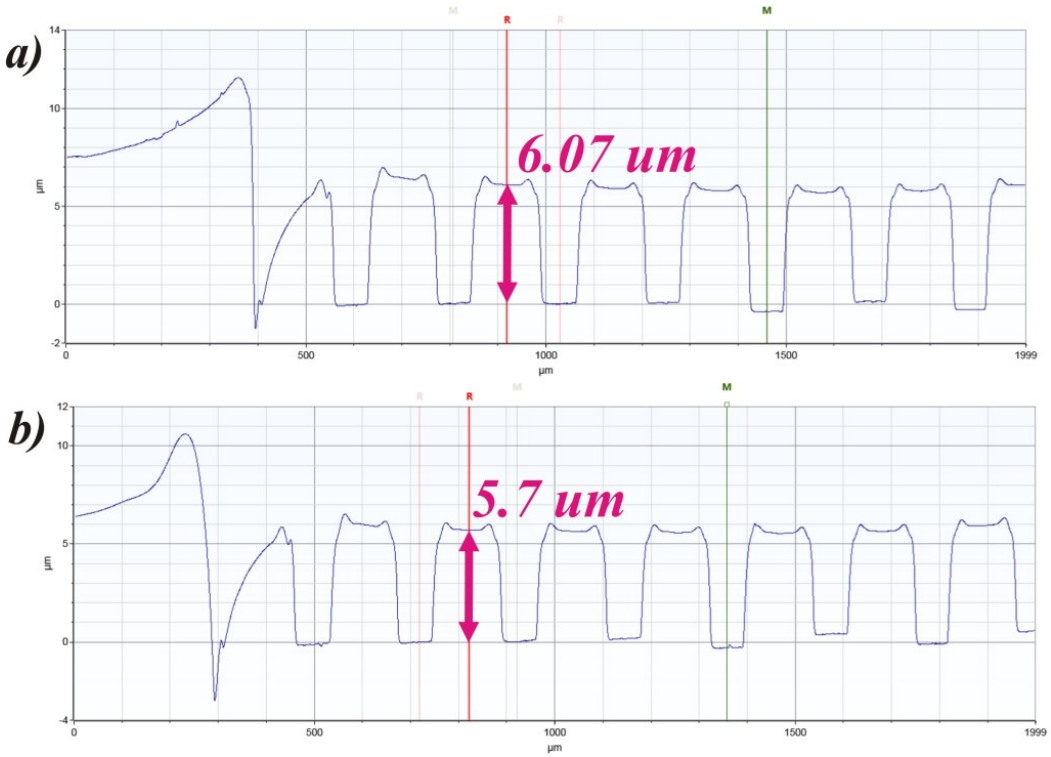

Figure 3.11: Dektak profilometer measurements before and after 7 min of nickel plating, showing the plating rate of about 0.05 μm/min.

This is followed by stripping the photoresist in acetone and wet-etching the Au and Cr layers using the electroplated Ni as a mask, Fig. 3.9(d). Gold etchant GE 8148 (50 Å/sec) and chromium cermet etchant TFE (20 Å/sec), both compatible with a nickel mask, are used during the wet-etching process. Backside of the SOI wafer with metal traces and contact pads reinforced with electroplated nickel is shown in Fig. 3.12. Nickel electroplating allows for increased thickness and hardness of metal. This enables reinforcement of metal traces and contact pads thereby assuring the increased reliability of the wire-bond connections to the electrical contact pads on parylene, Fig. 3.13. The backside thru-wafer Si etch completes the process, Fig.2.1(d).

Ni-reinforced metal traces on parylene hinges have been tested for continuity and resistivity, Fig. 3.14. Probe testing confirmed the metal traces continuity and revealed the electrical resistivity of < 221 $n\Omega$·m for 1 μm nickel electroplated metal traces (analytical value of

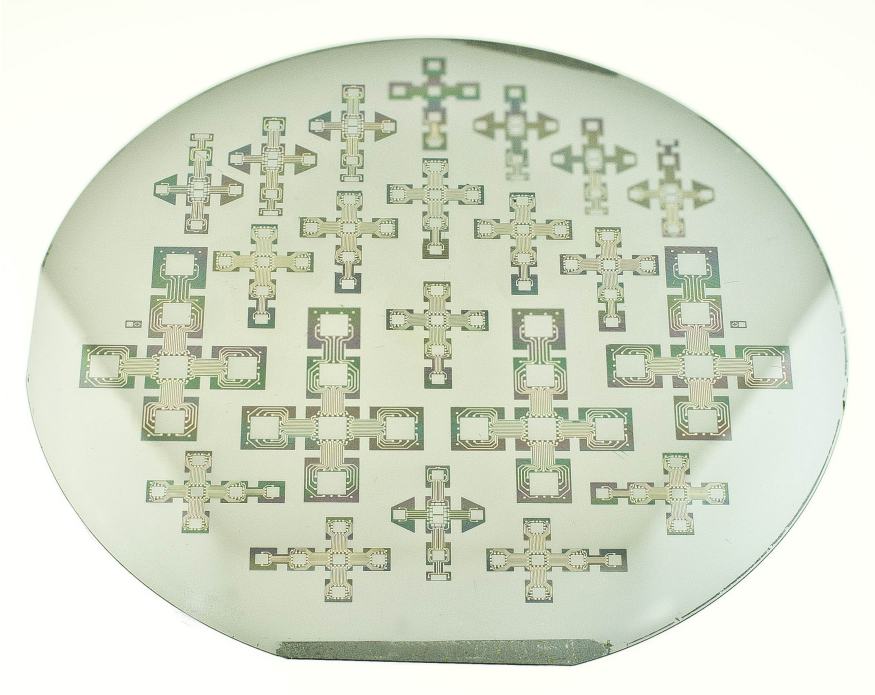

Figure 3.12: Metal traces and contact pads reinforced with electroplated nickel on wafer level.

electrical resistivity is 30 $n\Omega$·m).

Alternatively, Ni electroplating can be used for reinforcement of electrical contact pads only. The Cr layer (50 nm) and the Au layer (0.5 μm) are first deposited using E-Beam evaporation and the metal traces features are defined, Fig. 3.10(c). Next, the wafer is spin-coated with a thick layer of photoresist, the electrical contact pads are defined and covered with a ($0.7 \div 1$ μm thick layer of Ni, using wafer-level electroplating method, Fig. 3.10(d). The backside thru-wafer Si etch completes the process, Fig. 3.10(d).

The method of contact pads reinforcement, where only the pads are covered with Ni, is preferable for miniature IMU (<15 mm^3) since electroplating of the full length of traces results in partial delamination of thick traces from parylene during folding. However, for the 50 mm^3 IMU presented in this paper, the method of reinforcement using electroplating of the full length of traces was chosen. It has an advantage of the simplified process flow where one of the lithography steps is eliminated. For the IMU prototypes of this volume,

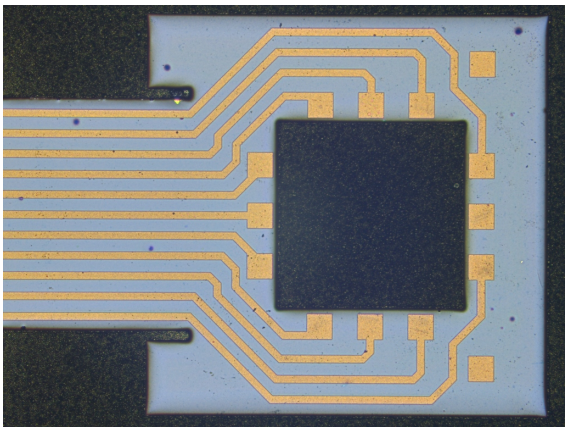

(a) Gold metal traces before nickel electroplating.

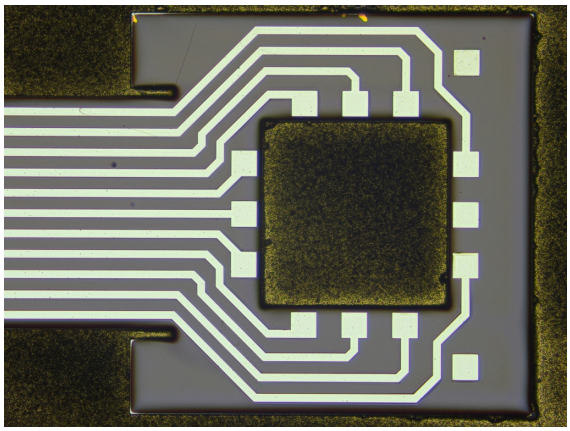

(b) Gold metal traces covered with electroplated nickel.

Figure 3.13: Metal traces and contact pads reinforced with electroplated nickel.

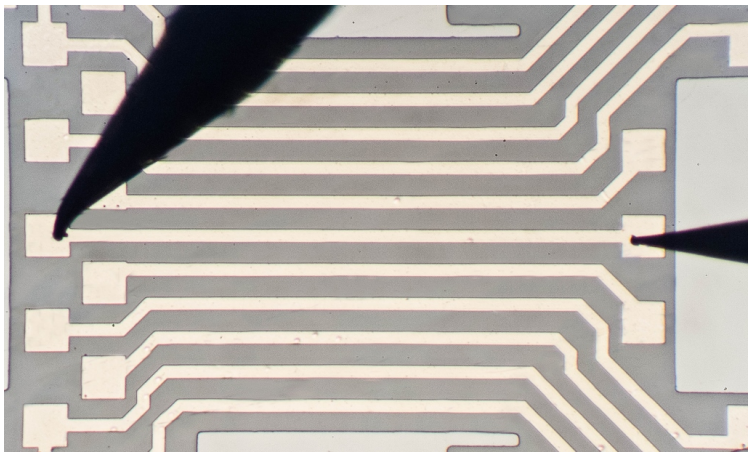

Figure 3.14: Probe testing confirmed metal traces continuity and revealed the electrical resistivity of < 221 $n\Omega$·m for 1 um nickel electroplated metal traces.

the delamination of Ni-reinforced traces was not observed.

In order to evaluate the method of pads reinforcement with Ni, the fabricated IMU prototypes were die-attached to a glass adapter board.The wire-bonding connections were then formed between the the sensors of the IMU sidewalls and Ni-reinforced contact pads, as well as between the Ni-reinforced contact pads and glass adapter board. The wire-pull tests showed that nickel reinforcement of the contact pads results in a greatly improved reliability of the wire-bonding connections.

3.2.3 Front-side processing: Foldable origami structure and inertial sensors

Once the backside processing is complete, the interconnects, the polymer and metal features are protected with a layer of photoresist. For more robust protection, a layer of dicing tape is applied on top of the photoresist. A carrier wafer is then attached using thermal grease as an adhesive while also providing a thermal conductive path to the fabrication wafer, Fig. 3.15(a).

Front-side processing starts with sensors silicon dioxide hard mask fabrication, Fig. 3.15(b).

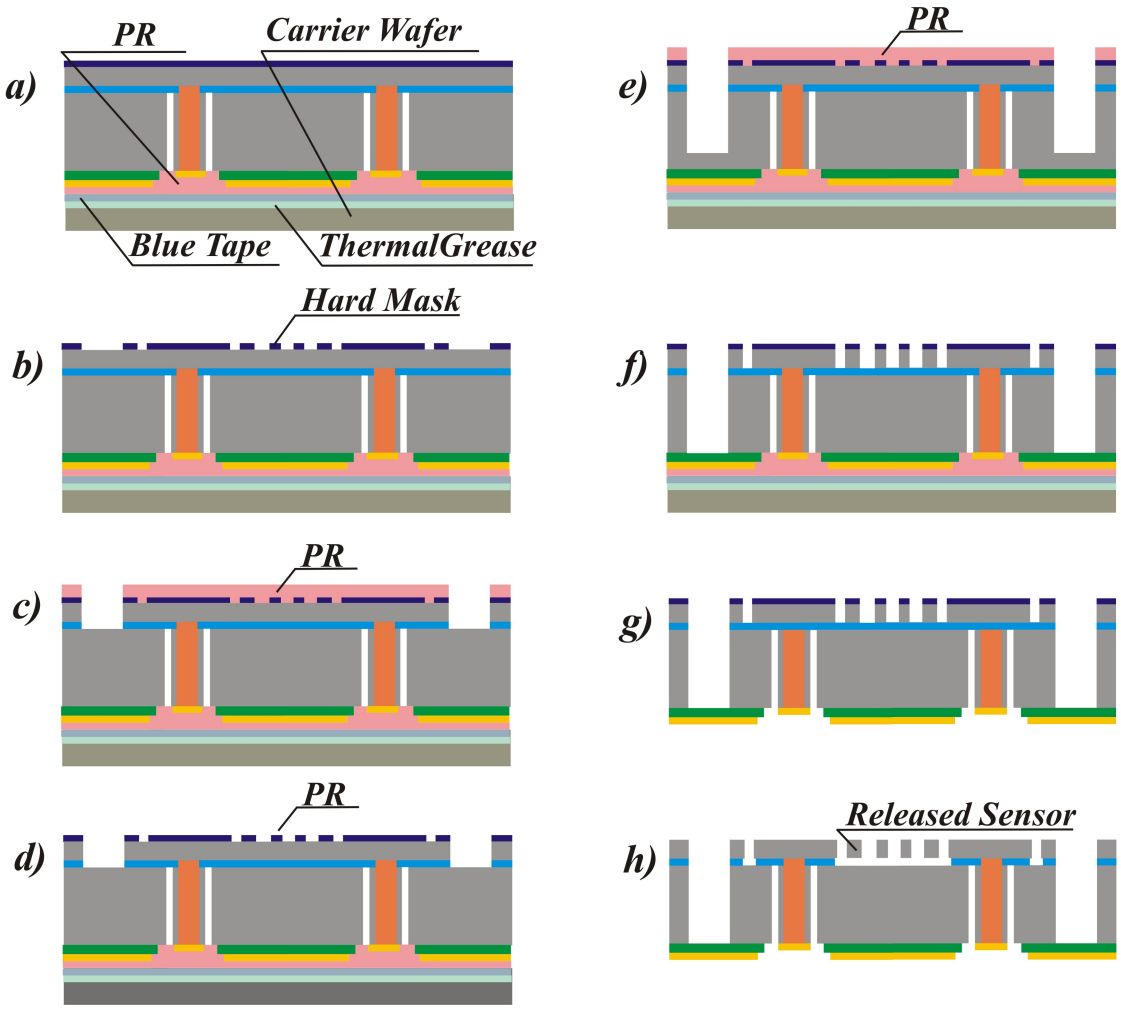

Figure 3.15: Folded IMU fabrication process: Topside processing.

Using positive Shipley 1827 photoresist, the wafers are spin-coated and patterned. The clean-room recipe for photolithography using Shipley 1827 photoresist is describes in Appendix A1. Next, 1 μm of LPCVD silicon nitride and 1.5 μm layer of thermal oxide is etched using advanced oxide etching (AOE), and photoresist mask is striped in acetone, Fig. 3.16.

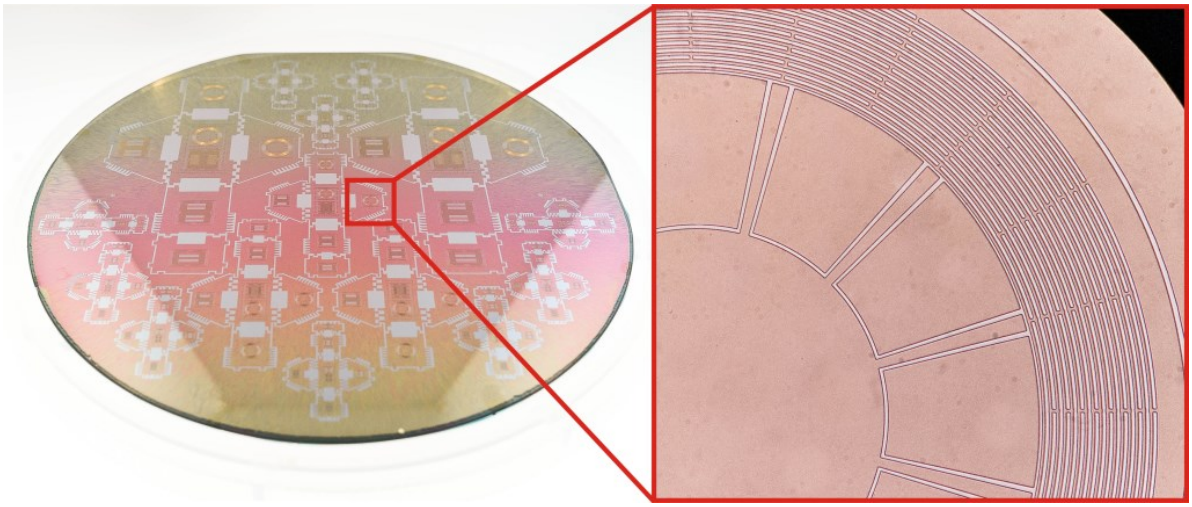

Figure 3.16: Sensors hard mask fabrication using Shipley 1827 photoresist

The sensors are then protected with photoresist, using Preetch mask, 100 μm device layer is etched using Deep Reactive Ion Etching (DRIE), and 5 μm buried oxide is etched, using Advanced Oxide Etching (AOE), Fig. 3.15(c). The main challenge at this step is related to burning of photoresist during the prolonged etching inside the AOE and DRIE tools. Another potential problem is related to wafer cracking due to the high pressure inside the air bubbles that are formed in between the SOI wafer and a protective layer of blue tape on back side of the wafer.

In order to keep sensors clean and to increase the overall yield of the IMU fabrication process, the additional PR stripping and lithography steps are introduced. After etching through the buried oxide, the resist layer is stripped in acetone, using sonication at the frequency of 37 kHz, Fig. 3.15(d). Next, another layer of photoresist is applied and the 370 μm handle wafer is etched, Fig. 3.15(e). The total etch height of 470 μm for the device layer and the handle wafer was estimated using Dektek XT profilometer, Fig. 3.17.

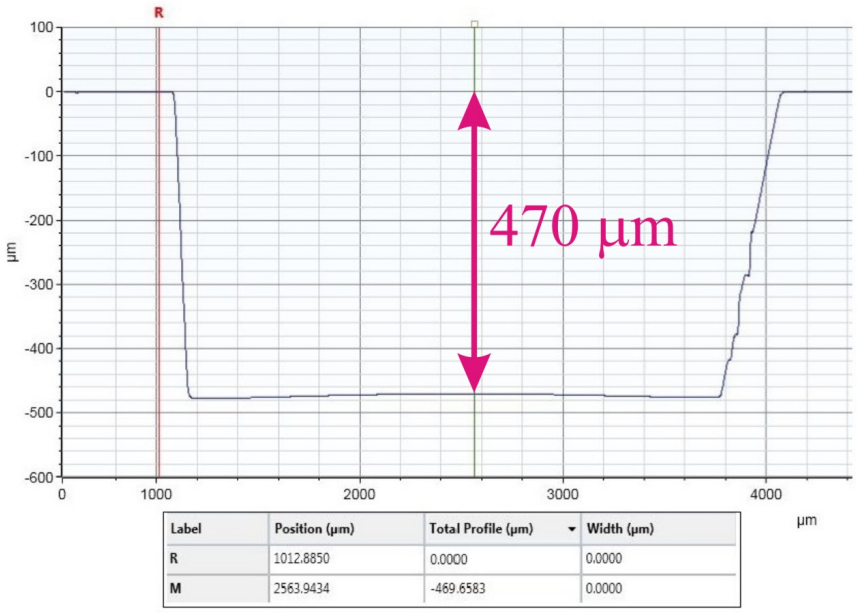

Figure 3.17: Wafer profile after DRIE etching of handle wafer

Figure 3.18: Fabricated unfolded IMU structures

After that, the resist layer is removed in acetone, exposing the oxide hard mask. Finally, the device layer and the last 100 μm of the handle wafer are etched in parallel, using DRIE, Fig. 3.15(f). The carrier wafer was then removed in acetone, leaving separate IMU structures, Fig. 3.15(g). IMUs of both medium and small size are shown in Fig. 3.18.

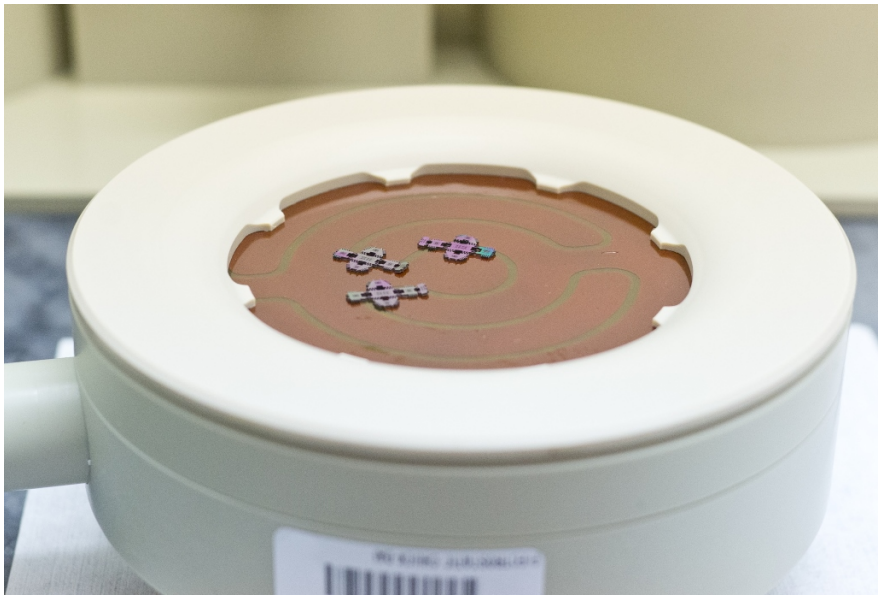

Figure 3.19: Unfolded IMU structures are placed on the electrostatic chuck of the IDONUS HF Vapor Phase Etcher.

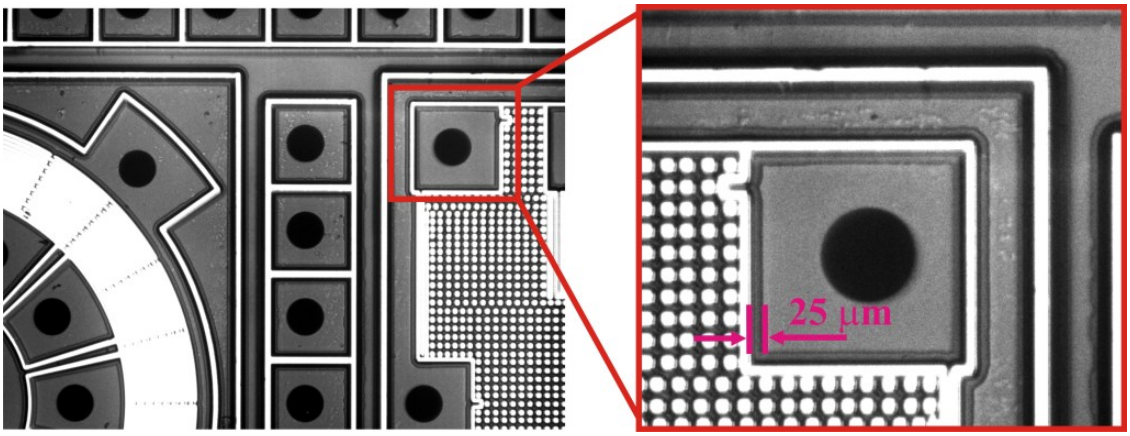

Figure 3.20: The under-etching of the buried SiO2 after 50 min of HF vapor etch time was estimated to be about 10 %.

After backside processing is complete, the inertial sensors are released, using a vapor HF stiction-free release process. Unfolded IMU structures are placed on the electrostatic chuck of the IDONUS HF Vapor Phase Etcher, Fig. 3.19. In order to release the perforated moving structures of the sensors, 5 μm buried oxide layer is etched away.

Etching was performed for the duration of 50 min at 36 °C. The etch rate can be estimated using IDONUS IR-Light Wafer Inspection Microscope. Silicon is a transparent material for

infrared light, and the IR light microscope illuminates the silicon substrate from the back-side and captures the light that transverses the substrate. Therefore, it becomes possible to inspect phenomena inside the silicon substrate, which are not visible with a conventional microscope. The under-etching of the buried SiO2 after 50 min of etch time was estimated to be about 10 %, which is acceptable for the 250 μm anchors, Fig. 3.20.

3.3 Characterization

3.3.1 Co-Fabrication Approach

Folded 3D MEMS process described in Section 2.2 allows for parallel fabrication of foldable structures and different types of SOI-based inertial sensors. IMU prototypes, featuring three single-axis accelerometers, a resonator (prototype of a reference clock), and three single-axis gyroscopes, is shown in Fig. 3.21. Performance of the stand-alone inertial sensors was demonstrated in [39], [139]. All sensors were modified for compatibility with the Folded MEMS process.

The static open-loop single-axis SOI accelerometer has a footprint of 3x3 mm and is comprised of a suspended proof-mass, Fig. 3.22(a). The key parameters of the accelerometer are summarized in Table 3.2. Accelerometers were designed to operate at the resonant frequency of 650 Hz, Fig. 3.23. Two pairs of differential electrodes with parallel plates are used for sensing the capacitance change under the applied acceleration.

For technology demonstration, a nominal gap of 7 μm between the parallel plates was chosen. However, for the double-sided fabrication process presented in this paper, the minimum gap is limited only by the silicon etching aspect ratio. Since the state-of-the-art DRIE aspect ratios are usually between 50:1 and 100:1 [137], the minimum gap in Folded IMU process

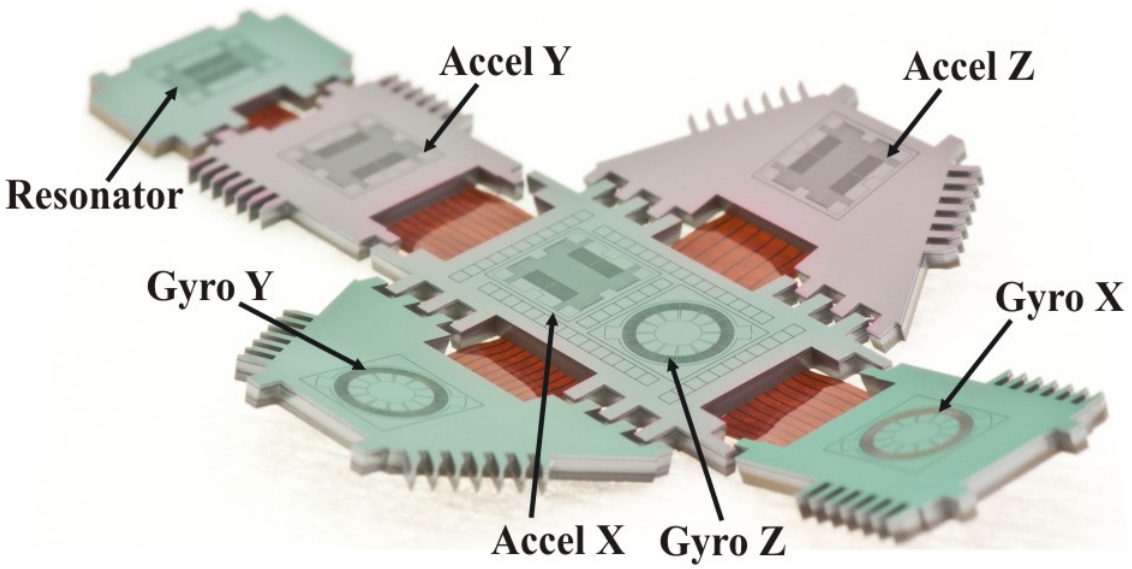

Figure 3.21: "Origami-like" Folded MEMS TIMU (Timing and Inertial Measurement Unit) with in-situ fabricated three gyroscopes, three accelerometers and a resonator (prototype of a reference clock).

can be potentially reduced to <2 μm.

Similar to the accelerometer, a resonator is comprised of the suspended proof-mass, Fig. 3.22(c). The sensor footprint is 2x3 mm. It is designed to operate at 5.6 kHz frequency. The resonator is included as a prototype of the master clock, which can serve all frequency-reference functions in IMU.

Single-axis SOI Toroidal Ring Gyroscope (TRG) were implemented on the sidewalls of the

Parameter	**Value**	**Units**
Footprint)	3x3	mm^2
Frequency	650	Hz
Nominal Gap	7	μm
Sense Capacitance	2.99	pF
Dynamic Range	± 4	g
Brownian Noise (Theoretical)	0.38	$\mu g/\sqrt{Hz}$.

Table 3.2: Key parameters of accelerometers integrated on the IMU sidewalls.

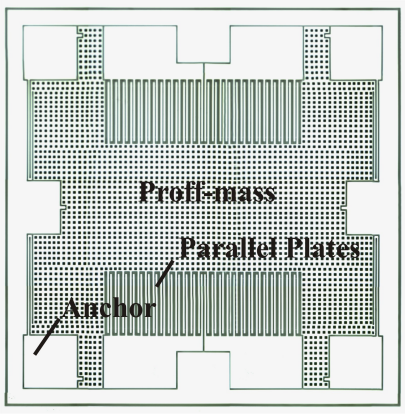

(a) Accelerometer architecture

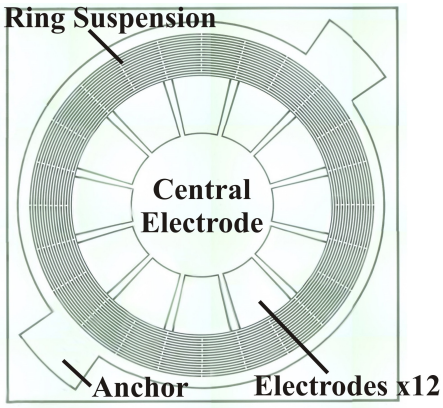

(b) Gyroscope architecture

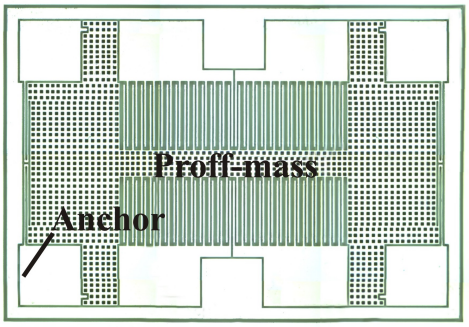

(c) Resonator architecture

Figure 3.22: IMU prototypes are comprised of three single-axis accelerometers (a), three single-axis gyroscopes (b), and resonator, prototype of a reference clock, (c).

Folded IMU test structures. The designs of this gyroscopes was previously introduced in [39]. In order to enable integration with the Folded IMU, the sensor dimensions and several critical features were modified as described below.

Parameter	**Value**	**Units**
Footprint)	3.1x3.1	mm^2
Diameter)	2.8	mm
Frequency	14	KHz
Nominal Gap	7	μm
Total Capacitance	0.8	pF

Table 3.3: Key parameters of Toroidal Ring Gyroscope (TRG) integrated on the IMU sidewalls.

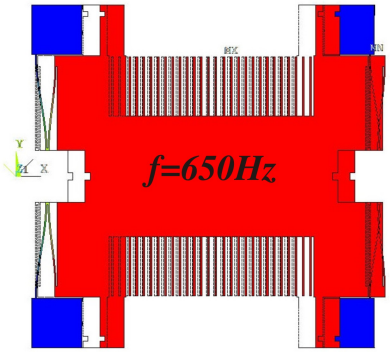

Figure 3.23: Static open-loop single-axis SOI accelerometer. Two pairs of differential electrodes with parallel plates are used for sensing the capacitance change under applied acceleration.

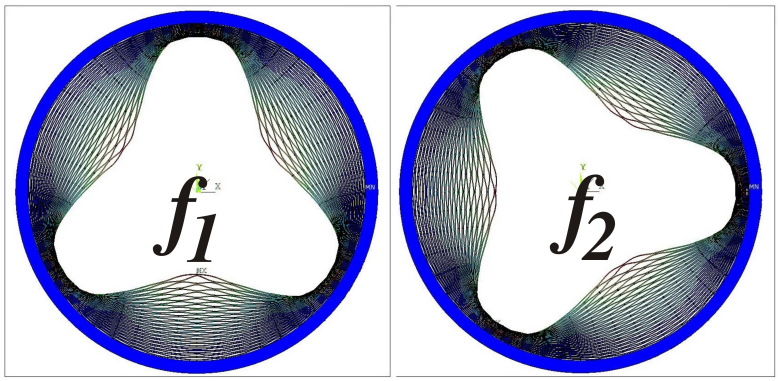

Figure 3.24: Toroidal Ring Gyroscope: n=3 wineglass modes of operation.

The Toroidal Ring Gyroscope (TRG), first implemented in the epitaxial silicon encapsulation (EpiSeal) process, was initially reported in [39]. It is comprised of an inner electrode assembly, an outer support, and a ring suspension, Fig. 3.22(b). The inner electrode assembly consists of 12 radial electrodes that are used as a forcer and as a pick-off for each

Parameter	**Value**	**Units**
Footprint)	3.1x3.1	mm^2
Frequency	8	KHz
Nominal Gap	6	μm
Total Capacitance	2.7	pF

Table 3.4: Key parameters of Dual Foucault Pendulum (DFP) integrated on the IMU sidewalls.

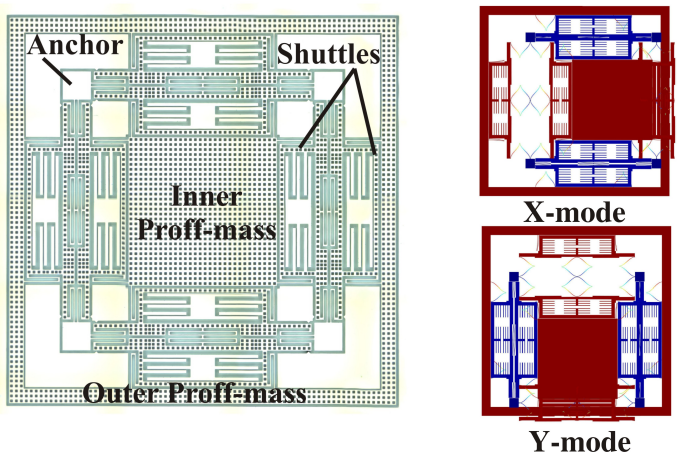

Figure 3.25: Central element of the Dual Foucault Pendulum (DFP) gyroscope is two mechanically coupled and dynamically equivalent proof-masses (inner mass and outer mass), oscillating in anti-phase motion, [139].

of the wineglass modes. Design adaptation for the Folded MEMS IMU process resulted in increased diameter (from 1.76 to 2.8 mm), increased capacitive gap (from 1.5 to 7 μm), and reduced operational frequency (from 60 kHz to 14 kHz). The suspension system was formed by the sixteen 10 μm thick concentric rings. The gyroscope was designed to operate in the n=3 wineglass modes (Fig. 3.24), which are the lowest in frequency ordering among all modes of the structure, [138]. Since the diameter of the TRG can be further reduced to approximately 1.4 mm, this design is most suitable for ultra-miniature IMUs with a volume of less than 15 mm^3. Key parameters of the gyroscope are summarized in Table 3.3.

Only one design of a gyroscope is sufficient for the IMU implementation. However, for the purpose of performance comparison, a different type of a single-axis SOI gyroscopes were implemented on the sidewalls of several of the Folded IMU test structures: Dual Foucault Pendulum (DFP). The dynamically balanced Dual Foucault Pendulum (DFP) gyroscope, fabricated using an SOI MEMS process, was first introduced in [139]. The central element of the sensor is two mechanically coupled and dynamically equivalent proof-masses (inner mass and outer mass), oscillating in anti-phase motion, Fig. 3.25. Dynamic balance is achieved by using identical (mirrored) suspension elements and shuttle assemblies as well

as by aligning the center of masses of each proof-mass. The center of mass of the system remains stationary during oscillation, causing the net force and torques generated by the combined system to be zero at all times. Electrostatic transduction of the sensor is realized using the arrays of parallel plates located within the shuttle assemblies. The design is most suitable for a medium-size IMUs. Key parameters of the gyroscope are summarized in Table 3.4. Each sidewall of a 50 mm^3 volume Folded IMU has a 3.16x3.16 mm opening for a sensor. To enable integration on the sidewalls of a Folded IMU device, the footprint of the original DFP design is reduced from 6.7 to 3.1 mm. In order to compensate for a significant reduction in sensor capacitance, the nominal gap was reduced from 8 to 6 μm, resulting in 2.7 pF total capacitance. The sensor was designed to operate in anti-phase mode at 8 kHz resonant frequency.

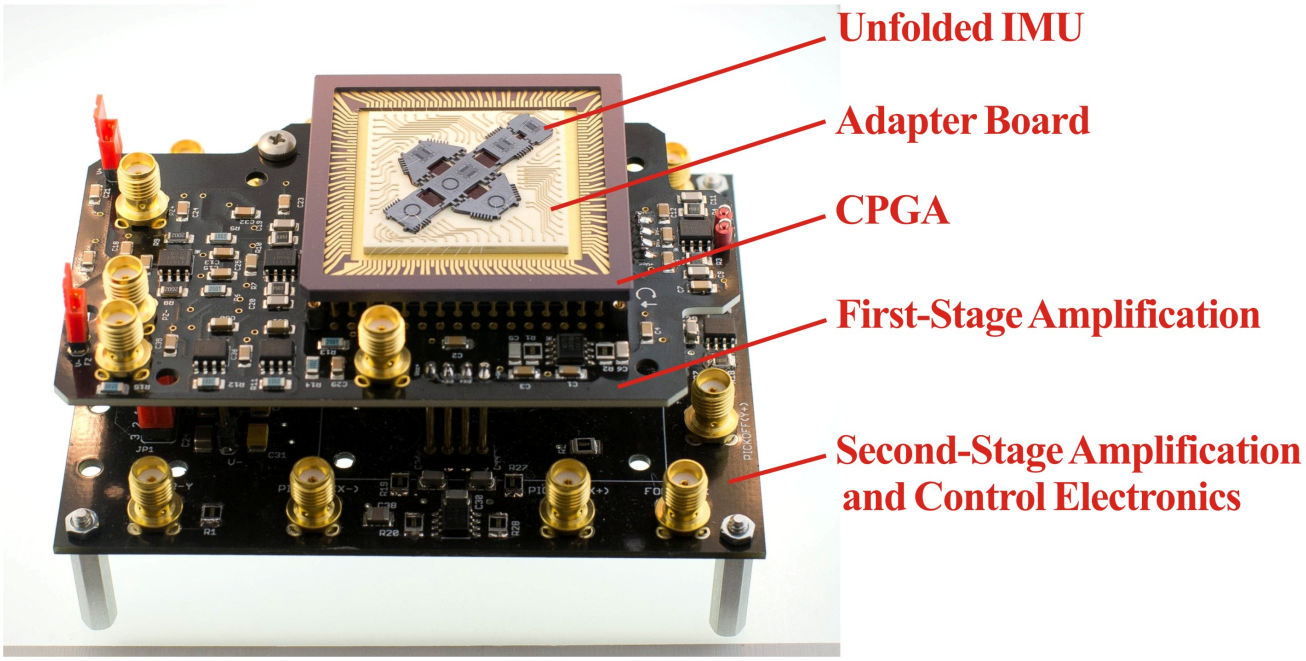

Figure 3.26: IMU prototype assembled with front-end electronics.

The double-sided Folded IMU fabrication run, with in-situ fabricated sensors and metal traces on polyimide, resulted in $> 80\%$ yield of operational sensors and yielded 10 out of 15 fully operational IMU devices (with all 7 sensors operational in the IMU).

For initial characterization, the unfolded IMU prototypes were die-attached to the adapter

board and then packaged into a 181-pin, gold plated through-hole Ceramic Pin Grid Array (CPGA) package (CPG18023, Spectrum Semiconductor Materials, Inc. San Jose, California, http://www.spectrum-semi.com/). The adapter board allows for transferring the electrical signals from the unfolded device to the rectangular pads on each edges, and enables easier wirebonding to CPG by reducing the length of the bonding wires. Packaged devices were assembled with front-end electronics, Fig. 3.26.

A double-stage Printed Circuit Board (PCB) contains three differential forcer and three differential detection channels for control of one gyroscope and one accelerometer in IMU. The detection circuit is based on a fully input/output differential amplifier (Texas Instrument Operational Amplifier THS4131) which is used in a transimpedance configuration. A capacitor of $10nF$ with a resistor value of $20K\Omega$ is used to provide a gain of 20k on the first stage (current to voltage). Outputs of the transimpedance amplifiers are cascaded into the bottom stage instrumentation amplifiers (Analog Devices AD8429) with a 20x gain amplification (voltage to voltage). The same instrumentation amplifiers (Analog Devices AD8429) are also used for forcer electronics on the bottom stage.

Table 3.5: Experimental freq. response characterization of the inertial sensors in-situ fabricated on the sidewalls of the same Folded TIMU device

Sensor	**Type**	**Frequency, f_c**	**Freq. Split, Δf**
Accel X	Accelerometer	648 Hz	-
Accel Y	Accelerometer	640 Hz	-
Accel Z	Accelerometer	670 Hz	-
Resonator	Resonator	5.57 kHz	-
Gyro X	Toroidal Ring Gyroscope (TRG)	14 kHz	10 Hz
Gyro Y	Toroidal Ring Gyroscope (TRG)	15 kHz	35 Hz
Gyro Z	Toroidal Ring Gyroscope (TRG)	16 kHz	220 Hz

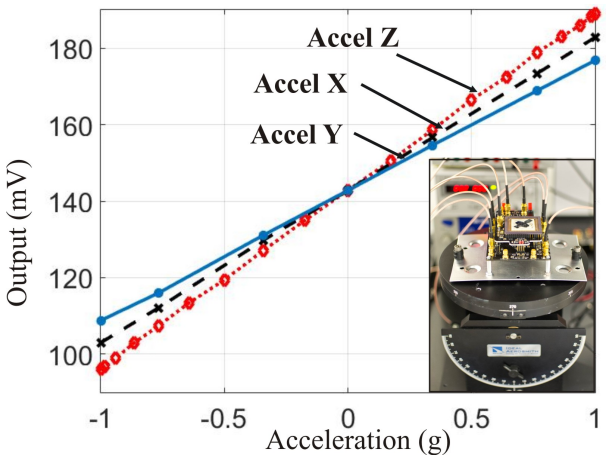

Figure 3.27: Tilt-table characterization of acccelerometer revealed SF of 39.9, 46.2, and 34 mV/g for three accelerometers.

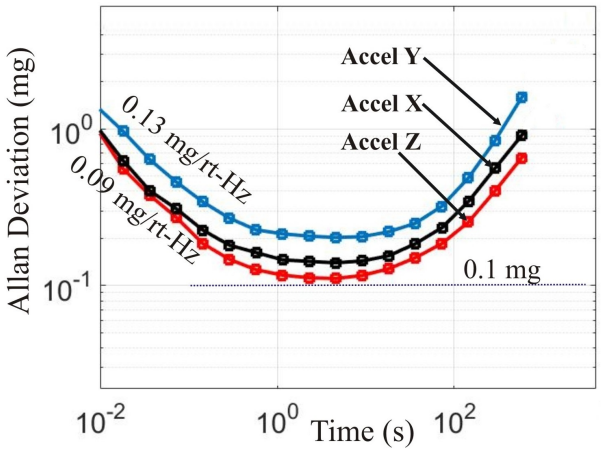

Figure 3.28: Accelerometer noise analysis revealed bias stability of 0.1 mg and velocity random walk (VRW) of 0.09 $mg/\sqrt{Hz}$.

Experimental characterization revealed several IMU prototypes in 50 mm^3 volume with all seven sensors operational, thus confirming feasibility of the proposed fabrication approach, Table 3.5. The accelerometers integrated on the IMU sidewalls were tested in air, and the gyroscopes were tested in a vacuum chamber at 0.5 mTorr vacuum.

Frequency domain characterization showed the resonant frequency of the resonator at 5.57 kHz and the resonant frequencies of 3 accelerometers spaced at 640, 648 and 670 Hz. Characterization of Toroidal Ring Gyroscopes co-fabricated on the IMU sidewalls revealed frequency splits of 10 Hz, 35 Hz and 220 Hz at the center frequencies of 14 kHz, 15 kHz, and 15.9 kHz, correspondingly, with a Q-factor of 100,000 at 0.5 mTorr vacuum. Frequencies of devices are separated by design in order to minimize cross-talk between sensors.

In order to derive the accelerometers scale factor, the IMU prototype and the signal processing electronics were mounted on the tilt-table. The accelerometer response test was conducted by tilting the stage 90 deg around the X and Y axes, providing ±1 g of acceleration amplitude. The carrier demodulation with a Zurich Instruments lock-in amplifier was used to measure the output current. A low-noise fully input/output differential amplifier (Texas Instrument Op. Amp. THS4131) was used in a transimpedance configuration in

order to convert current to voltage, as well as to increase the signal-to-noise ratio. The scale factors of 39.9, 46.2, and 34 mV/g were measured for X, Z, and Y accelerometers, correspondingly, 3.27. Experimental characterization of three accelerometers showed in-run bias instability as low as 0.1 mg and VWR of 0.09 $mg/\sqrt{Hz}$, 3.28.

Performance of the accelerometers was limited by noise of the signal processing electronics. Analytically calculated thermal mechanical noise of the accelerometer is lower than 0.38 $\mu g/\sqrt{Hz}$:

$$a_n = \sqrt{\frac{4k_bT\omega_o}{mQ}} = 0.38\,\mu g/\sqrt{Hz}, \tag{3.1}$$

where k_b is the Boltzmann's constant, m is the mass of a sensitive element, T is the temperature in K, ω_o is the resonant frequency, Q is the quality factor.

Electronics optimization may allow for improved performance. Six-channel front end PCB featuring low-noise amplifiers AD8066 (Analog Devices) was later developed for IMU control (Chapter 4). Utilizing this electronics, the scale factor and tilt-table experiment was performed for the similar design of the accelerometer (Table 3.2) implemented on the sidewall of the Folded IMU device. Tilt-table characterization revealed the scale factor of 59 mV/g, Fig. 3.29. Noise analysis revealed bias stability of 0.03 mg and velocity random walk (VRW) of 0.06 $mg/\sqrt{Hz}$, Fig. 3.30.

Dynamic response of the gyroscopes was tested using the capability of Ideal Aerosmith 2102 Series Two-Axis Position and Rate Table System, allowing to produce a rotation with programmed sinusoidal angular acceleration. Electrostatic actuation and capacitive detection were employed for gyroscopes operation. The gyroscopes were excited with a constant DC voltage and an AC voltage generated by a Phase Locked Loop. A carrier signal at frequency of 100 kHz was applied to the proof-mass, resulting in the amplitude modulation of the sensor output. The output signal was then demodulated to reveal the low frequency changes

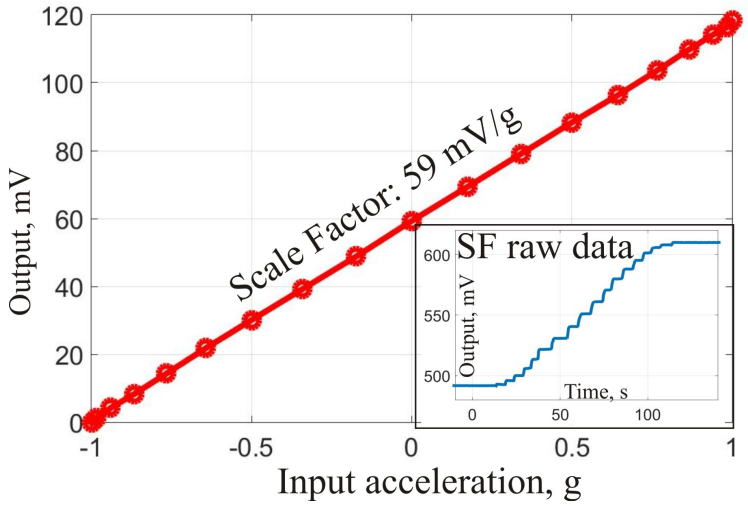

Figure 3.29: Tilt-table characterization revealed SF of 59 mV/g.

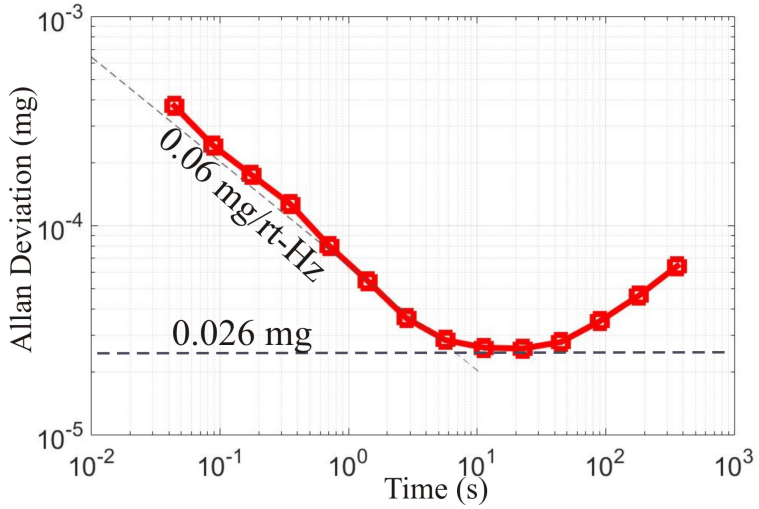

Figure 3.30: Noise analysis revealed bias stability of 0.03 mg and velocity random walk (VRW) of 0.06 $mg/\sqrt{Hz}$.

in capacitance. The amplitude of the drive-mode motion was stabilized, using an Automatic Gain Control (AGC), [141].

All loops were realized using a Zurich Instruments HF2LI digital lock-in amplifier. Initial characterization of TRG was performed in an open loop configuration without mode-matching of the devices. DFP frequency split was tuned down to <3 Hz, using electrostatic tuning with 28.5 V tuning voltage applied to the y-axis forcer electrodes. Lower DC bias voltages can be used if y mode pick-off electrodes are used for electrostatic tuning, in ad-

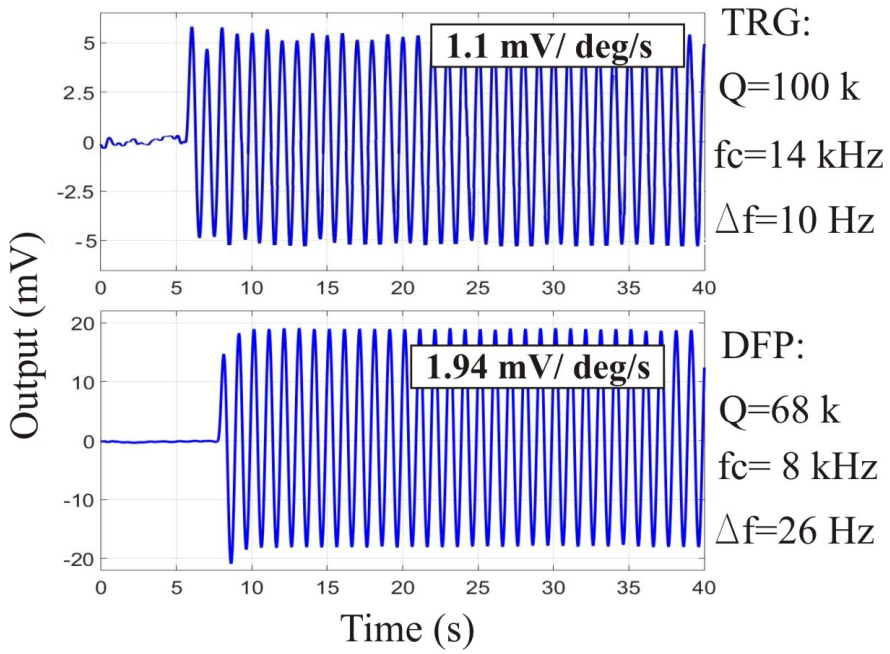

Figure 3.31: (a) TRG response to the rate-table sinusoidal input with amplitude of 5 deg and frequency of 1 Hz, (b) DFP response to the rate-table sinusoidal input with amplitude of 10 deg and frequency of 1 Hz.

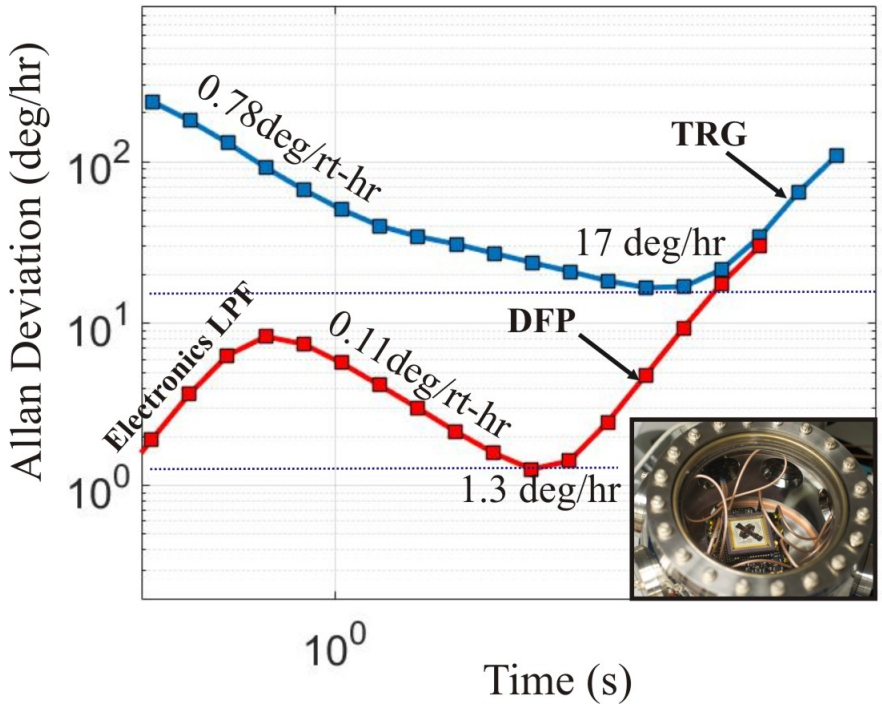

Figure 3.32: Noise analysis of the TRG revealed bias stability of <17 deg/h and ARW of 0.78 $deg/\sqrt{h}$; noise analysis of the DFP revealed bias stability of <1.3 deg/h and ARW of 0.11 $deg/\sqrt{h}$.

Table 3.6: Experimentally tested parameters of the accelerometers on the IMU sidewalls

	Accel X	**Accel Y**	**Accel Z**
Scale Factor, mV/g	39.9	34.0	46.2
Velocity Random Walk, $mg/\sqrt{Hz}$	0.09	0.09	0.13
Bias Instability, mg	0.14	0.1	0.2

Table 3.7: Experimentally tested parameters of the gyroscopes on the IMU sidewalls

	TRG	**DFP**
Scale Factor, $mV/(deg/s)$	1.1	1.94
Angle Random Walk, $deg/\sqrt{h}$	0.78	0.11
Bias Instability, deg/h	17	1.3
Quadrature Error, deg/s	237	404

dition to the forcer electrodes. Rate table experiment revealed the TRG scale factor of 1.1 mV/(deg/s) and the DFP scale factor of 1.94 mV/(deg/s), Fig. 3.31. The Root Allan Variance Analysis (r-AVAR) was used for identification of random noise characteristics. Experimental characterization of the TRG showed bias stability of <17 deg/h and ARW of 0.78 $deg/\sqrt{h}$; experimental noise analysis of the DFP showed bias stability of <1.3 deg/h and ARW of 0.11 $deg/\sqrt{h}$, Fig. 3.32.

Measured performance parameters of the sensors implemented on the IMU sidewalls are summarized in Tables 3.6 and 3.7. For tactical grade IMU, a quadrature error of the gyroscopes, arising from coupling between the drive and the sense modes, has to be considered. This error contributes to the gyroscope performance resulting in bias shifts [140]. For the TRG, the quadrature error of 237 deg/s without electromechanical compensation was measured before folding the device. During this test, a flat IMU device was attached to the ceramic package using a temporary attachment with an indium alloy. The device was then folded and the quadrature error of 227 deg/s was measured. This result suggested that the stresses during folding do not cause significant change in quadrature error.

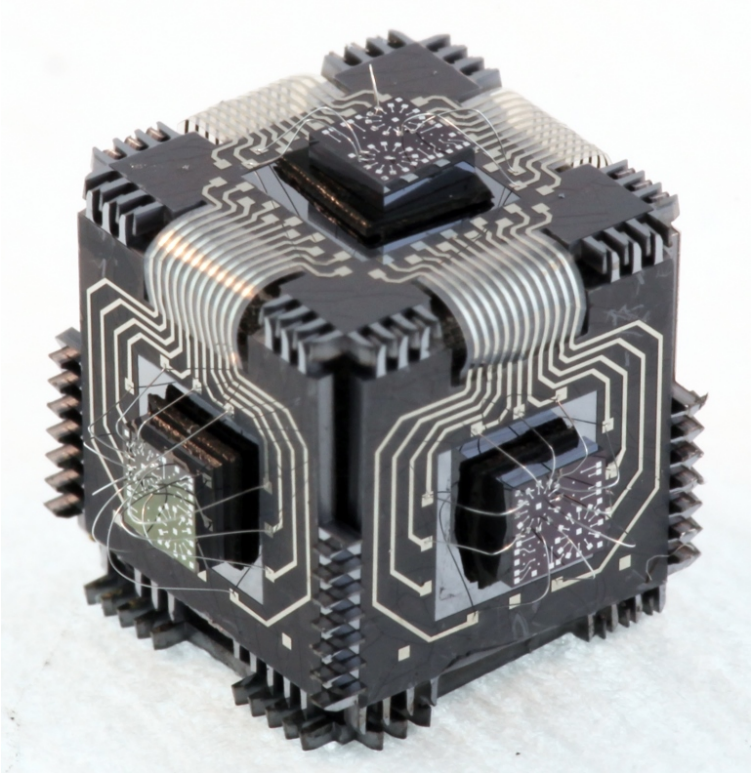

Figure 3.33: IMU prototypes with Ni-reinforces metal traces and electrical contact pads were folded into a 3D Cube configuration.

3.3.2 Integrated Approach

Initial characterization of IMU structures, manufactured using a co-fabrication process (Fig. 3.2), revealed fully operational prototypes, proving feasibility of the Folded MEMS approach for miniature IMU. The approach utilizes an array of single-axis sensors fabricated on a wafer-level and subsequently folded into a 3D IMU configuration using integrated flexible polymer hinges. Electrical signals from the sensors on sidewalls of the IMU are transferred through the dense network of metal traces on polymer, thus enabling the integration with signal processing electronics. In order to evaluate feasibility of the electrical conduction method as well as to illustrate the advantage of the folded MEMS process, an integrated approach has been employed. A miniature IMU, implemented using a foldable Si backbone, was integrated with stand-alone silicon encapsulated sensors [94] and the cross-talk between sensors was characterized.

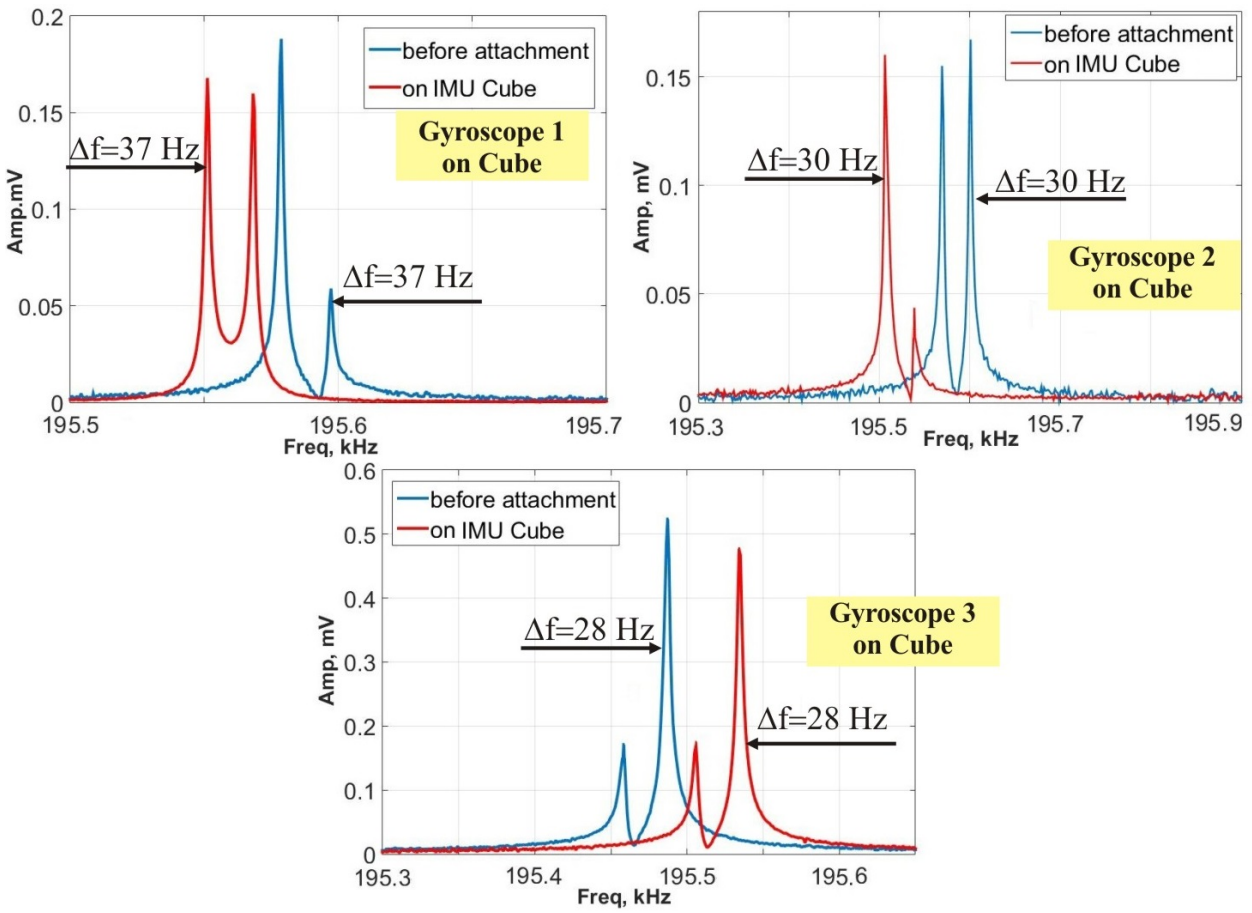

Figure 3.34: Frequency sweeps of three TRGs [39]: before (blue line) and after (red line) integration on a Folded Cube.

The foldable Si backbone was fabricated using the process flow in Fig. 3.9 for Ni-reinforced metal traces on parylene. In order to evaluate reliability of the contact pads on parylene, a die with inertial sensors, Toroidal Ring Gyroscopes (TRG) [39] and accelerometers, was integrated on each sidewall of the Folded IMU structure, 3.35. These stand-alone sensors were fabricated using a wafer-level Epitaxial Silicon Encapsulation (Epi-Seal) process [94]. In this process, movable silicon microstructures are encapsulated with a layer of epitaxially deposited silicon, allowing for an ultra-clean hermetic seal and resulting in high vacuum environment without the need for getter materials for absorption of sealing by-products.

IMU prototype folded into a 3D Cube configuration and integrated with stand-alone silicon encapsulated sensors is shown in Fig. 3.33. IMU devices were die-attached to a glass adapter

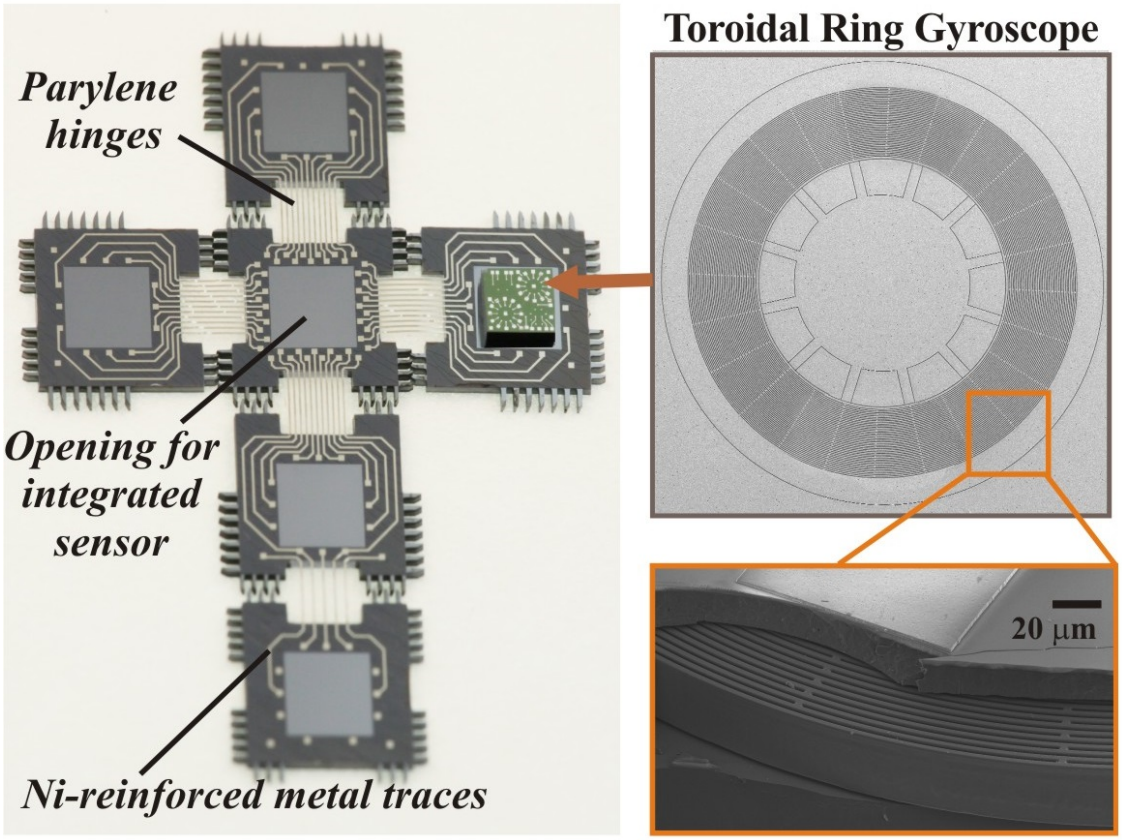

Figure 3.35: Foldable MEMS structures integrated with stand-alone single-axis Toroidal Ring Gyroscopes [39], implemented in Epi-Seal process.

board, packaged into a 181-pin, gold plated Ceramic Pin Grid Array (CPGA) package, and assembled with front-end electronics. Electrical connections between sensors on the IMU sidewalls and the package were realized using wire-bonds between the sensors and Ni-reinforced contact pads, metal traces on parylene, wire-bonds between the Ni-reinforced contact pads and glass adapter board, and wire-bonds from the adapter board to the package.

Frequency response characterization of the TRGs before and after IMU integration confirmed the feasibility of the electrical conduction method utilizing Ni-reinforced metal traces on parylene, Fig. 3.34. The observed shift in resonance frequency is related mainly to the die-attachment stresses and temperature drift between the two subsequent tests.

Cross-talk between the individual sensors in IMU contributes to the scale factor errors and

results in the increased noise, effecting the IMU performance. In case of MEMS vibratory sensors, the mechanical cross-talk, as well as the electrical cross-talk, have to be considered.

The mechanical cross-talk originates from the vibration propagation through the substrate, in case of a single-die IMU, and through the Cube sidewalls, in case of the Folded Cube approach. The electrical cross-talk is a result of capacitive and/or resistive coupling. In order to suppress the electrical cross-talk on the Printed Circuit Board (PCB) level, the front-end electronics circuits of devices operating at close frequencies, were separated. In a single-die IMU, the electrical cross-talk arises from capacitive coupling of the very closely spaced wire bonds and capacitive/resistive coupling through the substrate. The main source of the electrical cross-talk in the Folded IMU is the capacitive coupling between the metal traces on parylene.

The study of cross-talk between the sensors was performed using frequency domain characterization of two gyroscopes on the same die, Fig. 3.36 (a), and two gyroscopes on different sidewalls of the IMU Cube, Fig. 3.36 (b). The frequency response of the first gyroscope was obtained during the continuous oscillation of the second gyroscope at its own resonant frequency. In our experiments, all gyroscopes were excited with a 2.4 V constant DC voltage and a 100 mV AC voltage.

Crosstalk normally occurs when the operating frequencies of the sensors in IMU are close to each other. Frequency split between the two gyroscopes on the same die was 47 Hz and was similar to the frequency split between the two gyroscopes on different sidewalls of the Cube (48 Hz).

Experimental frequency response characterization of the first gyroscope indicated the interaction between sensors, which was observed around the resonant frequency of the second gyroscope. Experimental testing revealed a significantly higher level of interference of two sensors on the same die as compared to two sensors on different sidewalls of the Folded Cube

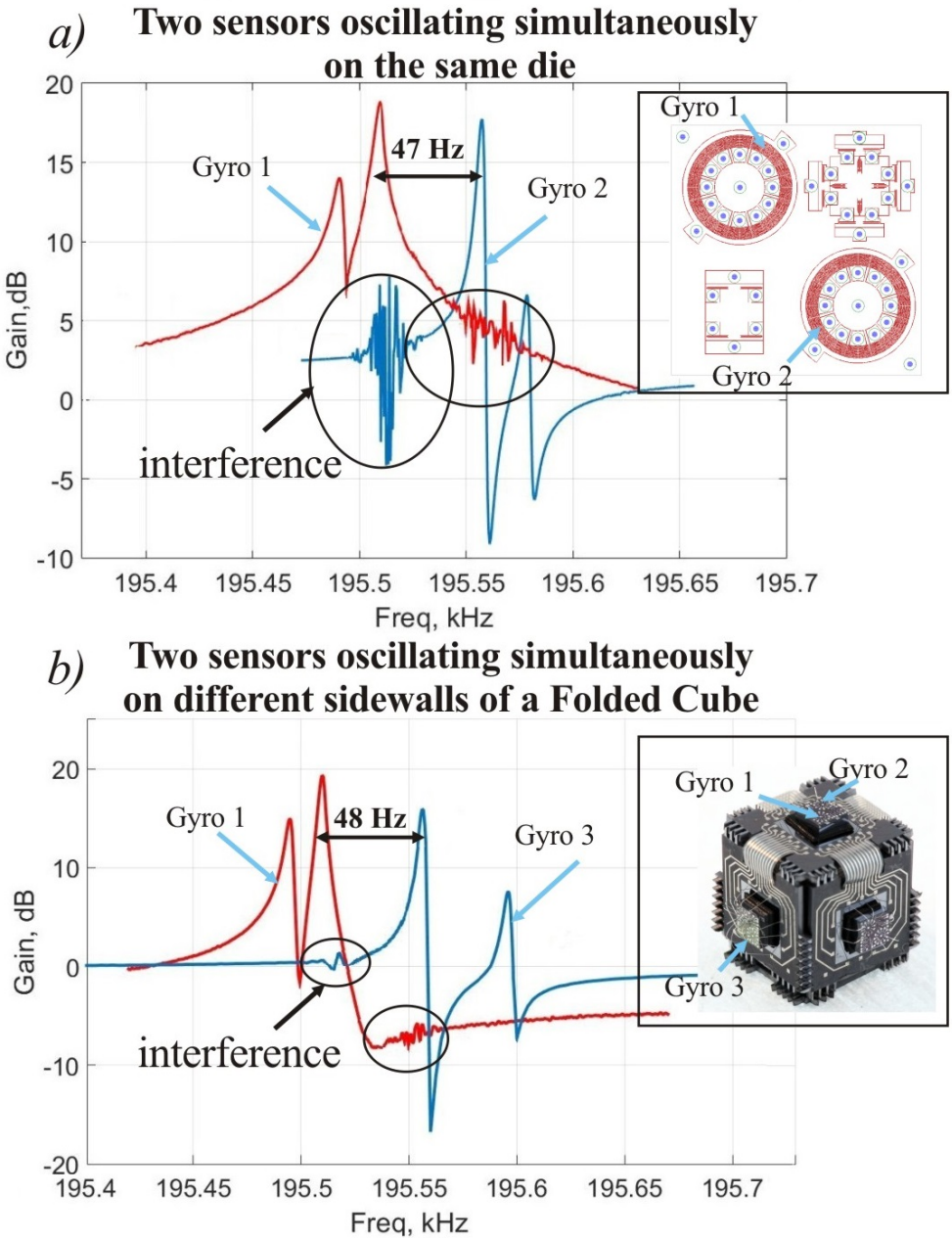

Figure 3.36: Higher level of interference of two sensors on the same die(a) vs on different sidewalls of the Cube(b).

(11.5 dB versus 2 dB).

Cross-talk between sensors affected the zero-rate output of the gyroscope 1, Fig. 3.37. In this experiment, the gyroscope 1 was excited with a constant DC voltage and AC voltage generated by a Phase Locked Loop. The amplitude of the drive-mode motion was stabilized, using an Automatic Gain Control (AGC). Gyroscopes 2 (on the same die) and 3 (on different

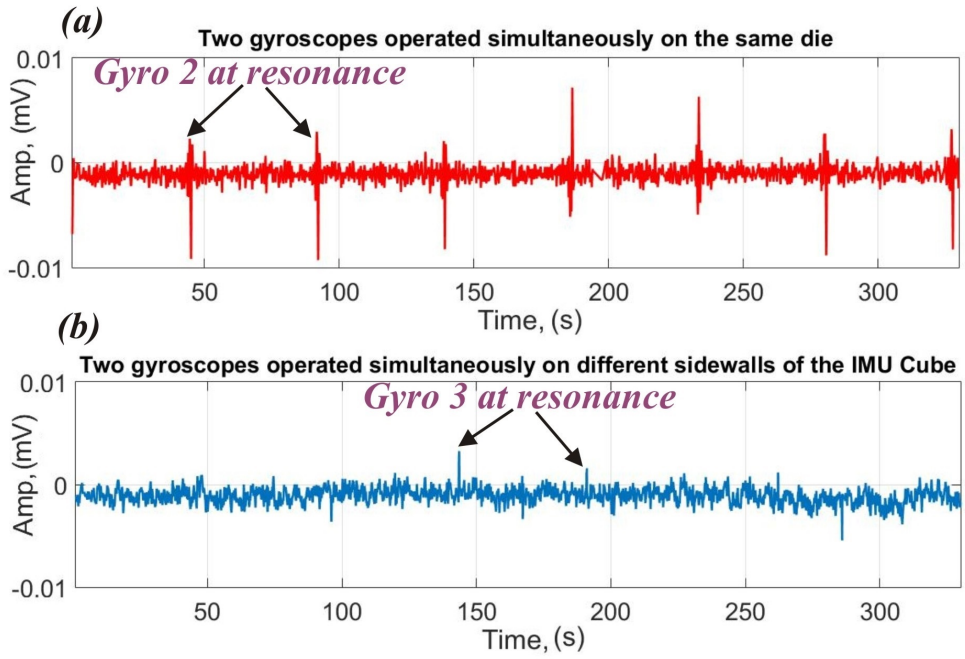

Figure 3.37: Zero-rate output of Gyro1: Higher level of interference of two sensors on the same die(a) vs on different sidewalls of the Cube(b).

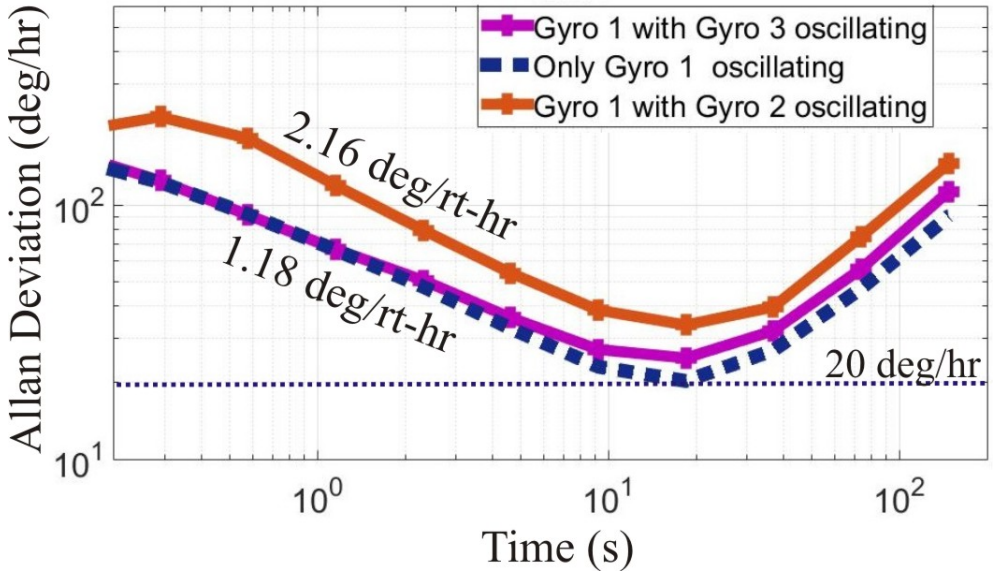

Figure 3.38: Interference between sensors results in higher ARW of Gyro1 with Gyro2 oscillating on a same die.

sidewall) were excited with a constant DC voltage and AC voltage with a frequency of the drive signal in the range from 195.45 kHZ to 195.65 kHz. High level peaks (approximately 15 dB) were observed on the zero-rate output of gyroscope 1, when the driving frequency of the gyroscope 2 reached the resonance. A significantly lower level of cross-talk (< 4 dB)

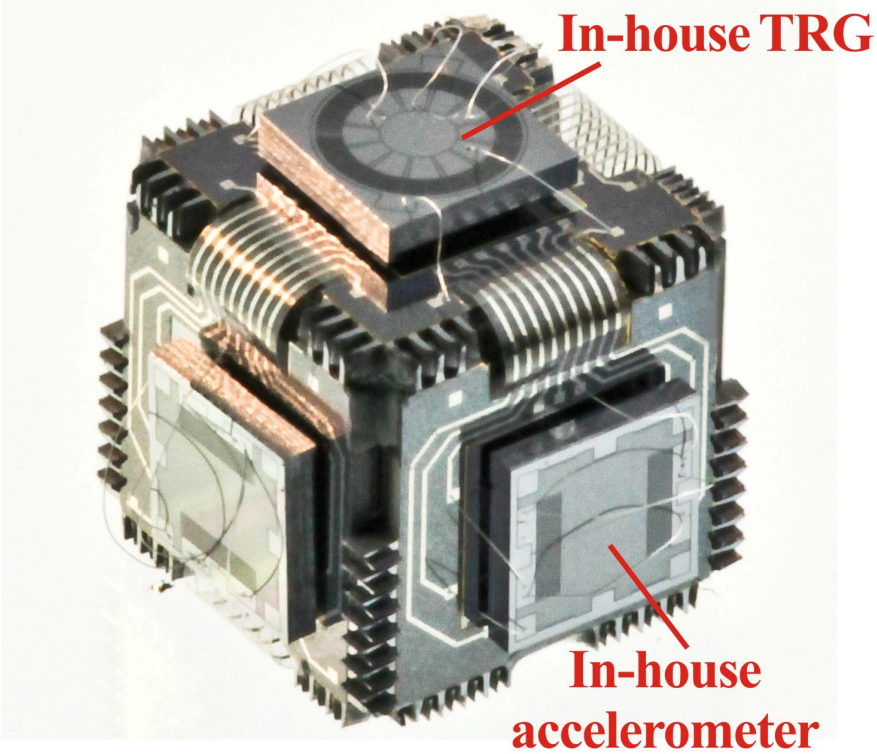

Figure 3.39: Foldable MEMS structures integrated with in-house stand-alone single-axis Toroidal Ring Gyroscopes [39] and in-house quasi-static accelerometers.

was observed on the zero rate response of the gyroscope 1, when gyroscope 3 was exited.

The Root Allan Variance Analysis (r-AVAR) was used for identification of random noise characteristics of the gyroscope 1. The interference between gyroscopes 1 and 2, on the same die, affected the noise of sensors and reflected on an Allan deviation plot, resulting in increased Angle Random Walk (ARW), from 1.18 to 2.16 $deg/\sqrt{hr}$, and higher Rate Random Walk (RRW) of the gyroscope 1, Fig. 7. Noise analysis of the gyroscope 1 in presence of the gyroscope 3, oscillating on the other sidewall of a Cube, revealed nearly no change in ARW and lower RRW. This suggests that the Folded IMU approach allows for lower cross-talk between the sensors as compared to a single-die approach.

In another IMU implementation, the in-house Toroidal Ring Gyroscopes (TRGs) and in-house accelerometers were fabricated on wafer-level as standalone sensors and then integrated on the sidewalls of the foldable Si backbone. Frequency response characterization

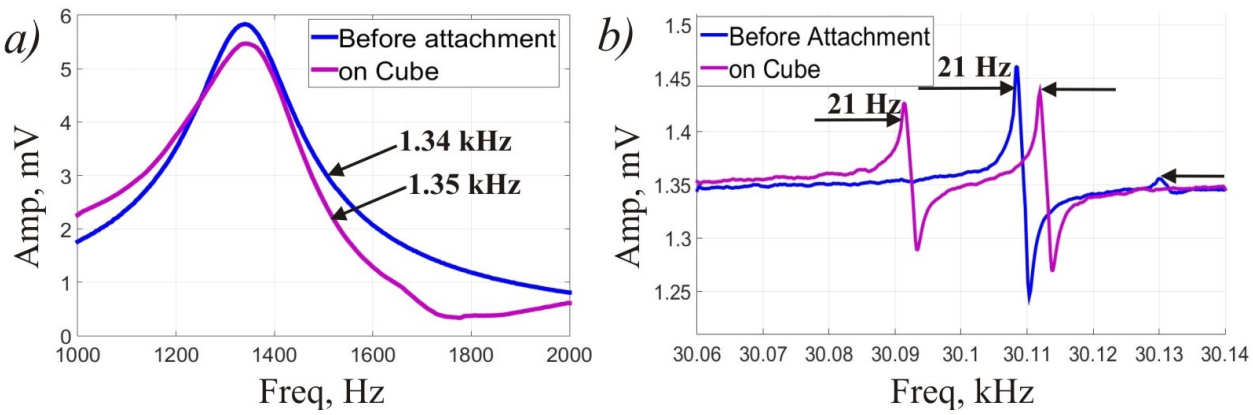

Figure 3.40: Frequency response of the sensors before and after integration on IMU sidewalls: (a) accelerometer (b) gyroscopes.

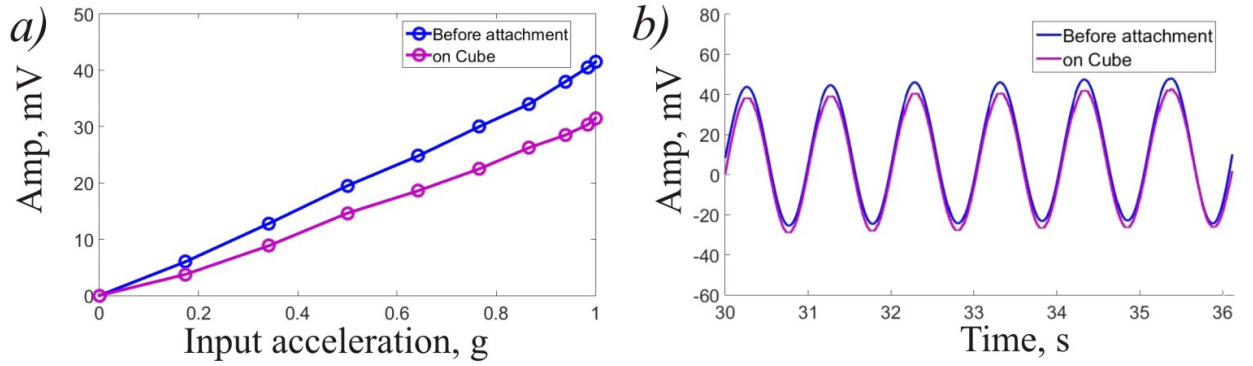

Figure 3.41: Before and after integration on IMU sidewalls: (a) accelerometer output under inclination of the tilt-table (b) gyroscope output under sinusoidal rotation of rate-table.

showed no loss of the signal after sensors integration on IMU sidewalls, Fig. 3.40. Scale factor characterization of the accelerometers and gyroscopes before and after IMU integration showed a close match, Fig. 3.41 This results illustrates that the electrical conduction method utilizing Ni-reinforced metal traces and contact pads on parylene is suitable for different IMU realizations, including IMU integrated with standalone Epi-seal inertial sensors and IMU co-fabricated/integrated with in-house inertial sensors.

3.4 Conclusions

We have presented a Folded MEMS approach for fabrication of miniature IMUs. The approach is based on folding an array of single-axis inertial sensors into a 3D IMU configuration, using polymer flexible hinges. This technique permits a significant reduction in IMU size while preserving the sensor performance. We introduced a new double-sided process for fabrication of flat foldable MEMS IMU structures on a wafer-level. In our process, inertial sensors are created on the device side of the wafer. In parallel, metal interconnects and polymer flexible hinges are formed on the handle side of the wafer. The double-sided process resulted in increased yield of the Folded IMU fabrication runs. In addition, due to introduction of TWI, the inner volume of the folded structure can be efficiently utilized for integration with signal processing electronics.

We studied different materials for implementation of flexible hinges, such as photo-definable polyimide and parylene-C. Despite simplicity of the fabrication steps for polyimide hinges, parylene-C was eventually selected as a preferable material for flexible hinges due to a superior quality of the film after folding.

Characterization of inertial sensors on the sidewalls of the Folded IMU prototypes proved feasibility of the Folded MEMS approach for a compact tactical grade performance unit. Characterization of accelerometers showed VRW of 0.09 $mg/\sqrt{Hz}$ and in-run bias instability of <0.1 mg. Noise analysis of the 2.8 mm TRG revealed bias stability of <17 deg/h and ARW of 0.78 $deg/\sqrt{h}$; noise analysis of the 3.1 mm DFP revealed bias stability of <1.3 deg/h and ARW of 0.11 $deg/\sqrt{h}$.

Electrical signals from the sensors on sidewalls of the IMU are transferred through the dense network of metal traces on polymer, thus enabling the integration with signal processing electronics. Folded IMU prototypes manufactured using the integrated approach were utilized to confirm the feasibility of the electrical conduction method. Experimental characterization

showed that Ni-reinforcing of contact pads and metal traces on parylene allows for improved robustness of the wire-boding connections and a simplified process of interfacing the IMU with electronics.

The cross-talk between sensors on the sidewalls of a folded 3D IMU was experimentally characterized. The study of cross-talk between the simultaneously operating sensors was performed using frequency domain characterization, gyroscopes zero rate output, and noise characterization. Experimental frequency response and a zero rate output of the gyroscopes showed a higher level of interference between two sensors on the same die vs on different sidewalls of the Folded Cube. The experimental results provided an evidence that the folded IMU process is advantageous to a single-die approach, showing a lower Angle Random Walk (ARW) of the gyroscopes when operated simultaneously on different sidewalls of the IMU Cube, 1.18 vs 2.16 $deg/\sqrt{hr}$.

For a tactical-grade IMU, temperature variations is an important factor to consider since temperature-induced long-term bias and scale-factor drifts may limit the IMU performance. One possible source of instability vs temperature is the change in Si panels alignment due to temperature. As we discussed in Section 2.1, IMU structural reinforcement allows for significant reduction of the sidewall misalignment angle under thermal loading. After the IMU panels are enforced by silicon welding, the next remaining most important sources of instability vs temperature in Folded IMU are the temperature sensitivity of the sensors resonant frequencies and frequency mismatch between the vibratory modes, as well as the temperature sensitivity of the Q-factor. In order to improve the long-term stability, different thermal compensation techniques can be potentially implemented. For example, the compensation method utilizing the resonant frequency as a measure of the sensor temperature, [142], or compensation technique utilizing a micro-oven co-fabricated with IMU sensors, [143]. However, these studies are outside the scope of this dissertation.

Folded IMU presented in this Chapter is the first demonstration of the double-sided fabri-

cation process. Device miniaturization by means of the shape optimization and reduction of the area occupied by a network of metal traces is possible. IMU prototypes fabricated in the most recent runs do not exceed 15 mm^3. In addition, thru-wafer vias would enable placing a part of the signal processing electronics inside the 3D structure, which may result in further reduction in volume.

Folded MEMS IMU can be potentially instrumented in stabilization, guidance and navigation applications, where extremely small size, low weigh and high performance are essential, such as in small unmanned vehicles, missiles, robotics, and personal navigation. Inertial navigation is an appealing solution for a self-sufficient guidance system, not relying on any external signals. Folded 3D MEMS process enables integration of tactical performance inertial sensors in a small volume, providing a 6-DOF IMU configuration. The process may serve as a technological platform for an integrated, self-contained, precision navigation system, offering a compelling solution of a PNT challenge in GPS-denied areas. Capable of producing 3D MEMS structures, using standard bulk and surface micro-machining tools, Folded MEMS process may find applications beyond inertial navigation.

Chapter 4

IMU Integration with Electronics and Packaging

Thru-wafer interconnects fabrication is an integral part of the Folded IMU double-sided process. Vertical electrical interconnects enable integration of the Folded IMU devices with signal processing electronics and, at the same time, facilitate the wafer-level packaging of IMUs. In this Chapter, we present a process for a high density array of vertical thru-wafer copper interconnects, providing an electrical interface between the inertial sensors on the front-side of the SOI wafer and the electrical components on the backside of the wafer (TWIDS process).

This Chapter also investigates a method of hermetic and vacuum packaging of Folded 3D IMU devices, utilizing "bubble-shell" glass lids, fabricated on a wafer-level using a microglassblown process.

4.1 Thru-Wafer Interconnects for Double-Sided (TWIDS) Fabrication of MEMS

4.1.1 Background

Thru-wafer electrical interconnects (TWI) have recently gained a lot of interest in semiconductor industry due to the continuous demands of the miniature MEMS devices for a faster signal transmission, better electrical performance, and compact packaging. The TWI technology is widely used in wafer-level packaging and multi-layer 3D integration of MEMS and CMOS.

The vertical interconnects find applications in 3D MEMS devices, for example, in compact, multi-layer, vertically-stacked fused silica microsystems, [57], and folded MEMS Inertial Measurement Units (IMU), [40]. In folded IMU (Fig. 3.1), thru-wafer interconnects provide a path for electrical signals from sensors on the device side of the wafer to ASIC (Application-Specific Integrated Circuit) components on the handle side of the wafer, and allow at the same time for assembly of the integrated MEMS sensor cluster in a 3D configuration, when folded in a 3D shape.

For enhanced environmental robustness of 3D MEMS devices and assemblies, high aspect ratio interconnects often have to be formed in a relatively thick wafer (>600 μm). MEMS devices, like Folded IMU, require electrical feed-through interconnects with low resistivity and low parasitic losses, assuring a low impedance path for electrical signals.

Current approaches for fabrication of vertical interconnects can be divided into three general categories based on the material of the interconnect: single-crystal silicon vias, polysilicon-filled vias, and electroplated metal-filled vias.

Vias of the first category are usually formed by isolating sections of a low-resistivity silicon wafer. The isolation can be done by incorporating a trench filled with a dielectric material, [103]-[105], or by using a glass-in-silicon reflow process to create vias in glass wafers, [106]. Another approach involves anodic bonding of a pre-etched silicon wafer to a glass wafer, and then filling the silicon mold with glass, using a high-temperature reflow process.

The method of forming the polysilicon-filled vias usually comprises the steps of patterning and etching through the silicon wafer, deposition of an insulating material, like silicon dioxide, then filling via holes with doped polysilicon, [107]-[108].

Fabrication of the electroplated metal-filled vias usually starts with forming of vertical via holes in a silicon wafer, using, for example, Bosch process, [109], or laser-ablation, [110]. This is followed by deposition of an insulation layer and a seed layer for the subsequent metal electroplating process. The via holes are then filled with metal, such as copper [110]-[112] or nickel [113]-[114], using electroplating methods. In some cases, a conductive seed layer is not applied, instead a sacrificial wafer is bonded to the silicon wafer, [115]-[116]. The sacrificial wafer is covered with a thin metal layer, for example copper or gold, to serve for initiation of the plating process.

Thru-wafer interconnects of the first category, single-crystal silicon vias, are usually formed by the wafer material itself, which significantly simplifies the fabrication process. However, silicon vias, generally, have a relatively higher resistance as compared to metal thru-wafer interconnects due to the lower conductivity of silicon versus metal. Polysilicon-filled vias are commonly preferred when high temperature processing steps follow the via fabrication. This technology is quite versatile but associated with a number of technical challenges, including uniformity of polysilicon filling in high aspect-ratio via holes and obtaining a high level of dopants during the deposition process, [117].

Metal thru-wafer interconnects deliver an advantage of high conductivity. However, the

technology for manufacturing interconnects of this category has a number of limitations. Although metal thru-wafer vias reported earlier have shown satisfactory performance, the realization of high aspect ratio (better than 10:1) and low resistance interconnects in thick (>600 μm wafers) is associated with a number of challenges, [118]. In high aspect-ratio via filling, void formation is a major concern. One main complication, which may occur in the fabrication of metal, e.g. copper electroplated interconnects, is uneven filling due to non-uniform deposition of insulation, barrier, and seed layers inside the narrow and deep via holes. TWI defects resulting from poor uniformity of these layers along the depth of the via hole have been discussed in [118]-[123]. Insufficient wettability of via sidewalls and poor electrolyte chemistry are some of the other reasons behind the voids formation. Besides that, most fabrication processes demonstrated previously are complex, require rather sophisticated fabrication steps: they either require deposition of multiple layers (for-example insulating layer, seed layer and conductive layer, such as electroplated metal or doped polysilicon) or bonding a sacrificial wafer. High complexity of the fabrication process in many cases leads to significantly decreased yield and increased cost.

In this work, a process for co-fabrication of MEMS sensors structures and copper-filled vertical interconnects in thick (up to 600 μm) Silicon-on-Insulator (SOI) wafers is presented. The technology of metal thru-wafer interconnects is based on the bottom-up seedless copper electroplating and allows for void-free high-aspect ratio features. Seedless electroplating of metals, which is based on the direct plating on the surface of a silicon wafer, has been previously reported in literature. L. D. Vargas Llona et al. explored seedless electroplating of nickel on bare and patterned silicon wafers, [124]. T. Fujita et al. described a process for direct gold electroplating on silicon wafer [125]. A method of through-glass copper via using the glass reflow and seedless electroplating processes was proposed in [126]. In [126], copper electroplating was performed directly on the silicon wafer bonded on top of the glass wafer.

In this Section we introduce a process where the single SOI wafer is used for co-fabrication of deep vertical copper interconnects and suspended micro structures (such as MEMS gyroscopes and accelerometers). Both sides of the wafer are processed, front side for patterning the device, back side for fabrication of seedless electroplated copper vias, where the highly doped Si device layer of the SOI wafer is used for direct deposition of copper. The double-sided process for thru-wafer interconnects co-fabricated with SOI sensors enables direct integration of MEMS sensors and 3D assemblies with ASIC or other types of heterogeneous integration.

4.1.2 Design and Fabrication

The Thru-Wafer Interconnects Double-Sided (TWIDS) process, [127], allows for a high density array of vertical electrical feedthrough, providing an electrical interface between the front-side and the backside of the Silicon-on-Insulator (SOI) wafer.

TWIDS process flow, [128], starts with a 600 μm thick 4 inch diameter SOI wafer with a 100 μm thick highly-doped device layer (resistivity: 0.001 Ohm·cm), up to 500 μm thick handle layer (resistivity: 1-10 Ohm·cm), a 5 μm buried oxide layer in between, and a 1 μm thick layer of low stress LPCVD silicon nitride on the the handle side, Fig. 4.1(a). First, the wafer is spin-coated with a thick layer of AZ P4620 photoresist, the blind thru-wafer via holes are photo-lithographically defined, and the silicon nitride layer is etched using the STS MESC MULTIPLEX AOE system with the etch rate of 0.067 μm/minute, Fig. 4.1(b).

The blind thru-wafer via holes are then created, using a Deep Reactive Ion Etching (DRIE) of the handle wafer, while a buried oxide layer serves as an etch stopper, Fig. 4.1(b). The UNAXIS VERSALINE fast deep silicon dry etching system FDSE III is utilized for the deep DRIE etching. At this step, the etch rate for silicon is 5 μm/minute.

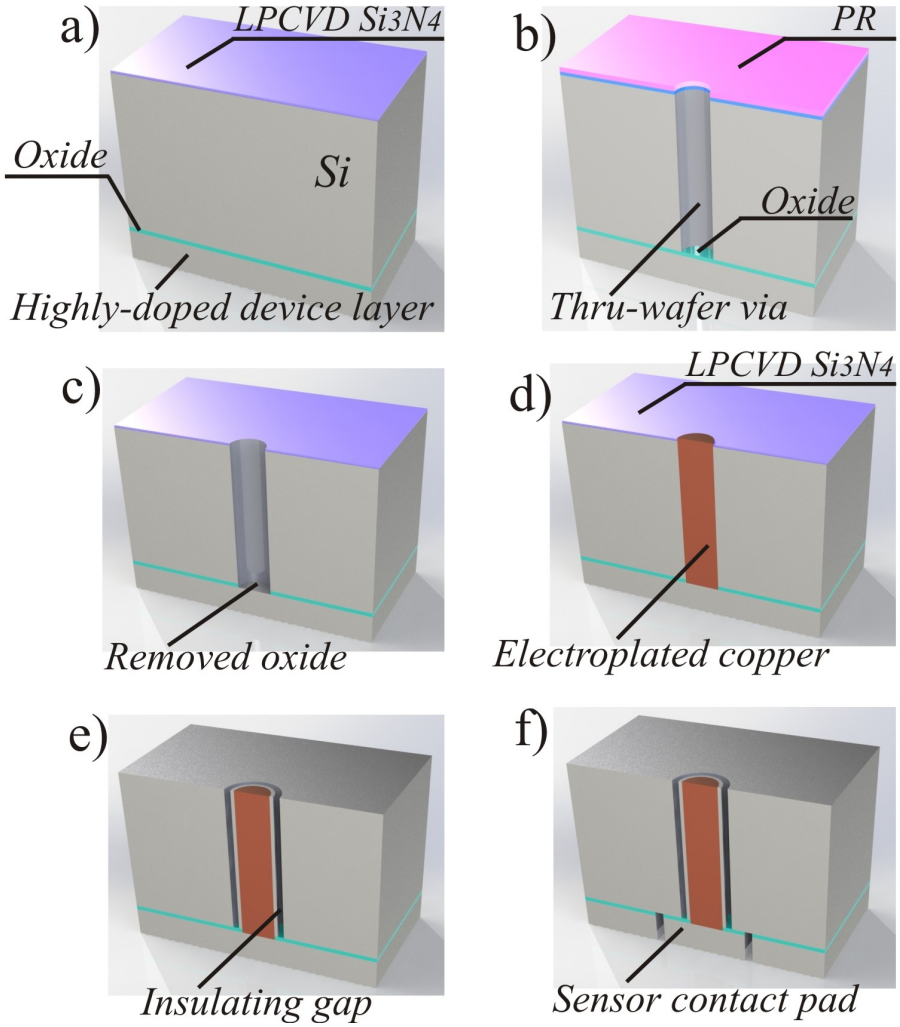

Figure 4.1: TWIDS fabrication process: (a) SOI wafer, (b) thru-wafer via DRIE etch, (c) buried oxide removal, (d) seedless copper electroplating and lapping, (e) defining insulating gaps, (f) sensor DRIE etch and release.

Etching is followed by removal of the buried oxide using a 20 % HF solution, Fig. 4.1(c). Then the solvent cleaning is performed to remove the photoresist layer, left after the silicon dry etching step, followed by the RCA-1 aggressive cleaning of the wafer to remove the residual organic material. Next, the via holes are filled with copper using a seedless electroplating method, which does not require a conductive seed layer deposition and utilizes a highly doped silicon device layer to initiate the bottom-up plating process, Fig. 4.1(d).

Electroplating is performed in a custom-designed plating setup, Fig. 4.2, which includes a 4 inch copper electrode, an Elmasonic P 120H Ultrasonic unit, a DC power supply, and a bath

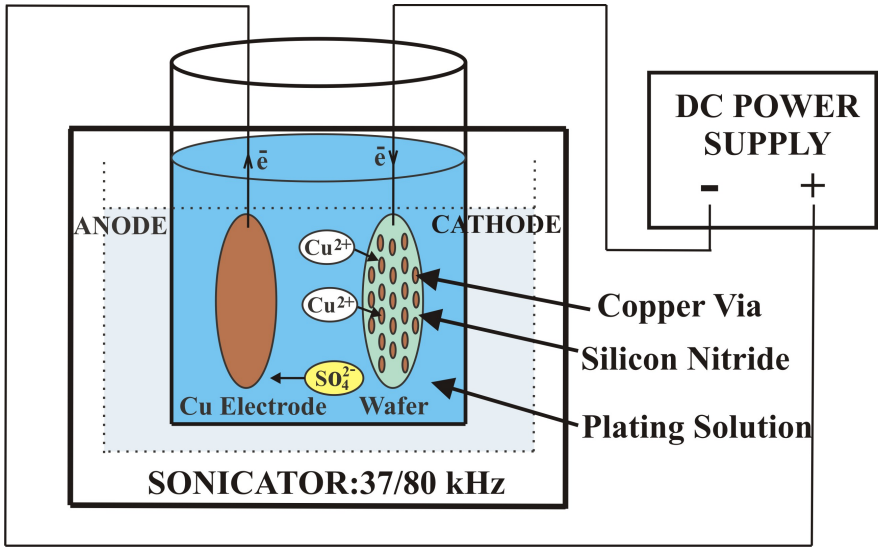

Figure 4.2: Custom-designed plating setup includes a 4 inch copper electrode, an Elmasonic P 120H Ultrasonic unit, a DC power supply, and a bath with copper electrolyte.

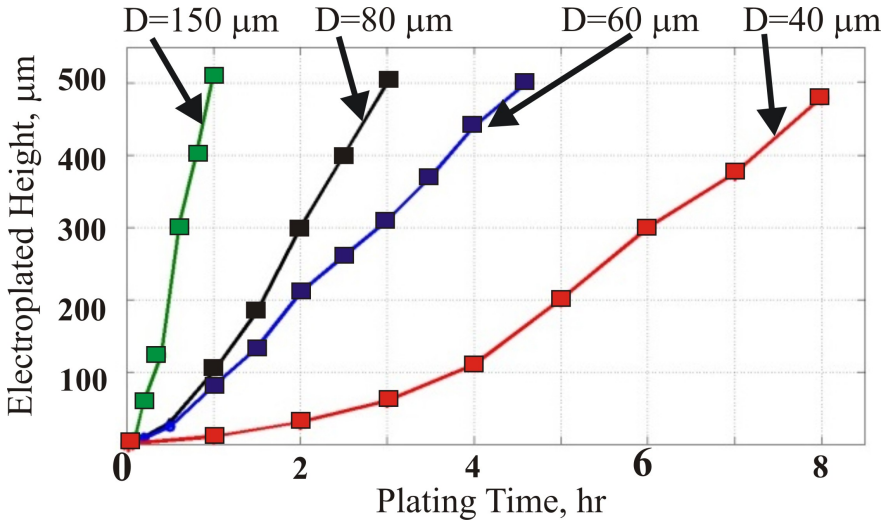

Figure 4.3: Total electroplating time to fill the 500 μm deep vias depends on the via diameter and varies in the range from 1 hr to 8 hr.

with copper electrolyte. Copper electrolyte is a copper plating acid type solution (provided by TRANSENE, USA), which consists of copper sulfate, hydrochloric acid, and sulfuric acid. Addition agents in a bath include a brightener and a leveler.

Electroplating was performed at room temperature with the current density of 5 mA/cm^2. The total electroplating time to fill the 500 μm deep vias depends on the via diameter and

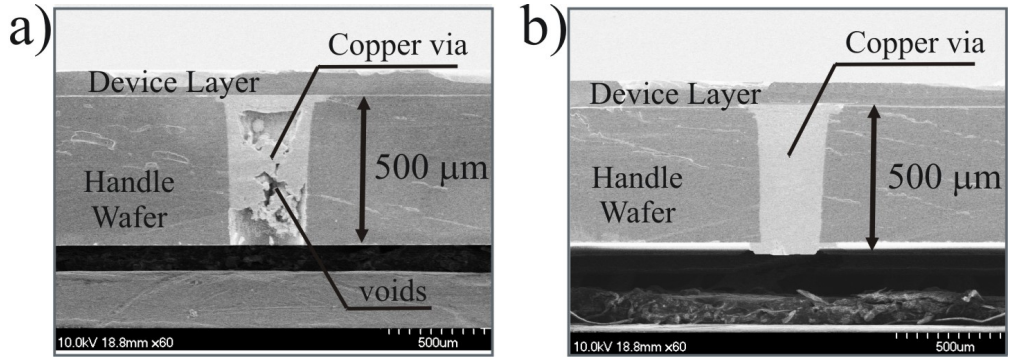

Figure 4.4: (a) vias electroplated in a silent mode, (b) vias electroplated in the presence of sonication.

varies in the range from 1 hr for 150 μm diameter vias to 8 hrs for 40 μm diameter vias, Fig. 4.3. LPCVD silicon nitride deposited on the handle side of the wafer acts as a barrier layer to prevent parasitic copper growth and to reduce the plating time.

To further improve quality of the filling, different conditions for copper electroplating were explored. Fig. 5 illustrates the cross-section of the vias electroplated with and without sonication. SEM analysis revealed that in a silent mode the electroplating solution could not penetrate into the high-aspect ratio via holes. As the result, interconnects were not completely filled with copper, Fig. 4.4(a). We observed in our experiments that sonication in the range of 37 kHz during the first 10 min of the plating process significantly improved the filling, allowing for high aspect ratio voids-free interconnects, Fig. 4.4(b).

Once plating is complete, the back side of the copper-electroplated wafer is lapped to prepare for the following photo-lithography step. Lapping is performed using a 12" MultiPrep Polishing System (available from Allied High Tech Inc.) and a set of diamond lapping films with a size of diamond particles 30, 15, 6, 3, and 1 μm. At the end of the polishing process, a diamond suspension with 0.25 μm particles is used for creating an optically smooth surface finish. Alternatively, a chemical mechanical polishing (CMP) can be utilized to polish the wafer surface.

Next, the wafer is spin-coated with a thick layer of AZ P4620 photoresist, the insulating

gaps are photo-lithographically defined around the copper-filled vias and are DRIE etched, Fig. 4.4(e). The SOI sensor's features are then defined on the front side of the wafer, Fig. 4.4(f). Sensor definition involves spin-coating the wafer with a thin layer of Shipley 1827 photoresist, photo-lithography to create the etch mask, followed by etching the 100 μm silicon device layer using the STS System DRIE. Photoresist stripping by solvent cleaning completes the fabrication process. The suspended MEMS structures are then released using a stiction-free vapor HF process to remove the buried oxide layer under the device suspension and proof mass. During this step, the vias side of the wafer is partially protected with blue tape and is placed in a close contact with the HF chamber electrostatic chuck to avoid the direct contact with HF vapor.

Depending on the application, the conductive vias can be mechanically reinforced by means of filling the insulating gaps with polymer or other dielectric materials.

4.1.3 Electrical Characterization of Interconnects

The key features of the vertical interconnects for 3D MEMS structures are the small footprint, high conductivity, and low parasitic losses, ensuring good electrical performance.

Theoretical resistance values for TWI are calculated as resistance of copper cylinder with a length of 500 μm and with a diameter in the range from 40 μm to 130 μm and parallel resistance of hollow Si cylinder with the wall thickness in the range from 20 μm to 35 μm. In our calculations, we assumed Cu resistivity of 1.7 μOhm·cm and Si handle wafer resistivity of 10 Ohm·cm. Fig. 4.5(a) depicts the total theoretical resistance of TWI as a function of the copper via diameter. The actual resistance of copper electroplated interconnects might be larger than bulk copper. An excess resistivity is associated with defects in electroplated film, [129]. The total resistance across the vertical interconnect also includes, connected in series, the resistance of a sensor contact pad. For the 380 μm contact pads with 100 μm

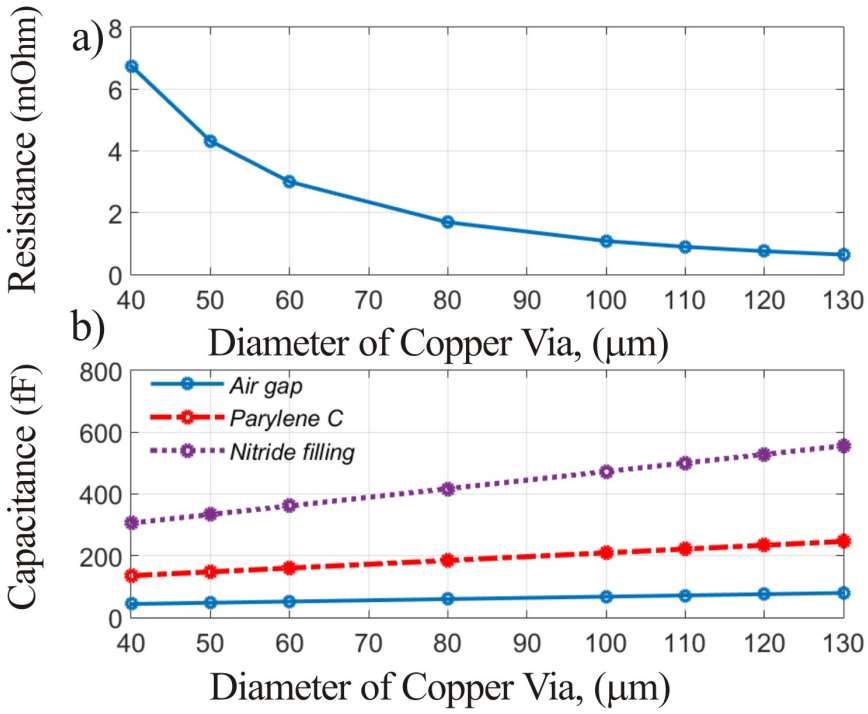

Figure 4.5: (a) Theoretical resistance and (b) theoretical parasitic capacitance values for TWI as a function of copper via diameter.

Table 4.1: Dimensions of the Fabricated Interconnects

	60 μm Via	**100 μm Via**
Cu diameter, D	60 μm	100 μm
Handle wafer thickness, h	500 μm	500 μm
Device layer thickness, d	100 μm	100 μm
Si wall thickness, s	20 μm	35 μm
Insulating gap width, g	30 μm	35 μm
Contact pad, P	300 μm	380 μm

diameter copper via the calculated theoretical value of the total resistance is 22.1 mΩ. For the 300 μm contact pads with 60 μm diameter copper via the calculated theoretical value of the total resistance is 29.6 mΩ.

TWI parasitic capacitance arises primarily from copper vias, surrounded by insulating gaps and forming capacitors with the silicon substrate. Excess parasitic capacitance can lead to signal degradation, especially in high-frequency applications. Substrate coupling capacitance

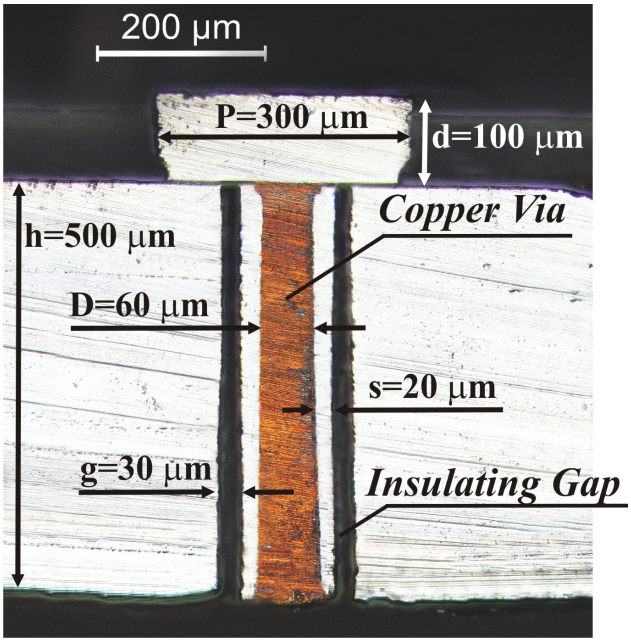

Figure 4.6: Optical Micro-photograph of the 60 μm diameter copper electroplated thru-wafer interconnect.

values were calculated as a function of the copper via diameter with a 35 μm donut-shaped gap, Fig. 4.5(b). For the air gap, the maximum value of 68 fF per interconnect was calculated for 100 μm diameter via. Isolation by filling the gaps with insulating material, such as silicon nitride or parylene, is also possible. The filling may improve the mechanical stability of interconnects, [56]. The filling of gaps, however, results in an increased parasitic capacitance

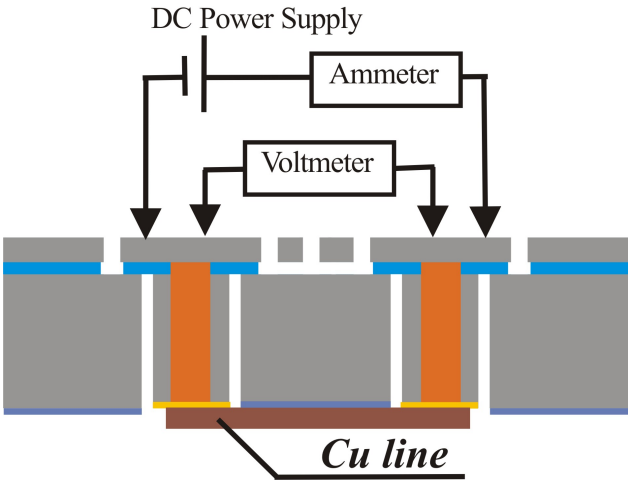

Figure 4.7: Four-point resistance measurement setup.

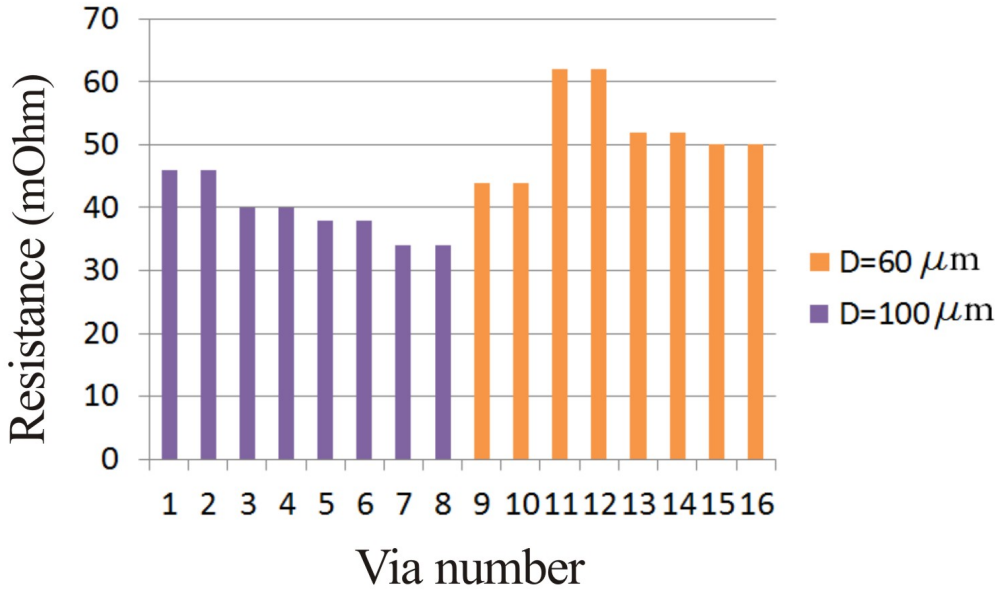

Figure 4.8: Measured resistance of the 60 μm diameter and 100 μm diameter copper electroplated thru-wafer interconnects.

of interconnects, Fig. 4.5(b).

Using TWIDS process, vertical interconnects with copper diameter of 60 and 100 μm were fabricated, Fig. 4.6. Dimensions of the fabricated interconnects are summarized in Table 4.1.

Resistance across the thru-wafer interconnects was measured using a four point probe method, which allows for eliminating the effect of contact resistance between a probe and an electrical contact pad, and allows for eliminating an error induced by the resistance of wires.

A schematic drawing of a measuring setup is shown in Fig. 4.7. In our measurement, a chain of two interconnects was connected on the backside of the wafer using a Cu line formed by a highly-conductive copper tape. The resistance value of individual via was calculated as:

$$R_{TWI} = 0.5(R_{meas} - R_{Cu-line}), \tag{4.1}$$

where R_{meas} is the measured resistance value of a pair of interconnects, $R_{Cu-line}$ is the resistance of the Cu backside line, which varied in the range from 35 to 68 mOhm for different pairs of interconnects.

The results of measurement of 8 via chains are shown in Fig. 4.8. The measured resistance of 100 μm via ranged from 34 to 46 mOhm, with an average value of 39.5 mOhm, and a standard deviation of 4.3 mOhm. The measured resistance of 60 μm via ranged from 44 to 62 mOhm, with an average value of 52 mOhm, and a standard deviation of 6.5 mOhm. The average value of the resistance is higher than the analytically predicted value. This error is mainly due to inaccuracy in measurement of the Cu line resistance and an additional contact resistance between the backside Cu line and a via.

4.1.4 SOI MEMS Gyroscope Integrated with TWI

Thru-wafer interconnects fabricated using TWIDS process can be utilized for SOI sensors with contact pads as small as 200 μm by 200 μm. Further reduction of the via is limited by the DRIE etch aspect ratio, which is currently 16:1 in our process.

A. Sensor Design

Prototypes of a miniature 3.3 mm by 3.3 mm MEMS Toroidal Ring Gyroscope, [139], with 100 μm diameter copper interconnects (wafer thickness to copper diameter is up to 6:1) were fabricated using the TWIDS process, Fig. 4.1. Fig. 4.9 shows the front and the backside view of the fabricated sensor.

Cu plating uniformity is an important issue since even closely placed vias may show different Cu plating rate, [131]. To improve the plating uniformity, Cu was over plated during the bottom-up electroplating step, Fig. 2(d). Once all the vias were filled, the wafer polishing was performed to remove the redundant Cu at the wafer backside. Scanning Electron Microscope (SEM) analysis was performed on the cross section of the die with electroplated thru-wafer vias and a continuous voids-free filling was demonstrated for several vias in a row, Fig. 4.10.

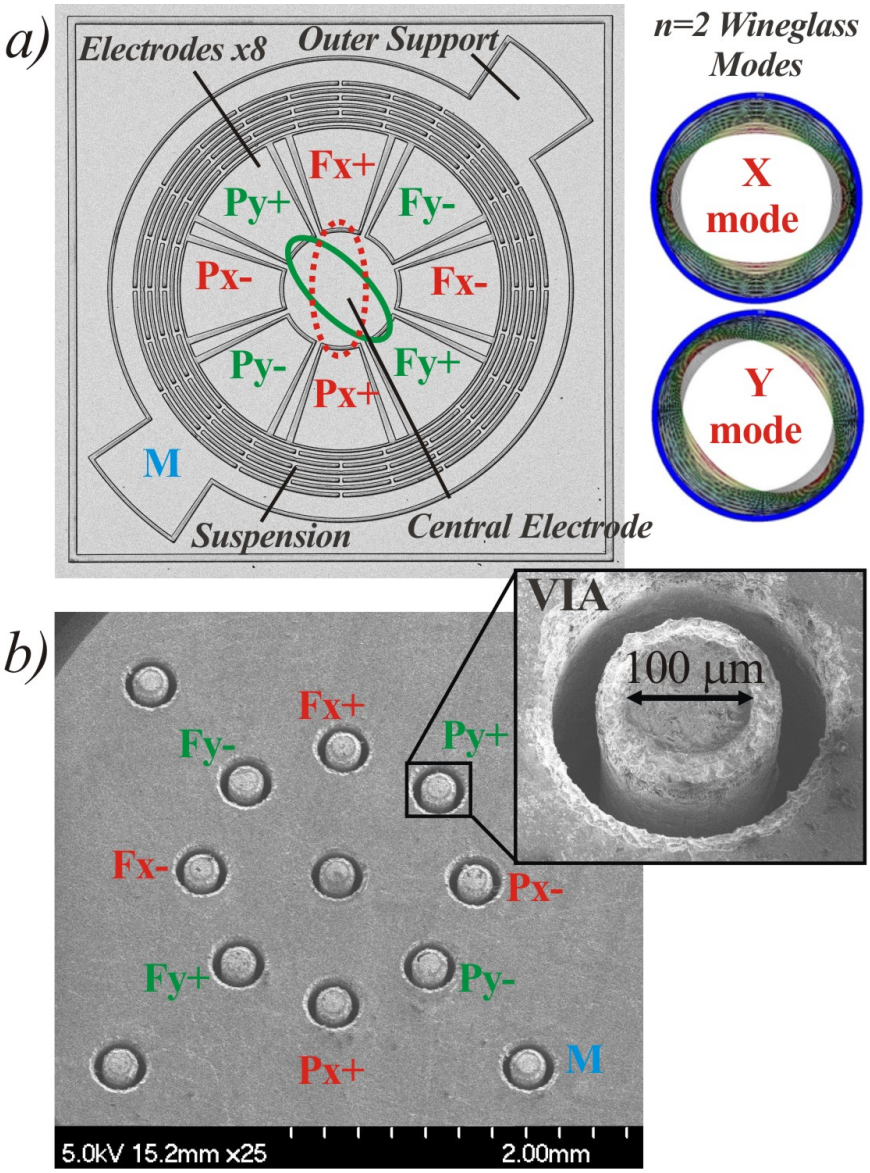

Figure 4.9: Prototype of MEMS Toroidal Ring Gyroscope with co-fabricated TWI: a) front-side (device) view, b) back-side (interconnect) view.

Toroidal Ring Gyroscope (TRG) is comprised of an inner electrode assembly, an outer support, and a concentric-ring suspension, Fig. 4.9(a). The mechanical element of the gyroscope is a planar resonating structure which has degenerate pairs of in-plane wineglass vibration modes. The gyroscope is designed to operate in the n=2 wineglass mode. The inner electrode assembly consists of 8 radial electrodes that are used as a forcer and as a pick-off, for each of the modes. The central star-shaped electrode has three functions: (1) it acts as a

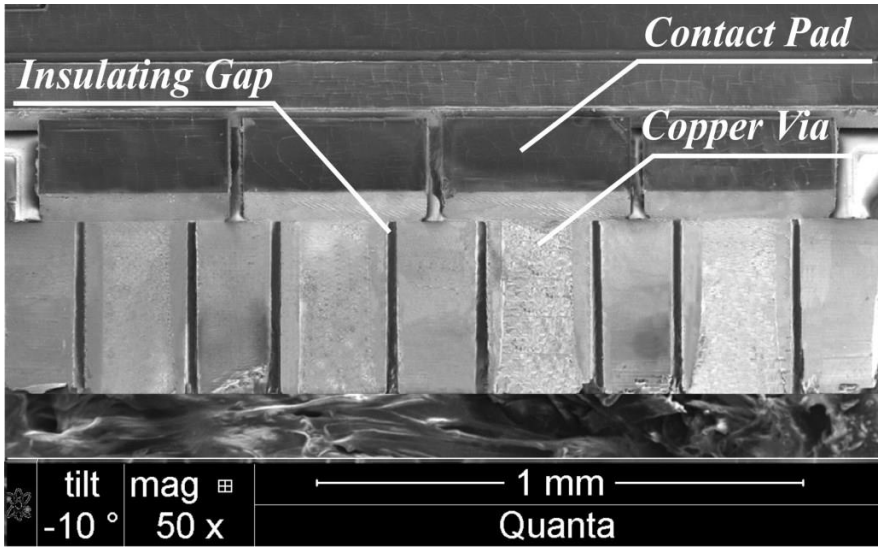

Figure 4.10: Cross-section of several vias, uniformly filled with copper.

shield by sinking parasitic currents between discrete electrodes, (2) it can function as a DC quadrature null electrode, and (3) it can be used for the gyroscope parametric excitation.

Enabled by the TWIDS process, one thru-wafer via is connected to the center electrode and one per each electrode in the inner electrodes assembly; two vias are connected to the outer anchor, and two are connected to the frame surrounding the sensor to be used for substrate grounding, Fig. 4.9(b). Thru-wafer interconnects allow for the electrical connection between the front side and the back side of the sensor die.

B. Experimental Results

Frequency response characterization of the sensors was performed using a custom-built test-bed, a Signatone probe station, and a set of probes for electrical connection of the device contact pads to the front-end PCB. The test-bed with a holder allows for testing the prototypes, using excitation/detection thru the top electrodes, when the sensor is "proof-mass-up", or thru the vertical interconnects, when the sensor is flipped, "proof-mass-down", Fig. 4.11.

The sensor was excited to oscillate in the first wineglass mode in n=2 pair, indicated as X

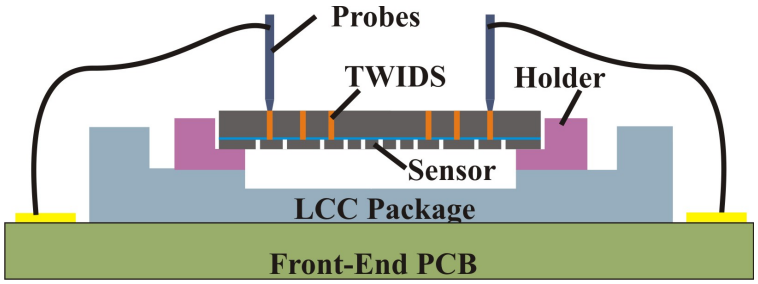

Figure 4.11: Custom-built test-bed with a holder for testing sensors, using excitation/detection thru top electrodes or thru vertical interconnects.

mode in Fig. 4.9(a). For the sensor excitation, one probe was used to apply a DC voltage of 24.8 V to the proof-mass (electrode M in Fig. 4.9(a), (b)) and two probes were used to apply a 1.5 V AC signal to the differential drive electrodes (electrodes Fx+ and Fx- in Fig. 4.9(a), (b)). Another two probes were connected to the differential electrodes Px+ and Px- for signal pick-off. A series of experimental sweeps of the same sensor were obtained, using excitation/detection with probes connected to the top electrodes and to the vertical interconnects, Fig. 4.12.

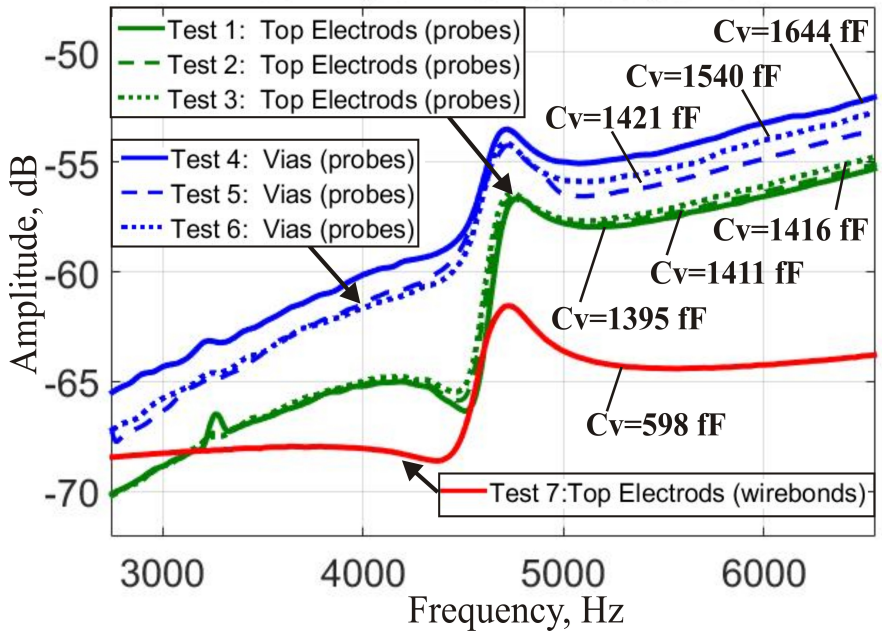

Figure 4.12: Series of experimental sweeps of the sensor, obtained using excitation thru the top electrodes and thru vias.

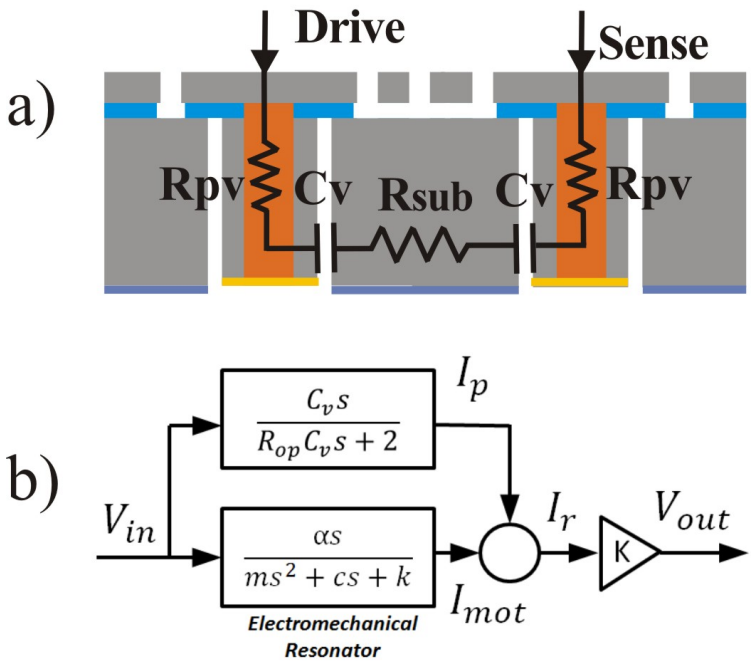

Figure 4.13: (a) Schematic of a system with excitation/detection using top electrodes, (b) transfer function model of the system including parasitic feed-trough current.

The observed distortion of the frequency response is caused by the parasitic feedthrough currents, including TWI to substrate coupling capacitance, pad-to-substrate capacitance, probe-to-probe capacitance, and PCB parasitic capacitance. In order to identify the main source of the parasitics, we performed an analytical analysis of the transfer function of the overall system, including the parasitic effects, [132]. Parasitic capacitance and resistance values were then extracted using a series of experimentally obtained responses, Fig. 4.12.

The transfer function of the electro-mechanical resonator system can be represented as:

$$\frac{V_0}{V_{in}} = K \frac{\chi_1 \chi_2 s}{ms^2 + cs + k}, \tag{4.2}$$

where K is the transimpedance amplifier gain, c and k are the damping and stiffness coefficients, correspondingly, and χ_1 and χ_2 are the coefficients for conversion from the input signal to mechanical force and for the mechanical displacement to motion induced current, correspondingly.

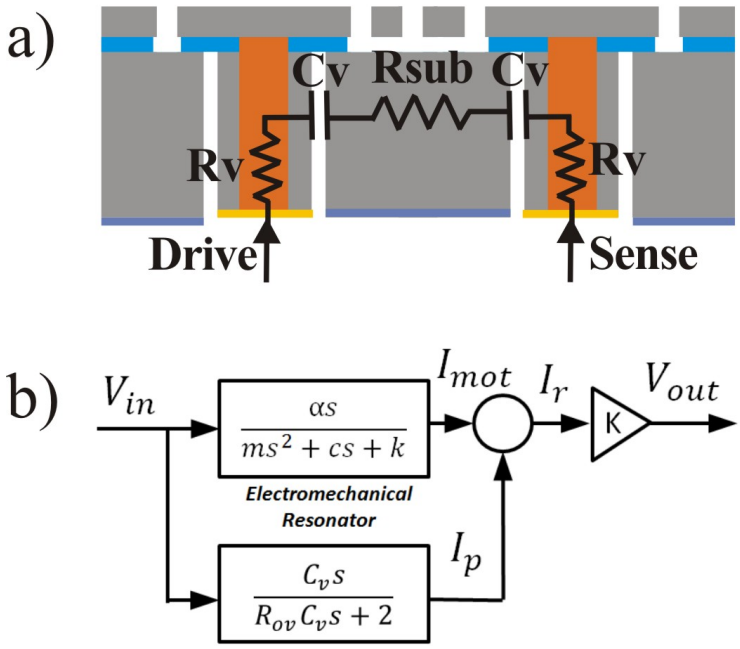

Figure 4.14: (a) Schematic of a system with excitation/detection using vias, (b) transfer function model of the system including parasitic feed-trough current.

In case of the sensor excitation/detection using top electrodes (Fig. 4.13), we included the parasitic feed-through current which runs through the driving contact pad, then through the first via, parasitic capacitance of the first insulating gap, through the substrate, then through parasitic capacitance of the second insulating gap, through the second via, and, finally, through the sensing contact pad:

$$\frac{V_0}{V_{in}} = K\frac{\chi_1\chi_2 s}{ms^2+cs+k} + K\frac{C_p s}{R_{op}C_p s+1} = K\frac{\chi_1\chi_2 s}{ms^2+cs+k} + K\frac{C_v s}{R_{op}C_v s+2}, \tag{4.3}$$

$$R_{op} = R_{pv1} + R_{sub} + R_{pv2},$$

$$R_{pv1} = R_{pad1} + R_{Cu1} + R_{Si1},$$

$$R_{pv2} = R_{pad2} + R_{Cu2} + R_{Si2},$$

where C_v is the parasitic capacitance of via, R_{pad1} and R_{pad2} are the resistance values of the driving and sensing contact pads, R_{Cu1} and R_{Cu2} are the resistance values of the first and

second copper vias, R_{Si1} and R_{Si2} are the resistance values of the silicon surrounding the first and second vias, R_{sub} is the resistance of the substrate.

In case of the sensor excitation/detection using vias (Fig. 4.14), we included the parasitic feed-through current which runs through the resistance and parasitic capacitance at the driving port via, through the substrate, then through the resistance and parasitic capacitance at the sensing port via:

$$\frac{V_0}{V_{in}} = K\frac{\chi_1\chi_2 s}{ms^2 + cs + k} + K\frac{C_v s}{R_{ov}C_v s + 2}, \tag{4.4}$$

$$R_{ov} = R_{v1} + R_{sub} + R_{v2},$$

$$R_{v1} = R_{Cu1} + R_{Si1},$$

$$R_{v2} = R_{Cu2} + R_{Si2}.$$

The real and imaginary parts of the frequency response (3) were then analyzed:

$$Re(n) = \frac{R_{op}C_v^2 w_n^2}{(R_{op}C_v w_n)^2 + 4}, \tag{4.5}$$

where $Re(n)$ is the offset in the real part of the experimentally extracted frequency response at frequency w_n, away from the resonance point, and

$$Im(r) = \frac{2C_v w_r}{(R_{op}C_v w_r)^2 + 4}, \tag{4.6}$$

where Im_r is the imaginary part of the experimentally extracted frequency response at resonant frequency w_r.

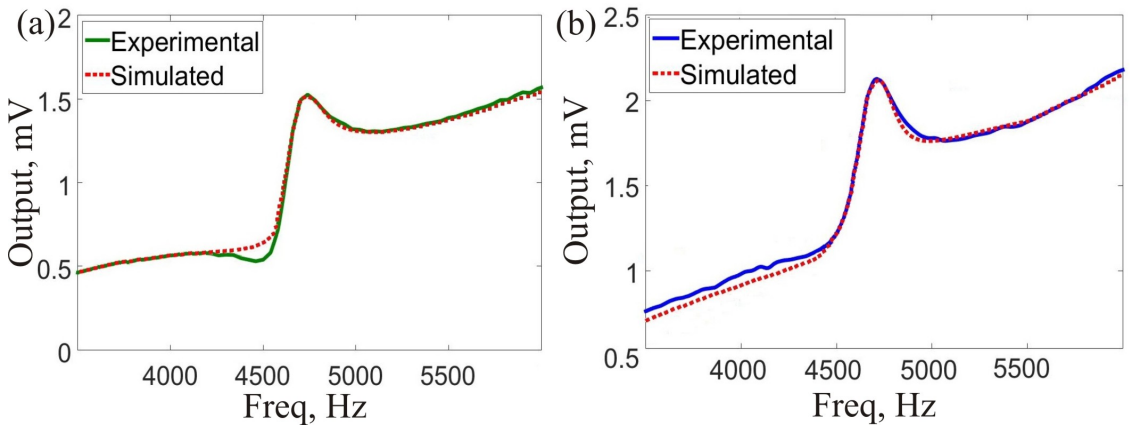

Figure 4.15: Experimental freq. response curves obtained using electrical connection through (a) top electrodes, (b) vias are fitted to the simulated response curves with the analytically identified system parameters.

Equations (2.5) and (2.6) were solved simultaneously to identify parasitic terms C_v (parasitic capacitance) and R_{op} (total resistance) for the system in Fig. 4.13. Following the described procedure, parasitic terms C_v and R_{ov} for the system in Fig. 4.14 were also identified using equation (2.4) and by examining the real and imaginary parts of experimentally obtained responses.

Fig. 4.15 shows the experimentally acquired frequency response curves fitted to the simulated response curves with the analytically identified system parameters. The close match between the experimental and simulated curves verifies the accuracy of the system parameters and parasitic terms estimation.

Calculated values of parasitic capacitance are shown in Fig. 4.12, including capacitance C_v for frequency sweeps obtained using electrical connection through top electrodes and parasitic capacitance C_v for frequency sweeps obtained using electrical connection through vias. The mean value of parasitic capacitance extracted from the frequency sweeps, obtained with excitation thru via was 1535 fF. The identified value of Rp was 2.2 MΩ. The mean value of parasitic capacitance extracted from the series of frequency sweeps, obtained with excitation thru top electrodes was 1407 fF.

The experimentally identified values of the parasitic capacitance are higher than the calculated theoretical values, Fig. 4.5(b). It has been hypothesized that the probe-to-probe capacitance is one of the major factors contributing into the parasitic feedthrough current. Including the probe-to-probe capacitance in parallel with the sensor results in a following transfer function of the system in Fig. 4.13:

$$\frac{V_0}{V_{in}} = K\frac{\chi_1\chi_2 s}{ms^2 + cs + k} + K\frac{C_v s}{R_{op}C_v s + 2} + C_{probe}s, \tag{4.7}$$

where C_{probe} is the probe-to-probe parasitic capacitance.

To eliminate the effect of the probe-to-probe capacitance, the sensor's top contact pads were wirebonded to the gold pads of the LCC (Leadless Chip Carrier) package. The value of parasitic capacitance $C_v = 598$ fF was then extracted using the equation (3) and the experimentally obtained frequency sweep, Fig. 4.12, Test 7. This result suggests that TWI parasitic contribution into the response distortion was significantly lower than the total parasitics of the setup, including the probe-to-probe capacitance. The additional sources of the parasitic feed-through currents are the pad-to-substrate capacitance, the pcb parasitic capacitance, and the fringing field induced parasitic capacitance (usually comparatively small).

To remove the parasitic effects from the sensor output, the carrier demodulation technique was used, [133]. For that purpose, a high-frequency carrier signal of 100 kHz and amplitude of 0.5 V was applied to the structure in addition to the driving signal. The carrier signal was multiplied by the time-varying sense capacitance of the resonating structure, resulting in motional current, frequency-shifted to sidebands around the carrier frequency and separated from the parasitic feedthrough currents at the drive frequency. The bandpass filtering was then applied to eliminate the low frequency parasitic feedthrough component. The subsequent demodulation back down to the resonance frequency yielded in a signal cleared from

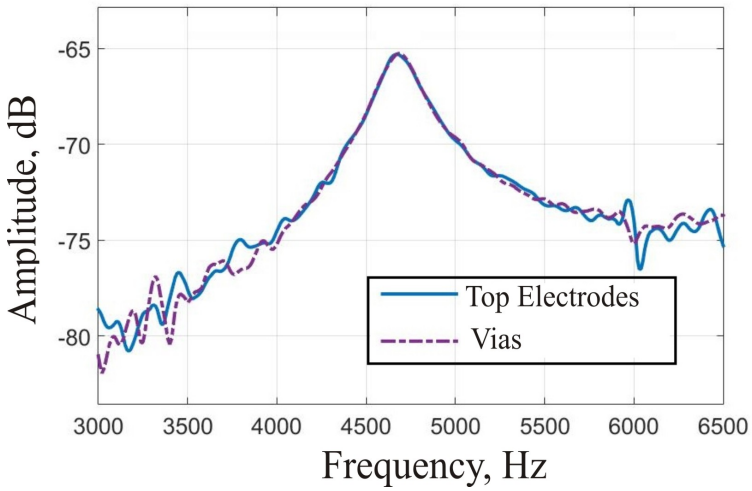

Figure 4.16: Frequency sweeps, obtained using carrier demodulation technique, showed a good match between excitation/detection thru device-side (top electrodes) and interconnect side (vias).

parasitic currents.

The described carrier demodulation technique was applied for frequency response characterization of the sensor with electrical connection through top electrodes, and through vias. Frequency sweeps, obtained using different electrical connection methods, showed a good match, indicating that the parasitic effects were successfully removed in both experiments, Fig. 4.16.

4.1.5 Limitations of TWIDS technology

In this Section, a new approach for co-fabrication of MEMS sensors and high-aspect ratio low-resistance vertical interconnects in thick (up to 600 μm) SOI wafers has been presented. The Thru-Wafer Interconnects Double-Sided (TWIDS) process is based on bottom-up seedless copper electroplating of through-wafer vias, using a highly doped device layer of an SOI wafer as a seed. The described method allows for voids-free features, low resistance (< 100 mΩ), and high aspect ratio (wafer thickness to copper diameter is up to 10:1), [56]. The design trade-offs, process flow, and characterization of interconnects have been described.

The presented through-wafer interconnects technology is compatible with a standard SOI MEMS fabrication process and is particularly appropriate for integration with SOI sensors, such as gyroscopes, accelerometers, and resonators, as well as for the 3D MEMS assemblies, such as Folded MEMS IMU. The TWIDS technology presented in this work may find applications in RF-MEMS devices, where ultra-low resistance and low parasitic capacitance interconnects are typically required for reduction of signal losses, [131].

Some limitations of the TWIDS technology are related to mechanical stability of the structure, that can be compromised due to a high-density array of insulating air gaps. The wafer-level mechanical reliability during processing is a concern because once the integrity is lost, the wafers are prone to breakage, [134]. In order to avoid wafer cracking during the sensors dry etching step, the handle side of the wafer was attached to a silicon carrier using a thin layer of thermal grease. The mechanical reliability of individual dies at the packaging assembly level, as well as during shock and vibrations, is also an important issue.

The solution is sought in filling the insulating trenches by a dielectric material, such as Parylene C or silicon nitride. The choice of the filling material depends on vias applications and is a trade-off between the electrical, thermal, and mechanical properties of the interconnects. Parylene C, which has low relative permittivity of 3.1, is a good candidate for gaps filling. It is applied at room temperature and does not introduce any concerns for thermo-mechanical reliability of copper via. Moreover, Parylene deposition rate (about 5 μm/hr) is comparatively high, making it a suitable material for filling even large gaps (up to 35 μm).

The mechanical stability of the interconnects and a method to enhance structural rigidity by means of filling the insulating gaps with Parylene C is discussed in detail in [135].

Another limitation of the presented TWIDS technology is related to vias thermal reliability. Potential thermal reliability issues are associated with Cu diffusion in Si and Si oxide at high temperatures (>300 °C, [136]), as well as the thermal stresses in Cu via. The samples

characterized in this Section, were annealed at 110-150 °C during the silicon dry etch step, which is within the temperature range requirements for consumer and automotive grade gyroscopes (-40+105 °C). However, if high temperature processing steps follow the vias fabrication, a different type of vias might be considered in this case, such as single crystal silicon or polysilicon vias.

4.2 Packaging

4.2.1 Background

Packaging for Micro-Electro-Mechanical Systems (MEMS) and Integrated Circuits (IC) is one of the important manufacturing steps before bringing the product into the market. It is also the most expensive process step in micromachining. Package provides the interface between the components and the overall system as well as serves for establishing an appropriate operating environment. Some MEMS devices can require specialized packages or packaging processes. For example, inertial sensors need to be hermetically sealed in order to protect the moving parts from environmental effects, such as humidity and dust. In addition, most MEMS gyroscopes, oscillators and resonant-type accelerometers require vacuum encapsulation. Therefore, unlike electronic packaging, where a standard package can be used for a variety of applications, MEMS packages tend to be customized.

Various packaging technologies have been developed for Integrated Circuits and MEMS. These can be grouped under two major categories according to the fabrication process: chip-level packaging and wafer-level packaging. The chip-level packaging allows for the improved time to market due to the capability of using a standard type of package. However, the wafer-level packaging is generally more cost effective, as it allows for sealing all devices on the wafer simultaneously, with a single fabrication step.

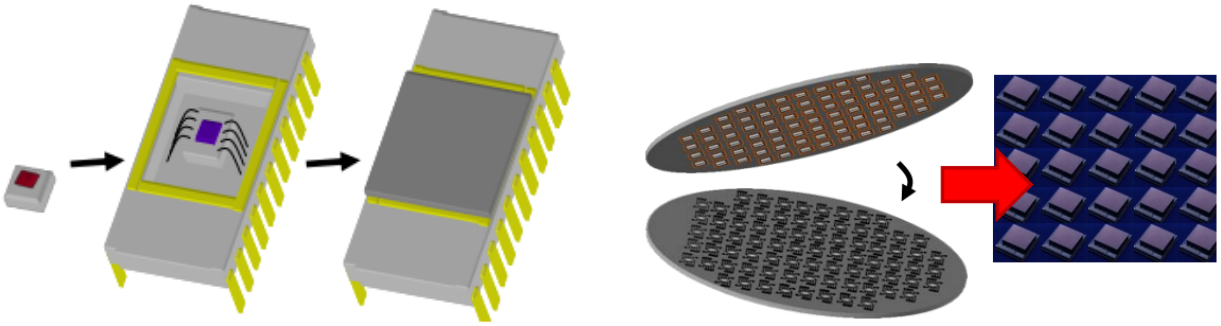

(a) Chip-level packaging (b) Wafer-level packaging

Figure 4.17: MEMS Packaging Approaches

Chip-level packaging category includes all commercially available metal packages, ceramic and plastic packages. Different companies offer a wide range of standard metal, ceramic, and plastic packages for different MEMS/IC applications. This includes Surface Mount Packages/Surface Mount Devices (SMD), Pin Grid Array Packages (PGA), Dual-in-Line Packages (DIP), leadless chip carriers (LCC), flat packs (F/P), and chip scale packages (CSP), [145]. Generally, a device is die-attached to the bottom of the package cavity, wirebonded to the bond pads and hermetically sealed using a lid. Commercially available packages usually come with flat ceramic, metal or glass lids.

Wafer-level packaging category includes thin film packaging and packaging based on hermetic wafer-to-wafer bonding techniques. Various approaches have been developed for wafer-level thin film packaging of MEMS devices, [145]-[147]. A packaging technology that employs an electroplated nickel film to vacuum seal a MEMS structure on wafer level was described in [146]. A thin-film encapsulation approach, using a 6 μm thick Low-Pressure Chemical Vapor Deposited (LPCVD) silicon nitride capping layer and a silicon oxide sacrificial layer was presented in [147].

A number of approaches for hermetic packaging based on wafer-to-wafer bonding techniques has been described in literature, [148]-[151]. For example, a method for manufacturing hermetically sealed MEMS devices has been described in [148]. The fabrication process

starts with etching the device layer of the first SOI wafer and releasing the sensor mechanical features, using hydrogen fluoride (HF) etching. The silicon cover wafer is then fusion or Au-eutectic bonded to the SOI wafer. Next, the handle layers of the cover wafer and the bottom SOI wafer are etched, using a conventional wet etching process, followed by applying metallization to form an electrical connection with the encapsulated device. A successful wafer-level packaging method for integrated MEMS with CMOS has been introduced by S. Nasiri et al. in [149]. The Nasiri-fabrication process involves fabrication of an Silicon-on-Insulator (SOI) wafer, where cavities are formed in the handle layer. The MEMS device is defined in the device layer, using DRIE. Then, the SOI wafer with the device definition is bonded directly to the Al electrical contact pads on the bottom CMOS wafer. A glass vacuum packaging method utilizing aluminum/silicon-to-glass bonding process has been presented in [150]. The packaging process starts with forming the polysilicon interconnect line, followed by deposition of an oxide/nitride/oxide sandwich layer for electrical insulation. Next, aluminum and polysilicon layers are deposited and patterned. A Pyrex glass capsule is then bonded on top of the device substrate.

Recent developments in the MEMS processing enable building complex-shaped 3D MEMS structures, including those using polymers to create 3D elements. A Folded MEMS Inertial Measurement Unit (IMU) presented in this dissertation is one example of such structures, Fig. 3.1. Another example is a Chip-Scale Combinatorial Atomic Navigator, which employs a double-folded structure with integrated Helmholtz coils, reflectors and a Rb vapor cell, [152].

A large variety of shapes and form-factors of MEMS devices makes it difficult to use standard wafer-level packaging techniques and standard packages. For example, common wafer-level packaging techniques are not suitable for packaging of MEMS 3-D devices, such as a Folded MEMS IMU. Wafer-level thin-film encapsulation approach is not compatible with 3D MEMS structures due to a limited thickness of a sacrificial layer, which defines the height of the

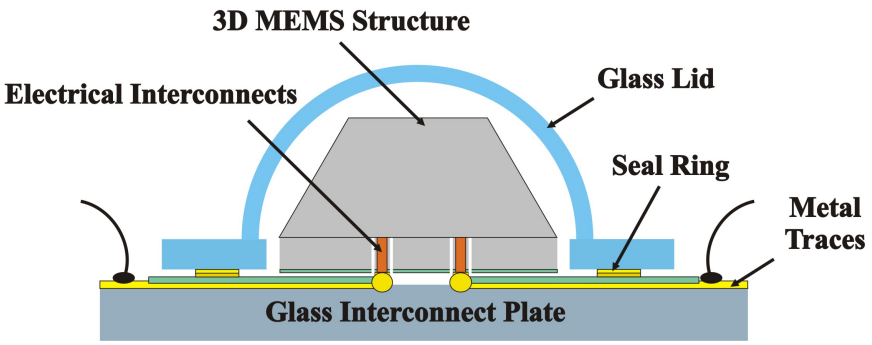

Figure 4.18: Hermetically sealed 3D MEMS device.

microcavity. Packaging approaches based on hermetic wafer-to-wafer bonding techniques successfully address the most of the packaging needs of the flat MEMS devices. However, in order to use these approaches for packaging of 3-D MEMS structures, some sophisticated fabrication steps are required, such as etching deep cavities in the handle Si/glass wafers (up to 10 mm deep).

In order to use a standard package with a standard lid for packaging of 3D MEMS structures, a significant modification in package geometry might be needed. This includes the increased depth of the package cavity (up to 10 mm deep). Using a customized package can result in increased cost of the final product. Alternatively, a metal or ceramic can package can be used to package a 3D MEMS structure. Can-type packages, however, are usually low pin-count, less than 24 pins, thus they are not suitable for many applications requiring a high number of electrical feedthrough interconnects, such as a 6-axis IMU device.

In this Section, we describe an alternative solution for hermetic packaging of 3D MEMS devices, such as Folded MEMS IMU. Our approach utilizes a micro glass-blowing process to fabricate a cap wafer with "bubble-shaped" glass structures. The glass cap wafer is bonded to the handle glass/Si wafer and metal traces are fabricated on the handle wafer to serve transferring signals from the sealed cavity of the bubble to the outside world, Fig. 4.18. The method can also be used for chip-level packaging of MEMS 3D devices, using "bubble-shaped glass lids and standard commercially available type of packages.

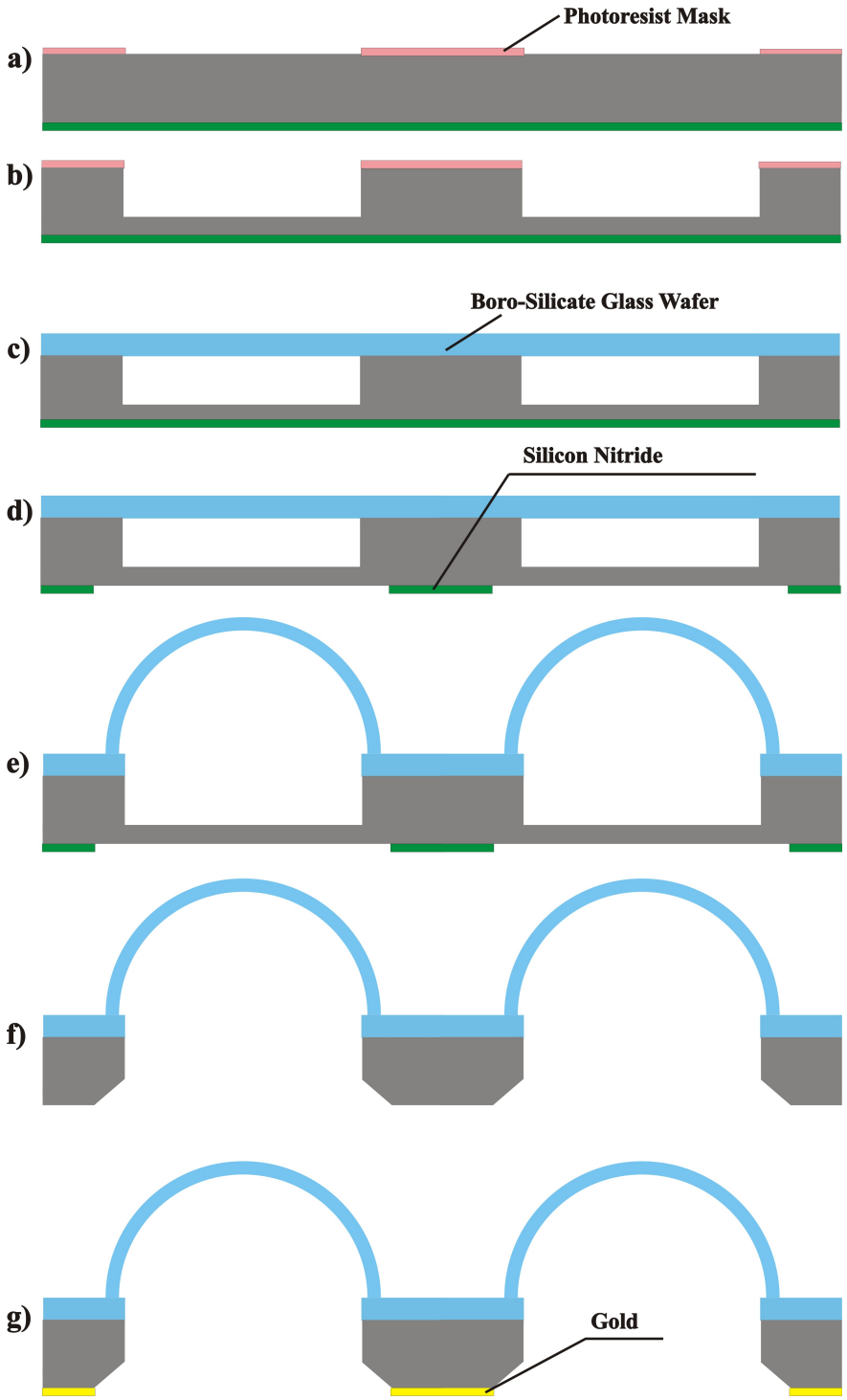

Figure 4.19: "Bubble-shaped" glass structures fabrication process steps: (a) Photoresist mask, (b) Si DRIE etching, (c) glass wafer anodic bonding, (d) silicon nitride patterning, (e) glass-blowing, (f) Si wet etching, (g) gold deposition using shadow mask.

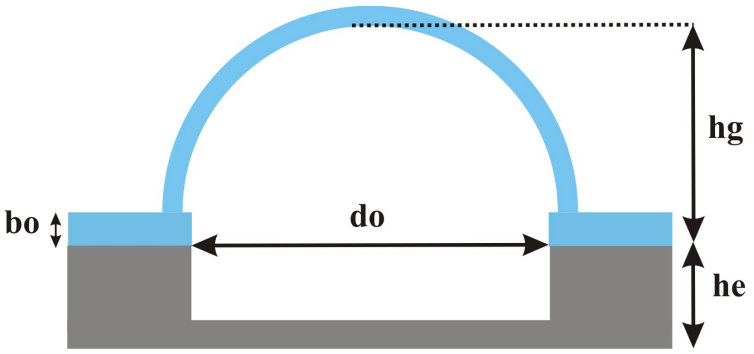

Figure 4.20: Geometry of the blown structure

Diameter of a cavity, $d0$, mm	**Height of a blown bubble, hg, mm**
8.6	6.2
9.6	6.5
10.6	6.8
11.6	7.0

Table 4.2: Predicted height of the blown structures.

4.2.2 Wafer-level vacuum packaging of MEMS 3D devices

The packaging process involves four steps:

1. "bubble-shaped" glass structures are fabricated on wafer-level, using glass-blowing process, [153];
2. metal traces are deposited on the "substrate" wafer;
3. 3D MEMS devices are attached to the "substrate" wafer, using flip-chip bonding;
4. "cap" wafer with "bubble-shaped" structures is bonded to the "substrate" wafer.

Wafer-level fabrication process for the "bubble-shaped" glass structures starts with patterning a 1 mm thick silicon wafer with a layer of photoresist, as illustrated in Fig. 4.19(a). 700 μm deep cavities are then etched using deep reactive ion etching (DRIE), Fig. 4.19(b). The photoresist is removed in acetone and a 100 μm thin borosilicate glass wafer is anodically bonded to the silicon wafer, Fig. 4.19(c). This is followed by pattering of silicon nitride mask for subsequent Si etching, Fig. 4.19(d). Next, the bonded wafers are placed inside a furnace at 350 Torr pressure and at a 850°C temperature (above the softening point of the glass).

Under the high temperature, the pressure of the trapped air inside the cavities increases and the glass deforms into spherical shapes, Fig. 4.19(e). The samples are then quickly removed from the furnace and cooled down to the room temperature. Once glass-blowing step is complete the 300 μm layer of the silicon handle wafer is removed, using wet etching process and a metal etch mask defined at the previous step, Fig. 4.19(f). Ethylenediamine pyrocatechol (EDP)-based etchant [154], or KOH-based etchant [155] can be used for this purpose. Finally, a 500 $\mathring{A}$ thick chromium adhesion layer and 5000 $\mathring{A}$ thick gold layer are deposited on the silicon side of the wafer stack, using a shadow mask, Fig. 4.19(g).

Analytical model developed in [153] was used to predict the shape of the bubble, Fig. 4.20. Glass-blowing takes place inside the furnace at 350 Torr pressure and 850°C temperature. The predicted geometry of the bubbles for different diameters of the etched cavities are summarized in Table 4.2.

Process flow for the "substrate" wafer is shown in Fig. 4.21. First, a 500 Å adhesion layer of chrome and a 5000 Å thick gold layer are deposited on the glass wafer, Fig. 4.21(a). Metal layers are then patterned in order to define the interconnection traces features, Fig. 4.21(b). Metal traces serve to transfer signals from the sealed cavity of the bubble to the outside world. The silicon nitride layer is than deposited to provide an electrical insulation, Fig. 4.21(c). Next, we deposit another 500 Å adhesion layer of chrome and 5000 Å layer of gold, and pattern these layers in order to define the seal ring features, Fig. 4.21(d).

Once the fabrication process is complete, the 3D MEMS devices are attached to the "substrate" wafer using flip-chip bonding and hermetically sealed by bonding a cap wafer with the "bubble-shaped" structures to the "substrate" wafer, Fig. 4.22. The sealing can be performed in vacuum, using gold eutectic bonding. Thin-film getter layer can be deposited inside the bubbles in order to maintain a high vacuum inside a hermetically sealed cavity.

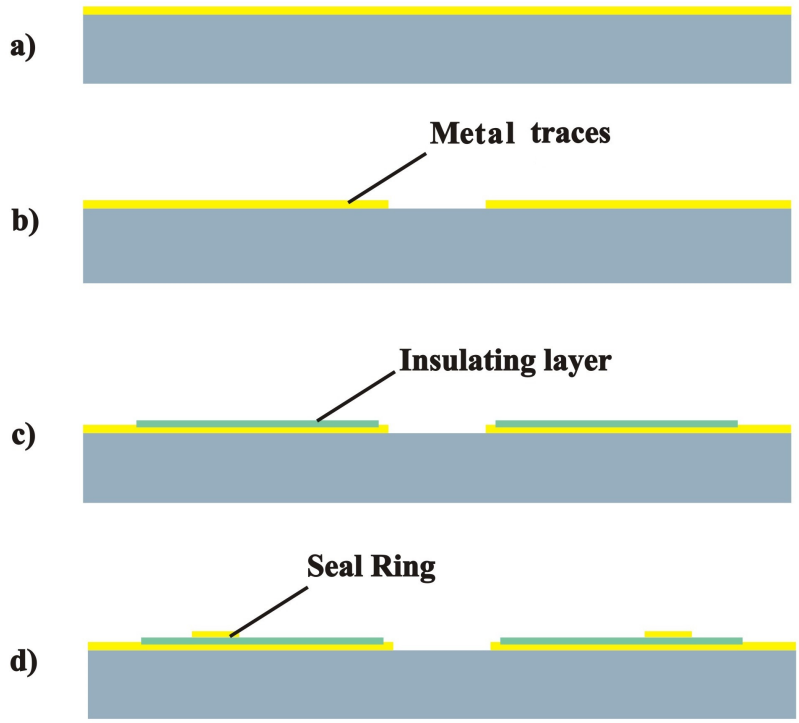

Figure 4.21: Fabrication process for the "substrate" wafer.

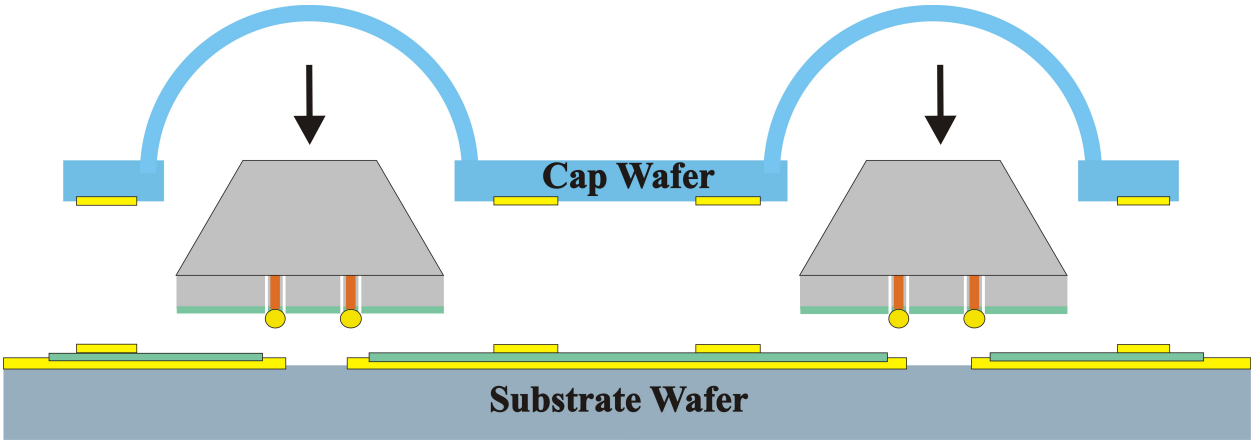

Figure 4.22: Wafer-level packaging of 3-D MEMS devices.

4.2.3 Chip-level vacuum packaging of MEMS 3D IMU

The micro glass-blowing technique was utilized to fabricate the "bubble-shell" glass lids for hermetic sealing of IMU on a chip level. "Bubble-shaped" glass lids fabrication process is similar to the one used for the wafer-level packaging and has been described in the previous

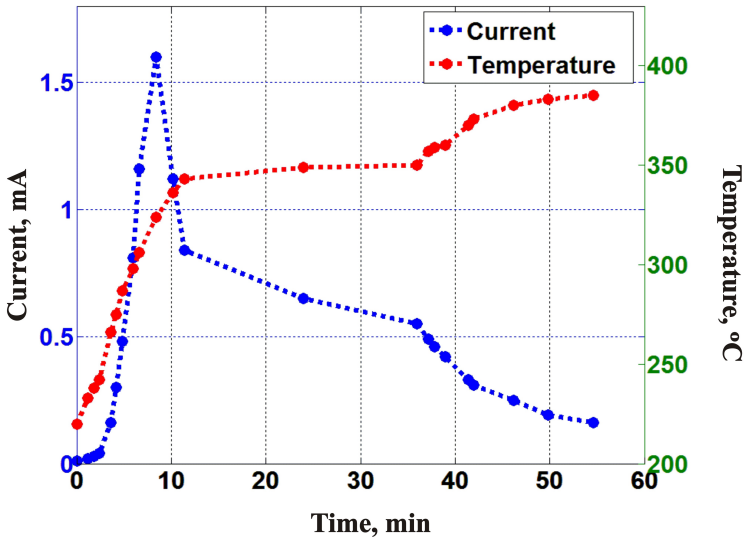

Figure 4.23: Time and temperature to anodically bond 100 μm thin borosilicate glass wafer to the Si wafer.

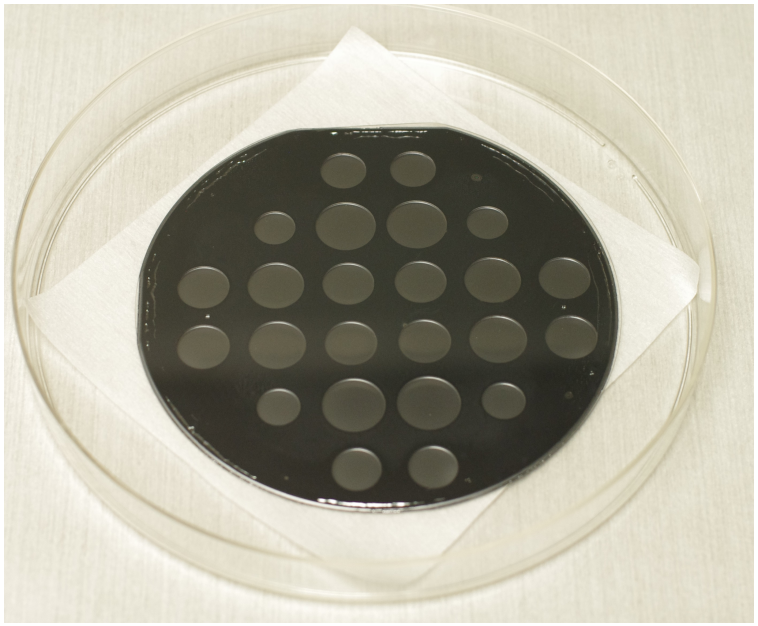

Figure 4.24: 100 μm thin borosilicate glass wafers anodically bonded to the Si wafer.

section, Fig. 4.19. Packaging of MEMS 3D IMU device can be performed by gold eutectic bonding in vacuum of the fabricated lids to the standard commercially available package, such as LCC package, DIP package, etc.

Following the process flow described in Fig. 4.19, the "bubble-shell" glass structures for

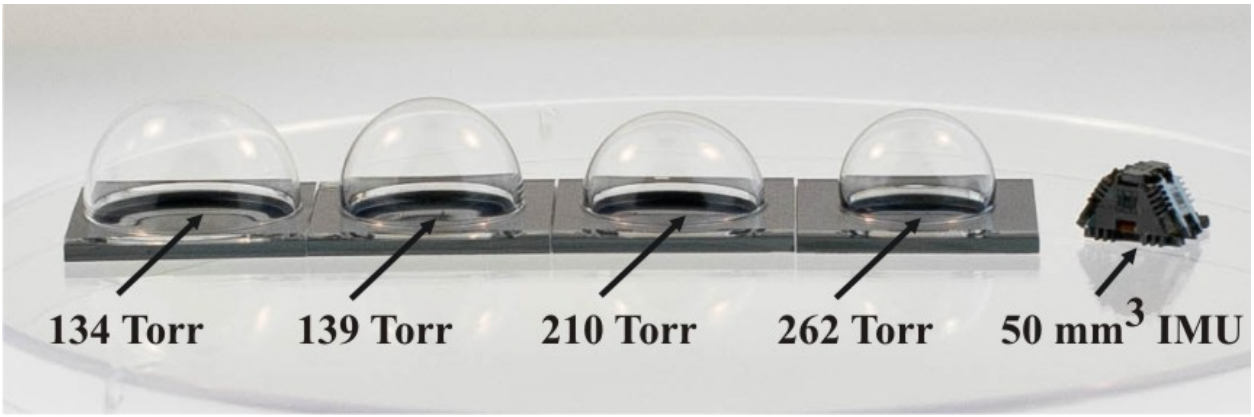

Figure 4.25: Glass bubbles blown at pressure in the range of 134 Torr - 262 Torr. The height of the bubble exceeds 10 mm. 50 mm^3 3-D MEMS IMU for the scale.

chip-level vacuum packaging of MEMS 3D structures were successfully built. In the first step, the 1 mm thick double-sided Si wafers were spin-coated with an AZ P4620 photoresist and the mask for the DRIE etch was photolitograthically defined. In the next step, 700 μm deep cavities were DRIE etched. A 100 μm thin borosilicate glass wafer was then anodically bonded to the silicon wafer, covering all the etched cavities. In the anodic bonding procedure, the wafers were assembled together and heated on a hotplate to about 400°C. The bonding profile is shown in Fig. 4.23. When an electric field is applied across the assembly, the current in the circuit starts increasing, indicating that the bonding process has started. The current reaches 1.6 mA at the temperature of 324°C and then starts decreasing indicating that the bonding is complete. Fig. 4.24 illustrates the stack of the glass-Si wafers.

Next, the bonded wafers were placed inside a furnace at 850°C temperature (above the softening point of the glass). The samples were blown at pressure in the range of 134 Torr - 262 Torr, Fig. 4.25. The height of the glass-blown lids exceeded 10 mm for blowing at mbox134 Torr pressure. The samples blown at lower pressure collapsed during the cooling process. Once the blowing process was complete, the 300 μm Si handle wafer was etched in order to open the bubble cavity and chrome and gold layers are deposited using a shadow mask.

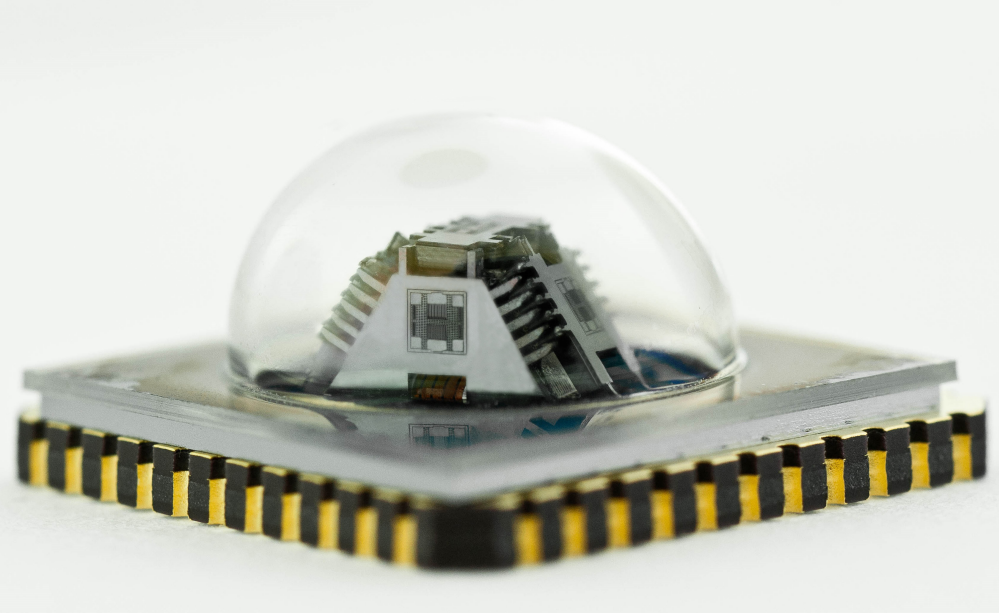

Figure 4.26: 50 mm^3 3D MEMS IMU in an LCC standard package with a "bubble-shell" glass lid.

Figure 4.27: 50 mm^3 3D MEMS IMU in an LCC standard package with a "bubble-shell" glass lid.

"Bubble-shell" glass lids can be used for dust protection, Fig. 4.26, as well as hermetic sealing and ultimately vacuum packaging of 3D folded IMU devices. To demonstrate the sealing process, an SST vacuum packaging tool was utilized to package a simple resonator device, using an LCC standard package and a "bubble-shell" glass lid, Fig. 4.27. The X-Ray analysis of the package after sealing did not reveal any visible voids in a seal ring. Frequency

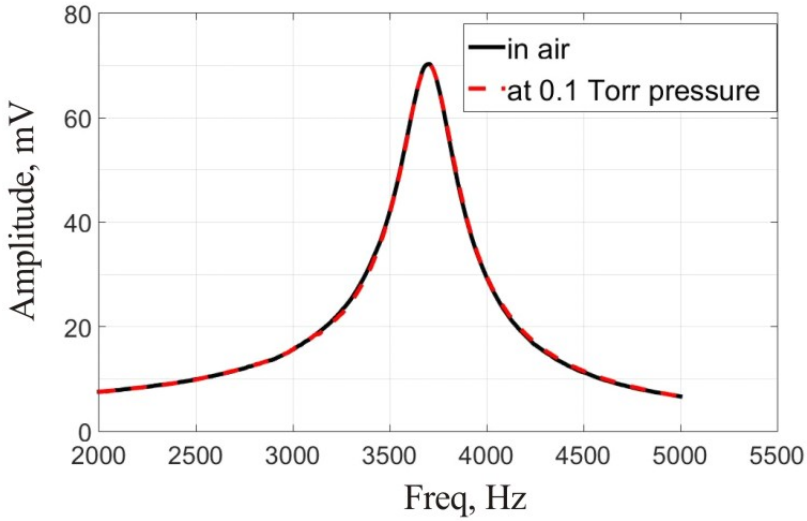

Figure 4.28: Frequency response characterization of the resonator in air before sealing and after sealing in vacuum chamber confirmed the successful hermetic sealing.

response characterization of the resonator in air before sealing and after sealing, in a vacuum chamber at 0.1 Torr pressure showed Q factor of 12, Fig. 4.28. This results confirmed the successful hermetic sealing, but demonstrated that the packaging process did not yield low pressure environment inside the "bubble". Further development of the packaging recipe for the SST vacuum packaging tool is necessary.

4.3 Conclusion

Thru-wafer interconnects fabrication is an integral part of the Folded IMU double-sided process. For enhanced environmental robustness of 3D MEMS IMU, high aspect ratio interconnects have to be formed in a relatively thick wafer (600 μm). In this Chapter, we introduced the novel approach for co-fabrication of Silicon-on-Insulator (SOI) MEMS sensors with low-resistance low parasitic losses vertical electrical interconnects. The Thru-Wafer Interconnects Double-Sided (TWIDS) process is based on bottom-up seedless copper electroplating, and allows for voids-free features and high aspect ratio (wafer thickness to copper

diameter ratio of 10:1). TWIDS technology is compatible with a standard SOI MEMS fabrication process and is applicable for Folded IMU, as well as for standalone micro sensors, such as accelerometers, gyroscopes, resonators, and RF MEMS devices. For the purpose of technology demonstration, prototypes of an SOI MEMS Toroidal Ring Gyroscope with 6:1 aspect ratio interconnects were fabricated using TWIDS process. The experimental characterization showed that the low-resistance interconnects with low parasitic losses are suitable for miniature capacitive sensors.

TWIDS technology enables integration of the Folded IMU devices with electronics as well as facilitates the wafer-level packaging of IMUs.

This Chapter introduced an approach for hermetic and vacuum packaging of 3D MEMS devices, such as Folded MEMS IMU, utilizing "bubble-shell" glass lids. The packaging method involves fabrication of a cap wafer with "bubble-shell" glass structures on a wafer-level, using a micro glass-blowing process. In wafer-level packaging, the glass cap wafer is bonded to the handle glass/Si wafer to seal the array of IMU devices. It was shown, that the "bubble-shell" glass lids, in combination with standard commercially available type of packages, might also be used for chip-level packaging of 3D IMUs and other MEMS devices and assemblies. We demonstrated hermetic sealing of the device packaged inside an SST vacuum packaging tool, using a fabricated "bubble-shell" glass lid and an LCC package.

Chapter 5

IMU-on-a-Chip

This Chapter explores a single-chip roll-pitch-yaw gyroscope as a base design for an ultra-compact multi-axis IMU, implemented using an "all-in-one-sensor" approach. The mechanical structure of the gyroscope employs a single vibrational element with a torsional drive mode and a multi-directional sense modes. Manufactured in wafer-level Epitaxial Silicon Encapsulation (Epi-Seal) process, [94], a single-chip device occupies an area of 1.2 mm^2. Initial characterization of the sensor presented in this Chapter includes a scale factor, a noise level, a cross-axis error, and a vibrational sensitivity measurement.

5.1 Introduction

MEMS gyroscopes find a wide scope of applications as rotation sensors in consumer electronics and gaming devices, for example, for activity detection, virtual and augmented reality, optical and electronic image stabilization. In general, in order to determine the orientation of a moving platform, it is necessary to measure rotation around three perpendicular axes: roll, pitch, and yaw. The most common methods to provide three axes of sensitivity are dis-

cussed in Chapter 1 of this thesis. The two main approaches for commercial IMUs include mounting of individual single-axis gyroscopes along the three non-collinear axes, [9] and a single-chip approach.

During the last decade, the development and commercialization of the single-chip MEMS IMUs has experienced a rapid growth, due to significant improvement in performance and cost reduction. For many applications, these devices more often replace the bulkier and more expensive assembled IMUs.

A number of single-chip multi-axis solutions have entered the market, for example, SM330 and LSM9DS0 iNEMO inertial modules by ST Microelectronics', Fig. 5.1, and later generations of these devices, [17]-[21]. The ST Microelectronics' IMUs contain three-axis gyroscopes and three- or single-axis accelerometers, fabricated on a single chip, using a surface micromachining Thick Epitaxial Layer for Micro-gyroscopes and Accelerometers (ThELMA) process.

The mechanical design of a three-axis gyroscope by ST Microelectronics' implements an idea of a triple tuning-fork structure with a single vibrating element, Fig. 5.2. The structure employs four suspended sensing masses, coupled to each other by means of the four folded springs. In drive mode, the sensing masses move in-plane inward/outward of the center anchor: on the whole, the structure cyclically expands and contracts, similarly to a beating heart. The yaw mode is formed by the in-plane, anti-phase motion of one pair of the sensing masses. In the pitch and roll modes, the corresponding pairs of sensing masses move out-of-plane, in anti-phase. The differential approach adopted in the structure design and a highly symmetric mechanical element assure a high level of rejection to linear acceleration and a low, around ± 2 %, cross-talk.

Another example of a single-chip IMU is the FIS-1100 IMU by Fairchild, [27]. FIS-1100 IMU incorporates a three-axis gyroscope and a three-axis accelerometer, Fig. 5.1 . The

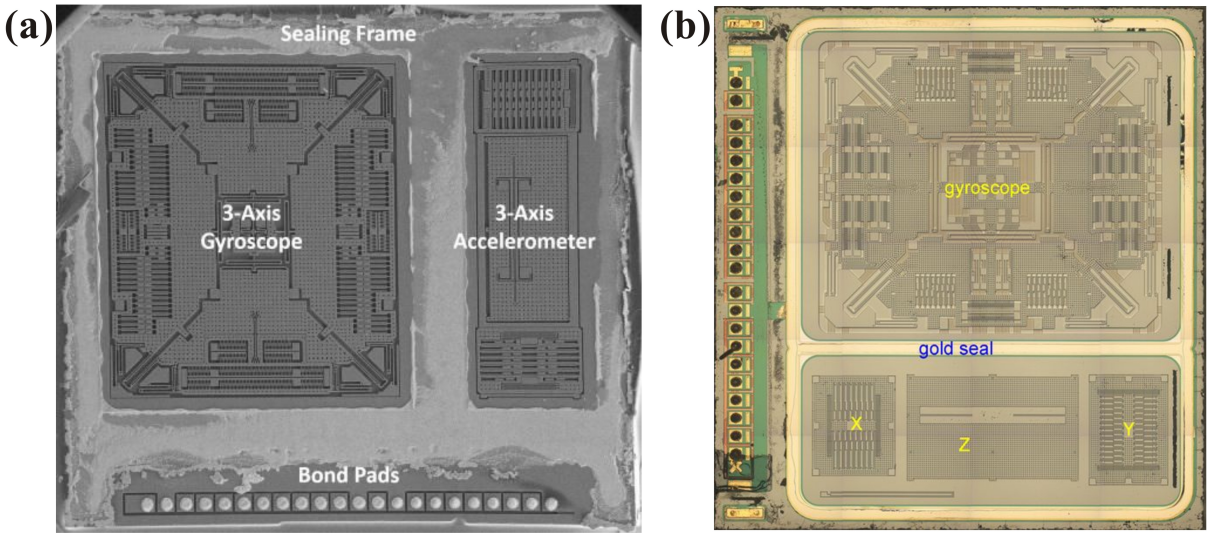

Figure 5.1: ST Microelectronics iNEMO inertial modules (Source: Chipworks reports): (a) LSM330, [17]; (b) LSM9DS0, [18].

single mechanical structure of a three-axis gyroscope is suspended using a central anchor, [156]. The drive mode is formed by the torsional motion of the driving structure around the Z axis, normal to sensor plane. The roll and the pitch mode proof-masses are formed each by the two symmetric portions of the single structure, and are designed to move out-of-plane in response to the rotation about the X-axis and Y axes. The sense-mode motion is detected using out-of-plane electrodes. The pair of the roll mode proof-masses is also employed for detection of the Z-axis rotation. In yaw mode, these proof-masses oscillate along the X-axis in anti-phase. This motion is detected by the in-plane electrodes with parallel plates. The mechanical element of a three-axis accelerometer is formed by the inner and outer frames, suspended using a central anchor. The outer frame is designed to move along the X-axis, in response to the X-axis acceleration, and along the Z-axis, in response to the Z-axis acceleration. Meanwhile, the inner frame is designed to move along the Y-axis, in response to the Y-axis acceleration.

Other examples of the single-chip sensors are the MPU-6700 IMU by InvenSense, Fig. 5.1(a), 3-axis accelerometer BMA280 by Bosch, Fig. 5.1(b), and BMI160 IMU by Bosch, [33].

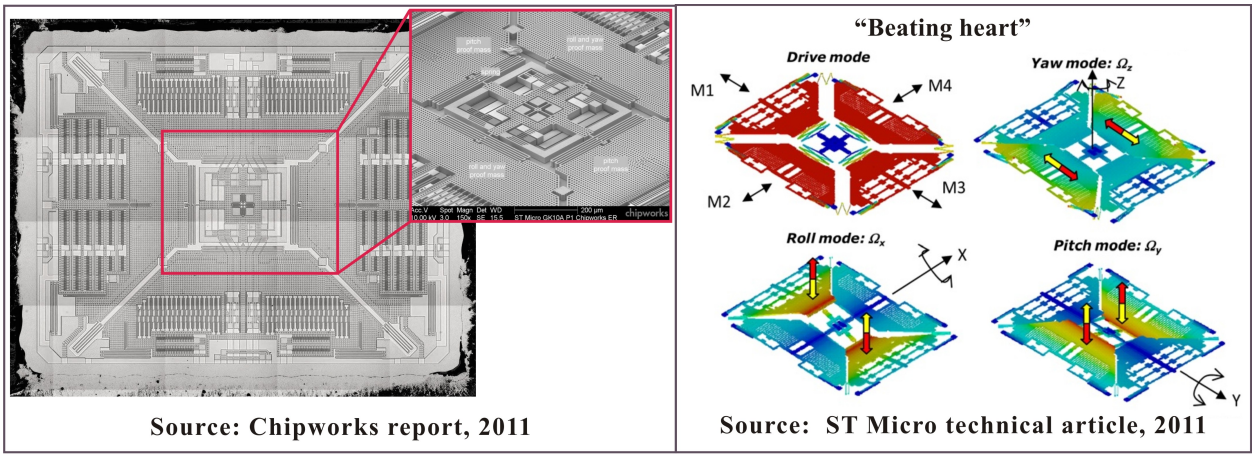

Figure 5.2: Architecture of the ST Microelectronics L3G4200D single-structure 3-axis MEMS gyroscope.

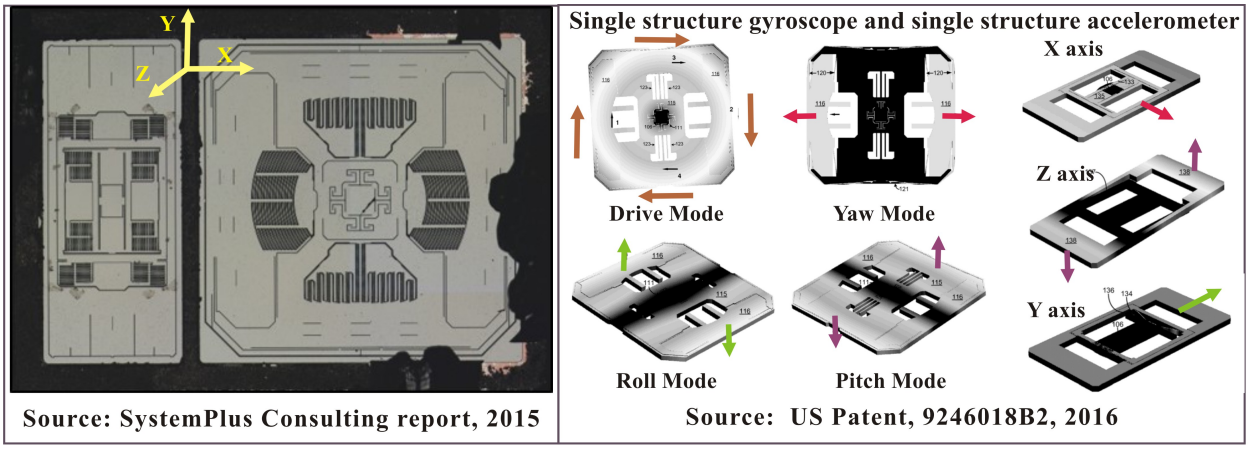

Figure 5.3: FIS-1100 single-chip IMU by Fairchild, [27]

.

An "all-in-one-sensor" approach, which involves measuring rotation around three axes using a single structural element, is very attractive for applications where low power, low cost, and extremely small volume are required, such as, for example, wearable devices and small unmanned air vehicles.

During the last few years, there has been a continuous improvement in noise characteristics of the low-cost consumer grade gyroscopes. In real-world applications, however, environmental performance, including vibration sensitivity is often one of the most significant factors influencing the gyroscope selection. External accelerations and mechanical vibrations in

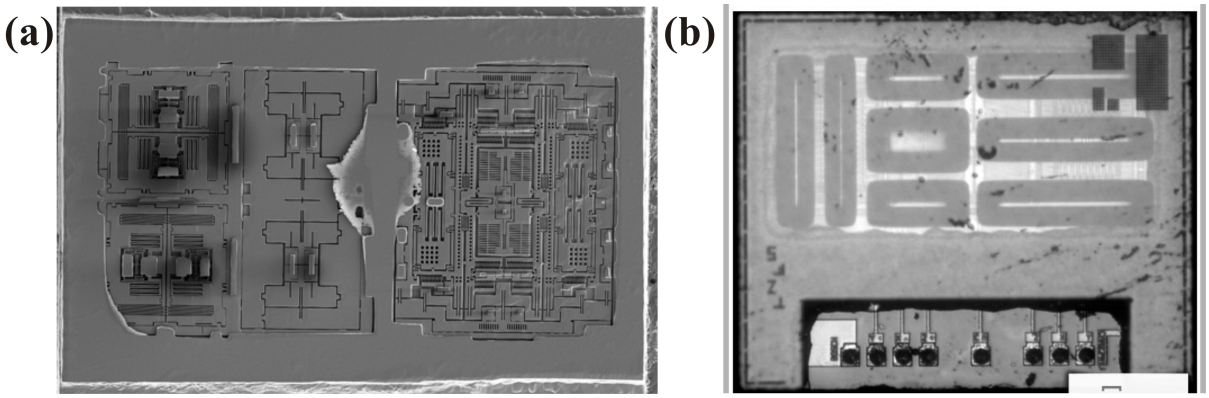

Figure 5.4: Single-chip MEMS IMUs (Source: Chipworks reports): (a) MPU-6700 by InvenSense, [26], (b) BMA280 by Bosch, [31]

.

MEMS vibratory gyroscopes can induce undesired displacements of the proof-mass creating significant output errors thus degrading device performance. Susceptibility to external linear accelerations (or g sensitivity) and vibration rectification (or g^2 sensitivity) impact the gyroscope's scale factor and bias. Gyroscope Vibration Rectification Error (VRE) is a measure of the apparent shift in gyro steady state bias error as a function of a change in the applied random vibration level. This effect may be nonlinear with vibration level, and may also depend on the spectrum.

Some gyroscopes are designed with multiple proof-masses vibrating in anti-phase and enabling common mode rejection of accelerations, for example, Tuning Fork Gyroscope [59], Quadruple Mass Gyroscope [60], and Dual Foucault Pendulum [139]. Such designs attempt to compensate for g and vibration sensitivity. However, in practice, all gyroscopes have some sensitivity to acceleration due to asymmetry of their mechanical structure induced by fabrication errors.

Among some of the most successful companies on the market, developing single-chip consumer grade gyroscopes are STMicroelectronics, TDK InvenSense, and Bosch. Key parameters of several gyroscopes manufactured by these companies are summarized in Table 5.1. Unfortunately, most data-sheets for consumer grade gyroscopes do not mention sensitivity

	ST Micro L3GD20H	**TDK InvenSense ITG-1010**	**Bosch BMG160**	**ADI ADXRS646**	**Units**
Package	3×3×1	3×3×0.9	3×3×0.95	7×7×3	mm
Axes of Sensitivity	3	3	3	1	
Meas. Range	±245÷2000	±250÷2000	±125÷2000	±250	dps
Bandwidth	50	250÷3600	12÷230	1000	Hz
Zero-g Offset	±25	±15	±1	N/A	dps
Cross-Sensitivity	2	2	N/A	N/A	%
Non-Linearity	0.2	0.2	N/A	0.01	% FS
Noise Density	0.011	0.01	0.014	0.01	dps/$\sqrt{Hz}$
ARW	N/A	N/A	N/A	0.6	dps/$\sqrt{hr}$
Zero-rate offset over temperature	±0.04	±0.17	±0.015	±0.037	dps/°C
Temp. Range	-40+85	-10+75	-40+85	-55+105	°C
Shock Survivability	N/A	10,000 g	10,000 g x 200 μs	10,000 g x 500 μs	
Linear Acceleration Sensitivity	N/A	N/A (0.1 for ITG-3200)	N/A	0.015	dps/g
Vibration Rectification	N/A	N/A	N/A	0.0001 (25g rms, 50 Hz to 5 kHz)	dps/g^2

Table 5.1: Performance of commercial miniature MEMS gyroscopes

to linear acceleration and vibrations. For comparison, parameters of the industrial grade gyroscope developed by ADI for harsh environments are also presented in Table 5.1.

In this Chapter, we investigate an ultra-compact single-chip sensor, which is designed to measure angular rate around three axes with minimal, less than 0.3 % cross talk and reduced sensitivity to external vibrations over a wide range of frequencies. The sensor is implemented in wafer-level Epitaxial Silicon Encapsulation (Epi-Seal) process.

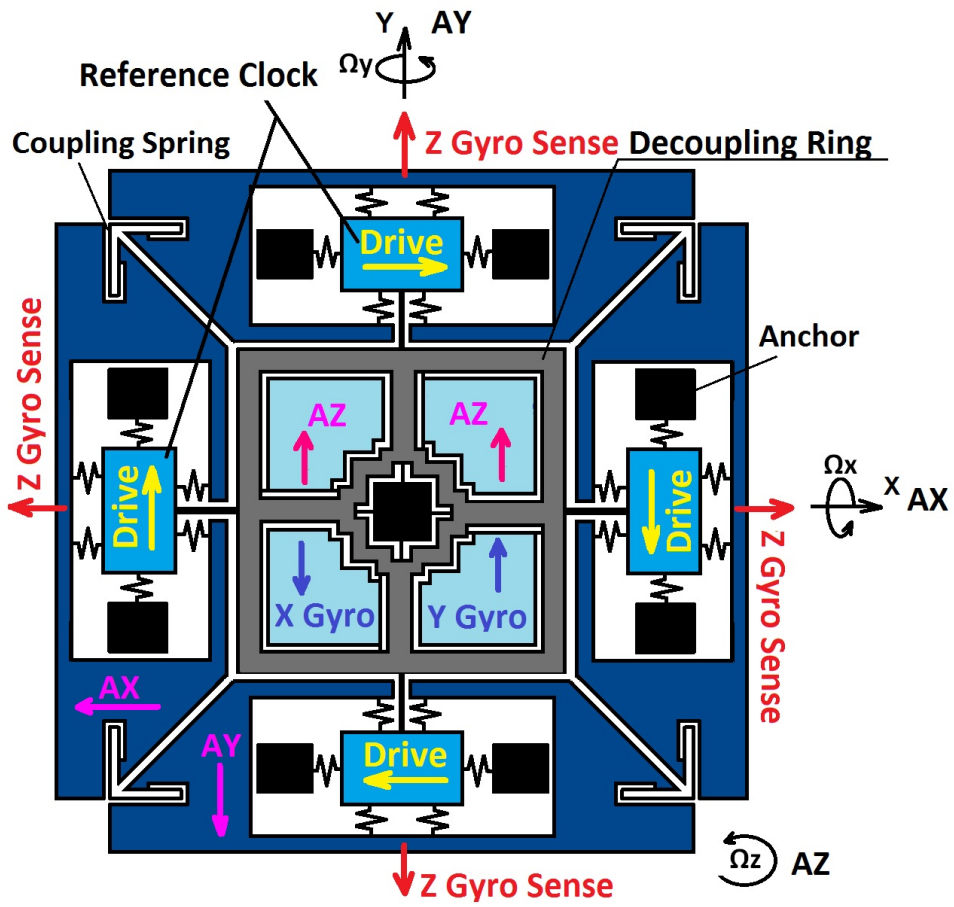

Figure 5.5: In 'all-in-one" sensor approach, a single-structure is used for measuring angular rate and acceleration around three perpendicular axes.

5.2 "All-In-One-Sensor" IMU

For an "all-in-one-sensor" IMU implementation, we propose a device design, where a single-structure is used for measuring angular rate and acceleration around three perpendicular axes, Fig. 5.5. The single-die sensor employs a torsional drive and multi-directional sense modes.

The single driving structure is comprised of four shuttles connected by means of the central rigid frame and four flaps linked to the frame. The drive mode consists of a torsional motion of the single driving structure around the Z axis, Fig. 5.6(a). The Z-axis sense

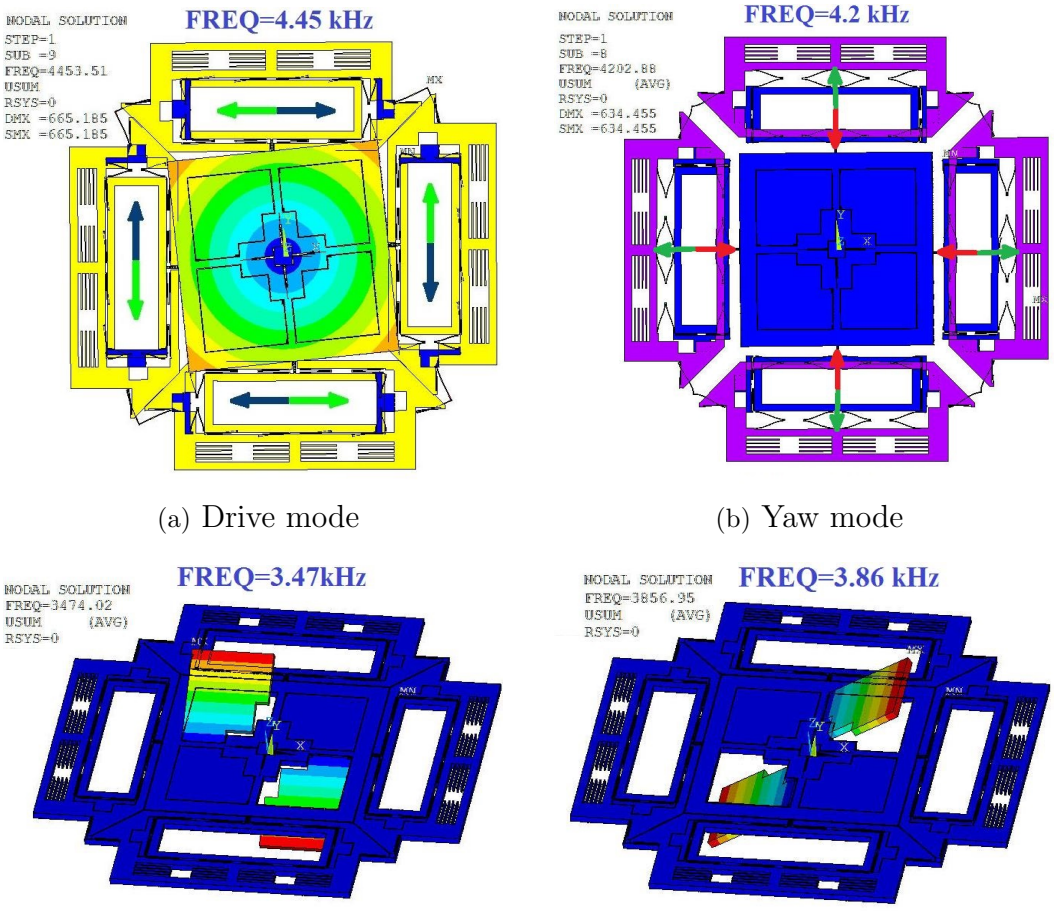

(a) Drive mode

(b) Yaw mode

(c) Pitch mode

(d) Roll mode

Figure 5.6: Operational modes of the single-chip MEMS IMU

structure is formed by four proof-masses connected to the drive shuttles and mechanically coupled by means of corner springs. In the yaw mode, the Z-axis proof-masses move in-plane towards/outwards the enter anchor of the structure, Fig. 5.6(b). The XY-axis proof-masses are formed by the flaps suspended inside the central rigid frame. The roll (X-axis) and pitch (Y-axis) sense modes consist of the out-of-plane anti-phase motion of the flaps, Fig. 5.6(c) and Fig. 5.6(d).

Along with the angular rate measurement, the Z-axis proof-masses can be used for detection of acceleration along the X and Y axes. The angular rate signal at resonant frequency of the device can be separated from low frequency accelerations with the synchronous demodulator and a low-pass filter. Similarly, the X-axis and Y-axis proof-masses can be used for detection of acceleration along the Z axis.

5.3 Single-Chip Thee-Axis Gyroscope

5.3.1 Gyroscope Design

A simplified version of a single-chip IMU was designed for implementation in a wafer-level Epitaxial Silicon Encapsulation (Epi-Seal) process, [94]. The three-axis gyroscope design in Fig. 5.7 is based on the design of a single-chip IMU presented in Section 5.2. To minimize the sensor's footprint, the number of shuttles in the single driving structure was reduced by two. The shuttles are connected by means of the central rigid frame, and four flaps are linked to the frame, Fig. 5.7(a). The drive mode consists of a torsional motion of the single driving structure around the Z axis, Fig. 5.7(b).

The Z-axis sense structure is formed by two proof-masses connected to the drive shuttles and mechanically coupled by means of corner springs and a lever. The mechanical coupling allows

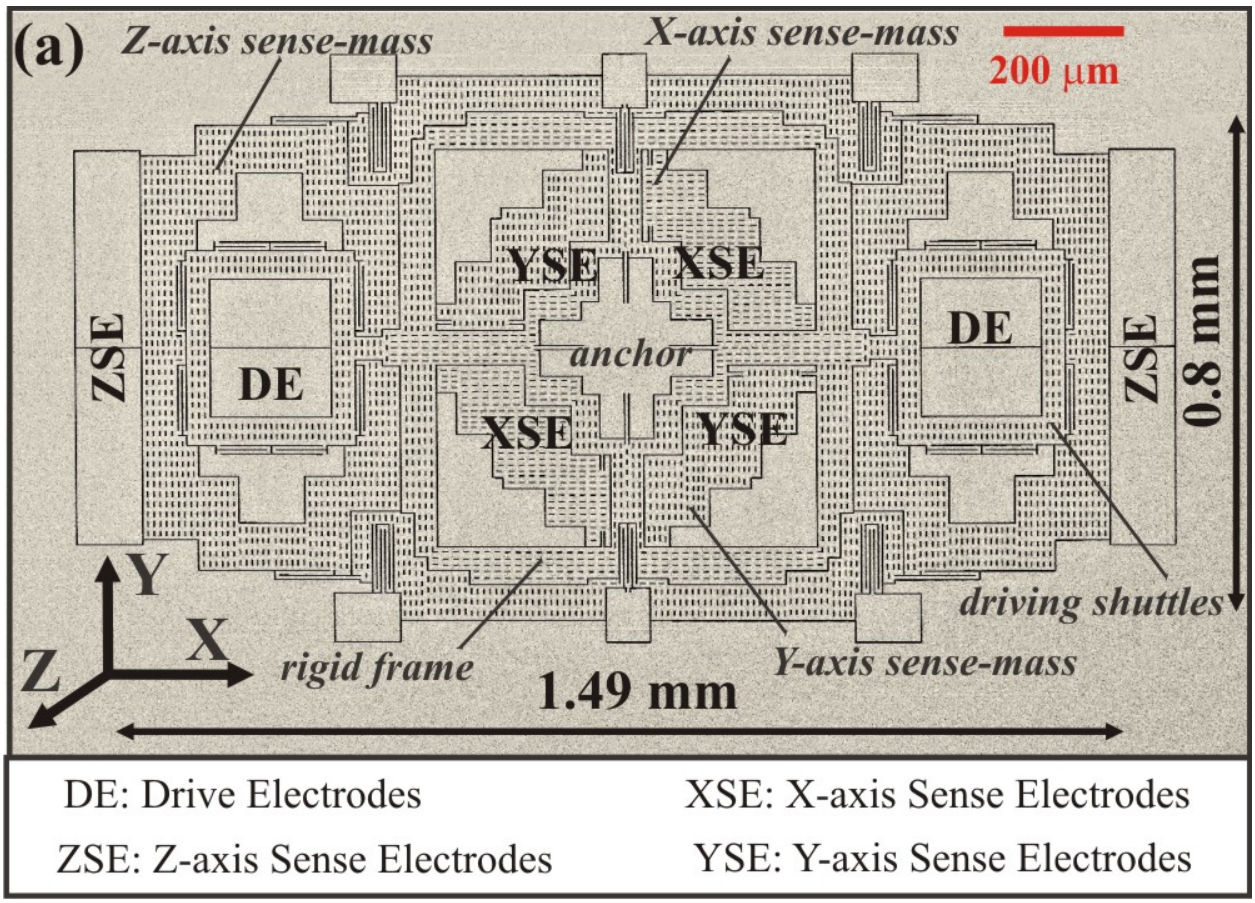

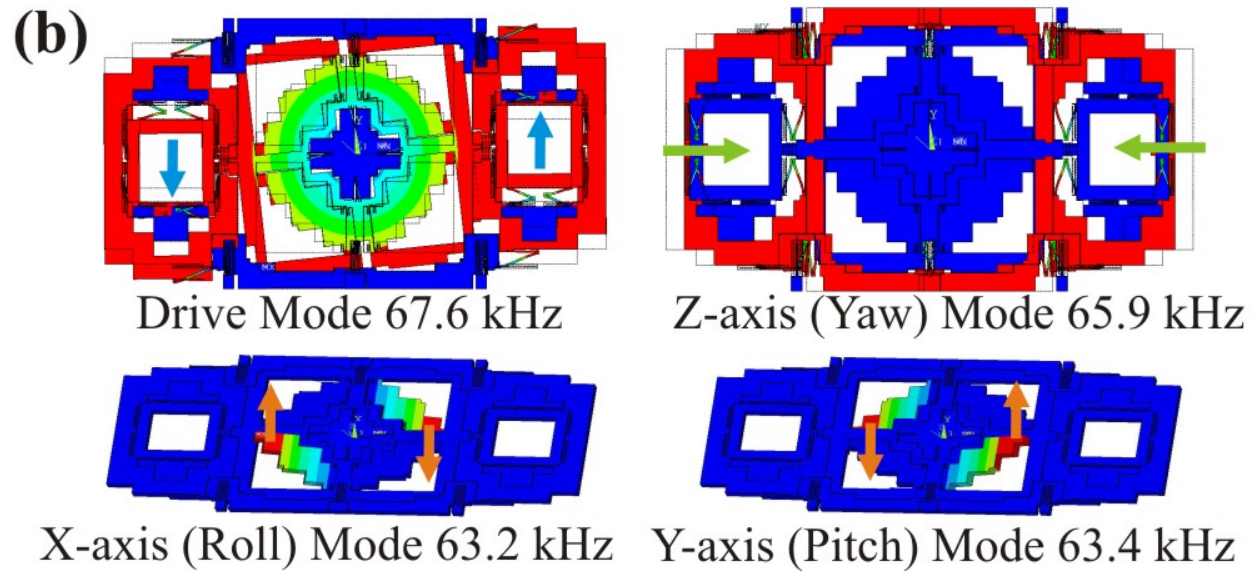

Figure 5.7: (a) Micro-photograph of a single-chip three-axis gyroscope prototype, implemented in wafer-level Epitaxial Silicon Encapsulation (Epi-Seal) process; (b) Mode-shapes and resonant frequencies of the device.

for a single resonant frequency. In the yaw mode, the Z-axis proof-masses move in-plane, in anti-phase.

The XY-axis proof-masses are formed by the four flaps suspended inside the central rigid frame. The roll (X-axis) and pitch (Y-axis) sense modes consist of out-of-plane anti-phase motion of the two pairs of flaps.

A rigid frame connected to the center anchor separates the roll, pitch, and yaw sense-masses, effectively reducing the coupling between the three axes of sensitivity. This feature differentiates this design from some of the previously reported single-structure 3-axis gyroscopes, where the same portion of a proof-mass is often used for detection of rotation around more than one axis, for example [157] and [158].

5.3.2 Fabrication Process

Prototypes of a three-axis gyroscope were fabricated using a wafer-level Epitaxial Silicon Encapsulation (Epi-Seal) process, [94]. In this process, movable silicon microstructures are encapsulated with a layer of epitaxially deposited silicon, allowing for an ultra-clean hermetic seal and resulting in a high vacuum environment. All devices were fabricated in a standard ("Hot Dog") Epi-Seal process with a 40 μm thick device layer and 1.5 μm capacitive gaps. The out-of-plane motion of the proof-masses was detected using the top-electrodes. In "Hot Dog" Epi-Seal process, out-of-plane electrodes were formed by portions of the top Si layer isolated using nitride plugs, [94].

Devices were designed to operate at relatively high resonant frequencies (>63 kHz) to improve the robustness to shock and vibrations. A small capacitive gap enabled by Epi-Seal technology, allows for increased strength of the driving force and sensitivity enhancement.

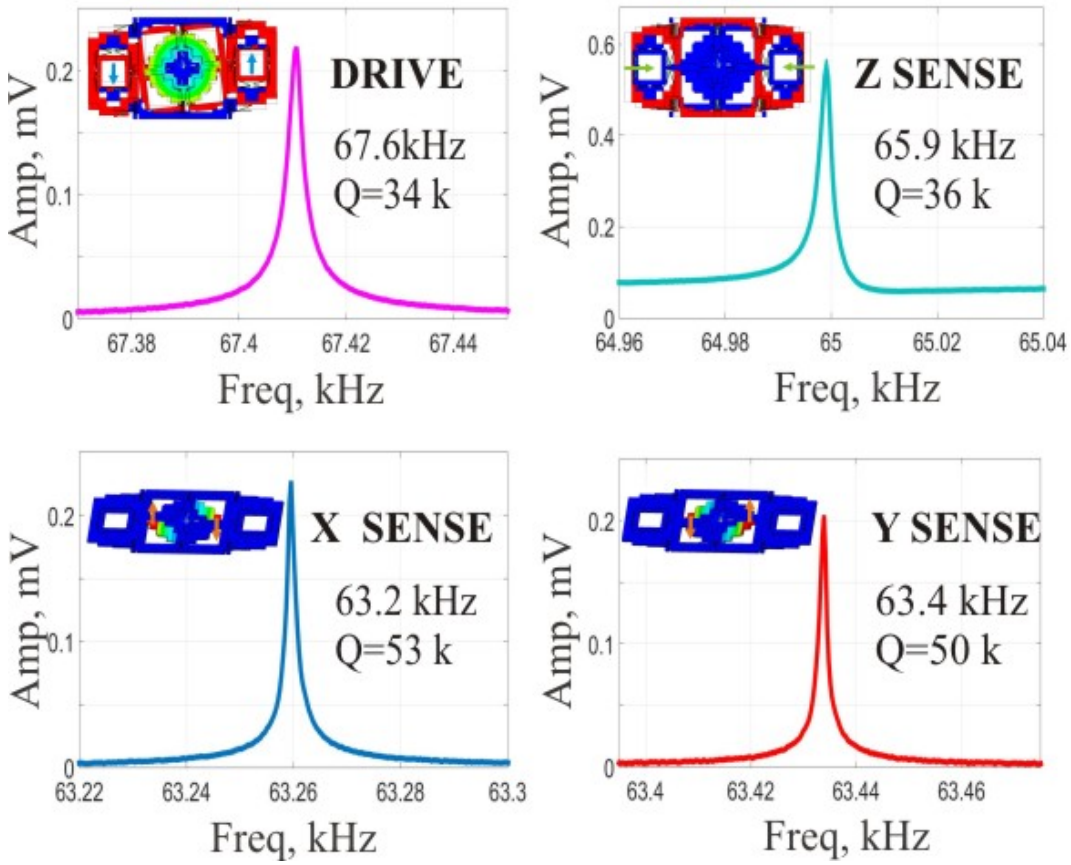

Figure 5.8: Experimental sweeps of the sensor for roll, pitch, yaw, and drive modes.

5.4 Experimental Results

Fabricated prototypes of a single-chip three-axis gyroscope were die-attached to the ceramic carrier and interfaced with the front-end signal conditioning electronics. Frequency response characterization of the sensors was performed using electrostatic excitation with a DC voltage of 2 V applied to the proof mass and 100 mV AC signal applied to the drive electrodes. Resonant peaks were measured at 63.26 kHz (roll mode), 63.43 kHz (pitch mode), 65 kHz (yaw mode), and 67.41 kHz drive mode), Fig. 5.8.

Gyroscope scale factors along three axes were derived using a testing platform with the Ideal Aerosmith 2102 series rate table and a two-axes Ideal Aerosmith tilt-table, Fig. 5.9. A carrier signal at the frequency of 550 kHz was applied to the proof-mass, resulting in

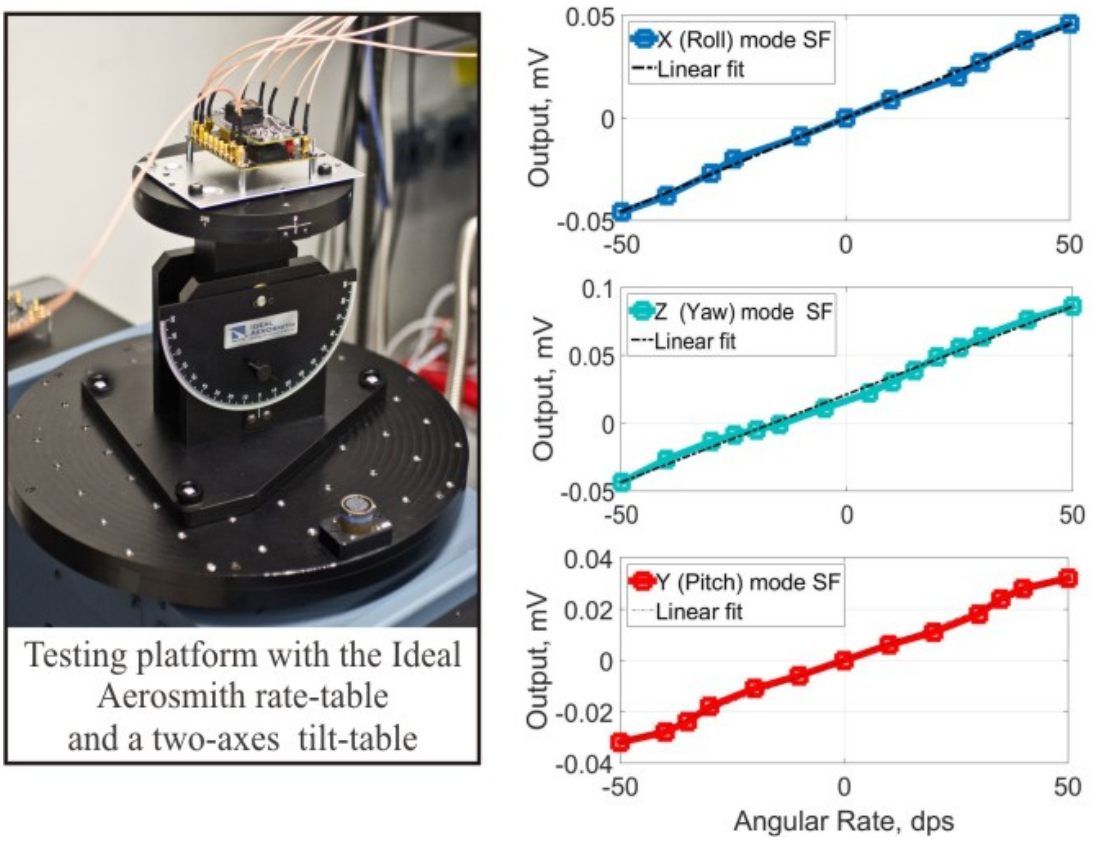

Figure 5.9: Gyroscope's scale factors along the three axes were derived using a testing platform with the Ideal Aerosmith rate table and a two-axes tilt-table.

amplitude modulation of the sensor output. The output signal was then demodulated to reveal the low frequency changes in capacitance. The amplitude of the drive-mode motion was stabilized, using an Automatic Gain Control (AGC). All loops were realized using a Zurich Instruments HF2LI digital lock-in amplifier.

The gyroscope was calibrated to compensate for the misalignment of the mechanical element relative to the testing platform. Calibration process involves identification of unique correction formulas to enable an internal frame alignment, which minimizes cross-axis sensitivity and improves the sensitivity accuracy.

Following the procedure described in Appendix B2, first, the gyroscope's zero-rate outputs of three sensitivity channels were recorded. Next, the gyroscope's outputs of three sensitivity

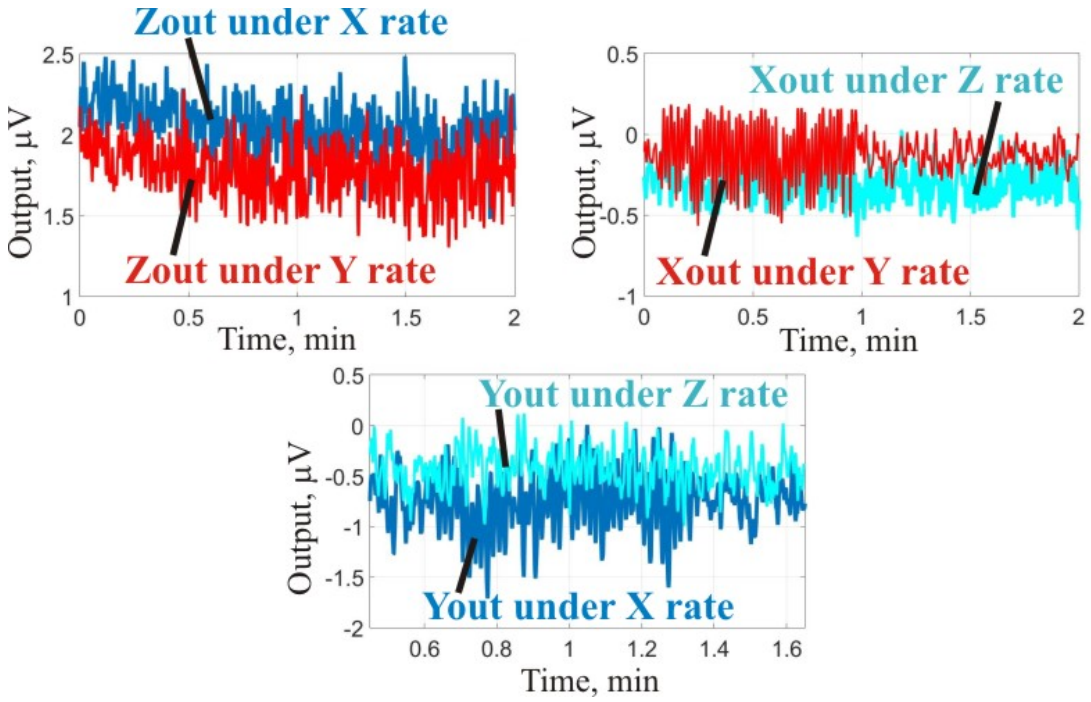

Figure 5.10: Gyroscope's off-axis outputs of three sensitivity channels.

channels were recorded under rotation of the rate-table around X, Y, and Z axes. Fig. 5.10 shows the responses to angular rates along the directions perpendicular to the sensitivity axes of three channels.

The true angular velocities can be expressed as:

$$\Omega_B = K * \Omega_I, \tag{5.1}$$

where $[\Omega_B]$ is a 3×n matrix with true angular rate datasets from rate-table, K is a 3×3 correlation and scaling matrix, Ω_I is a 3×n matrix with the measured data.

The linear least-squares criterion is used to find the best fit for K over the measured datasets. The matrix K of calibration coefficients was estimated as:

$$\begin{bmatrix} 1.49 & -0.03 & -0.14 \\ -0.03 & 0.99 & -0.17 \\ 0.55 & 0.29 & 6.55 \end{bmatrix} * 1e^6, \tag{5.2}$$

	Roll	Pitch	Yaw
Cross-Axis Sensitivity	±1.5 %	±1.5 %	±0.8 %
Cross-Axis Sensitivity (after calibration)	±0.23 %	±0.26 %	±0.1 %

Table 5.2: Cross-axis sensitivity after calibration does not exceed 0.3%.

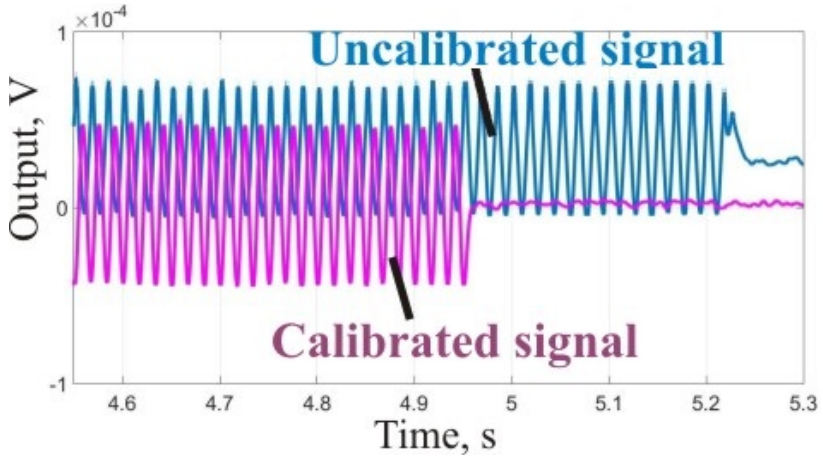

Figure 5.11: Z-channel output under the sinusoidal rotation of the rate-table.

Fig. 5.11 reflects the gyroscope's Z-channel output under the sinusoidal rotation of the rate-table, including raw output and calibrated signal. The amplitude of the calibrated signal is significantly higher due to correction for misalignment from the Z-axis sensitivity axis. The experimentally derived scale factors for three channels were 0.92 μV/dps, 0.66 μV/dps, and 1.72 μV/dps for the roll, pitch, and yaw modes. After initial calibration was performed, a cross-axis sensitivity of less than 0.3% was measured for all three axes, Table 5.2.

The Root Allan Variance Analysis (r-AVAR) was used for identification of random noise characteristics, Fig. 5.12. Experimental characterization of the yaw channel revealed in-run bias of 0.003 dps and ARW of 0.011 $dps/\sqrt{Hz}$; noise analysis of the roll and pitch channels revealed in-run bias of <0.01 dps and ARW of <0.029 $dps/\sqrt{Hz}$.

Vibration sensitivity of the gyroscope has been measured using a SPEKTRA Primary Calibration System with a high-frequency vertical shaker and a laser vibrometer. For this purpose, the device in an LCC package and front-end amplification PCB were placed on a vibration platform, Fig. 5.13.

Sinusoidal vibration at 1 kHz frequency and amplitude in the range from 1g to 15g has been applied along the axis perpendicular to the sensor die. During this experiment the zero-rate output has been recorded separately for Y channel, Fig. 5.14 and Z channel. Experimental testing revealed vibration sensitivity of 0.015 dps/g for the gyroscope's Y channel and vibration sensitivity of 0.03 dps/g for the gyroscope's Z channel, 5.15. It is important to notice that g-sensitivity of devices may vary over the rotational rate. For full vibration characterization of the sensor, the device and a vibrating shaker would need to be placed on a rate table. Vibration experiments presented in this Section, are only limited to evaluation of the zero-rate output of the sensor.

In addition, g-sensitivity usually varies due to frequency of vibration. Fig. 5.16 represents the

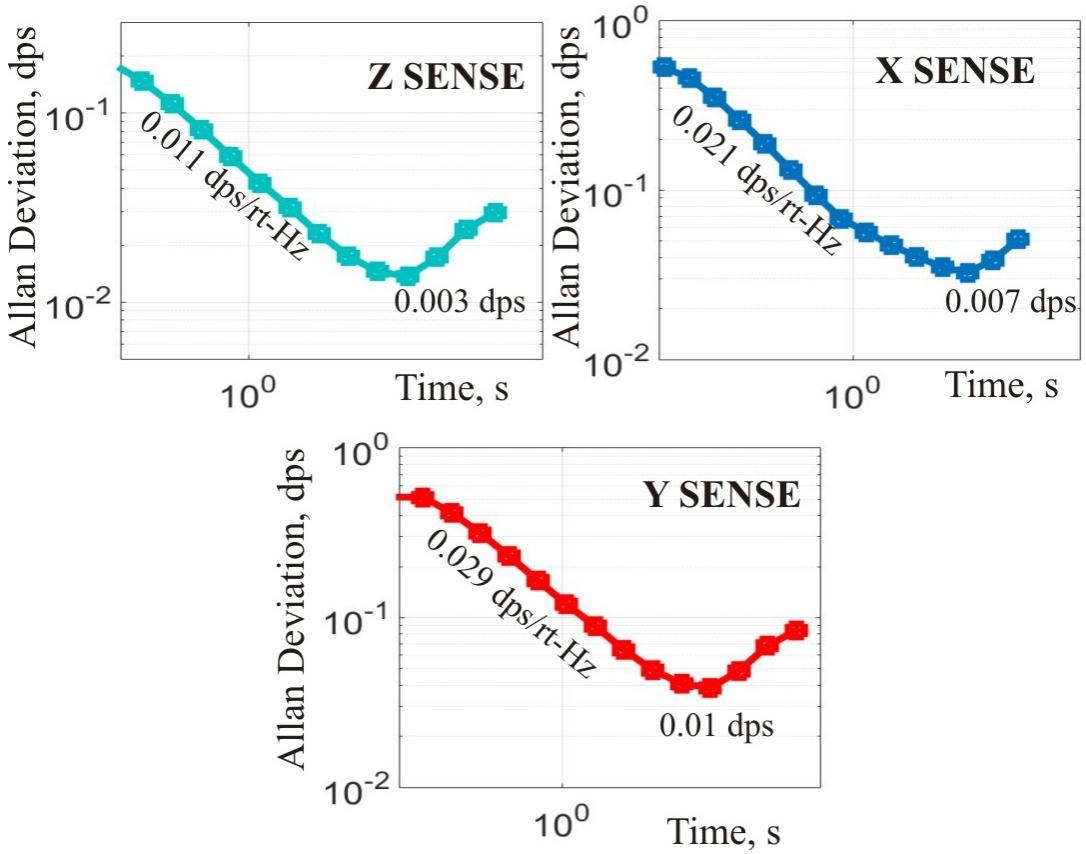

Figure 5.12: Noise analysis of Z axis revealed in-run bias of 0.003 dps and ARW of 0.011 $dps/\sqrt{Hz}$; noise analysis of the roll and pitch channels revealed in-run bias of <0.01 dps and ARW of <0.029 $dps/\sqrt{Hz}$.

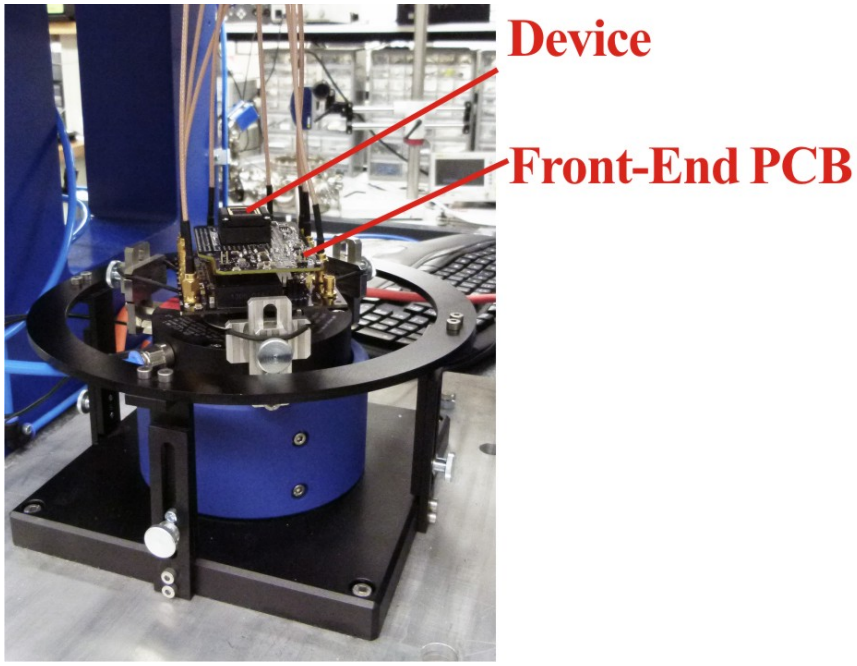

Figure 5.13: Prototype of a three-axis gyroscope and front-end amplification PCB mounted on a platform of a vertical shaker.

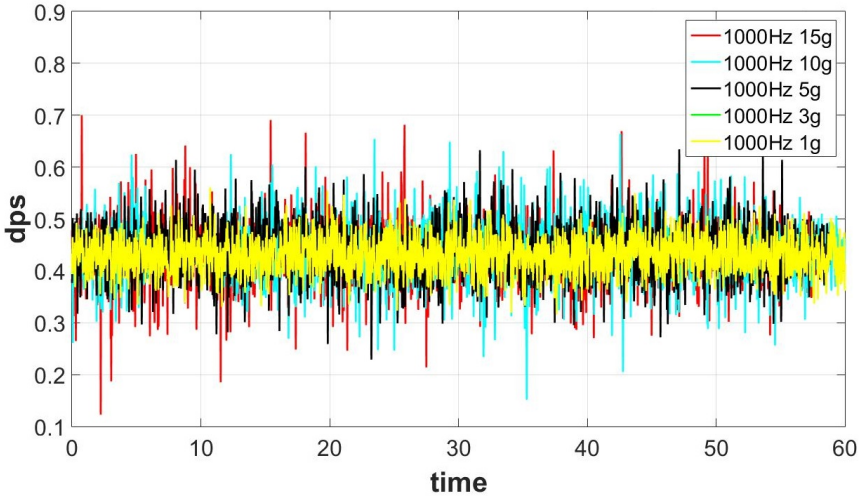

Figure 5.14: Y-channel zero-rate output under sinusoidal vibration at 1 kHz frequency. Experimental testing revealed vibration sensitivity of 0.015 dps/g.

Y-channel zero-rate output under sinusoidal vibration at 300 kHz frequency. Experimental testing revealed vibration sensitivity of 0.92 dps/g. Fig. 5.17 and Fig. 5.18 demonstrate the gyroscope Y channel and Z channel bias response to a 7 g sinusoidal vibration over the 200 Hz to 1 kHz range. The highest peaks are at 330 Hz and 580 Hz, for Y channel, 235 Hz and 315

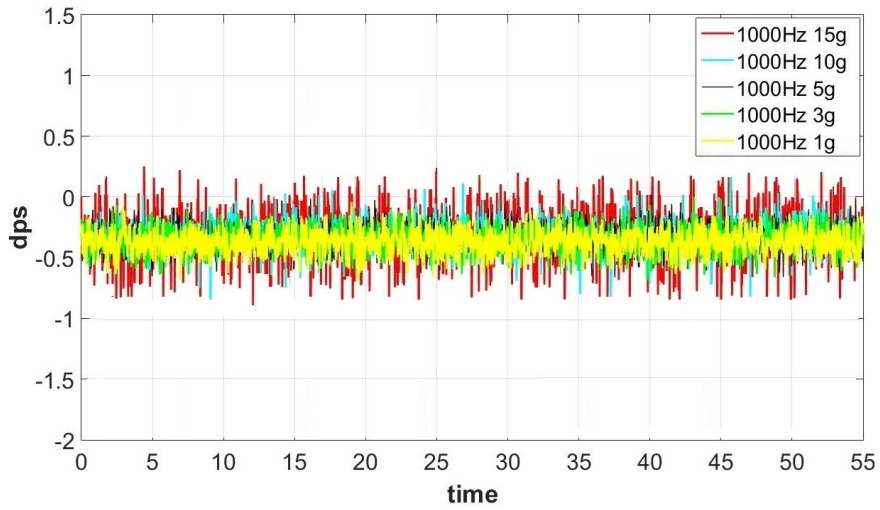

Figure 5.15: Z-channel zero-rate output under sinusoidal vibration at 1 kHz frequency. Experimental testing revealed vibration sensitivity of 0.03 dps/g.

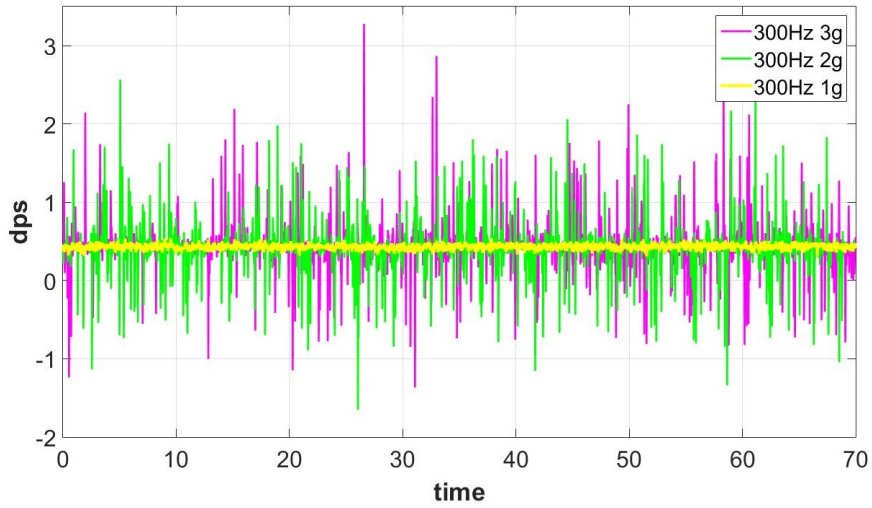

Figure 5.16: Y-channel zero-rate output under sinusoidal vibration at 300 Hz frequency. Experimental testing revealed vibration sensitivity of 0.92 dps/g.

Hz, for Z channel. Since the lowest resonant frequency of the gyroscope's mechanical element is >60 kHz, it has been hypothesized that reduction in vibration immunity at vibration frequencies below 1 kHz could be caused by the angular vibration of the mounting platform and the sensor PCB on the shaker.

Critical vibration frequencies of the mounting were identified using a laser vibrometer, focused on the bottom surface of an empty LCC package placed on a front-end PCB. Fig.

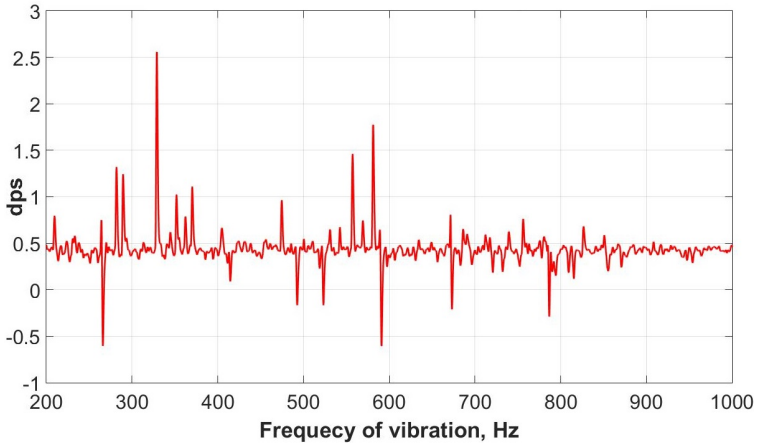

Figure 5.17: Y-channel zero-rate output under 7 g sinusoidal vibration over the 200 Hz to 1 kHz range.

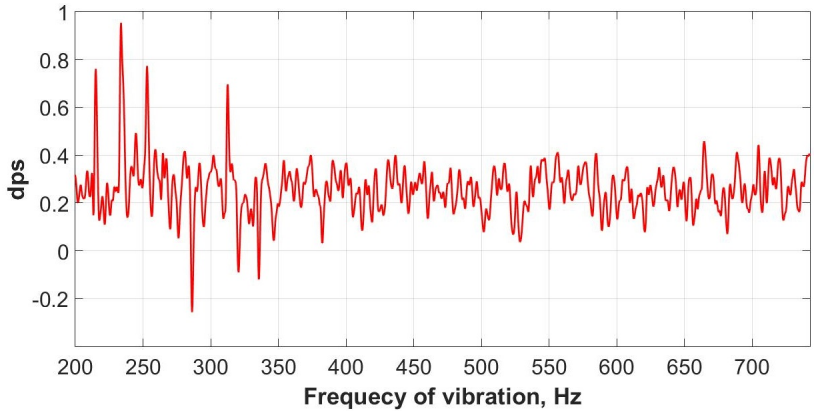

Figure 5.18: Z-channel zero-rate output under 7 g sinusoidal vibration over the 200 Hz to 1 kHz range.

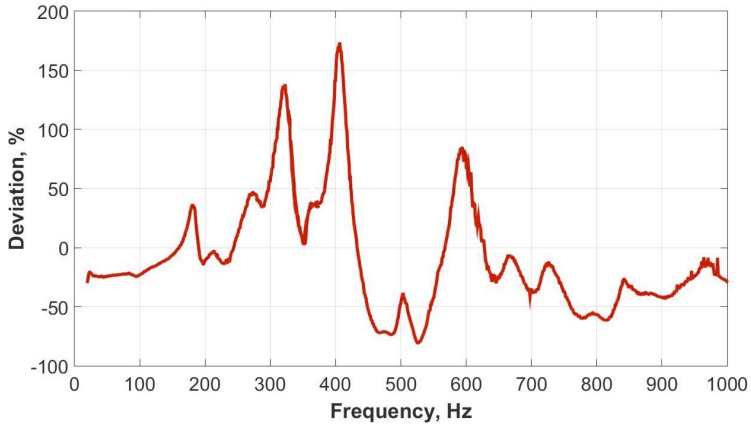

Figure 5.19: Laser Vibrometer tests showed critical vibration frequencies of the mounting at 320 Hz, 406 Hz, and 600 Hz.

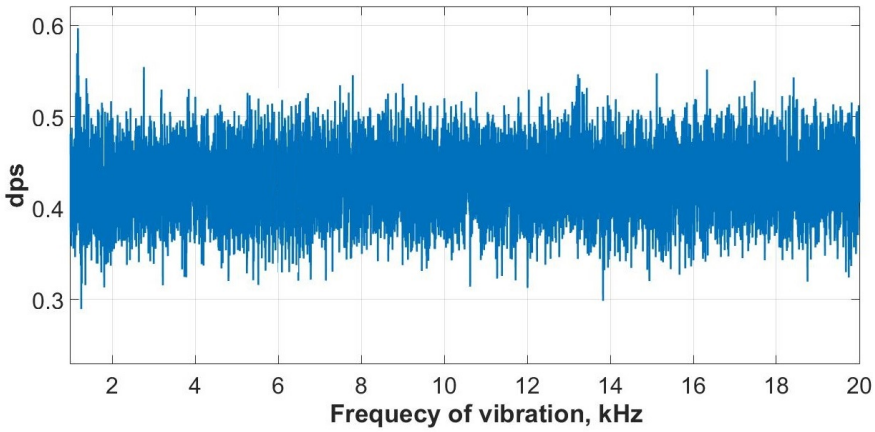

Figure 5.20: Y-channel zero-rate output under 7 g sinusoidal vibration over the 1kHz to 20 kHz range: Vibration Rectification Error (VRE) is < 0.0025 dps/g^2.

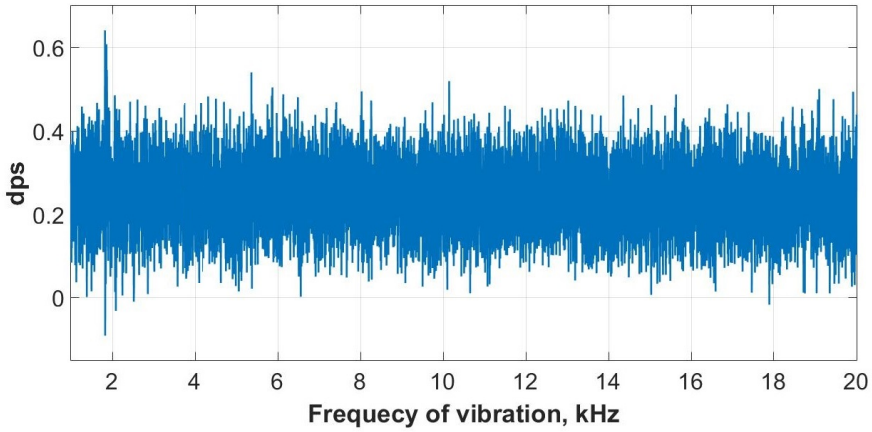

Figure 5.21: Z-channel zero-rate output under 7 g sinusoidal vibration over the 1kHz to 20 kHz range: Vibration Rectification Error (VRE) is < 0.004 dps/g^2.

5.19 showed that maximum deviation peaks occur at 320 Hz, 406 Hz, and 600 Hz vibration frequencies. This experiment shows that the high peaks of the gyroscope bias response in Fig. 5.17 and 5.18 can be attributed to the angular vibration of the mounting.

The gyroscope Y channel bias response to a 7 g (5 g rms) sinusoidal vibration over the 1 kHz to 20 kHz frequency range is shown in Fig. 5.20. Vibration Rectification Error (VRE) of 0.0025 dps/g^2 was measured as the offset shift vs. rms vibration amplitude. The gyroscope Z channel bias response to a 7 g (5 g rms) sinusoidal vibration over the 1 kHz to 20 kHz frequency range is shown in Fig. 5.21. Vibration Rectification Error (VRE) of 0.004 dps/g^2 was measured for this channel.

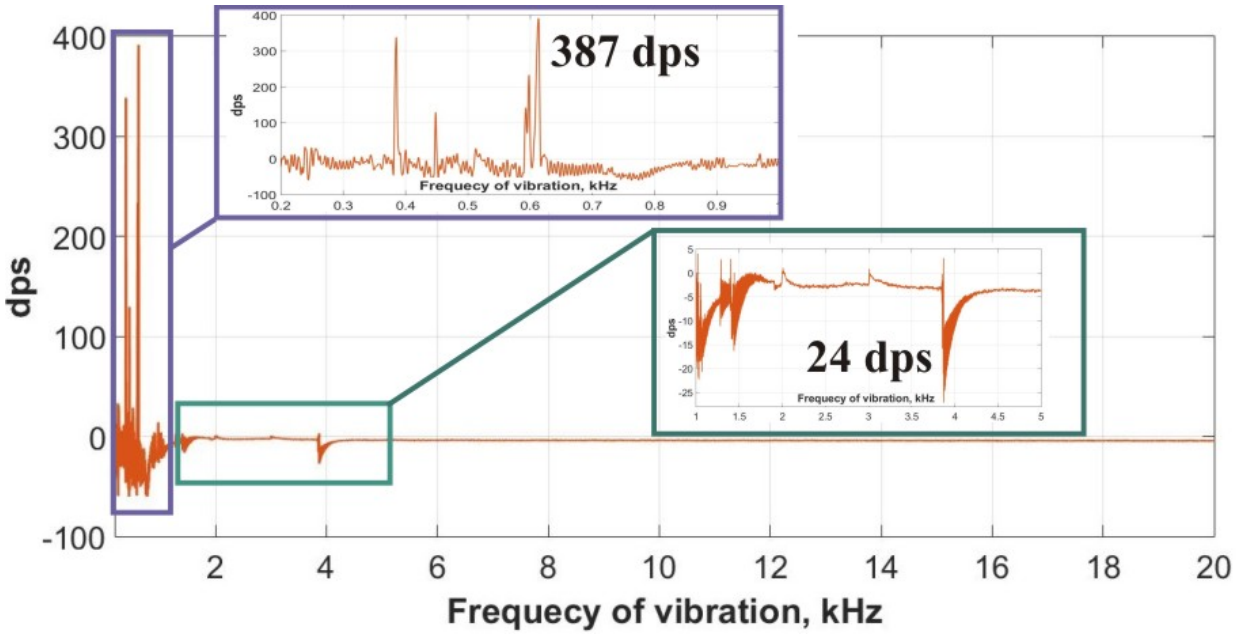

Figure 5.22: Bias response of the sensor under a 1 g sinusoidal vibration.

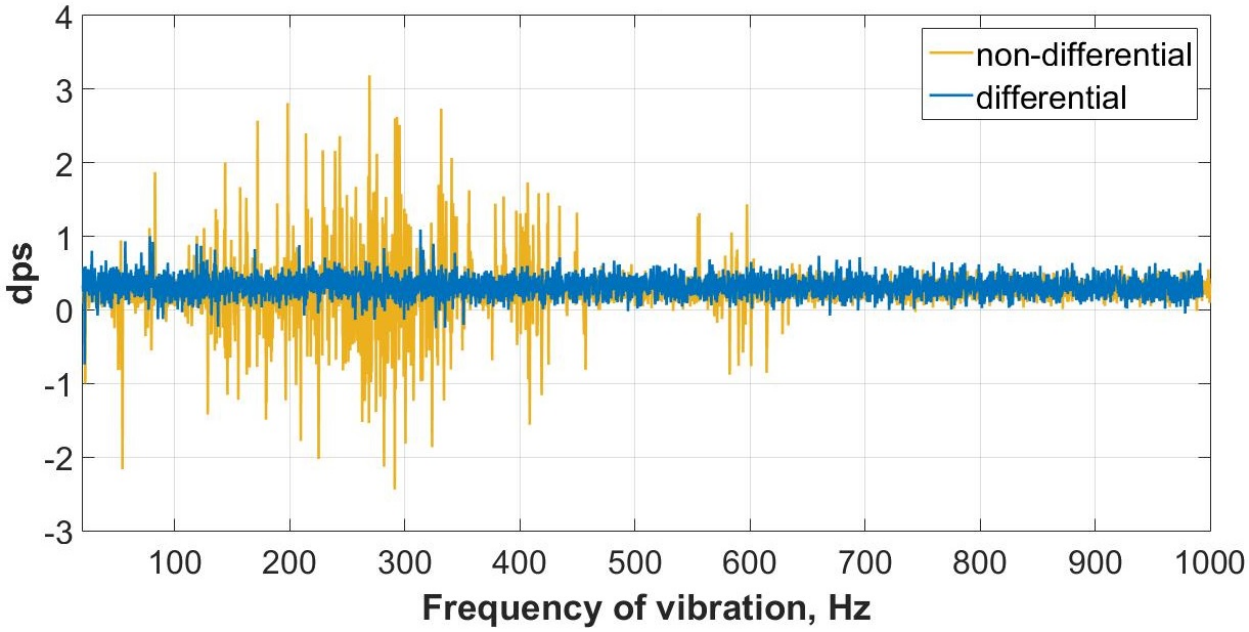

Figure 5.23: Z-channel bias response under 3 g sinusoidal vibration: differential architecture allows for 3.1 times improvement in vibration rejection.

In order to estimate the effect of increased resonant frequency of the gyroscope for improving vibration immunity, an "in-house" low frequency single-mass SOI gyroscope was tested. The operational frequency of the mode-matched sensor is 3.85 kHz. Fig. 5.22 shows the bias

response of the sensor under a 1 g sinusoidal vibration over the range of frequencies from 200 Hz to 20 kHz. As compared to a 60 kHz single-chip Epi-Seal gyroscope, a significantly increased vibration sensitivity (peaks as large as 387 dps) can be observed at vibration frequencies $<$ 1kHz. Significant peaks (up to 24 dps) are observed at vibration frequencies of 3.85 kHz, 1.4 kHz 2 kHz, and 3 kHz, which correspond to the resonant frequencies of the sense mode and "parasitic" in-plane and out-of-plane modes of the mechanical element.

Multi-mass design with differential sensing is another effective way to enhance vibrational immunity, [59], [60], [139]. Similar idea is utilized design of a three-axis gyroscope. In X and Y mode, the pair of proof masses move out-of-plane in anti-phase responding to Coriolis force. Differential architecture enable removing the external g-forces which appear as common-mode signals. In Z mode, the pair of mechanically coupled shuttles move in-plane in anti-phase responding to Coriolis force. Some prototypes of the tree-axis gyroscope were designed with differential architecture of the Z mode sense electrodes to allow for rejection of linear and angular acceleration, while some prototypes were designed with a non-differential Z mode sense electrodes. The results of the vibration testing of these two types of sensors were compared. Fig. 5.23 shows 3.1 times improvement in vibration rejection in case of a device with differential architecture.

5.5 Conclusion

Consumer electronics market has an increasing demand for the multi-axis ultra-compact angular-rate sensors. Motivated by this demand, we investigated a design of a miniature roll-pitch-yaw gyroscope. Thanks to the mechanical design with a decoupled sense modes, our three-axes solution allows for low cross-axis error.

Prototypes of a three-axis gyroscope were fabricated using a wafer-level Epitaxial Silicon

Encapsulation (Epi-Seal) process. The unique feature of the Epi-Seal "Hot Dog" process is that it is optimized for high frequency and small capacitive gaps. Increasing the working frequency of MEMS gyroscopes is an effective method of improving the vibration robustness. The presented vibration testing results showed that a 60 kHz 3-axis gyroscope has 800 times lower vibration sensitivity as compared to a 3.8 kHz device. Meanwhile, the reduction in sensitivity, arising from increasing from high working frequency, is effectively compensated for using small capacitive gaps, enabled by the Epi-Seal process.

Presented single-chip gyroscope is capable of simultaneous measurement of angular rate around three perpendicular axes. It can be used in combination with a three-axis accelerometer to provide a 6-DOF IMU configuration.

Chapter 6

Conclusions

This dissertation investigates two different solutions for a compact IMU: 1) based on an "Origami-like" folded MEMS fabrication process, and 2) utilizing a multi-axis sensing element. We also investigated two discrete inertial sensor design concepts for potential integration with the "Origami MEMS" process: Dual Foucault Pendulum (DFP) Gyroscope and Toroidal Ring Gyroscope (TRG).

6.1 Contributions of the Dissertation

Specific contributions of the dissertation are listed below:

1. **Design of a dual-mass dynamically amplified gyroscope,** where the increase in structural degrees of freedom is used to improve sensitivity, linearity, and to reduce drift. In a dynamically amplified gyroscope, the first, "drive mass", is actively driven to oscillate at a small amplitude of motion, in a linear operation regime. Meanwhile, the mechanically coupled "slave mass" is used for sensing the Coriolis signal. The

amplitude of motion of the "slave mass" is dynamically amplified, resulting in increased scale factor of the gyroscope. This was the first implementation of such concept in the UCI MicroSystems Lab in-house process and the first demonstration of the gyroscope operation.

2. **Developed a method for precision electrostatic frequency tuning of operational modes** in a multi-degree-of-freedom dual-mass MEMS vibratory gyroscope. The tuning procedure is based on estimation of the modes mismatch and coupling between the modes, utilizing the experimental frequency response data. The analytical model is then used to determine the necessary tuning voltages to permit the removal of anisoelasticity and the mismatch of principal axes of stiffness, thus enabling the gyroscope operational modes to be matched. The electrostatic compensation method was verified using experimental frequency tuning of a dual-mass dynamically amplified gyroscope, where the coupling between the drive and sense modes was compensated and the frequency split between the modes was reduced from 26 Hz down to 50 mHz, resulting in 17.5X increase in the scale factor of the gyroscope.

3. **Demonstrated a principle of ordering the fundamental wine-glass modes in a Toroidal Ring Gyroscope (TRG) with suspension formed by a series of concentric rings.** It was demonstrated that anisotropy introduced by interconnecting spokes between multiple rings in concentric ring suspension enables reordering the fundamental wine-glass modes, placing the desired operational mode before any other pair of degenerate modes. Mode ordering phenomenon was verified by experimental characterization of the TRG prototypes, where stiffening the frequencies of the undesired modes is critical for vibration immunity, and potentially for improved performance of miniature devices.

4. **Double-sided "Origami-like" Folded 3D MEMS process for IMU fabrication.** The approach involves folding an array of single-axis sensors into a 3D configuration,

using polymer flexible hinges. In the double-sided process, inertial sensors are created on the device side of the SOI wafer. In parallel, metal interconnects and polymer flexible hinges are formed on the handle side of the wafer. Thru-wafer interconnects provide a path for electrical signals from sensors on the device side of the wafer to electrical components on the handle side of the wafer, enabling IMU integration with signal processing electronics. Folded MEMS technique enables an efficient way to integrate the high-end inertial sensors into a miniature tactical grade IMU and may serve as a technological foundation for other types of devices (microphones, antennas, magnetometers, etc.)

5. **For the first time, the Folded IMU prototype with all sensors operational was demonstrated,** proving feasibility of the Folded MEMS approach for a compact tactical-grade performance unit. Characterization of accelerometers showed VRW of 0.09 $mg/\sqrt{Hz}$ and in-run bias instability of <0.1 mg. Noise analysis of the 2.8 mm Toroidal Ring Gyroscope (TRG) revealed bias stability of <17 deg/h and ARW of 0.78 $deg/\sqrt{h}$; noise analysis of the 3.1 mm Dual Foucault Pendulum (DFP) revealed bias stability of <1.3 deg/h and ARW of 0.11 $deg/\sqrt{h}$.

6. **Experimental characterization of the cross-talk between sensors on the sidewalls of a folded 3D IMU.** The study of cross-talk between the simultaneously operating sensors provided an evidence that the folded IMU process is advantageous to a single-die approach, showing a lower level of interference of two sensors on different sidewalls of the IMU Cube (2 dB versus 11.5 dB) and lower Angle Random Walk (ARW) of the gyroscopes when operated simultaneously on different sidewalls of the IMU Cube (1.18 $deg/\sqrt{h}$ versus 2.16 $deg/\sqrt{h}$).

7. **Approach for co-fabrication of MEMS sensors and high-aspect ratio low-resistance vertical interconnects** in thick (up to 600 μm) SOI wafers. The Thru-Wafer Interconnects Double-Sided (TWIDS) process was developed based on a method

of bottom-up seedless copper electroplating of through-wafer vias, where a highly doped device layer of an SOI wafer is used as a seed. For the first time, seedless copper electroplating was applied for co-fabrication of thick MEMS SOI structures with vertical electrical interconnects.

8. **A method for hermetic and potentially vacuum packaging of 3D MEMS devices and assemblies, utilizing a micro glass-blowing process**. Fabricated on a wafer-level, "bubble-shell" glass lids are utilized for chip-level packaging of MEMS IMUs using a standard LCC package. Demonstrated the hermetic sealing.

9. **Design and implementation of a single-chip 3-axis gyroscope**, a major building block of the ultra-compact 6-axis IMU. Mechanical element with a single driving structure allows for simultaneous measurement of angular rate around three perpendicular axes. Manufactured in wafer-level Epitaxial Silicon Encapsulation (Epi-Seal) process, a single-chip device occupies an area of 1.2 mm^2. Experimental characterization of the sensor showed less than 0.3% cross talk between the axes of sensitivity and improved immunity to external vibrations (vibration sensitivity of <0.03 dps/g and Vibration Rectification Error (VRE) is <0.004 dps/g^2.)

6.2 Future Research Directions

6.2.1 Thermal Compensation Techniques

Temperature sensitivity of the inertial sensors is one of the critical factors limiting the IMU performance. Temperature variations result in temperature-induced long-term bias and scale-factor drifts. Different thermal compensation techniques can be potentially implemented in order to improve the gyroscopes and accelerometers long-term stability. For example, the compensation method utilizing the drive-mode frequency as a built-in ther-

mometer for temperature self-sensing and compensation, [89], or compensation technique utilizing a micro-oven co-fabricated with IMU sensors, [90].

6.2.2 Mechanical trimming methods for permanent tuning of gyroscope operational modes

Electrostatic tuning is an active compensation technique, which is widely used for mode-matching of a MEMS gyroscope. In Chapter 2, such technique was successfully employed for tuning a dual-mass dynamically amplified gyroscope. Electrostatic tuning, however, often requires high voltages for precision mode-matching, which results in a degraded performance due to zero-rate level and the scale factor sensitivity to power supply fluctuations. Fig. 6.1 demonstrates the effect of the electrostatic tuning of two prototypes of a dynamically amplified gyroscope. Noise analysis of the Gyroscope I, which was electrostatically tuned from 16 Hz to 3 Hz, showed a higher in-run bias instability (5.8 deg/h versus 4.5 deg/h) and higher ARW (0.062 $deg/\sqrt{h}$ versus 0.045 $deg/\sqrt{h}$), as compared to the Gyroscope II with untuned as-fabricated frequency split of 5.6 Hz.

In addition, ultra-miniature sensors might not have enough tuning capability to electrostatically compensate for large frequency splits between the modes. For these reasons, in many cases mechanical trimming methods might be preferable. The main advantage of mechanical trimming techniques is a permanent change of the sensor structure, enabling minimization of voltages necessary for subsequent electrostatic tuning. Such permanent modification of the structure might be performed by means of selective adding/removing material to/from the vibrational element using, for example, laser ablation, focused ion beam, and selective deposition.

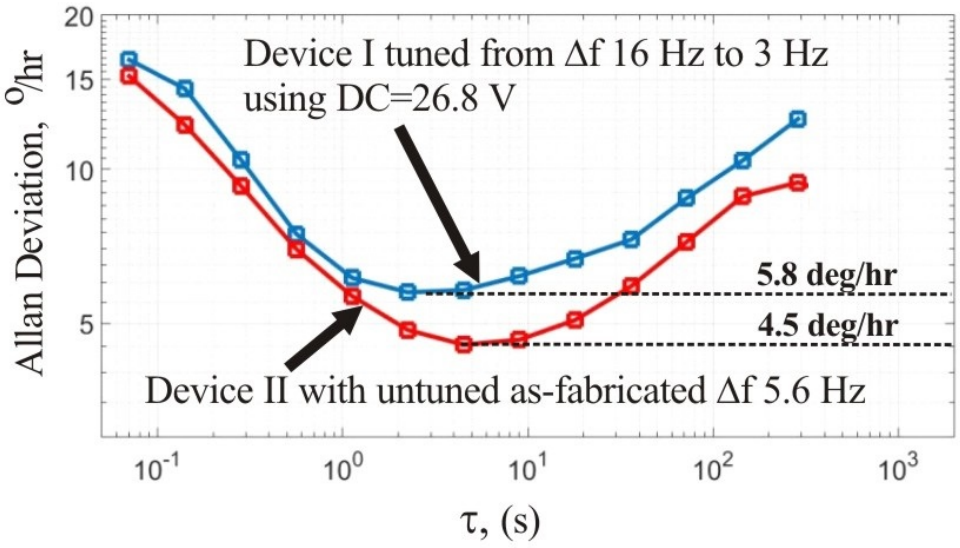

Figure 6.1: Effect of electrostatic tuning: Gyroscope I was electrostatically tuned from 16 Hz to 3 Hz, resulting in increased in-run bias instability from 4.5 to 5.8 Hz and increased ARW from 0.045 $deg/\sqrt{h}$ to 0.062 $deg/\sqrt{h}$, as compared to Gyroscope II with untuned as-fabricated frequency split of 5.6 Hz.

6.2.3 IMU integration with ASIC

Thru-wafer interconnects fabrication is an integral part of the Folded MEMS IMU double-sided process. Vias allow for electrical connection between the front and the back side of the SOI wafer. Once IMU is folded into a 3D configuration, thru-wafer interconnects enable a path for electrical signals from inertial sensors on the front side of the IMU device to the network of metal traces inside of a 3D IMU. This creates an opportunity for efficient utilization of the IMU inner volume by integrating the Application-Specific Integrated Circuits (ASIC) on the inner side of the IMU structure panels.

6.2.4 Vacuum Packaging

A packaging process for hermetic sealing of 3D MEMS IMU devices, utilizing "glass-blown" lids was described in Chapter 4. Sealing process, which has been performed in SST vacuum

packaging tool, did not yield low pressure environment under the "bubble-shell" lid and further development of the packaging recipe for the SST is necessary. In addition, a step of thin-film getter deposition can be introduced into the lids fabrication process, which was investigate in this thesis. Getters are necessary to maintain a high vacuum inside a hermetically sealed cavity and to ensure a successful operation of MEMS gyroscopes and resonant accelerometers for long duration.

6.2.5 Single-Chip IMU

Chapter 5 presented a novel design of an ultra-compact roll-pitch-yaw gyroscope which is designed to measure angular rate around three axes with minimal, less than 0.3% cross talk, and reduced sensitivity to external vibrations over a wide range of frequencies. The presented sensor is a first step towards implementation of a miniature single-chip IMU. To provide information about the acceleration along the X, Y, and Z axes, a three-axis accelerometer might be fabricated on the same chip with the roll-pitch-yaw sensor or placed along side with it.

The "all-in-one" sensor approach, where a single-structure is used for measuring the angular rate and acceleration around three perpendicular axes is also proposed in Chapter 5, Fig. 5.5. A similar structure was only characterized for the rate measurements. For the 3-axis IMU functionality, the acceleration measurements are necessary.

Bibliography

[1] D.M. Rozelle, *The hemispherical resonator gyro: From wineglass to the planets*, Proc. 19th AAS/AIAA Space Flight Mechanics Meeting, 1157-1178, (2009).

[2] Honeywell, *HG9900 IMU*, www.honeywell.com, (2009).

[3] L3 Space & Navigation, *CIRUS-A Strategic Grade Inertial Measurement Unit*, www2.l-3com.com, (2015).

[4] Northrop Grumman, *LN-200C fiber-optic gyro (FOG) inertial measurement unit (IMU)*, www.northropgrumman.com, (2015).

[5] Analog Devices, *ADIS16485 Tactical Grade Six Degrees of Freedom Inertial Sensor*, www.analog.com (2017).

[6] A. D. Challoner, H. H. Ge, and J.Y. Liu, *Boeing Disc Resonator Gyroscope*, Proc. Position Location and Navigation Symposium (PLANS 2014), Monterey, CA, USA, May 5-8, (2014).

[7] Igor P. Prikhodko, Alexander A. Trusov, Andrei M. Shkel, *North-Finding with 0.004 Radian Precision Using a Silicon MEMS Quadruple Mass Gyroscope with Q-Factor of 1 Million*, Pro. IEEE MEMS 2012 Conf., Paris, France, Jan 28-Feb 2, 2012.

[8] Y. Mulgaonkar, A. Makineni, K. Mohta, C. J. Taylor, V. Kumar, *Fast Autonomous flight with micro unmanned vehicles*, Proc. Solid-State Sensors, Actuators and Mi-

crosystems Workshop (Hilton Head'2016), Hilton Head Island, South Carolina, June 5-9, (2016).

[9] Honeywell, *HG1930 IMU*, www.honeywell.com, (2012).

[10] Honeywell, *HG1900 IMU*, www.honeywell.com, (2012).

[11] Honeywell, *HG1120 IMU*, www.honeywell.com, (2017).

[12] Systron Donner, *SDI500 Tactical Grade IMU*, www.systron.com (2014).

[13] Northrop Grumman, *LN-200 Fiber-optic IMU*, www.northropgrumman.com (2013).

[14] Sensonor, *STIM300 IMU*, www.sensonor.com, (2014).

[15] Analog Devices, *ADIS16485 Tactical Grade Six Degrees of Freedom MEMS Inertial Sensor*, www.analog.com (2016).

[16] Analog Devices, *ADIS16334 Low-profile Six Degree of Freedom Inertial Sensor*, www.analog.com (2013).

[17] ST Micro, LSM330 iNEMO Inertial Module, www.st.com (2013).

[18] ST Micro, LSM9DS0 iNEMO Inertial Module, www.st.com (2013).

[19] ST Micro, *LSM6DSM iNEMO Inertial Module*, www.st.com (2016).

[20] ST Micro, *LSM6DS33 iNEMO Inertial Module*, www.st.com (2017).

[21] ST Micro, *LSM330DLC iNEMO Inertial Module*, www.st.com (2017).

[22] ST Micro, *Everything about ST Microelectronics 3-Axis Digital MEMS Gyroscopes*, Technical article, www.st.com (2011).

[23] InvenSense, *ICM-20600 Motion Tracking Device*, www.invensense.com (2016).

[24] InvenSense, *ICM-20601 Motion Tracking Device*, www.invensense.com (2017).

[25] InvenSense, *ITG-1010 High Performance 3-axis Gyro for General Motion-Sensing Applications*, www.invensense.com (2017).

[26] InvenSense, *MPU-6700 MEMS Motion Tracking Device*, www.invensense.com (2014).

[27] Fairchild, *FIS1100 MEMS Inertial Measurement Unit*, www.fairchildsemi.com (2015).

[28] VectorNav, *VN-100 Inertial Measurement Unit*, www.vectornav.com (2014).

[29] MicroStrain, *3DM-GX4 Industrial-Grade Inertial Measurement Unit*, www.microstrain.com (2016).

[30] MicroStrain, *3DM-GX3 Industrial-Grade Inertial Measurement Unit*, www.microstrain.com (2016).

[31] Bosch, *Digital Triaxial Acceleration Sensor*, www.bosch-sensortec.com (2014).

[32] Bosch, *BMI055 6-Axis Inertial Sensor*, www.bosch-sensortec.com (2014).

[33] Bosch, *BMI160 Inertial Measurement Unit*, www.bosch-sensortec.com (2015).

[34] Z. Cao, Y. Yuan, G. He, R.L. Peterson, and K. Najafi, *Fabrication of Multi-Layer Vertically Stacked Fused Silica Microsystems*, Proc. 17th Int. Solid-State Sensors, Actuators and Microsystems Conf. (Transducers'13), Barcelona, SPAIN, June 16-20, (2013).

[35] F. Ayazi, *Multi-DOF inertial MEMS: From gaming to dead reckoning*, Proc. 16th Int. Solid-State Sensors, Actuators and Microsystems Conf. (Transducers'11), Beijing, China, June 5-9, (2011).

[36] H. Wen, A. Daruwalla, and F. Ayazi, *Resonant Pitch and Roll Silicon Gyroscopes with Sub-micron-gap Slanted Electrodes: Breaking the Barrier Toward High-*

performance Monolithic Inertial Measurement Units, Microsystems and Nanoengineering, Vol. 3, (2017).

[37] W. Zhu, C. Wallace, and N. Yazdi, *A tri-fold inertial measurement unit fabricated with a batch 3-D assembly process*, Proc. IEEE Inertial Sensors Conf. 2016 (Inertial'16), Laguna Beach, CA, USA, February 22-25, (2016).

[38] S. Dellea, F. Giacci, A. Longoni, P. Rey, A. Berthelot, and G.Langfelder, *Large full scale, linearity and cross-axis rejection in low-power 3-axis gyroscopes based on nanoscale piezoresistors*, Proc. IEEE MEMS 2015 Conf., Estoril, Portugal, 18 - 22 January, (2015).

[39] D. Senkal, S. Askari, M. J. Ahamed, E. Ng, V. Hong, Y. Yang, C. Hyuck Ahn, T. W. Kenny, A. M. Shkel, *100k Q-Factor Toroidal Ring Gyroscope Implemented in Wafer-level Epitaxial Silicon Encapsulation Process*, Proc. IEEE MEMS 2014 Conf., San Francisco, CA, USA, January 26-30, (2014).

[40] A. Efimovskaya, D. Senkal, A. M. Shkel, *Miniature origami-like folded MEMS TIMU*, Proc. 18th Int. Solid-State Sensors, Actuators and Microsystems Conf. (Transducers'15), Alaska, USA, June 21-25, (2015).

[41] K. Suzuki, I. Shimoyama, and H. Miura, *Insect-Model Based Microrobot with Elastic Hinges*, IEEE Journal of Microelectromechanical Systems, Vol. 3, No. 1, March (1994).

[42] M. Gel and I. Shimoyama, *Parallel-plate electrostatic actuation withvertical hinges*, IOP Journal of Micromechanics and Microengineering, Vol. 11, pp. 555-560, (2001).

[43] J. M. Zara, S. Yazdanfar, K. D. Rao, J. A. Izatt, and S. W. Smith, *Electrostatic micromachine scanning mirror for optical coherence tomography*, Optics Letters, Vol. 28, No. 8, April 15, (2003).

[44] M. Ataka and H. Fujita, *Micro Actuator Array on a Flexible Sheet-Smart MEMS Sheet*, Proc. IEEE MEMS 2013 Conf., Taipei, Taiwan, January 20 24, (2013).

[45] F. Herrault, S. Yorish, T. Crittenden, and M.G. Allen, *Microfabricated, Ultra-Dense, Three-Dimentional Metal Coils*, Proc. 15th Int. Solid-State Sensors, Actuators and Microsystems Conf. (Transducers'09), Denver, CO, USA, June 21-25, (2009).

[46] Y. Zheng, X. Sun, X. Li, and H. Zhang, *Flexible Parylene-Based Folded Inductors with Magnetic Core*, Proc. 17th Int. Solid-State Sensors, Actuators and Microsystems Conf. (Transducers'13), Barcelona, Spain, June 16-20, (2013).

[47] Z. Ding, P. Wei, and B. Ziaie, *Self-Folding Smart 3D Microstructures Using a Hydrogel-Parylene Bilayer*, Proc. 18th Biennial University/Government/Industry Micro/Nano Symposium (UGIM'10), West Lafayette, IN, USA, June 28-July 1, (2010).

[48] C. Chen, S. Chuang, H. Su, W. Hsu, T. Yew, Y.Chang, S. Yehcd, and D. Yao, *A Three-Dimensional Flexible Microprobe Array for Neural Recording Assembled through Electrostatic Actuation*, RSC Journal Lab Chip, Vol. 11, pp. 16471655, (2011).

[49] J. Kuo, B. Kim, S. Hara, C. Lee, L. Yu, C. Gutierrez, T. Hoang, V. Pikov, and E. Meng, *3D Parylene Sheath Probes for Reliable, Long-Term Neuroprosthetic Recordings*, Proc. IEEE MEMS 2013 Conf., Taipei, Taiwan, January 20 24, (2013).

[50] Y.Liu, J. Park, R. Lang, A. Emami-Neyestanak, S. Pellegrino, M. Humayun, and Y.Tai, *Parylene Origami Structure for Intraocular Implantation*, Proc. 17th Int. Solid-State Sensors, Actuators and Microsystems Conf. (Transducers'13), Barcelona, Spain, June 16-20, (2013).

[51] A. Trusov, M. Rivers,S. Zotov, A. Shkel, *Three dimensional folded MEMS technology for multi-axis sensor systems*, US Patent 8368154 B2.

[52] S. A. Zotov, M. C. Rivers, A. A. Trusov, A. M. Shkel *Folded MEMS Pyramid Inertial Measurement Unit*, IEEE Sensors Journal, Vol. 11, No. 11, pp. 2780-2789, (2011).

[53] A. Efimovskaya, Y. Lin, and A. M. Shkel, *Origami-Like 3-D Folded MEMS Approach for Miniature Inertial Measurement Unit*, IEEE/ASME Journal Microelectromech. Syst., Vol. 26, No. 5, pp. 1030-1039, (2017).

[54] A. Efimovskaya, D. Senkal, S. Askari, A. M. Shkel, *Origami-like folded MEMS for realization of TIMU: fabrication technology and initial demonstration*, Proc. IEEE Inertial Sensors Conf. 2015 (Inertial'15), Hawaii, USA, March 23-26, (2015).

[55] M. Rivers *Folded MEMS 3-D Structures for Inertial Measurement Applications*, Ph.D. Thesis, UC Irvine, (2015).

[56] A. Efimovskaya, Y. Lin, and A. M. Shkel, *Thru-Wafer Interconnects for Double-Sided (TWIDS) Fabrication of MEMS*, Proc. IEEE Inertial Sensors Conf. 2016 (Inertial'16), Laguna Beach, CA, USA, February 22-25, (2016).

[57] Z. Cao, Y. Yuan, G. He, R.L. Peterson, and K. Najafi, *Fabrication of multi-layer vertically stacked fused silica microsystems*, Proc. 17th Int. Solid-State Sensors, Actuators and Microsystems Conf. (Transducers'13), Barcelona, Spain, June 16-20, (2013).

[58] D. Senkal, A. Efimovskaya, A. M. Shkel, *Dual Foucault Pendulum gyroscope*, IEEE International Conf. on Solid-State Sensors, Actuators and Microsystems (Transducers'2015), Alaska, USA, June 21-25, (2015).

[59] J. Bernstein, S. Cho, A.T. King, A. Kourepenis, P. Maciel, M. Weinberg, *A micromachined comb-drive tuning fork rate gyroscope*, Proc. IEEE International Conf. on Micro Electro Mechanical Systems (MEMS'1993), Fort Lauderdale, FL, USA, USA, Feb 10-10, (1993).

[60] A. Trusov, A. Schofield, A. M. Shkel, *Micromachined rate gyroscope architecture with ultra-high quality factor and improved mode ordering*, Journal Sensors and Actuators A: Physical, Vol. 165, Issue 1, pp. 26-34, (2011).

[61] C. Acar and A. M. Shkel, *Inherently Robust Micromachined Gyroscopes with 2-DOF Sense-Mode Oscillator*, IEEE Journal of Microelectromechanical Systems, Vol. 15, No. 2, pp. 380-387, (2006).

[62] C. Painter, A. M Shkel, *Dynamically Amplified Rate Integrating Gyroscopes*, U.S. Patent 6,928,874, (2005).

[63] C. Painter, A. M Shkel, *Dynamically Amplified Rate Integrating Gyroscopes*, Proc. NSTI Nanotechnology Conference and Trade Show Nanotech 2003, San Francisco CA, USA, February 23-27, (2003).

[64] B. Gallacher, J. Hedley, J. S. Burdess, A. J. Harris, and M. E. McNie, *Multi-modal tuning of a vibrating ring using laser ablation*, SAGE Mechanical Engineering Science Journal, Institution of Mechanical Engineers, Vol. 217, 2003, pp. 1503-1513, (2003).

[65] K. Zhao, L. Feng, Q. Wang, M. Liu, B. Wang, F. Cui, and Y. Sun, *Suppressing the mechanical quadrature error of a quartz double-H gyroscope through laser trimming*, IOP Chinese Physics Journal, Vol. 22, No. 11, (2013).

[66] T. Lam and R. Darling, *Modeling of focused ion beam trimming of cantilever beams*, Proc. 3rd Int. Conf. Modelling and Simulation of Microsystems, San Diego, CA, USA, March 27-29, (2000).

[67] D. Joachim and L. Lin, *Selective polysilicon deposition for frequency tuning of MEMS resonators*, Proc. IEEE International Conf. on Micro Electro Mechanical Systems (MEMS'2002), Las Vegas, NV, USA, 24-24 Jan. 2002, pp 727730, (2002).

[68] David M. Schwartz, Dennis Kim, Philip Stupar, Jeffrey DeNatale, and Robert T. MCloskey, *Modal Parameter Tuning of an Axisymmetric Resonator via Mass Perturbation*, IEEE Journal of Microelectromechanical Systems, Vol. 24, No. 3, pp. 545-555, (2015).

[69] T. Remtema and L. Lin, *Active Frequency Tuning for Microresonators by Localized Thermal Stressing Effects*, Solid-State Sensor Actuator Workshop, Hilton Head Island, SC, 4-8 June, pp. 363-366, (2000).

[70] E. Tatar, S.Alper, and T. Akin, *Quadrature-Error Compensation and Corresponding Effects on the Performance of Fully Decoupled MEMS Gyroscopes*, IEEE Journal of Microelectromechanical Systems, Vol. 21, No. 3, pp. 656-667, (2012).

[71] Z. Hu, B. Gallacher, J. Burdess, C. Fell, and K. Townsend, *Precision mode matching of MEMS gyroscope by feedback control*, Proc. IEEE Sensors'2011 Conf., Limerick, Ireland, 28-31 Oct., (2011).

[72] J. Jeltema and G. Cevat, *Adaptive resonance tuning through feedback*, American Control Conf., Portland, OR, USA, 810 June, (2005).

[73] C. Painter, and A. M. Shkel, *Active Structural Error Suppression in MEMS Vibratory Rate Integrating Gyroscopes*, IEEE Sensors Journal, Vol. 3, No. 5, October, 2003, pp. 595-606, (2003).

[74] Z.X. Hu, B. J. Gallacher, J.S. Burdess, S.R. Bowles and H.T.D. Grigg, *A Systematic Approach for Precision Electrostatic Mode Tuning of a MEMS Gyroscope*, IOP Journal of Micromechanics and Microengineering, Vol. 24, No. 12, (2014).

[75] T. Juneau, A. Pisam, J. Smith, *Dual Axis Operation of a Micromachined Rate Gyroscope* Proc. Int. Solid-State Sensors, Actuators and Microsystems Conf. (Transducers'97), Chicago, IL, USA, 19-19 June, (1997)

[76] S. Adamsy, F. Bertsch, K. Shaw, P. Hartwell, F. Moon, and N. MacDonald, *Capacitance based tunable resonators*, IOP Journal of Micromechanics and Microengineering, Vol. 8, pp. 1523 (1998).

[77] F. Ayazi and K. Najafi, *A HARPSS polysilicon vibrating ring gyroscope*, IEEE Journal of Microelectromechanical Systems, Vol. 10, No. 2, pp. 169-179, (2001).

[78] N. Chekurov, L. Aaltonen, J. Gronicz, M. Kosunen, I. Tittonen, *Design and fabrication of a tuning fork shaped voltage controlled resonator with additional tuning electrodes for low-voltage applications*, Proc. Eurosensors XXIV, September 5-8, 2010, Linz, Austria, (2010).

[79] I. Prikhodko, A. Trusov, A. M. Shkel, *Compensation of drifts in high-Q MEMS gyroscopes using temperature self-sensing*, Journal Sensors and Actuators A: Physical, Vol. 201, 15 Oct. 2013, pp. 517-524, (2013).

[80] D. Senkal, S. Askari, M. J. Ahamed, E. Ng, V. Hong, Y. Yang, C. Hyuck Ahn, T. W. Kenny, A. M. Shkel, *100k Q-Factor Toroidal Ring Gyroscope Implemented in Wafer-level Epitaxial Silicon Encapsulation Process*, Proc. IEEE International Conf. on Micro Electro Mechanical Systems (MEMS'2014), San Francisco, CA, USA, January 26-30, (2014).

[81] J. Cho, J. Gregory, and K. Najafi, *High-Q, 3 kHz single-crystalsilicon cylindrical rate-integrating gyro (CING)*, Proc. IEEE International Conf. on Micro Electro Mechanical Systems (MEMS'2012), Paris, France, 29 Jan. - 2 Feb., pp. 172-175, (2012).

[82] J. Cho, J. Woo, J. Yan, R. Peterson, and K. Najafi, *Fused-silica micro birdbath resonator gyroscope (μ-BRG)*, IEEE Journal of Microelectromechanical Systems, Vol. 23, No. 1, Feb. 2014, pp. 66-77, (2014).

[83] P. Shao, C. L. Mayberry, X. Gao, V. Tavassoli, and F. Ayazi, *A polysilicon micro-*

hemispherical resonating gyroscope, IEEE Journal of Microelectromechanical Systems, Vol. 23, No. 4, pp. 762-764, (2014).

[84] P. Taheri-Tehrani et al., *Micro-scale diamond hemispherical resonator gyroscope*, in Proc. IEEE Solid-State Sens., Actuators, Microsyst. Workshop, Hilton Head Island, SC, USA, Jun. 2014, pp. 289292, (2014).

[85] D. Senkal, M. J. Ahamed, A. A. Trusov, and A. M. Shkel, *Achieving sub-Hz frequency symmetry in micro-glassblown wineglass resonators*, IEEE Journal of Microelectromechanical Systems, Vol. 23, No. 1, Feb. 2014, pp. 3038, (2014).

[86] C. Painter and A. Shkel, *Identification of anisoelasticity for electrostatic trimming of rate integrating gyroscopes*, Proc. 2002 SPIE Annual International Symposium on Smart Structures and Materials, San Diego, CA, March 17, (2002).

[87] A.S. Phani, and A. A. Seshia, *Identification of Anisoelasticity and Nonproportional Damping in MEMS Gyroscopes*, Proc. NSTI Nanotechnology Conference and Trade Show Nanotech 2004, Boston, Massachusetts, USA, March 7-11, (2004).

[88] D. D. Lynch, *Vibratory gyro analysis by the method of averaging*, Proc. 2nd St. Petersburg Conf. on Gyroscopic Technology and Navigation, St. Petersburg, Russia, vol. 1, pp. 2634, (1995).

[89] SPTS Technologies, *SPTS APS PM*, www.spts.com, (2017).

[90] SPTS Technologies, *STS System DRIE*, www.spts.com, (2017).

[91] I. Prikhodko, S. Zotov, A. Trusov, A. M. Shkel, *What is MEMS Gyrocompassing? Comparative Analysis of Maytagging and Carouseling*, IEEE Journal of Microelectromechanical Systems, Vol. 22, No. 6, pp. 1257-1266, (2013).

[92] A. M. Shkel, C. Acar, and C. Painter, *Two Types of Micromachined Vibratory Gyroscopes*, Proc. IEEE Sensors Conf., Irvine, CA, USA, 31 Oct-3 Nov, pp. 531-536, (2005).

[93] A. Trusov, et al., *Force Rebalance, Whole Angle, and Self-Calibration Mechanization of Silicon MEMS Quad Mass Gyro*, Proc. IEEE Inertial Sensors Conf. 2014 (Inertial'14), Laguna Beach, CA, USA, February 25-26, (2014).

[94] R. N. Candler, M. A. Hopcroft, B. Kim, W-T. Park, R. Melamud, M. Agarwal, G. Yama, A. Partridge, M. Lutz, T. W. Kenny, , *Long-Term and Accelerated Life Testing of a Novel Single-Wafer Vacuum Encapsulation for MEMS Resonators*, IEEE Journal of Microelectromechanical Systems, Vol. 15, No. 6, pp. 1446-1456, (2006).

[95] R.L. Kubena, et al., *Disc Resonator Gyroscopes*, US Patent 7,581,443, (2009).

[96] S. Nitzan, et al., *Epitaxially-encapsulated polysilicon disk resonator gyroscope*, Proc. IEEE International Conf. on Micro Electro Mechanical Systems (MEMS'2013), pp. 625-628, (2013).

[97] B.J. Gallacher, J. Hedley, J.S. Burdess, A.J. Harris, A. Rickard, and D.O. King, *Electrostatic Correction of Structural Imperfections Present in a Microring Gyroscope*, IEEE Journal of Microelectromechanical Systems, Vol. 14, No. 2, pp. 221-234, (2005).

[98] D. D. Lynch, *Coriolis Vibratory Gyros*, Proc. Symposium Gyro Technology, Stuttgart, Germany, (1998).

[99] A. Efimovskaya, D. Wang, Y. Lin, and A. M. Shkel, *On Ordering of Fundamental Wineglass Modes in Toroidal Ring Gyroscope*, Proc. IEEE Sensors 2016, Orlando, FL, USA, Oct 30-Nov 2, (2016).

[100] B. Simon, S. Khan, A. Trusov, A. M. Shkel, *Mode ordering in tuning fork structures with negative structural coupling for mitigation of common-mode g-sensitivity*, Proc. IEEE Sensors, Busan, South Korea, 1-4 Nov, (2015).

[101] E. Yilmaz, et al., *Effects of Imperfections on Solid-Wave Gyroscope Dynamics*, Proc. IEEE Sensors Conf., Baltimore, USA, Nov. 3-6, (2013).

[102] C. O. Chang, et al., *In-plane free vibration of a single-crystal silicon ring*, Journal of Solids and Structures, Vol. 45, pp. 6114-6132, (2008).

[103] T. Bauer, *High Density Through Wafer Via Technology*, NSTINanotech, Vol. 3, pp. 116119, (2007).

[104] T. Bauer, *Vias and method of making*, US Patent 2010/0052107 A1, (2010).

[105] Y. Huang, *Through-Wafer Interconnection*, US Patent 8,105,941 B2, (2012).

[106] R. M. Haque and Kensall D. Wise, *A Glass-in-Silicon Reflow Process for Three-Dimensional Microsystems*, IEEE Journal of Microelectromechanical Systems, Vol. 22, No. 6, December 2013, pp.1470-1477, (2013).

[107] E. M. Chow, V. Chandrasekaran, A. Partridge, T. Nishida, M. Sheplak, C. F. Quate, and T. W. Kenny, , *Process compatible polysilicon-based electrical through-wafer interconnects in silicon substrates*, IEEE Journal of Microelectromechanical Systems, Vol. 11, No. 6, pp. 631-640, (2002).

[108] S. A. Esfahany, Y. Loke, , *Semi-Conductor Sensor Fabrication*, Patent US 8445304 B2, (2013).

[109] F. Laermer, A. Schilp, *Method of Anisotropically Etching Silicon*, Patent No. DE 4241045 (Patent US 5501893), (1994).

[110] Y. Suzuki, H. Hirano, Y. Nonomura, H. Funabashi and S. Tanaka, *1300 μm Deep Though Silicon Via in Laser-Ablated CMOS Multi-Project Wafer for Cost-Effective*

Development of Integrated MEMS, Proc. IEEE MEMS 2017 Conf., Las Vegas, NV, USA, January 22-26, (2017).

[111] S. Dhong, K. Nowka, M. Shapiro, *Method for integrated circuit power and electrical connections via through-wafer interconnects*, Patent US 6221769 B1, (2001).

[112] H. T. Soh, C. P. Yue, A. McCarthy, C. Ryu, T. H. Lee, S. S. Wong, and C. F. Quate, *Ultra-Low Resistance, Through-Wafer Via (TWV) Technology and Its Applications in Three Dimensional Structures on Silicon*, IOP Japanese Journal of Applied Physics, vol. 38, no. Part 1, No. 4B, pp. 23932396, (1999).

[113] S. Akram et al., *Through-wafer interconnects for photoimager and memory wafers*, Patent US 2008/0111213 A1, (2008).

[114] M. E. Tuttle, *Methods for forming through-wafer interconnects and structures resulting therefrom*, Patent US 7517798 B2, (2007).

[115] N. T. Nguyen, E. Boellaard, N. P. Pham, V. G. Kutchoukov, G. Craciun, and P. M. Sarro, *Through-wafer copper electroplating for three-dimensional interconnects*, IOP Journal of Micromechanics and Microengineering, vol. 12, no. 4, pp. 395-399, (2002).

[116] C. S. Premachandran, R. Nagarajan, C. Yu, Z. Xiolin, and C. Choong, *A novel electrically conductive wafer through hole filled vias interconnect for 3D MEMS packaging*, Proc. of IEEE 53rd Electron. Components Technology Conf. 2003, No I, pp. 627630, (2003).

[117] V. Lindroos, M. Tilli, *Handbook of Silicon Based MEMS Materials and Technologies*, Published by Elsevier Inc., (2010).

[118] P. Dixit and J.Miao, *Aspect-Ratio-Dependent Copper Electrodeposition Technique for Very High Aspect-Ratio Through-Hole Plating*, ECS Journal of The Electrochemical Society, 153 Vol. 153, No. 6, (2006), pp. G552-559.

[119] M. Wolf, T. Dretschkow, B. Wunderle, N. Jurgensen, G. Engelmann, O. Ehrmann, A. Uhlig, B. Michel, H. Reichl, *High aspect ratio TSV copper filling with different seed layers*, Proc. 58th IEEE Electronic Components and Technology Conference, May 27-30, Lake Buena Vista, FL, USA, (2008), pp. 56370.

[120] R. Abbaspour, D. K. Brown, and M. S. Bakir, *Fabrication and electrical characterization of sub-micron diameter through-silicon via for heterogeneous three-dimensional integrated circuits*, IOP Journal of Micromechanics and Microengineering, Vol. 27, No. 2. (2017).

[121] I. Abhulimen, T. Lam, A. Kamto, S. Burkett, L. Schaper, and L. Cai, *Effect of via profile on copper seed layer deposition for electroplating*, Proc. 2007 IEEE Region 5 Technical Conference, April 20-21, Fayetteville, AR USA, (2007).

[122] P. Dixit, J.Miao, and R. Preisser, *Fabrication of High Aspect-Ratio 35 μm Pitch Through-Wafer Copper Interconnects by Electroplating for - Wafer Stacking*, Electrochemical and Solid-State Letters, Vol. 9, No.10, pp.305-308, (2006).

[123] B. Kim, C. Sharbono, T. Ritzdorf, and D. Schmauch, *Factors Affecting Copper Filling Process Within High Aspect Ratio Deep Vias for 3D Chip Stacking*, Proc. 2006 IEEE Electronic Components and Technology Conference, San Diego, CA, USA, May 30 - June 02, (2006), pp. 838-843.

[124] L. D. Vargas Llona, H V Jansen and M C Elwenspoek, *Seedless electroplating on patterned silicon*, IOP Journal of Micromechanics and Microengineering, Vol. 16, pp. s1-s6, (2006).

[125] T. Fujita, S. Nakamichi, S. Ioku, K. Maenaka, and Y. Takayama, *Selective and Direct Gold Electroplating on Silicon Surface for MEMS Applications,* Proc. IEEE MEMS 2006 Conf., Istanbul, Turkey, January 22-26, pp. 290-293, (2006).

[126] J. Lee, S. Lee, S. Lee and J. Park, *Through-glass copper via using the glass reflow and seedless electroplating processes for wafer-level RF MEMS packaging,* IOP Journal of Micromechanics and Microengineering, Vol. 23, pp. 1-10, (2013).

[127] A. Efimovskaya and A. Shkel, *Thru-Wafer Interconnects for MEMS Double-Sided Fabrication Process (TWIDS)*, Patent US 9611138 B2, (2017).

[128] A. Efimovskaya, A. M. Shkel, *160 Milli-Ohm Electrical Resistance Thru-Wafer Interconnects with 10:1 Aspect Ratio*, IMAPS 2014 Conf., October 13-16, San Diego,CA, (2014).

[129] T. Moffat and D. Josell, *Superconformal Electrodeposition for 3D Interconnects*, Israel Journal of Chemistry 2010, Vol. 50, pp. 312-320, (2010).

[130] D. Senkal, E. Ng, V. Hong, Y.Yang, C. H. Ahn, T. W. Kenny, A. M. Shkel, *Parametric Drive of a Toroidal MEMS Rate Integrating Gyroscope Demonstrating < 20 ppm Scale Factor Stability*, Proc. IEEE MEMS 2015 Conf., Estoril, Portugal, January 18-22, (2015).

[131] J. Tian, S. Sosin, J. Iannacci , R. Gaddi, M. Bartek,*RF-MEMS wafer-level packaging using through-wafer interconnect*, Journal Sensors and Actuators A: Physical, Vol. 142, pp. 442-451, (2008).

[132] C. Acar, *Robust Micromachined Vibratory Gyroscopes*, PhD thesis, University of California at Irvine, (2004).

[133] C. Nguyen, *Micromechanical Signal Processors*, PhD thesis, University of California at Berkeley, (1994).

[134] A. Polyakov, M. Bartek, and J. Burghartz, *Mechanical Reliability of Silicon Wafers with Through-Wafer Vias for Wafer-Level Packaging*, Elsevier Journal of Microelectronics Reliability, Vol. 42, pp. 1783-1788, (2002).

[135] A. Efimovskaya, Y. Lin, and A. M. Shkel, *Double-Sided Process for MEMS SOI Sensors Co-fabricated with Deep Vertical Thru-Wafer Interconnects*, submitted for publication at IEEE Journal of Microelectromechanical Systems, (2017).

[136] C. Bo, J. Yan-Hui, L. Gong-Ping, and C. Xi-Meng, *Atomic diffusion in annealed Cu/SiO2/Si (100) system prepared by magnetron sputtering* Journal Chinese Physics: B, Vol. 19, No. 2, pp. 66011-66014 (2010).

[137] K. J. Owen, B. VanDerElzen, R. L. Peterson, K. Najafi, *High Aspect Ratio Deep Silicon Etching*, Proc. IEEE MEMS 2012 Conf., Paris, France, January 29-February 02, (2012).

[138] A. Efimovskaya, D. Wang, Y. Lin, and A. M. Shkel, *On Ordering of Fundamental Wineglass Modes in Toroidal Ring Gyroscope*, Proc. IEEE Sensors Conf., Orlando, FL, USA, October 30-November 2, (2016).

[139] D. Senkal, A. Efimovskaya, A. M. Shkel, *Dual foucault pendulum gyroscope*, Proc. 18th Int. Solid-State Sensors, Actuators and Microsystems Conf. (Transducers'15), Alaska, USA, June 21-25, (2015).

[140] M. S. Weinberg, *Error Sources in In-Plane Silicon Tuning-Fork MEMS Gyroscopes*, IEEE Journal Microelectromechanical Systems, Vol. 15, No. 3, pp. 479-491, (2006).

[141] I. Prikhodko, S. Zotov, A. Trusov, A. M. Shkel, *What is MEMS Gyrocompassing? Comparative Analysis of Maytagging and Carouseling*, IEEE Journal Microelectromechanical Systems, Vol. 22, no. 6, pp. 1257-1266, (2013).

[142] I P. Prikhodko, Alexander A. Trusov, Andrei M. Shkel, *Achieving Long-Term Bias Stability in High-Q Inertial MEMS by Temperature Self-Sensing with a 0.5 Millicelcius Precision*, Solid-State Sensors, Actuators, and Microsystems Workshop 2012, Hilton Head Island, South Carolina, USA, June 3-7, (2012).

[143] C.H. Ahn, V.A. Hong, W. Park, Y. Yang, Y. Chen, E.J. Ng, J. Huynh, A.D. Challoner, K.E. Goodson, and T.W. Kenny, *On-chip ovenization of encapsulated Disk Resonator Gyroscope (DRG)*, Proc. 18th Int. Solid-State Sensors, Actuators and Microsystems Conf. (Transducers'15), Alaska, USA, June 21-25, (2015).

[144] G. H. Golub, C. F. Van Loanel, *Matrix Computations, 4th ed.*, Johns Hopkins Studies in the Mathematical Sciences, Johns Hopkins University Press, (2013).

[145] M. G. da Silva, *Standard Open Tool Packages for MEMS Enabled Products*, Advanced Packaging Journal, Vol. 13, No. 9, pp. 2629., (2004).

[146] B. H. Stark and K. Najafi, *A Low-Temperature Thin-Film Electroplated Metal Vacuum Package*, IEEE Journal of Microelectromechanical Systems, Vol. 13, No 2, (2004)

[147] F. Santagata et al., *Mechanical Design and Characterization for MEMS Thin-Film Packaging*,IEEE Journal of Microelectromechanical Systems, Vol. 21, No. 1, (2012).

[148] P. H. LaFond, L. Yu, *Wafer Level Packaged MEMS Device*, US Patent 8,685,776 B2 (2014).

[149] S. Nasiri, A. Flannery, *Vertically Integrated MEMS Structure with Electronics in a Hermetically Sealed Cavity*, US Patent US 2005/0166677 A1 (2005).

[150] Yu-T. Cheng, Wan-Tai Hsu, Khalil Najafi, Clark T.-C. Nguyen, and Liwei Lin, *Vacuum Packaging Technology Using Localized Aluminum/ Silicon-to-Glass Bonding*, IEEE Journal of Microelectromechanical Systems, vol. 11, No. 5, (2012).

[151] J.Chae, J. M. Giachino, and K. Najafi, *Fabrication and Characterization of a Wafer-Level MEMS Vacuum Package With Vertical Feedthroughs*, IEEE Journal of Microelectromechanical Systems, vol. 17, No 1, (2008).

[152] R. Noor, V. Gundeti, and A. M. Shkel, *A Status on Components Development for Folded Micro NMR Gyro*, IEEE Inertial Sensors 2017 Conf. (Inertial'2017), Kauai, HI, USA, March 27-30, (2017).

[153] E. Jesper Eklund and Andrei M. Shkel, *Glass Blowing on a Wafer Level*, IEEE Journal of Microelectromechanical Systems, Vol. 16, No. 2, pp. 232-239, 2007.

[154] Finne, R. M. and D. L. Klein, *A Water-Amine-Complexing Agent System for Etching Silicon*, ECS Journal of The Electrochemical Society, Vol. 114, 965-970, (1967).

[155] K.E Bean, *Anisotropic etching of silicon*, Electron Devices, IEEE Transactions, Vol. 25, No. 10, pp. 1185-1193, (1978).

[156] C. Acar, *Micromachined monolithic 3-axis gyroscope with single drive*, US Patent 9455354B2, 2016.

[157] S. Sonmezoglu, P. Taheri-Tehrani, C. Valzasina, L.G. Falorni, S. Zerbini, S. Nitzan, and D.A. Horsley, *Single-Structure Micromachined Three-Axis Gyroscope With Reduced Drive-Force Coupling*, IEEE Electron Device Letters, Vol. 36, No. 9, pp. 953-956, (2015).

[158] S. Wisher, P. Shao, A. Norouzpour-Shirazi, Y. Yang, E. Ng, I. Flader, Y. Chen, D. Heinz, T. Kenny, F. Ayazi, *A High-Frequency Epitaxially Encapsulated Single-Drive Quard-Mass Tri-Axial Resonant Tuning Fork Gyroscope*, Proc. IEEE International Conf. on Micro Electro Mechanical Systems (MEMS'2016), Shanghai, China, January 24-28, (2016).

[159] E. Margan, *Transimpedance Amplifier Analysis,* White paper, $URL :< http : //www-f9.ijs.si/margan/Articles/transzamplifier.pdf >$, Viewed: 15 Nov 2017.

[160] D. Titterton, *Strapdown Inertial Navigation Technology*, Vol. 17, IET, (2004).

[161] M. El-Diasty, S. Pagiatakis, *Calibration and Stochastic Modeling of Inertial Navigation Sensor Errors*, Journal of Global Positioning Systems, Vol. 7 No. 2, pp. 170-182, (2008).

[162] S. Poddar, V. Kumar, A. Kumar, *A Comprehensive Overview of Inertial Sensor Calibration Techniques*, Journal of Dynamic Systems, Measurement, and Control, Vol. 139, No. 01, (2017).

[163] Z. Syed, P.Aggarwal, C. Goodall, X., Niu, and N. El-Sheimy, *A New Multi-Position Calibration Method for MEMS Inertial Navigation Systems*, IOP Measurement Science and Technology Journal, Vol. 18, No. 7, pp. 1897-1907, (2007).

[164] M. Jorgensen, D. Paccagnan, M. Larsen, *IMU Calibration and Validation in a Factory, Remote on Land and at Sea*, IEEE/ION Position Location and Navigation Symposium (PLANS), Monterey, CA, USA, 05- 08 May, (2014).

[165] J. Li, F. Jiao, J. Fang, *Integrated Calibration Method for Dithered RLG POS Using Hybrid Analytic/Kalman Filter Approach*, IEEE Transactions on Instrumentation and Measurement Journal, Vol. 62, No. 12, (2013).

[166] Q. Cai, G. Yang, N. Song, Y. Liu, *Systematic Calibration for Ultra-High-Accuracy Inertial Measurement Units*, IEEE Sensors Journal, Vol. 16, (2016).

[167] D. Unsal, K. Demirbas, *Estimation of Deterministic and Stochastic IMU Error Parameters*, IEEE/ION Position Location and Navigation Symposium (PLANS), Myrtle Beach, SC, USA, 23-26 April, (2012).

Appendix A

IMU control electronics development

A.1 IMU Front-End PCB

This Section describes the multi-channels front-end PCB electronics used in this dissertation for characterization of the IMU device. The multi-channel PCB is designed for simultaneous operation of six sensors and is comprised of two boards: bottom board with forcer and carrier channels for 3 gyroscopes and 3 accelerometers; top board with pick-off channels for 3 gyroscopes and 3 accelerometers.

A.1.1 Bottom Stage PCB

The bottom board has a size of 5.8x4.0 inch, Fig. A.1. It includes forcer channels for 3 accelerometers and 3 gyroscopes. It also includes two low power DC-DC converters PQB3-D12-D12-D to provide ± 12 V supply voltage for amplifiers. In order to amplify the AC signal, the instrumentation amplifier AD8429 BRZ (Analog Devices) is used in the forcer channels of the bottom board, A.2. The feedback resistor value was chosen to be 750 Ω,

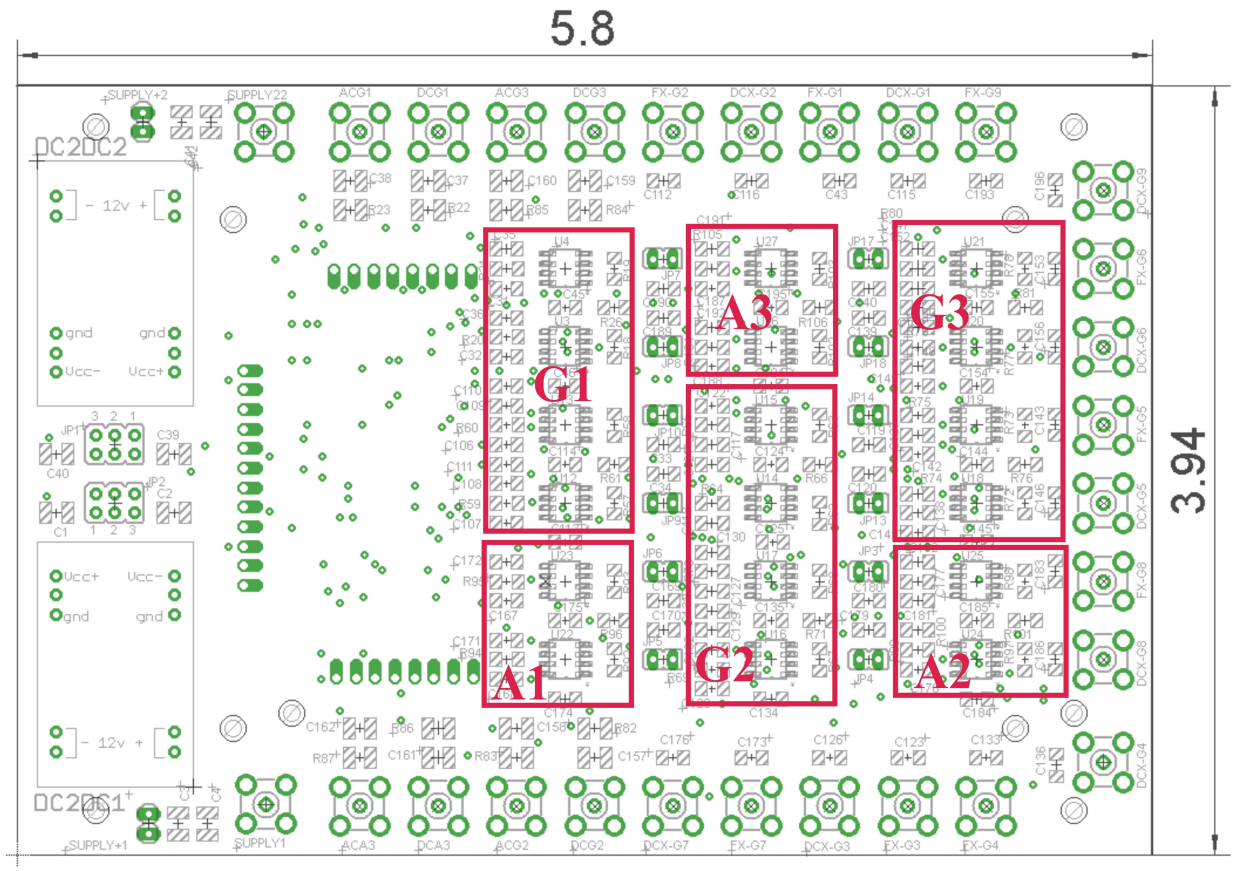

Figure A.1: Layout of the bottom PCB. A1-A3: forcer channels for accelerometers 1-3; G1-G3: forcer channels for gyroscopes 1-3.

resulting in 9x amplification. Bottom board includes four independent carrier channels to provide frequency carrier signal for amplitude modulation technique, Fig. A.3. Fig. A.4 shows an assembled bottom board.

A.1.2 Top Stage PCB

Top PCB was developed for IMU devices packaged in the standard 44-pin LCC packages, Fig. A.5. The top board has a size of 5.8x3.94 inch. It includes pick-off channels for 3 accelerometers and 3 gyroscopes. One DC-DC converter PQB3-D12-D12-D is used to provide ±12 V supply voltage for amplifiers. Assembled top board is shown in Fig. A.6.

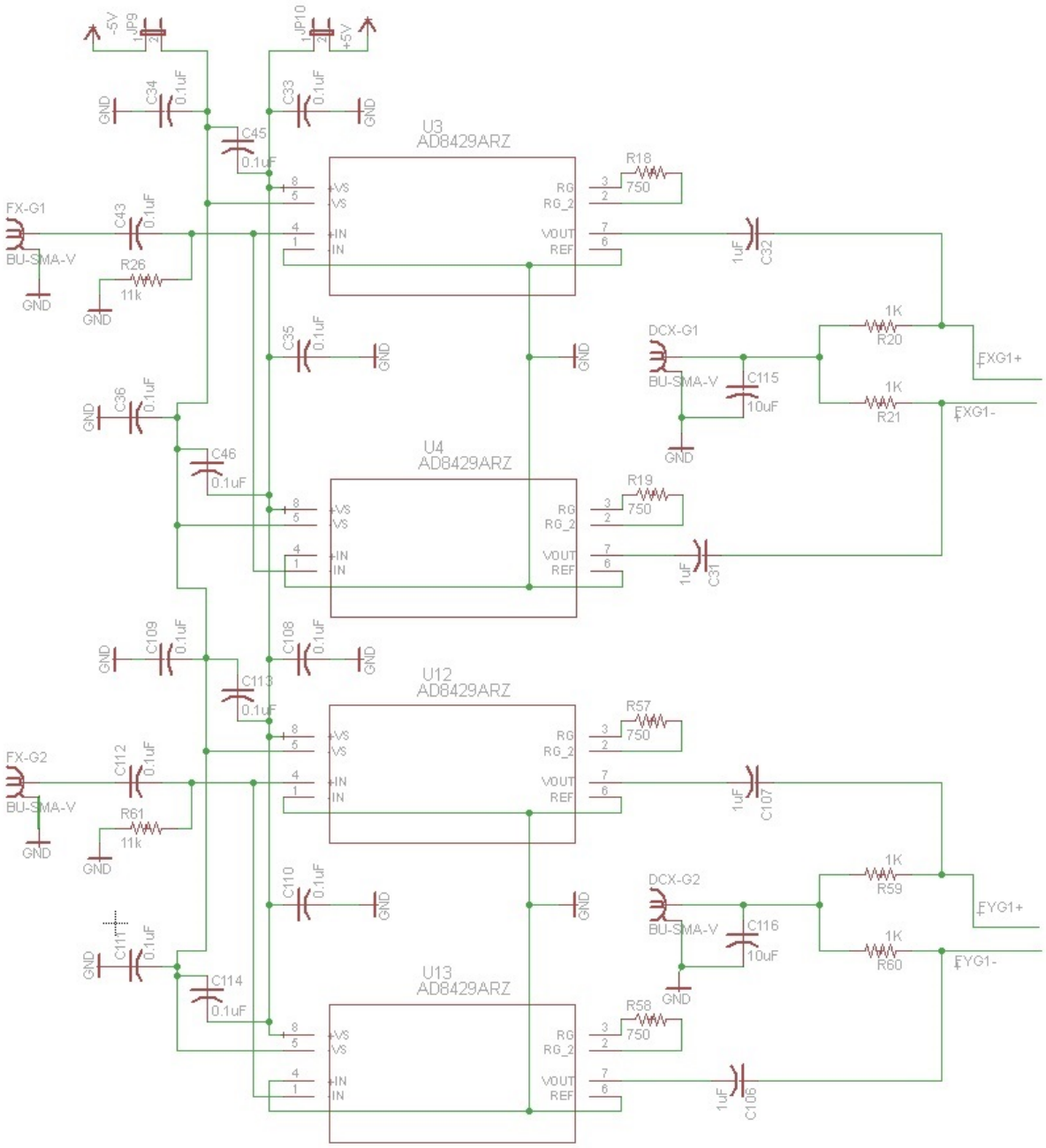

Figure A.2: Schematic of bottom board two forcer channels of one gyroscope.

On the electronic schematic level, a detection circuit for each sensor is based on precision low noise amplifiers AD8066 (Analog Devices) and instrumentation amplifiers AD8429 BRZ (Analog Devices). AD8066 is a fully input/output differential amplifier, which was used in a transimpedance configuration to sense the small current signal from the gyroscope or

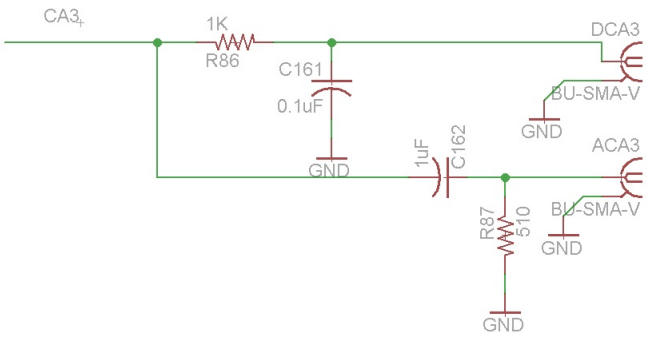

Figure A.3: Schematic of one of the carrier channels.

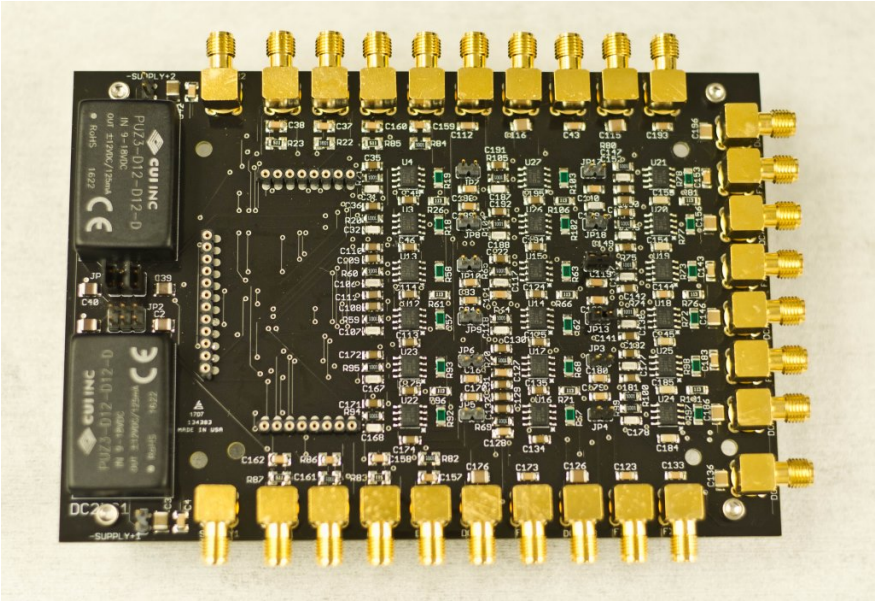

Figure A.4: Assembled bottom PCB with forcer and carrier channels for 3 gyroscopes and 3 accelerometers.

accelerometer and to convert it into voltage. The main advantage of the differential detection as opposed to a single ended detection is to cancel out the overall unwanted parasitic capacitance from the supplies and interfaces.

The general schematic of a transimpedance amplifier is show in Fig. A.7. The output of the ideal operational amplifier at DC and low frequencies can be expressed by:

$$V_o = -R_f * I \tag{A.1}$$

However, due to the presence of the source stray capacitance C_i and because of the amplifier's own limitations, the amplifier response varies with frequency, [159]:

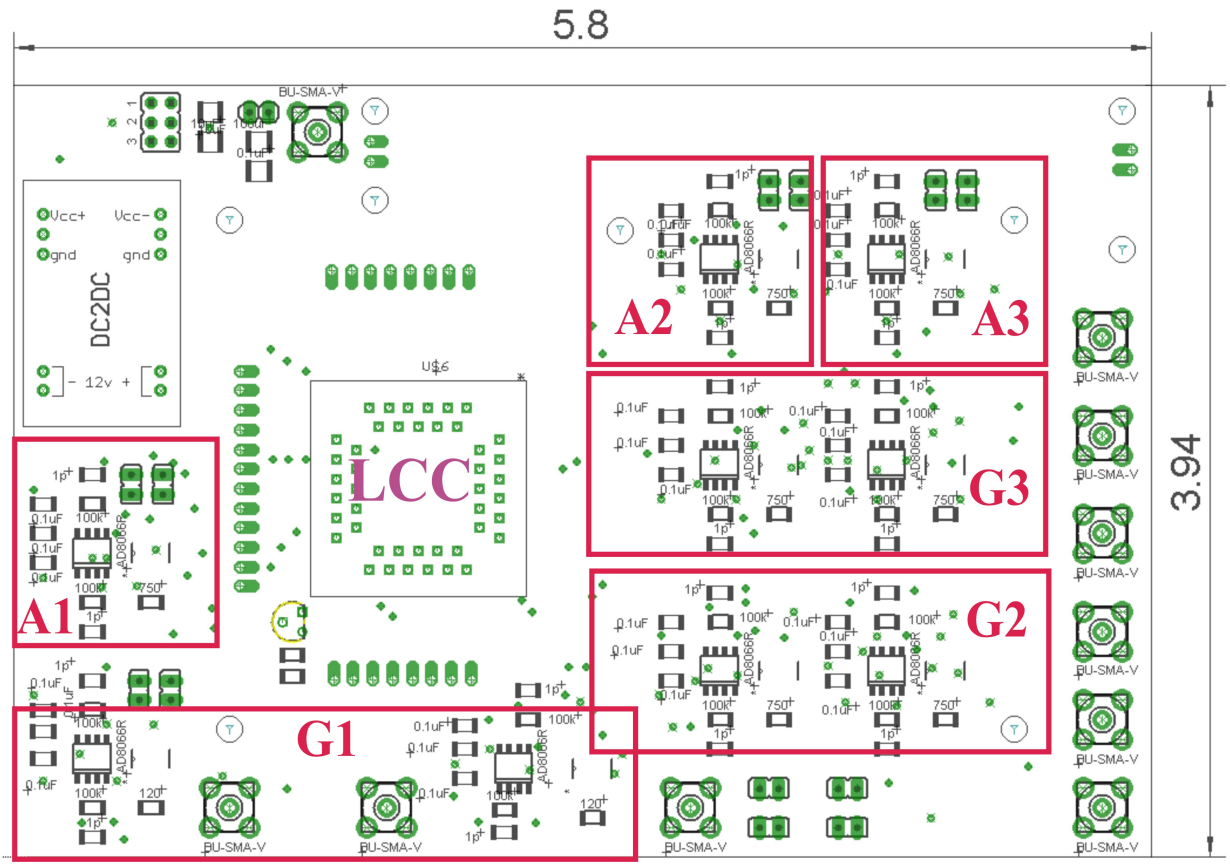

Figure A.5: Layout of the top PCB. A1-A3: pick-off channels for accelerometers 1-3; G1-G3: pick-off channels for gyroscopes 1-3.

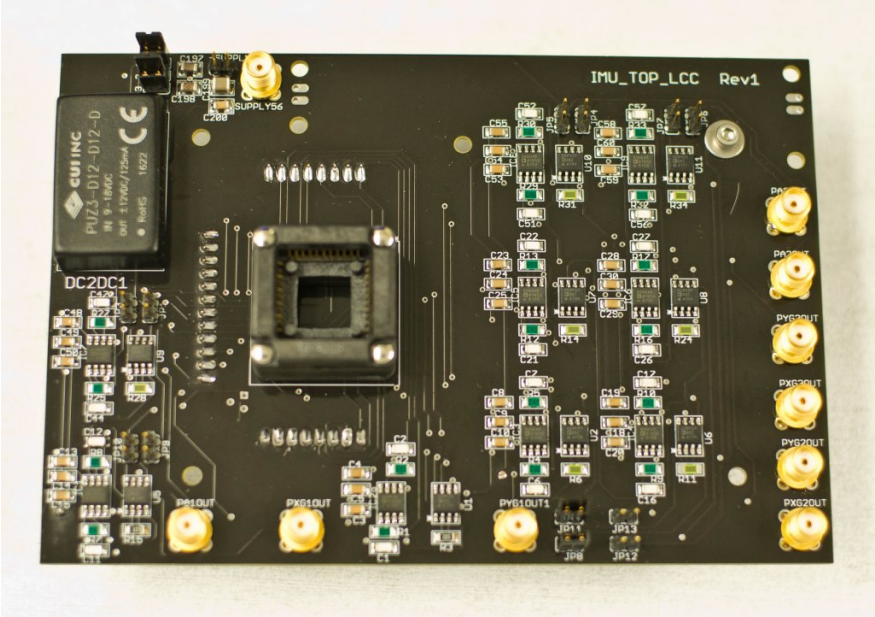

Figure A.6: Assembled top PCB with pick-off channels for 3 gyroscopes and 3 accelerometers.

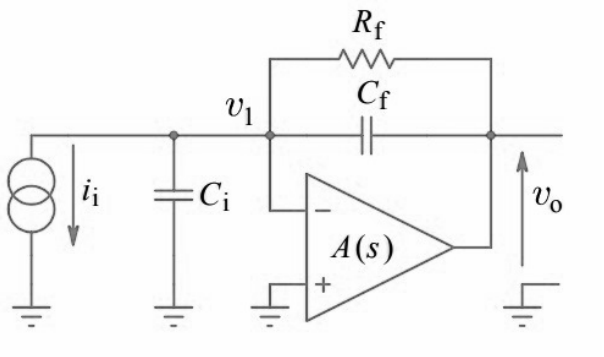

Figure A.7: Generalized schematic of transimpedance system.

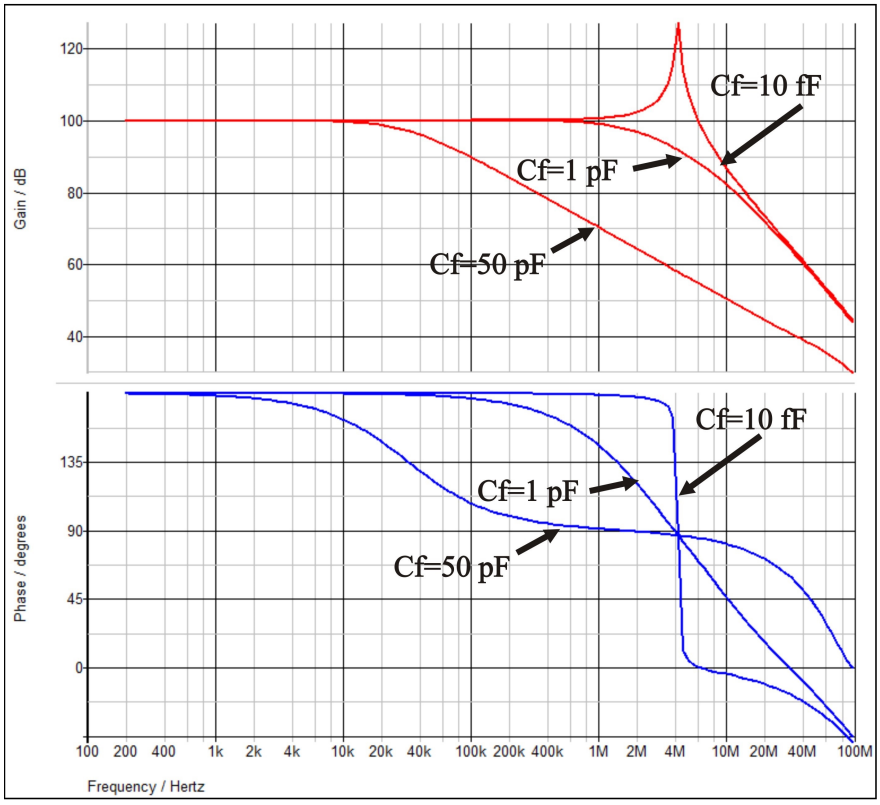

Figure A.8: Generalized schematic of transimpedance system.

$$\frac{V_o}{I} = -A_o * \frac{\omega_o}{s + \omega_o}, \tag{A.2}$$

where s is a complex frequency variable, A_o is an amplifier's open loop DC gain, ω_o is an open loop cut-off frequency.

The amplifier is chosen on the basis of its noise performance and with enough bandwidth to cover the frequency range of interest. The gain of the amplifier is set by the value of

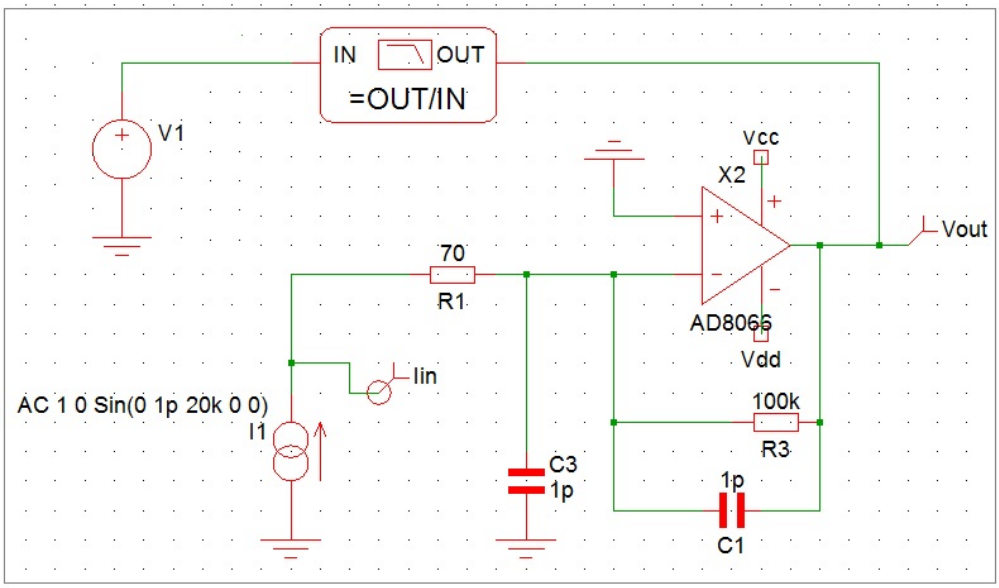

Figure A.9: AD8066 amplifier model in ADIsimPE simulator (Analog Devices).

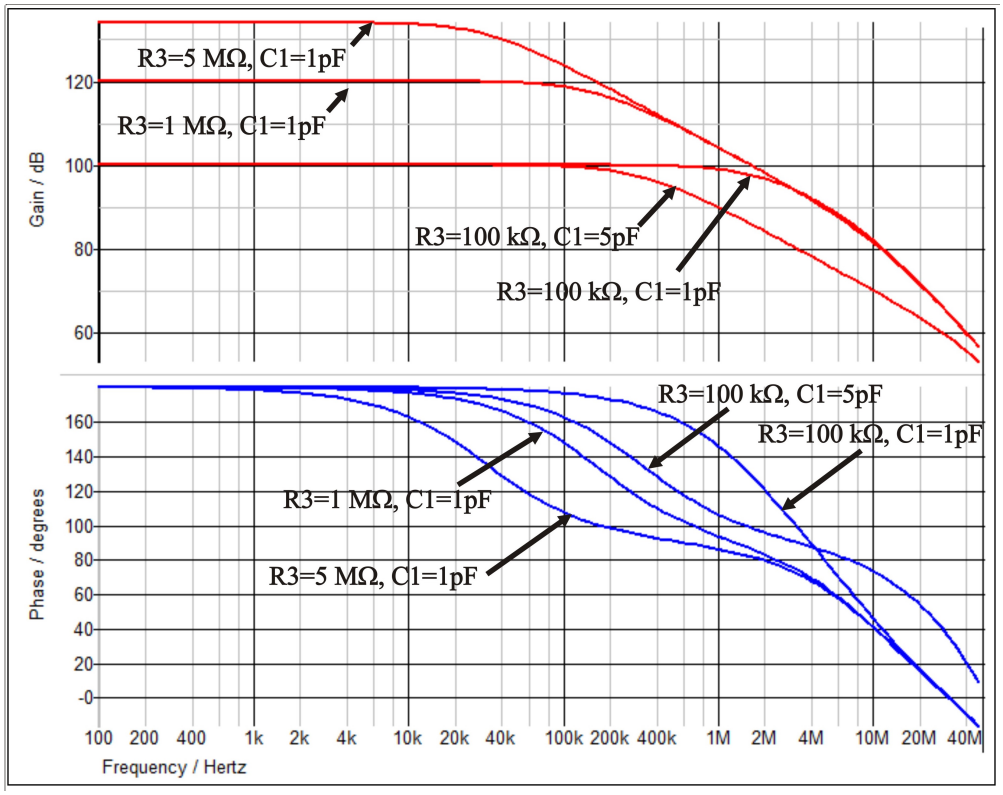

Figure A.10: Simulated transfer function (absolute value in dB) and phase angle of AD8066 amplifier).

a feedback resistor $R_{f]}$. Generally, we would like to have some standard voltage value for a standard amount of input power, so we need to select a suitable value of the feedback

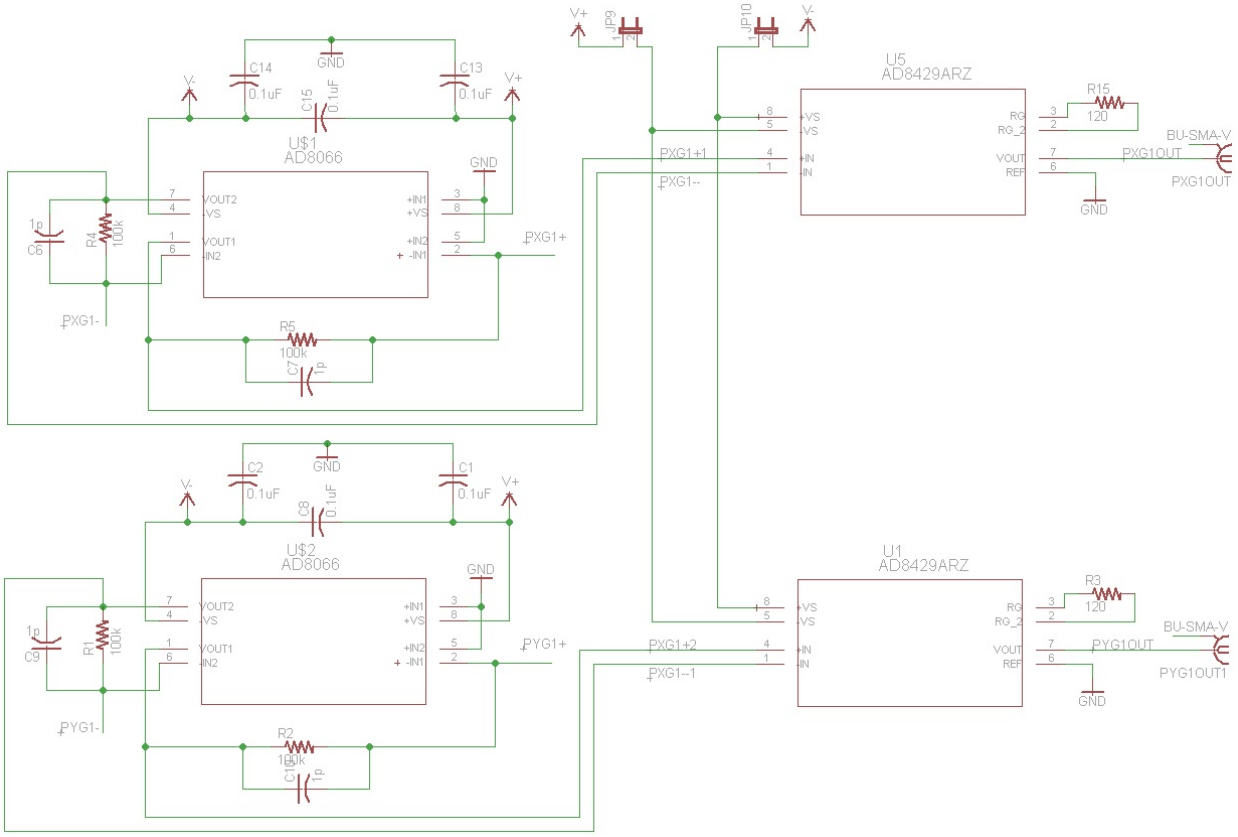

Figure A.11: Schematic of first and second stage amplification for two pick-off channels (drive and sense) of one gyroscope.

resistance to satisfy the relation $V_o = -R_f * I$ for constant input. The value of C_f cannot be chosen at will. Too large value results in a slow response of a system, too small value results in a large overshoot and long ringing, or even sustained oscillations, Fig. A.8.

In order to identify the optimum values of the resistor and the capacitor for the transimpedance configuration of the AD8066 amplifier in the pick-off circuit, the amplifier frequency and phase response were modeled using ADIsimPE simulator (Analog Devices), Fig. A.9. Simulated transfer function (absolute value in dB) and phase angle are shown in Fig. A.10. 100 kΩ resistor and 1 pF capacitor were chosen for the flat gain at up to 1 MHz frequency, fast raise time without overshooting, and maximized flat phase response. Gain flatness plays a crucial role in the systems employing amplitude modulation schemes. Linear phase response is also important since it allows for maximized flat envelop delay (phase

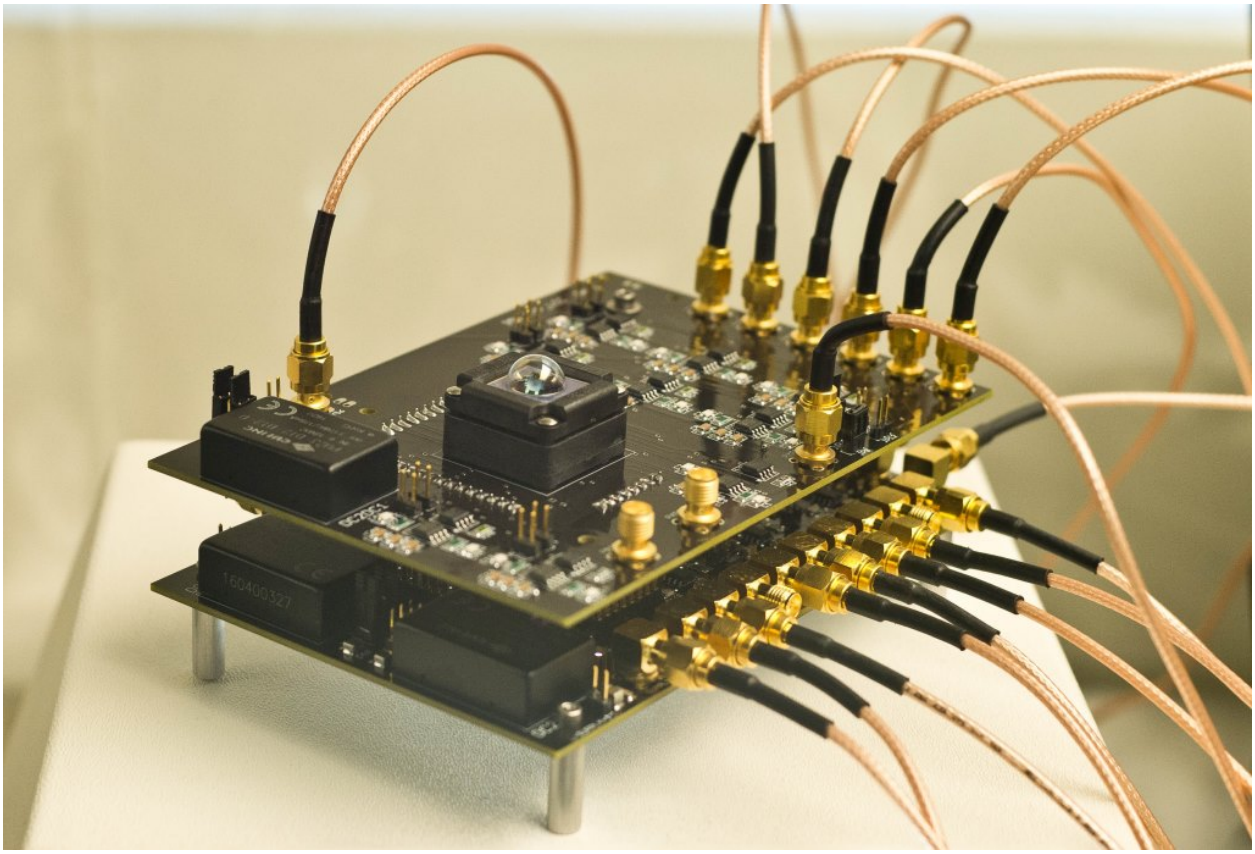

Figure A.12: Fully operational double-stage front-end PCB for 3 gyroscopes and 3 accelerometers.

derivative against frequency) meaning that all the frequencies will pass through the system with equal delay without signal distortion.

Fig. A.11 shows schematic of first and second stage amplification for two pick-off channels (drive and sense) of one gyroscope. The accelerometer pick-off electronics is similar to one of the pick-off channels of a gyroscope. The gain of each pick-off channel is 100k followed by 51x second amplification (voltage to voltage). The cut-off frequency is around 1.2 MHz, high enough to perform amplitude modulation technique using high frequency carrier signal to reduce and unwanted parasitic capacitance.

Fig. A.12 shows the assembled top board (pick-off channels) and the bottom board (forcer channels).

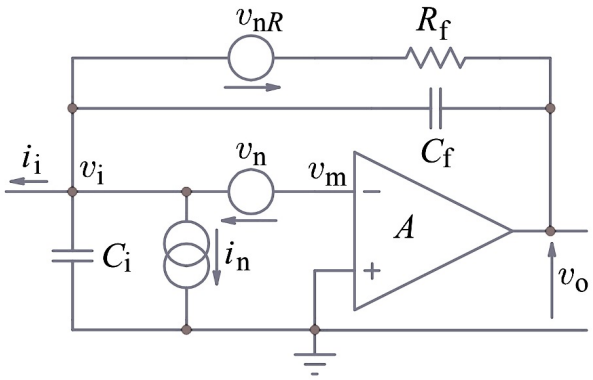

Figure A.13: Thermal noise sources in amplifier.

A.1.3 Noise Analysis

The gyroscope rate equivalent noise due to electronics can be estimated as, [141]:

$$\Omega_{rw_e} = \frac{V_n}{SF} \times 0.0167,$$

where V_n is the output voltage noise of the transimpedance amplifier, SF is the gyroscopes scale factor, 0.0167 is a factor to convert from (deg/hr)/rt-Hz to (deg/rt-hr).

The two non-coherent thermal noise sources of the transimpedance amplifier circuit are the differential voltage noise source e_n and input current noise source i_n, Fig. A.13. In addition, the resistor has its own thermal noise source e_{nR}. The equivalent output voltage noise V_n can be estimated as:

$$V_n = \sqrt{4k_bTR_f + e_n^2 + i_n^2R_f^2},$$

where e_n and i_n are the voltage noise and current noise of the amplifier, T is the absolute temperature in K, k_b is the Boltzmann thermodynamic constant ($k_b = 1.38e^{-23}J/K$).

For the commercial off-the-shelf precision low noise and low input bias current operational amplifier (AD8066), the values are $e_n = 7nV/\sqrt{Hz}$ and $i_n = 0.6fA/\sqrt{Hz}$. The resulting total thermo-electrical noise is Vn = 41 nV/$\sqrt{Hz}$.

The gyroscope scale-factor is determined by the pick-off scheme and by the gyroscope dy-

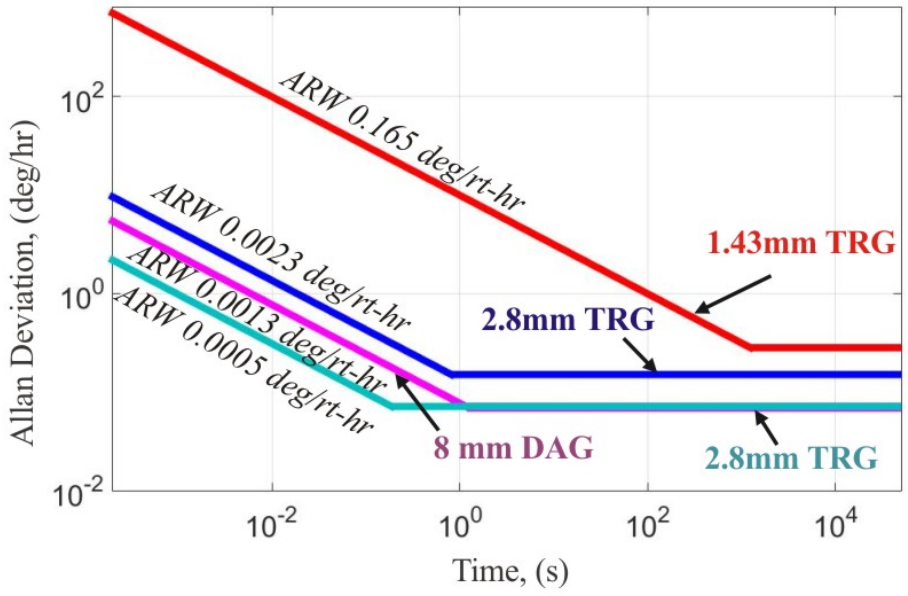

Figure A.14: Projected performance of the gyroscopes limited by the eletroniccs noise.

namics. It can be estimated analytically as:

$$SF = SF_{elec} \times SF_{mech},$$

Moreover, gyroscope SF can be extracted using a rate table experiment. For the 1.43 mm diameter TRG the SF was shown to be 4.16 nV/(deg/hr). For the 2.8 mm diameter TRG the SF was shown to be 0.31 uV/(deg/hr). For the 3.1 mm DFP the SF was shown to be 0.538 uV/(deg/hr). For the 8 mm DAG the SF was shown to be 1.34 uV/(deg/hr).

The resulting rate equivalent noise due to electronics is:

$$\Omega_{rw_e}(TRG1) = \frac{41nV/\sqrt{Hz}}{4.16nV/(deg/hr)} \times 0.0167 = 0.165 \text{ deg/rt-hr}.$$

$$\Omega_{rw_e}(TRG2) = \frac{41nV/\sqrt{Hz}}{0.31uV/(deg/hr)} \times 0.0167 = 0.0023 \text{ deg/rt-hr}.$$

$$\Omega_{rw_e}(DFP) = \frac{41nV/\sqrt{Hz}}{0.538uV/(deg/hr)} \times 0.0167 = 0.0013 \text{ deg/rt-hr}.$$

$$\Omega_{rw_e}(DFP) = \frac{41nV/\sqrt{Hz}}{1.34uV/(deg/hr)} \times 0.0167 = 0.0005 \text{ deg/rt-hr}.$$

Fig. A.14 reflects the projected performance of the gyroscopes limited by the electronics noise. In addition to these noise sources, the gyroscope output signal has its own thermo-mechanical noise component, not covered in this Section.

Appendix B

IMU Calibration

Inertial Measurement Unit (IMU) is one of the core elements of the Inertial Navigation System (INS). It contains three accelerometers and three gyroscopes mounted along the three mutually orthogonal axes. The linear acceleration and rotation rate information obtained from these sensors is fed to the navigational system for estimation of the position and body orientation. The accuracy of these estimates, however, depends on the inertial sensors performance grade and the errors embedded in these sensors. The errors accumulate and grow with time of integration and result in increasing of position and velocity errors over time, [160]. Hence, a mechanism of errors identification and removal is necessary.

The inertial sensor errors can be divided into two broad categories: (1) random or stochastic error and (2) deterministic or systematic error, [161]. Random errors, including sensors noise, occur due to random fluctuations in the system response. These errors need to be approximated using stochastic modeling. On the other hand, deterministic errors, including the bias, scale factor, and the non-orthogonality/misalignment errors, can be removed using specific calibration procedures. The process of identification and removal of systematic errors from the sensor is known as calibration.

Calibration is a process of comparing the sensors output with the known reference information and determining the coefficients that force the output to fit the known reference. Different techniques for calibration of inertial sensors have been widely studied in literature, including a six-position method, [162], a multi-position based calibration method, [163], a Kalman filter based method, [164], and a hybrid analytic/Kalman filter approach, [165]. A six-position method is among the most common techniques for calibration of sensors in the laboratory. This technique is applied for calibration of IMU.

B.1 Six-Position Calibration Method

The standard methodology for calibrating the IMUs using a six-position technique within a laboratory environment requires the mounting of the IMU on a multi-axes tilt/turntable. The six-position static and rate tests are conducted for calibrating the accelerometers and gyroscopes. It involves aligning the triad of orthogonal sensors with the vertical axis of local frame, pointing alternately up and down, thus generating a total of six different positions as shown in Fig. B.1.

Fig. B.2 represents an IMU calibration setup with a rate-table and a two-axis tilt table.

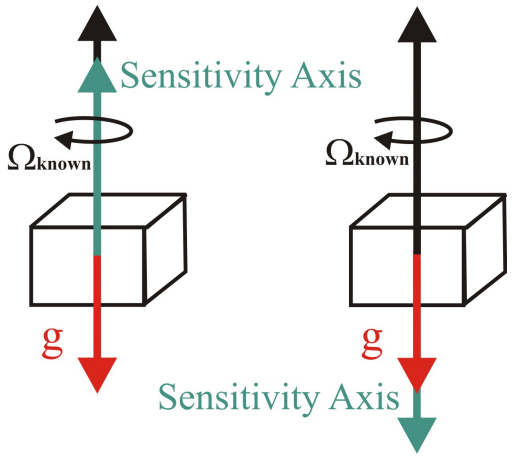

Figure B.1: Up and down positions of the IMU for calibration of one axis.

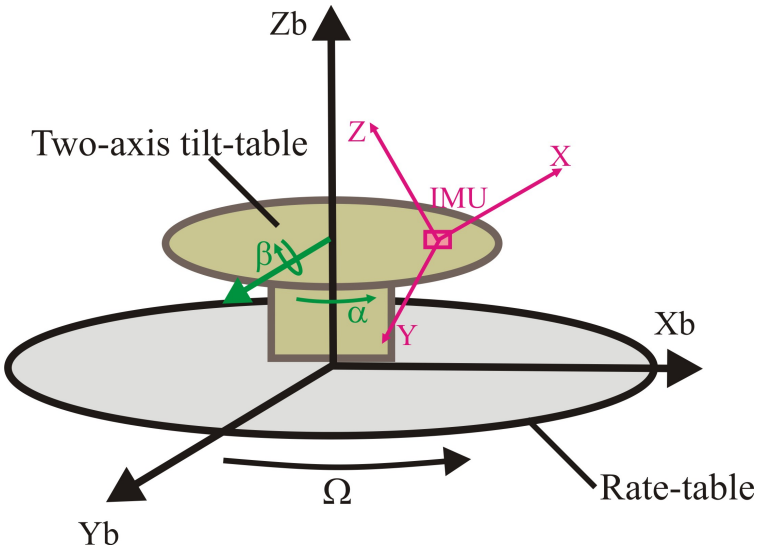

Figure B.2: IMU laboratory calibration setup.

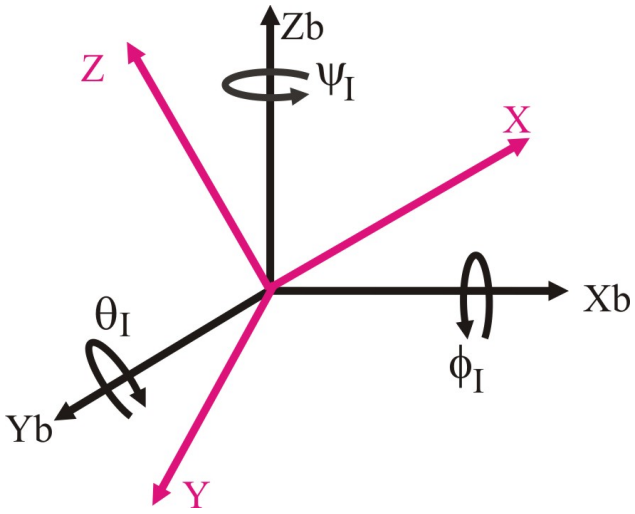

Figure B.3: IMU frame relative to the body frame.

In a general case, when the IMU frame is misaligned relative to the body/rate-table frame. Depending on how the IMU is mounted on the rate-table, there will be rotations φ_I, ψ_I, θ_I of the IMUs coordinate axes relative to the body axes, illustrated in Fig. B.3.

B.2 Gyroscopes Calibration

The IMU gyroscopes measure the angular rates ω_X, ω_Y, ω_Z in coordinate frame X,Y,Z associated with the IMU. These measurements are not affected by the location of the IMU relative to the body frame, but only affected by the orientation of the IMU frame relative to the body frame, which is given by angles φ_I, θ_I, ψ_I, Fig. B.3.

The calibration model for the gyroscopes triad is defined in the body frame (true angular rate in the body frame):

$$\Omega_B = [J_g] * [SF_g] * \omega_I - [K_n] * \Omega_B^{(2)} - [K_{cross}] * \Omega_B^{(cross)} - [G] * g_l, \tag{B.1}$$

$$\omega_I = \acute{\omega_I} - \omega_0 - \omega_n.$$

Here Ω_B is the true angular velocity of the body; $[J_g]$ is the misalignment matrix defined by angles φ_I, ψ_I, θ_I; $[SF_g]$ is a scale factor matrix, $\acute{\omega_I}$ is a gyroscope raw measurement data including noise, ω_0 - gyroscope bias, ω_n-gyroscope noise, $[K_n]$- nonlinear SF matrix, $[K_{cross}]$-cross-coupling matrix, $[G]$ is the g-sensitivity coefficients matrix; g_l is the acceleration vector in body frame.

The true angular velocity for each of the three axes in body reference frame X_B, Y_B, Z_B, can be then expressed as:

$$\begin{bmatrix} \Omega_{XB} \\ \Omega_{YB} \\ \Omega_{ZB} \end{bmatrix} = \begin{bmatrix} K_{11} & K_{12} & K_{13} \\ K_{21} & K_{22} & K_{23} \\ K_{31} & K_{32} & K_{33} \end{bmatrix} * \begin{bmatrix} \acute{\omega}_X - K_{10} \\ \acute{\omega}_Y - K_{20} \\ \acute{\omega}_Z - K_{30} \end{bmatrix} - \begin{bmatrix} K_{nXX} & 0 & 0 \\ 0 & K_{nYY} & 0 \\ 0 & 0 & K_{nZZ} \end{bmatrix} * \begin{bmatrix} \Omega_{XB}^2 \\ \Omega_{YB}^2 \\ \Omega_{ZB}^2 \end{bmatrix} -$$

$$- \begin{bmatrix} K_{crossXY} & K_{crossXZ} & 0 \\ K_{crossYX} & 0 & K_{crossYZ} \\ 0 & K_{crossZX} & K_{crossZY} \end{bmatrix} * \begin{bmatrix} \Omega_{XB}\Omega_{YB} \\ \Omega_{XB}\Omega_{ZB} \\ \Omega_{YB}\Omega_{ZB} \end{bmatrix} - \begin{bmatrix} G_{XX} & G_{XY} & G_{XZ} \\ G_{YX} & G_{YY} & G_{YZ} \\ G_{ZX} & G_{ZY} & G_{ZZ} \end{bmatrix} * \begin{bmatrix} g_{lX} \\ g_{lY} \\ g_{lZ} \end{bmatrix}, \quad \text{(B.2)}$$

The described model accounts for the sensor bias, SF, misalignment/nonorthogonality errors, g-sensitive angular rate bias, SF non-linearity and second-order cross-coupling terms. This expanded model is necessary to satisfy the requirement of ultra-high accuracy navigation-grade IMUs, [166]. However, in the case of a consumer- or tactical- grade IMU, a simplified sensor error model is often used for identification of the calibration parameters:

$$\Omega_B = [J_g] * [SF_g] * \omega_I, \quad \text{(B.3)}$$

$$\omega_I = \acute{\omega}_I - \omega_0 - \omega_n.$$

This simplified calibration model allows for correction of the misalignment/nonorthogonality errors, which introduce major inaccuracies into the IMU measurements.

Using a simplified model, the true angular velocity for each of the three axes in body reference frame X_B, Y_B, Z_B, can be then expressed as:

$$\begin{bmatrix} \Omega_{XB} \\ \Omega_{YB} \\ \Omega_{ZB} \end{bmatrix} = [J_g] * \begin{bmatrix} SF_{gX} & 0 & 0 \\ 0 & SF_{gY} & 0 \\ 0 & 0 & SF_{gZ} \end{bmatrix} * \begin{bmatrix} \acute{\omega}_X - \omega_{X0} \\ \acute{\omega}_Y - \omega_{Y0} \\ \acute{\omega}_Z - \omega_{Z0} \end{bmatrix} = \begin{bmatrix} K_{11} & K_{12} & K_{13} \\ K_{21} & K_{22} & K_{23} \\ K_{31} & K_{32} & K_{33} \end{bmatrix} * \begin{bmatrix} \acute{\omega}_X - K_{10} \\ \acute{\omega}_Y - K_{20} \\ \acute{\omega}_Z - K_{30} \end{bmatrix}, \quad \text{(B.4)}$$

where ($\acute{\omega}_X$, $\acute{\omega}_Y$, $\acute{\omega}_Z$) are the raw measurements of the gyroscope, (ω_{X0}, ω_{Y0}, ω_{Z0}) are the zero-rate level or bias on each axis, J is a cross correlation matrix, (SF_X, SF_Y, SF_Z) are the the scale factors along the X, Y, Z axes, and $K_{11} - K_{30}$ are the 12 calibration parameters.

In order to compare the expanded and simplified error models, the calibration process was

	ST L3G4200D	ADIS 16135
ARW	0.03 dps/rt-Hz	0.75 deg/rt-hr
SF non-linearity	0.2% FSR	0.008% FSR
Output noise	0.42 dps	0.27 dps
G-sensitivity	0.1 dps/g	0.03 dps/g

Table B.1: Commercially available sensors.

simulated for two types of commercially available IMUs: tactical-grade, and consumer-grade, Table B.1.

Fig.B.4 shows the simulated uncalibrated and calibrated outputs of the three ST Micro gyroscopes under the angular rotation applied around the Z axis in the body/rate-table frame. We considered a sinusoidal input of the rate-table with a frequency of 1 Hz and amplitude of 1 deg. In our simulation, the angle of misalignment between the IMU axes and rate-table axes $\theta = 30deg$.

The calibrated data was obtained using a simplified and an expanded error models. The simplified model only accounts for misalignment/nonorthogonality errors. The expanded

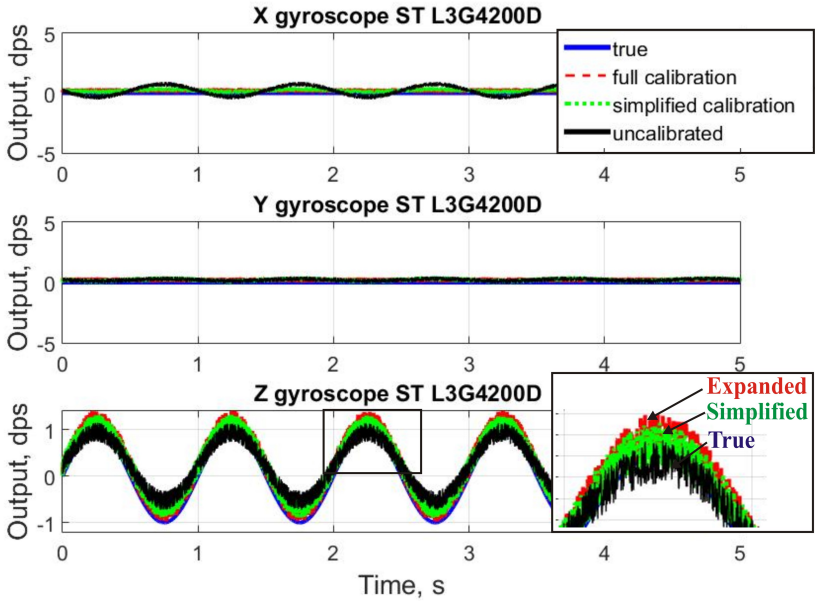

Figure B.4: Simulated calibrated outputs of the three ST Micro L3G4200D gyroscopes.

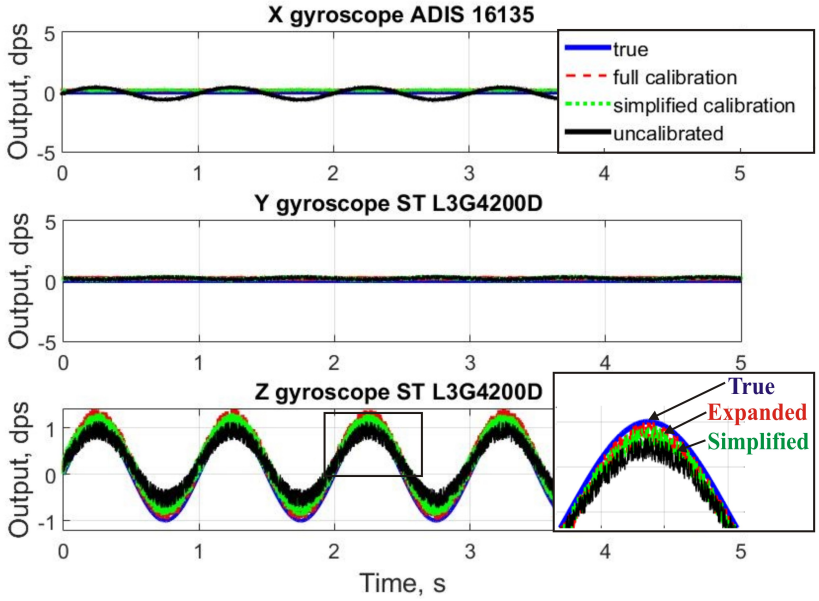

Figure B.5: Simulated calibrated outputs of the three ADIS 16135 gyroscopes.

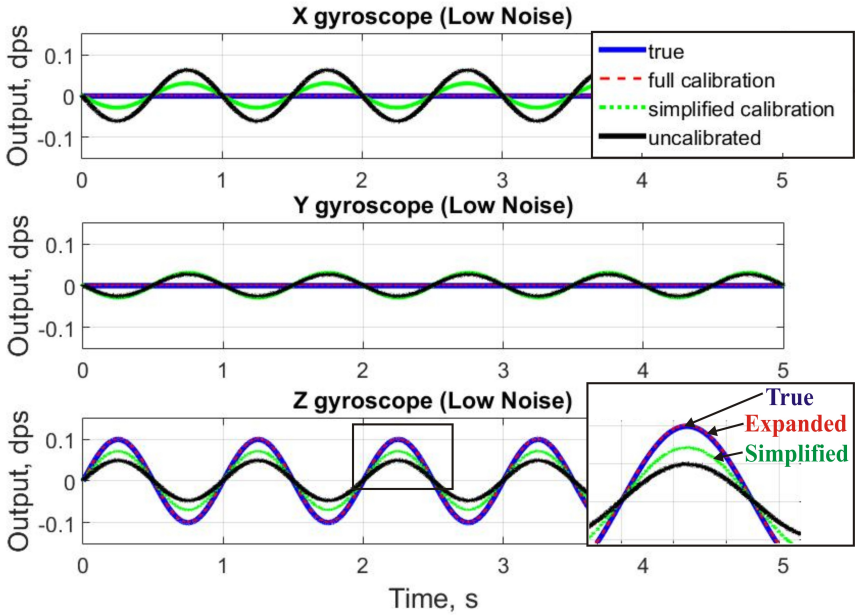

Figure B.6: Simulated calibrated outputs of the three low-noise gyroscopes.

model also includes the g-sensitive angular rate bias, and SF non-linearity errors. Stochastic errors, [167], such as bias instability and noise density, were also included into the model. Due to the dominating factor of the sensor noise, the expanded error model does not improve the residual calibration error. Hence, in this case, the simplified linear error model is sufficient

for the IMU calibration.

Fig.B.5 shows the simulated uncalibrated and calibrated outputs of the three ADIS gyroscopes under the angular rotation applied around the Z axis in the body/rate-table frame. Similar to the first case, the simplified linear model is sufficient for the IMU calibration since the gyroscope noise is dominating.

In addition, we explored a case of a low noise (navigational grade level) IMU, Fig. B.6. During this simulation, the other parameters of the gyroscopes are kept similar to the ADIS 16135 IMU. The simulation experiments show that as the noise of the IMU is reduced, the G-sensitivity and the non-linearity terms of the gyroscope error model start playing a important role, defining the calibration accuracy. Using the expanded model, the calibration error was reduced approximately 17 times.

This analysis confirms that a simplified model can be used for calibration of a tactical grade or a consumer grade IMU. However, in order to meet the requirements of the low-noise navigational grade IMU, the expanded model, including the g-sensitive angular rate bias, SF non-linearity and second-order cross-coupling terms might be necessary.

The step-by-step calibration procedure for three gyroscope channels involves:

- Mount the IMU PC board on the leveled top surface of the tilt-table mounted on top of the Ideal Aerosmith rate-table.
- Power on the device and wait a few minutes for it to warm up.
- Collect 100 samples of data for three gyroscope channels and then average those samples as the zero-rate level ω_{X0}, ω_{Y0}, ω_{Z0}.
- Let the rate-table start spinning counterclockwise at Ω_Z= +20 dps and $\Omega_X = \Omega_Y = 0$ dps.

- Wait until the spin table angular velocity becomes stable. Then start collecting the three gyroscope channels raw data for one full round.
- Stop the spin table.
- Let the spin table start spinning clockwise at Ω_Z= -20 dps and $\Omega_X = \Omega_Y = 0$ dps. Then repeat steps (5) and (6) to collect the three gyroscope channels raw data.
- Let the spin table start spinning counterclockwise at Ω_Z= +40 dps and $\Omega_X = \Omega_Y = 0$ dps. Then repeat steps (5) and (6) to collect the three gyroscope channels raw data.
- Let the spin table start spinning clockwise at Ω_Z= -40 dps and $\Omega_X = \Omega_Y = 0$ dps. Then repeat steps (5) and (6) to collect the three gyroscope channels raw data.
- Rotate the tilt-table by 90 degree clockwise around X axis. The Y-axis of the IMU is now facing up on the rate-table. Then repeat steps (4) to (9) to collect the three gyroscope channels raw data along the Y-axis.
- Return the tilt-table to the original state leveled up with the rate-table. Rotate the tilt-table by 90 degree clockwise around Z axis then by 90 degree clockwise around X axis. The X-axis of the IMU is now facing up on the rate-table. Repeat steps (4) to (9) to collect the three gyroscope channels raw data along the X-axis.
- Gyroscope channels calibration is done.
- Construct the known applied angular rate data into a matrix $[\Omega_B]$ and construct the three gyroscope channels raw data into the matrix $[\Omega_I]$=$[\acute{\omega} - \omega_0]$.

B.3 Accelerometers Calibration

The accelerometers measure the combined effect of the translational acceleration of the body frame a_B, local gravity in the body frame g_l, as well as radial a_R and tangential accelerations

a_T induced by the off-center rotation of the IMU relative to the body frame origin located in the center of gravity of the body:

$$a_B + a_R + a_T + g_l = [J_a] * [SF_a] * a_I, \tag{B.5}$$

$$a_I = \acute{a_I} - a_0 - a_n.$$

Here $[J_a]$ is the misalignment matrix/ rotational matrix defined by angles φ_I, θ_I, ψ_I, $[SF_a]$ scale factor matrix, $\acute{a_I}$ - accelerometer raw measurement data, a_0- accelerometer bias, a_n- accelerometer noise.

During the accelerometers calibration step, the rate-table is kept stationary. $a_R = 0$, $a_T = 0$. In addition the translational acceleration of the body frame $a_B = 0$. Hence the model of accelerations for each axes specified in the body frame can be represented as:

$$\begin{bmatrix} g_{XB} \\ g_{YB} \\ g_{ZB} \end{bmatrix} = [J_a] * \begin{bmatrix} SF_{aX} & 0 & 0 \\ 0 & SF_{aY} & 0 \\ 0 & 0 & SF_{aZ} \end{bmatrix} * \begin{bmatrix} \acute{a}_X - a_{X0} \\ \acute{a}_Y - a_{Y0} \\ \acute{a}_Z - a_{Z0} \end{bmatrix} = \begin{bmatrix} C_{11} & C_{12} & C_{13} \\ C_{21} & C_{22} & C_{23} \\ C_{31} & C_{32} & C_{33} \end{bmatrix} * \begin{bmatrix} \acute{a}_X - C_{10} \\ \acute{a}_Y - C_{20} \\ \acute{a}_Z - C_{30} \end{bmatrix}, \tag{B.6}$$

where $[J_a]$ is the misalignment matrix/ rotational matrix defined by angles φ_I, θ_I, ψ_I, $[SF_a]$ scale factor matrix; SF_{aX}, SF_{aY}, SF_{aZ} are the scale factors along the X, Y, Z axes, $[g_{XB}; g_{YB}; g_{ZB}]$ is the gravity vector in the body frame used for calibration. and C_{11} - C_{30} are the 12 calibration parameters.

The step-by-step calibration procedure for three accelerometer channels involves:

- Mount the IMU front-end electronics board on the leveled top surface of the tilt-table mounted on top of the Ideal Aerosmith rate-table.

- Power on the IMU and wait a few minutes for it to warm up.
- Collect 100 samples of three accelerometer channels data and then average those samples as the bias level a_{X0}, a_{Y0}, a_{Z0}.
- Rotate the tilt-table counterclockwise 45 deg around Yb axis. Collect the three accelerometer channels data.
- Rotate the tilt-table clockwise 45 deg around Yb axis. Collect the three accelerometer channels data.
- Rotate the tilt-table counterclockwise 90 deg around Yb axis. The X-axis accelerometer is now facing up. Collect the three accelerometer channels data.
- Rotate the tilt-table clockwise 90 deg around Yb axis. The X-axis accelerometer is now facing down. Collect the three accelerometer channels data.
- Return the tilt-table to the initial position.
- Rotate the tilt-table by 90 degree counterclockwise around Zb axis.
- Rotate the tilt-table counterclockwise 45 deg around Yb axis. Collect the three accelerometer channels data.
- Rotate the tilt-table counterclockwise 90 deg around Yb axis. The Y-axis accelerometer is now facing up. Collect the three accelerometer channels data.
- Rotate the tilt-table clockwise 45 deg around Yb axis. Collect the three accelerometer channels data.
- Rotate the tilt-table clockwise 90 deg around Yb axis. The Y-axis accelerometer is now facing down. Collect the three accelerometer channels data.
- Return the tilt-table to the initial position.

- Rotate the tilt-table by 90 degree clockwise around Yb axis.
- Rotate the tilt-table counterclockwise 45 deg around Yb axis. Collect the three accelerometer channels data.
- Rotate the tilt-table counterclockwise 90 deg around Yb axis. The Z-axis accelerometer is now facing up. Collect the three accelerometer channels data.
- Rotate the tilt-table clockwise 45 deg around Yb axis. Collect the three accelerometer channels data.
- Rotate the tilt-table clockwise 90 deg around Yb axis. The Z-axis accelerometer is now facing down. Collect the three accelerometer channels data
- Return the tilt-table to the initial position.
- Three accelerometer channels calibration is done.
- Construct the known applied gravity vector data into a matrix g_B and construct the three accelerometer channels raw data into the matrix a_I.

B.4 Least Squares method

Once the calibration procedure is complete, the Least Squares method is applied to determine the 12 calibration parameters. For both gyroscopes and accelerometers, the problem can be written as:

$$\Omega_B = K * \Omega_I, \tag{B.7}$$

where $[\Omega_B]$ is a 3×n matrix with true angular rate datasets from rate-table, K is a 3×3 correlation and scaling matrix, Ω_I is a 3×n matrix with the measured data.

The linear least-squares criterion is used to find the best fit for K over the measured datasets. Each column in B.8 represents a dataset, X,Y, Z. The objective of the least-squares problem is to determine the vectors in the column space of K that is closest to the vectors in Ω_B. In the least-squares sense, this means to find the minimum in the square norm of the residual vector:

$$\underbrace{min}_{\Omega_I} \|\Omega_B - K * \Omega_I\|^2 . \tag{B.8}$$

Here, residual vector e is computed from the data and the vector of estimates as:

$$e = \Omega_B - K * \Omega_I. \tag{B.9}$$

The final solution to the problem is:

$$\Omega_B = K \cdot \Omega_I$$

$$\Omega_B \cdot \Omega_I^T = K \cdot \Omega_I \cdot \Omega_I^T$$

$$K = \Omega_B \cdot \Omega_I^T \cdot (\Omega_I \cdot \Omega_I^T)^{-1} = \Omega_B \cdot \Omega_I^+, \tag{B.10}$$

where Ω_I^+ is the Moore-Penrose pseudoinverse and will exist and be unique for any Ω_I [144].

Appendix C

Cleanroom Recipes and Protocols

C.1 Shipley 1827 Lithography with 10 W power

Overview	
Input	Si/SOI wafer(s), photomask
Consumables	Shipley 1827 photoresist, aluminum foil, cleanroom wipes, wafer tweezers, MF-319 photoresist developer
Equipment	MA6 aligner, Laurell spinner, soft-bake furnace (90°C), dehydration-bake furnace (120°C), HMDS oven
Output	Photoresist patterned wafers
Process Parameters	
Prebake	45 mins dehyration @ 120°C
HMDS coat	in HMDS oven
Photoresist Coat	500 rpm: 10 secs, 4500 rpm: 30 secs (ACCL 5 for both)
Soft-bake	30 minutes @ 90°C
Exposure	Soft-contact @ 25 μm gap, 20 secs exposure @ 10 W lamp power
Development	MF-319 developer, 30 seconds to 1 minute

Table C.1: Shipley 1827 lithography equipment.

Important Notes

Recipe is only valid for 10 W power on MA6, do not use if the lamp power is different.

Recipe results in uniform photoresist coating with a thickness of 2.98 μm. If thicker film is required, refer to process parameters in Table C.2.

Process

1. Place a large enough aluminum foil into soft-bake furnace. Place wafers on this aluminum foil processing-side up.

2. Dehydrate the wafers at 120°C in the clean dehydration furnace for 45 minutes.

3. Apply hexamethyldisilizane (HMDS) inside the HMDS oven.

   NOTE: Alternatively, HMDS can be spin-coated using Laurell spinner: 5000 rpm: 40 sec. However, the YES HMDS vapor prime oven allows for more even coating, reduced chemical consumption and less wafer contamination.

4. Check to see that the HMDS oven pump is on, check vacuum gauge to verify they are in range, check HMDS level. Watch the LCD screen during your run to make sure the HMDS is actually doing its job. Make sure that the yellow light is blinking at the end of your run.

5. Spinning:

   (a) Make sure the spinner is clean, if previous user left resist residue clean with acetone and wipe with cleanroom wipes.

   (b) Set Laurell spinner to:

      i. 1st step: 500 rpm, accel. 5, 10 seconds

      ii. 2nd step: 4500 rpm, accel. 5, 30 seconds

   (c) Use a dummy sample to do a dry run and make sure the program works.

   (d) Place the wafer on the spinner, check for vacuum, center the wafer.

(e) Blow nitrogen on the wafer.

(f) Pour photoresist to about 2/3 of the wafer, do not use the pippette. At this step pouring more than necessary is always better than pouring not enough.

(g) Spin the resist, put the wafer into the soft-bake furnace for 30 minutes onto the aluminum foil.

NOTE: Never place wafers into furnaces without an extra layer of aluminum foil. We have double-sided processes that are very sensitive to contamination on the back-side of your wafer.

(h) When done, wipe the photoresist bottle with a dry cleanroom wipe, this minimizes dried resist particulates next time you do lithorgraphy.

(i) Cleanup the spinner.

6. Exposure:

(a) When soft-bake is done, get your wafers and mask ready near MA-6.

(b) Inspect the photomask visually, if there is any visible photoresist residue do a solvent clean on the photomask. If it does not remove the residue, a proper mask clean is required.

(c) Place the mask chrome side up, blow nitrogen on it, load it.

(d) Do a lamp test on the MA-6 aligner before your first run. It should read 10 W.

(e) Set the mask aligner to soft-contact with 25 μm gap. 20 seconds exposure time.

(f) Load the wafer.

(g) Align the wafer if alignment is needed.

(h) Expose.

(i) Keep wafers in a dark container while transferring them to the development room.

7. Development:

(a) Fill one plastic container with 250 ml MF-319 developer. Do not dilute.

NOTE: If you don't use enough, development time starts drifting from wafer to wafer.

(b) Fill another container with DI water.

(c) Develop for 30 seconds to 40 seconds.

(d) Shake the bowl once every 10 seconds.

(e) Dip the wafer into the container with DI water.

(f) Rinse the wafer under the running DI water.

(g) Place the wafer on a cleanroom wipe face-side up.

(h) Blow nitrogen.

(i) Repeat this procedure every time you remove the wafer from the developer.

(j) Inspect the wafer under the microscope after 30 seconds of development time. Look at the wafer at multiple positions, make sure there is no rainbow color in the gaps of the pattern. Look at the finest features on the wafer to see if they have fallen off or are deformed. If development is not complete, develop for another 10 seconds.

Shipley 1827 Photoresist thickness

Thickness	center: 2.98 μm, edge: 2.98 μm	center: 3.6 μm, edge: 3.47 μm	center: 4.2 μm, edge: 3.85 μm
Spin coating	500 rpm: 10 secs, 4500 rpm: 30 secs	500 rpm: 10 secs, 3500 rpm: 30 secs	500 rpm: 10 secs, 2500 rpm: 30 secs
Exposure	20 sec	25 sec	30 sec

Table C.2: Critical process parameters: Shipley 1827 lithography.

C.2 AZ4620 1000 rpm Lithography with 10 W power

Overview	
Input	Si/SOI wafer(s), photomask
Consumables	AZ4620 photoresist, aluminum foil, cleanroom wipes, wafer tweezers, AZ400K photoresist developer
Equipment	MA6 aligner, Laurell spinner, soft-bake furnace (90°C), dehydration-bake furnace (120°C), HMDS oven
Output	Photoresist patterned wafers
Process Parameters	
Prebake	45 mins dehyration @ 120°C
HMDS coat	in HMDS oven
Photoresist Coat	500 rpm: 10 secs, 1000 rpm: 40 secs (ACCL 5 for both)
Soft-bake	20 minutes @ 90°C
Exposure	Soft-contact @ 25 μm gap, 100 secs exposure @ 10 W lamp power
Development	AZ400K developer:DI water (1:3.5), 7.5 minutes

Table C.3: AZ4620 lithography equipment.

Important Notes

Recipe is only valid for 10 W power on MA6, do not use if the lamp power is different.

Process

(a) Place a large enough aluminum foil into soft-bake furnace. Place wafers on this aluminum foil processing-side up.

(b) Dehydrate the wafers at 120°C in the clean dehydration furnace for 45 minutes.

(c) Apply hexamethyldisilizane (HMDS) inside the HMDS oven.

NOTE: Alternatively, HMDS can be spin-coated using Laurell spinner: 5000 rpm: 40 sec. However, the YES HMDS vapor prime oven allows for more even coating, reduced chemical consumption and less wafer contamination.

(d) Check to see that the HMDS oven pump is on, check vacuum gauge to verify they are in range, check HMDS level. Watch the LCD screen during your run to make sure the HMDS is actually doing its job. Make sure that the yellow light is blinking at the end of your run.

(e) Spinning:

i. Make sure the spinner is clean, if previous user left resist residue clean with acetone and wipe with cleanroom wipes.

ii. Set Laurell spinner to:

A. 1st step: 500 rpm, accel. 5, 10 seconds

B. 2nd step: 1000 rpm, accel. 5, 40 seconds

iii. Use a dummy sample to do a dry run and make sure the program works.

iv. Place the wafer on the spinner, check for vacuum, center the wafer.

v. Blow nitrogen on the wafer.

vi. Pour photoresist to about 2/3 of the wafer, do not use the pippette. At this step pouring more than necessary is always better than pouring not enough.

vii. Spin the resist, put the wafer into the soft-bake furnace for 20 minutes onto the aluminum foil.

NOTE: Never place wafers into furnaces without an extra layer of aluminum foil. We have double-sided processes that are very sensitive to contamination on the back-side of your wafer.

viii. When done, wipe the photoresist bottle with a dry cleanroom wipe, this minimizes dried resist particulates next time you do lithorgraphy.

ix. Cleanup the spinner.

(f) Exposure:

i. When soft-bake is done, get your wafers and mask ready near MA-6.

ii. Inspect the photomask visually, if there is any visible photoresist residue do a solvent clean on the photomask. If it does not remove the residue, a proper mask clean is required.

iii. Place the mask chrome side up, blow nitrogen on it, load it.

iv. Do a lamp test on the MA-6 aligner before your first run. It should read 10 W.

v. Set the mask aligner to soft-contact with 25 μm gap. 100 seconds exposure time.

vi. Load the wafer.

vii. Align the wafer if alignment is needed.

viii. Expose.

ix. Keep wafers in a dark container while transferring them to the development room.

(g) Development:

i. Mix in a plastic container AZ400K developer:DI water (1:3.5)

NOTE: If you don't use enough, development time starts drifting from wafer to wafer.

ii. Fill another container with DI water.

iii. Develop for 30 seconds to 60 seconds.

iv. Shake the bowl once every 30 seconds.

v. Dip the wafer into the container with DI water.

vi. Rinse the wafer under the running DI water.

vii. Place the wafer on a cleanroom wipe face-side up.

viii. Blow nitrogen.

ix. Repeat the last six steps procedure every time you remove the wafer from the developer.

x. Inspect the wafer under the microscope after every 30 seconds of development time. Look at the wafer at multiple positions, make sure there is no rainbow color in the gaps of the pattern. Look at the finest features on the wafer to see if they have fallen off or are deformed.

C.3 Backside etching of blind via holes

C.3.1 Hard mask etching

Overview	
Input	SOI wafer(s) with patterned photoresist layer
Equipment	UCLA STS AOE Oxide Etcher
Output	Wafers with patterned hard mask
Process Parameters	
Cleaning	"O2 Clean", 30 minutes
Oxide etching	"Oxidapic", 20 minutes
Nitride etching	"LJYDBOX", 15 minutes

Table C.4: Vias fabrication: hard mask etching equipment.

Important Notes

The photoresist mask for this step is defined using lithography procedure described in Section C.2.

Process

(a) UCLA STS AOE: 30 min "O2 Clean" recipe

(b) Measure initial oxide thickness using Nanospec. For the SOI wafer with a 500 μm handle layer, a 3-5 μm thick oxide layer is usually required.

(c) Place wafer in AOE, gently N2 blow away dust particles, and etch for 5 min using the "Oxidapic" recipe (note orientation in chuck). NOTE: If you etch longer at a time, the PR may burn, depending on the He leak rate.

(d) Measure oxide thickness using Nanospec.

(e) Place wafer in AOE, gently N2 blow away dust particles, and etch for 5 min using the "Oxidapic" recipe (orient with a 90 degree rotation as compared to previous etch)

(f) Measure oxide thickness using Nanospec. Estimate the etch rate and time necessary to complete the etch. For a 5 μm thick oxide, the total etch time is approximately 20 minutes.

(g) Place wafer in AOE, gently N2 blow away dust particles, and etch using the "Oxidapic" recipe for the time estimated at previous step.

(h) Next, a 1 μm thick LPCVD nitride layer has to be etched.

(i) Etch wafer in AOE for 5 min using the "LJYDBOX" recipe (note orientation in chuck).

(j) Measure nitride thickness using Nanospec.

(k) Place wafer in AOE, gently N2 blow away dust particles, and etch for 5 min using the "LJYDBOX" recipe (orient with a 90 degree rotation as compared to previous etch)

(l) Measure nitride thickness using Nanospec. Estimate the etch rate and time necessary to complete the etch. For a 1 μm thick nitride, the total etch time is

approximately 15 minutes.

(m) Measure nitride thickness using Nanospec to make sure the nitride is etched.

(n) Use the UCLA Matrix Asher to remove PR.

C.3.2 Silicon etching

Overview	
Input	SOI wafer(s) with patterned oxide mask
Equipment	UCLA FDRIE
Output	Wafers with ethed holes thru the handle wafer
Process Parameters	
Cleaning	"O2 Clean", 30 minutes
Silicon etching	"FN", 100 minutes

Table C.5: Vias fabrication: silicon etching equipment.

(a) UCLA FDRIE: 30 min "O2 Clean".

(b) Place wafer into FDRIE, gently N2 blow away dust particles, and etch using the "FN" recipe.

(c) Time to etch 500 μm layer of silicon is approximately 100 minutes, but actual value changes over time.

C.4 Etching of device layer

C.4.1 Hard mask etching using UCLA STS AOE Oxide Etcher

Important Notes

The photoresist mask for this step is defined using lithography described in Section C.1.

Overview	
Input	SOI wafer(s) with patterned photoresist layer
Equipment	UCLA STS AOE Oxide Etcher
Output	Wafers with patterned hard mask
Process Parameters	
Cleaning	"O2 Clean", 30 minutes
Oxide etching	"Oxidapic", 6 minutes

Table C.6: Sensors fabrication: hard mask etching equipment (UCLA).

Process

(a) UCLA STS AOE: 30 min "O2 Clean" recipe

(b) Measure initial oxide thickness using Nanospec. SOI waferswith a 1.5 μm thick layer of TOX were used in the Folded MEMS process.

(c) Place wafer in AOE, gently N2 blow away dust particles, and etch for 60 sec using the "Oxidapic" recipe (note orientation in chuck). NOTE: If you etch longer at a time, the PR may burn, depending on the He leak rate.

(d) Measure oxide thickness using Nanospec.

(e) Place wafer in AOE, gently N2 blow away dust particles, and etch for 60 sec using the "Oxidapic" recipe (orient with a 90 degree rotation as compared to previous etch)

(f) Measure oxide thickness using Nanospec. Estimate the etch rate and time necessary to complete the etch. For a 1.5 μm thick TOX, the total etch time is approximately 6 minutes.

(g) Repeat steps 5) and 6) until the etching is complete.

(h) Use acetone to remove the photoresist layer

NOTE: Alternatively, the hard mask can be etched using the UCI SPTS APS PM.

Overview	
Input	SOI wafer(s) with patterned photoresist layer
Equipment	UCI SPTS APS PM
Output	Wafers with patterned hard mask
Process Parameters	
Cleaning	"O2 Clean", 30 minutes
Oxide etching	"UCI SiO2 PR", 8 minutes

Table C.7: Sensors fabrication: hard mask etching equipment (UCI).

C.4.2 Hard mask etching using UCI SPTS APS PM

Important Notes

The photoresist mask for this step is defined using lithography described in Section C.1.

UCI SPTS APS PM uses an electrostatic chuck for holding a wafer. If the wafer to be processed has an oxide or a nitride layer on the back, then deposition of a thin metal layer on the back side is required prior to processing the wafer in SPTS APS PM.

Process

(a) UCI SPTS APS PM: 30 min "O2 Clean" recipe

(b) Measure initial oxide thickness using Nanospec. SOI waferswith a 1.5 μm thick layer of TOX were used in the Folded MEMS process.

(c) Place wafer in SPTS, gently N2 blow dry, and etch for 120 sec using the "UCI SiO2 PR" recipe (note orientation in chuck). NOTE: If you etch longer at a time, the PR may burn, depending on the He leak rate.

(d) Measure oxide thickness using Nanospec.

(e) Place wafer in SPTS, gently N2 blow away dust particles, and etch for 120 sec using the "UCI SiO2 PR" recipe.

(f) Measure oxide thickness using Nanospec. Estimate the etch rate and time necessary to complete the etch. For a 1.5 μm thick TOX, the total etch time is approximately 8 minutes.

(g) Repeat steps e) and f) until the etching is complete.

(h) Use acetone to remove the photoresist layer

C.4.3 Device layer etching using UCLA FDRIE

Overview	
Input	SOI wafer(s) with patterned oxide hard mask
Equipment	UCLA FDRIE
Output	Wafers with etched SOI sensors
Process Parameters	
Cleaning	"O2 Clean", 30 minutes
Oxide etching	"Darkfield 2", 54 minutes

Table C.8: Sensors fabrication: silicon etching equipment (UCLA).

Important Notes

The photoresist mask for this step is defined using lithography described in Section C.1.

Process

(a) UCLA FDRIE: 30 min "O2 Clean".

(b) Place wafer into FDRIE, gently N2 blow away dust particles, and etch using the "Darkfield 2" recipe.

(c) Time to etch 100 μm layer of silicon is approximately 54 minutes, but actual value changes over time and depends on the sensors features.

NOTE: Alternatively, the device layer can be etched using the UCI STS.

C.4.4 Device layer etching using UCI STS DRIE

Overview	
Input	SOI wafer(s) with patterned oxide hard mask
Equipment	UCI STS DRIE
Output	Wafers with etched SOI sensors
Process Parameters	
Cleaning	"O2 Clean", 30 minutes
Oxide etching	"Process b", 57 minutes

Table C.9: Sensors fabrication: silicon etching equipment (UCI).

Important Notes

The photoresist mask for this step is defined using lithography described in Section C.1.

Process

(a) UCI STS DRIE: 30 min "O2 Clean".

(b) Place wafer into STS, gently N2 blow away dust particles, and etch using the "Process b" recipe.

NOTE: Alternatively, "Process a" can be used: it has a slower etch rate but allows for better uniformity.

(c) Time to etch 100 μm layer of silicon using "Process b" recipe is approximately 57 minutes, but actual value changes over time and depends on the sensors features.

C.5 Nickel Electroplating

Important Notes

When handling the plating solution, wear the prescribed protective clothing as detailed

Overview	
Input	Si/SOI wafer(s) with Cr/Au seed layer
Consumables	Nickel bar anode, pyrex glass beaker, Techni Nickel HT-2 RTU (Technic Inc.), cleanroom wipes, wafer tweezers, alligator clip wires, copper tape, dicing tape (blue tape), thermometer, magnetic stir bar
Equipment	DC power supply: BK Precision 9122A Single Output Programmable DC Power Supply, hotplate, fume hood
Output	Nickel electroplated wafers
Process Parameters	
Plating	15 mins @ 54°C

Table C.10: Nickel electroplating equipment

in the appropriate material safety data sheet. Perform electroplating inside the fume hood.

Process

(a) Seed Layer Deposition

In Folded MEMS IMU process, nickel is deposited on top of the 0.5 μm thick Au layer (for reinforccemrent of metal traces and contact pads). No addition "seed layer" deposition is necessary.

(b) Prepare the Technic Nickel HT-2 RTU (ready-to-use) nickel sulfamate electroplating solution in a beaker large enough for a 4 inch wafer (2000 mL). The volume of the solution should be enough to cover the area on the wafer to be electroplated. NOTE: this is truly "ready to use" solution since it has all the necessary components, and has already been balanced by the manufacturer.

(c) Use Dektek to measure in several locations the distance between the photoresist and gold layer (photoresist thickness before plating).

(d) Prepare the sample:

i. Protect the front side of the wafer (device side) with a dicing tape (to avoid contamination or damaging of oxide layer).

ii. The bottom side of the wafer is covered with a thick layer of photoresist. The photoresist layer is photolithographically patterned to open the areas to be electroplated (metal traces and contact pads or contact pads only).

iii. To make a reliable electrical contact without breaking the wafer, the copper tape and an alligator clip can be used. Connect one end of the copper tape to the gold layer of the wafer.

NOTE:Sometimes the pattern to be electroplated is too close to the edge of the wafer. In this case, the solution might cover the area of the electrical contact. To prevent parasitic Ni growing, cover the area of the electrical contact and the length of the copper inside the solution with the insulating tape.

iv. Rinse the wafer with DI water prior to the electroplating.

(e) Place the beaker on the hot plate.

(f) Put the magnetic stirring bar into the solution.

(g) Immerse the nickel anode into the the solution and connect the positive terminal of the power supply to the anode using an alligator clip wire.

(h) Immerse the wafer into the the solution and connect the negative terminal of the power supply to the end of the copper tape using an alligator clip wire.

(i) Turn on the hotplate. Adjust the temperature in order to meet the operating parameters. Nickel electroplating is performed at 54 °C temperature. Wait until the solution temperature stabilizes. Use thermometer to measure the temperature of the solution.

(j) Apply the current to meet the desired current density value. For the samples described in this dissertation, the total plating time for 1 μm layer of nickel was approximately 15 min with a current of 8.3 mA (0.3 V).

NOTE: Deposition thickness is proportional to applied current density. At high

current densities deposition rate is higher; however, stress and hardness of the electroplated film increase with increased current density.

(k) Perform the electroplating process until you reach the desired thickness of nickel.

(l) Remove the wafer from solution, rinse with DI water and blow dry.

(m) Remove the nickel anode from solution, rinse with DI water and blow dry.

(n) Use Dektek to measure in several locations the distance between the photoresist and gold layer (photoresist thickness after plating). The difference in photoresist thickness before and after plating equals to the thickness of the plated nickel layer.

C.6 Copper Electroplating

Overview	
Input	SOI wafer(s) with thru-wafer blind via holes
Consumables	4 inch copper anode, pyrex glass beaker, acid type copper electroplating solution (TRANSENE, USA), brightener and leveler additives (JCU Co., CU-BRIGHT EP-30), cleanroom wipes, wafer tweezers, alligator clip wires, copper tape, dicing tape (blue tape), 20 % HF solution
Equipment	DC power supply: BK Precision 9122A Single Output Programmable DC Power Supply, hotplate, fume hood, Elmasonic P 120H Ultrasonic unit
Output	SOI wafer(s) with copper electroplated thru-wafer vias
Process Parameters	
Sonication	5 mins @ room temperature under 37 kHz sonication, no current applied
Plating under sonication	10 mins @ room temperature under 37 kHz sonication, current density of 5 mA/cm^2
Plating in silent mode	8 hrs @ room temperature in a silent mode, current density of 5 mA/cm^2

Table C.11: Copper electroplating equipment

Important Notes

When handling the plating solution, wear the prescribed protective clothing as detailed in the appropriate material safety data sheet. Perform electroplating inside the fume hood.

Process

(a) Seed Layer Deposition

In Folded MEMS IMU process, the highly-doped device layer of the SOI wafer is used as a seed for initiating of a bottom-up copper electroplating process. No addition "seed layer" deposition is necessary.

(b) Prepare the copper electroplating solution in a beaker large enough for a 4 inch wafer (2000 mL). Mix in the brightener and leveler additives (JCU Co., CU-BRIGHT EP-30) to the acid type copper electroplating solution (TRANSENE, USA). The volume of the solution should be enough to cover the area on the wafer to be electroplated.

(c) Use Dektek to measure in several locations the distance between the photoresist and gold layer (photoresist thickness before plating).

(d) Prepare the sample:

i. Protect the front side of the wafer (device side) with a dicing tape (to avoid Cu deposition).

ii. Usually, copper electroplating process is performed immediately after the HF etching step. During this step, a 5 μm thick layer of buried oxide on the bottom of the blind thru-wafer via holes is removed. Otherwise, additional HF dip step might be required to remove native oxide on the bottom of the thru-wafer via holes. For this purpose, immerse the wafer into 20 % HF solution for 30 secs. Rinse the wafer with DI water.

iii. The bottom side of the wafer is covered with a LPCVD nitride layer. Only the blind via holes are exposed. On the front side of the wafer, remove dicing tape from a small area on the edge of the wafer in order to permit an electrical contact with the device layer, clear this area from TOX and nitride (by immersing only this area into a 40 % HF solution until Si layer can be seen) .

iv. Rinse the wafer with DI water prior to the electroplating.

v. To make a reliable electrical contact without breaking the wafer, the copper tape and an alligator clip can be used. Connect one end of the copper tape to the area on the front side of the wafer cleared from the dicing tape.

NOTE:Sometimes the pattern to be electroplated is too close to the edge of the wafer. In this case, the solution might cover the area of the electrical contact. To prevent parasitic Cu growing, cover the area of the electrical contact and the length of the copper inside the solution with the insulating tape.

(e) Place the beaker into a sonicator. Fill the sonicator tank with water.

(f) Put the magnetic stirring bar into the plating solution.

(g) Immerse the copper anode into the the solution and connect the positive terminal of the power supply to the anode using an alligator clip wire.

(h) Immerse the wafer into the the solution and connect the negative terminal of the power supply to the end of the copper tape using an alligator clip wire.

(i) Start the sonicator: 37 kHz for 5 min, no current applied.

(j) Apply the current to start the plating process: 10 mins @ room temperature under 37 kHz sonication, current density of 5 mA/cm^2.

(k) Turn off the sonicator. Continue plating: 8 hrs @ room temperature in a silent mode, current density of 5 mA/cm^2.

NOTE: Deposition rate is proportional to the applied current density. At high current densities deposition rate is higher; however, voids can form at high current density.

(l) Perform the electroplating process until all the via holes are filled with copper.

NOTE: Cu plating uniformity is an important issue since even closely placed vias may show different Cu plating rate. To improve the plating uniformity, Cu has to be over plated during the electroplating step. Once all the vias are filled, the wafer polishing is performed to remove the redundant Cu on the backside of the wafer.

(m) Remove the wafer from solution, rinse with DI water and blow dry.

(n) Remove the Cu anode from solution, rinse with DI water and blow dry.

C.7 Chrome and Gold Deposition (Metal Traces)

Overview	
Input	Si/SOI wafer(s)
Consumables	Chrome and Gold targets
Equipment	E-beam evaporator
Output	Si/SOI wafer(s) covered with Cr/Au layers
Process Parameters	
Cr	0-500 Angstroms, 0.3 A/sec
Au	0-500 Angstroms, 0.5 A/s
Au	500-4500 Angstroms, 1 A/s
Au	4500-5000 Angstroms, 0.5 A/s

Table C.12: Chrome and gold deposition equipment.

Process

(a) Load wafers into E-beam evaporator along with Chrome and Gold targets. Wafers fixed on edges with Kapton tape.

(b) Let the machine pump down.

(c) Deposition process:

i. Cr: 500 Angstroms, 0.3 A/s;

ii. Au: 0-500 Angstroms, 0.5 A/s;

iii. Au: 500-4500 Angstroms, 1 A/s;

iv. Au: 4500-5000 Angstroms, 0.5 A/s.

(d) Let the machine pump down.

(e) Remove wafers and targets.

C.8 Chrome and Gold Etching (Metal Traces)

Overview	
Input	Si/SOI wafer(s) covered with Cr/Au layers
Consumables	Chromium cermet etchant TFE, gold etchant GE 8148, poly containers.
Equipment	Metal Etch Bench
Output	Si/SOI wafer(s) with Cr/Au layers patterned
Process Parameters	
Au	GE 8148 (50 Angstrom/sec)
Cr	Cermet etchant TFE (20 Angstrom/sec)

Table C.13: Chrome and gold etching equipment.

Important Notes

The photoresist mask for this step is defined using lithography described in Section C.1.

When handling the metal etchants, wear the prescribed protective clothing as detailed in the appropriate material safety data sheet. Perform etching inside the fume hood of a metal etch bench.

Process

(a) Pour Gold etchant GE 8148 into a poly container.

(b) Pour Chromium cermet etchant TFE into a poly container.

(c) Pour DI water into two poly containers.

(d) Quickly immerse wafer into a Gold etchant, PR layer up, into liquid.

(e) Leave wafer in liquid for 2 min, agitating at least every 30 sec.

(f) Quickly remove wafer from liquid to see if gold has been removed completely.

(g) If some gold remains, immerse the wafer into gold etchant for another 2 min.

NOTE: If you are reusing the gold etchant, the etch time will increase over time.

(h) After gold is removed, immerse wafer into a first DI water container, then rinse under the running DI water.

(i) N2 blow dry.

(j) Quickly immerse wafer into a Chrome etchant, PR layer up, into liquid.

(k) Leave wafer in liquid for 2 min, agitating at least every 30 sec.

(l) Quickly remove wafer from liquid to see if chrome has been removed completely.

(m) If some gold remains, immerse the wafer into Chrome etchant for another 2 min.

NOTE: If you are reusing the Chrome etchant, the etch time will increase over time.

(n) After chrome is removed, immerse wafer into a second DI water container, then rinse under the running DI water.

(o) N2 blow dry.

C.9 Metal Lift Off Process

Overview	
Input	Si/SOI wafer(s), photomask
Consumables	AZ nLoF 2035 Photoresist, AZ 300 MIF developer, poly containers.
Equipment	MA6 Mask Aligner, hotplate
Output	Si/SOI wafer(s) with Cr/Au layers patterned
Process Parameters	
Dehydration	15 min @ 110 °C on hotplate
Photoresist Coat	500 rpm: 10 secs, 1500 rpm: 30 secs (ACCL 5 for both)
Bake	60 seconds @ 110 °C on hotplate
Exposure	Soft-contact @ 25 μm gap, 22 secs exposure @ 10 W lamp power
Bake	60 seconds @ 110 °C on hotplate
Development	AZ 300 MIF developer, 30 seconds to 40 seconds
Cr/Au deposition	E-Beam deposition of 0.05 μm layer of Cr + 0.5 μm layer of Au
PR removal	Acetone, overnight

Table C.14: Metal lift-off process equipment.

Process

(a) AZ nLoF 2035 Photoresist Lithography

i. Dehydrate wafer on a hot plate at @ 110 °C for 15 minutes.

ii. Spinning:

A. Make sure the spinner is clean, if previous user left resist residue clean with acetone and wipe with cleanroom wipes.

B. Set Laurell spinner to:

C. 1st step: 500 rpm, accel. 5, 10 seconds

D. 2nd step: 1500 rpm, accel. 5, 30 seconds

E. Use a dummy sample to do a dry run and make sure the program works.

F. Place the wafer on the spinner, check for vacuum, center the wafer.

G. Blow nitrogen on the wafer.

H. Pour photoresist to about 2/3 of the wafer, do not use the pippette. At this step pouring more than necessary is always better than pouring not enough.

I. Spin the resist.

iii. Bake wafer on a hot plate at @ 110 °C for 60 seconds.

iv. Exposure:

A. Get your wafers and mask ready near MA-6.

B. Inspect the photomask visually, if there is any visible photoresist residue do a solvent clean on the photomask. If it does not remove the residue, a proper mask clean is required.

C. Place the mask chrome side up, blow nitrogen on it, load it.

D. Do a lamp test on the MA-6 aligner before your first run. It should read 10 W.

E. Set the mask aligner to soft-contact with 25 μm gap. 22 seconds exposure time.

F. Load the wafer.

G. Align the wafer if alignment is needed.

H. Expose.

v. Bake wafer on a hot plate at @ 110 °C for 60 seconds.

vi. Keep wafers in a dark container while transferring them to the development room.

vii. Development:

A. Fill one plastic container with 250 ml AZ 300 MIF developer. Do not dilute.

NOTE: If you don't use enough, development time starts drifting from wafer to wafer.

B. Fill another container with DI water.

C. Develop for 30 seconds to 40 seconds

D. Shake the bowl once every 10 seconds.

E. Dip the wafer into the container with DI water.

F. Rinse the wafer under the running DI water.

G. Place the wafer on a cleanroom wipe face-side up.

H. N2 blow dry.

I. Repeat this procedure every time you remove the wafer from the developer.

J. Inspect the wafer under the microscope after 30 seconds of development time. Look at the wafer at multiple positions, make sure there is no rainbow color in the gaps of the pattern. Look at the finest features on the wafer to see if they have fallen off or are deformed. If development is not complete, develop for another 10 seconds.

(b) Deposit 0.05 μm thick layer of Cr and 0.5 μm thick layer of Au, using procedure described in Section C.7.

(c) Soak sample in acetone overnight in a poly container, remove extraneous material with squirt bottle.

NOTE: Close the container with a lid (not tight!) to prevent acetone from evaporating.

(d) N2 blow dry.

C.10 Polyimide deposition and curing

Overview	
Input	Si/SOI wafer(s), photomask
Consumables	HD-4110 polyimide, adhesion promoter VM-652, PA-401D developer, PA-400R developer, poly containers.
Equipment	MA6 Mask Aligner, hotplate, nitrogen environment oven, dehydration-bake furnace (120°C)
Output	Si/SOI wafer(s) with polyimide layer patterned
Process Parameters	
Dehydration	30 min @ 120 °C in furnace
VM-652 Adhesion promoter application	500 rpm: 10 secs, 2500 rpm: 30 secs;
Bake	60 seconds @ 120 °C on hotplate
HD-4110 polyimide application	500 rpm: 10 secs, 1500 rpm: 40 secs;
Bake	12 minutes @ 120 °C on hotplate
Exposure	Soft-contact @ 25 μm gap, 60 secs exposure @ 10 W lamp power
Bake	5 minutes @ 120 °C on hotplate
Development	200 ml PA-401D and 20 ml of PA-400R: 2 minutes; spray rinse PA-400R
Curing	Nitrogen environment: 200°C for 30 minutes; 375°C for 30 minutes

Table C.15: Polyimide deposition and curing equipment.

Process

(a) Dehydrate wafer i dehydration oven for 30 minutes @ 120°C.

(b) Apply adhesion promoter VM-652:

i. Pour adhesion promoter VM-652 onto entire wafer, let sit for 10 seconds.

ii. Spin dry at 2500 rpm for 30 seconds.

iii. Bake wafer on a hot plate at @ 120 °C for 1 minute.

NOTE: Potentially, thin layer of Cr can be used to improve adhesion between the silicon and polyimide.

(c) Pour on liquid HD-4110 polyimide resin in a liberal amount.

NOTE: Polyimide bottle has to be open @ room temperature to avoid contamination with moisture. Remove the bottle outside the refrigerator the night before the polyimide deposition.

(d) Remove bubbles by pushing to edge of wafer with tweezers.

(e) Spin the polyimide:

i. 1st step: 500 rpm, 10 seconds

ii. 2nd step: 1500 rpm, 40 seconds

iii. Bake wafer on a hot plate at @ 120 °C for 12 minutes.

(f) Exposure:

i. Get your wafers and mask ready near MA-6.

ii. Inspect the photomask visually, if there is any visible photoresist residue do a solvent clean on the photomask. If it does not remove the residue, a proper mask clean is required.

iii. Place the mask chrome side up, blow nitrogen on it, load it.

iv. Do a lamp test on the MA-6 aligner before your first run. It should read 10 W.

v. Set the mask aligner to soft-contact with 25 μm gap. 60 seconds exposure time.

vi. Load the wafer.

vii. Align the wafer if alignment is needed.

viii. Expose.

(g) Bake wafer on a hot plate at @ 120 °C for 5 minutes.

(h) Development:

i. Fill one plastic container with 200 ml of PA-401D and 20 ml of PA-400R. Do not dilute.

NOTE: If you don't use enough, development time starts drifting from wafer to wafer.

ii. Fill a spray bottle with PA-400R. Do not dilute.

iii. Immerse in solution of 200 ml PA-401D and 20 ml of PA-400R 2 minutes.

iv. Shake the bowl once every 10 seconds.

v. Spray PA-400R rinse on sample for 30 seconds in separate container.

vi. Repeat the last two steps until fully developed. NOTE: Do not rinse the wafer under water.

vii. Place the wafer on a cleanroom wipe face-side up.

viii. N2 blow dry.

ix. Repeat this procedure every time you remove the wafer from the developer.

x. Inspect the wafer under the microscope to ensure it was developed.

(i) Polyimide curing

i. Use the furnace with nitrogen environment.

ii. Set up the temperature profile:

A. ramp rate from room temperature to 200°C: 7°C per minute;

B. 200°C for 30 minutes;

C. ramp rate from 200°C to 375°C: 7°C per minute;

D. 365°C for 60 minutes;

E. gradual cooling to room temperature.

C.11 Parylene deposition and etching

Overview	
Input	Si/SOI wafer(s)
Consumables	Parylene-C dimer, aluminum foil
Equipment	UCI SCS parylene coater, UCI Trion RIE
Output	Si/SOI wafer(s) with parylene-C layer patterned
Process Parameters	
Parylene coating	Pyrolysis temperature: 650 °C, deposition temperature: 25 °C, deposition pressure: 30 mTorr
Ti hard mask deposition	E-Beam: 1500 Angstrom thick layer of Ti
Pattern Ti mask	AZ nLoF 2035 photoresist lithography
Etching of Ti hard mask	UCI Trion RIE: Pressure: 50 mT; O2: 5 sccm; CF4: 45 sccm; Power: 100 W; Time: 5 minutes
Chamber preconditioning	Pressure: 150 mT; O2: 50 sccm; Power: 0 W; Time: 60 seconds
Etching of Photoresist and Parylene-C	Pressure: 150 mT; O2: 50 sccm; Power:100 W; Time: 30 minutes

Table C.16: Parylene deposition and etching equipment.

Important Notes

Cr layer (500 Angstroms thick) can be used to improve adhesion between the parylene an a Si/SOI wafer.

Process

(a) Parylene coating using UCI SCS parylene coater:

i. Fill the liquid nitrogen tank;

ii. Thoroughly clean the inside of the vacuum chamber (peel off the parylene film from previous run);

iii. Make a boat out of aluminum foil;

iv. Place the aluminum foil boat on the scale, and zero the scale;

v. Add the Parylene-C dimer into the boat until the desired weight (each gram correspond to approximately 0.5 μm thickness of film);

vi. Insert the boat with the dimer into the furnace chamber;

vii. Turn the emergency stop and press the power button to start the machine;

viii. Pump down the chamber;

ix. Vent the chamber, load wafer(s) on loading tray of the parylene coater;

x. Place the lid on to close the chamber;

xi. Pump down the chamber;

xii. Connect to the liquid nitrogen tank (make sure the tank is at least half-full), turn on the liquid nitrogen;

xiii. Wait until pressure stabilize below 30mT;

xiv. Turn "Vacuum" to "Vacuum" position;

xv. Turn the "Furnace" to "Enable" position;

xvi. Press the green button to start;

xvii. The furnace temperature and gauge reading should start to increase;

xviii. Enable the vaporizer when the furnace temperature reaches 650° C and press start to initiate coating process (pressure will increase, once the vacuum pressure stabilizes around the set pressure, the coating process is completed);

xix. Press the green button to stop the process;

xx. Disable the furnace and vaporizer, make sure the switch is at the off position;

xxi. Turn the vacuum to "Vent" position;

xxii. Turn off the liquid nitrogen;

xxiii. Remove the wafer tray from the chamber, and collect the wafers;

xxiv. Press the emergency stop button to shut the machine off;

xxv. Make sure to remove the thin layer of Parylene coated on the chamber sidewalls, the lid, and wafer holder.

xxvi. After cleaning everything, place the wafer holder and lid back.

(b) Ti hard mask deposition and patterning:

i. Follow the operating procedure for E-Beam evaporator to deposit 1500 Angstrom thick layer of Ti;

ii. Pattern Ti mask using AZ nLoF 2035 photoresist lithography, described in Section C.9;

(c) RIE etching of Ti hard mask, photoresist and Parylene-C using UCI Trion RIE:

i. Etching of Ti hard mask:

Pressure: 50 mT; O2: 5 sccm; CF4: 45 sccm; Power: 100 W; Time: 5 minutes.

ii. Chamber preconditioning:

Pressure: 150 mT; O2: 50 sccm; Power: 0 W; Time: 60 seconds.

iii. Photoresist and Parylene-C:

Pressure: 150 mT; O2: 50 sccm; Power:100 W; Time: 30 minutes.

NOTE: Immersing the wafer into 20 % HF solution for about 1 minute might be necessary to remove a thin film of redeposited Ti.

Overview	
Input	SOI wafer(s) or SOI sensor dies
Consumables	40% Hydrofluoric (HF) acid, cleanroom wipes, tweezers, protection gloves, protective clothing, shield
Equipment	Idonus HF VPE-100, Chemical Workbench, IDONUS IR-Light Wafer Inspection Microscope
Output	released sensors

Table C.17: SOI sensors release equipment.

C.12 SOI Sensors Release Using Vapor Phase HF Etcher

Important Notes

HF is a very dangerous acid. If you get in contact with HF you will not recognize the effects instantly but it will attack your bones. Special precautions must be taken when handling HF acid.

Before you start working with the apparatus, make sure that the safety requirements are accomplished:

- Wear protection gloves;
- Wear a shield to protect your eyes and your face;
- Wear protective clothing;
- The air extraction of your fume hood has to be operational.

HF Ether Equipment diagram

The Vapor Phase Etcher (HF VPE) apparatus consists of the following components:

- Container;

- Wafer holder with connection cable;
- Controller box;
- Mechanical clamping ring.

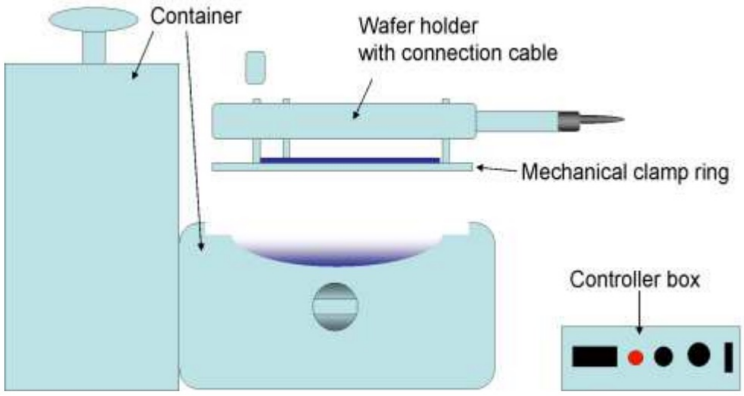

Figure C.1: Vapor Phase Etcher diagram.

The container consists of:

- Reaction chamber;
- Reservoir;
- Reservoir handle;
- Valve;
- Lid.

The container is a system composed of a reaction chamber and a reservoir. The reservoir has the function to store HF acid when the HF VPE apparatus is not in operation and allows a simple and safe transfer of the acid in and out of the reaction chamber. The working principle of the reservoir and the container is called communicating vessels. When the reservoir is in high position, (i.e. the reservoir handle is pulled up) the liquid can flow into the reaction chamber (if the valve is open). If the reservoir

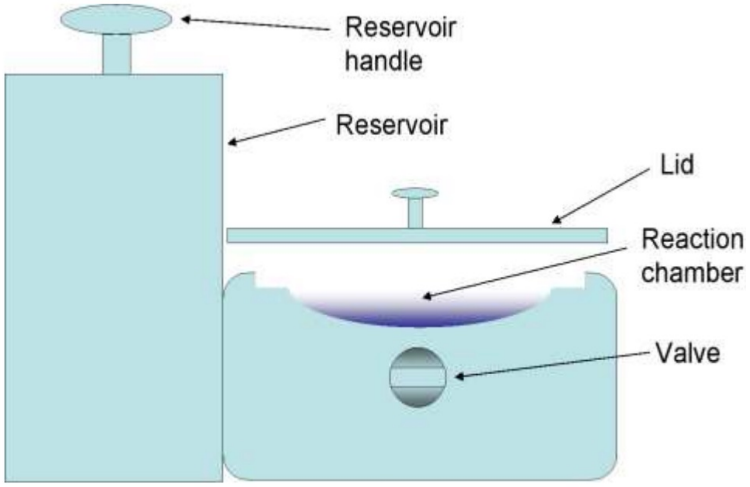

Figure C.2: Container diagram.

is in low position, (i.e. reservoir handle is down) the liquid flows from the reaction chamber into the reservoir. The valve is open if the tap is vertical and closed if the tap is horizontal. The tap can be turned in both directions and does not have a stopper.

The wafer holder consists of:

- Heating plate;
- Handle with connection cable;
- Mechanical clamp ring;
- Electrostatic chuck.

Controller Box:

- Main switch;
- Temperature controller;
- Socket for connection to wafer holder;
- Switch for electrostatic clamping;

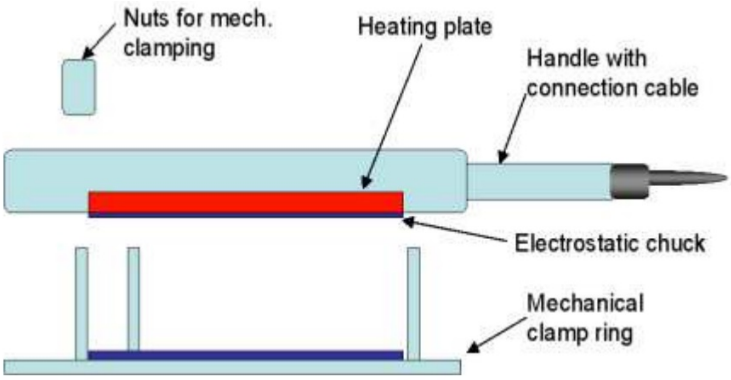

Figure C.3: Wafer holder diagram.

- Potentiometer for adjusting electrostatic clamping force;
- Socket for power supply;
- Fuse.

Process

(a) Make sure the reservoir is filled with HF. If not, ask the responsible person for service (SERVICE MODE).

(b) Connect the connection cable of the wafer holder to the socket of the controller box.

(c) Switch the main power switch of the controller box ON.

(d) Program the temperature controller to the desired temperature. To do this press the P button once and select the desired temperature. SOI sensors presented in this dissertation were released at $36°C$ or at $45°C$. Higher release temperature allows to reduce the risk of stiction but results in a slower etch rate.

(e) Wait until the desired temperature is reached (1-5 min). The temperature of the heating plate is indicated on the temperature controller.

(f) Place the wafer holder in front of you so that the electrostatic chuck is facing upward.

(g) Place your wafer or chip on the electrostatic chuck so that the surface to be etched is facing you.

(h) Switch the power for the electrostatic chuck to ON position. Adjust the force by turning the potentiometer.

(i) Make sure your wafer is fixed, use a tweezer to move the wafer/ devices around. If they are stuck (or hard to move), then the chuck is working fine.

(j) Place the wafer holder on the reaction chamber with the wafer facing down.

(k) Lift reservoir handle up.

(l) Turn the security pin to fix the reservoir in high position

(m) Open the valve (tap vertical)

(n) Start your timer. The etching process starts immediately. For different designs of sensors presented in this dissertation, the etching time varied between 35 min and 1 hour 30 min.

The Etch rate depends on two critical settings; 1) Temperature (Lower, the faster), 2) Time (at lower temperature, shorter time is needed to etch, and vice versa). Note that higher etch rate, there will be less consistency; and lower etch rate, higher consistency in etched areas.

The etch rate can be estimated using IDONUS IR-Light Wafer Inspection Microscope. Silicon is transparent for infrared light, and the IR light microscope illuminates the silicon substrate from the back-side and captures the light that transverses the substrate. Therefore, it becomes possible to inspect the undercut of the buried oxide layer.

(o) 30-40 seconds before the processing time is finished release the security pin and push down the reservoir handle to place reservoir in low position. Now the acid flows into the reservoir.

(p) When the process time is finished, lift the wafer holder and place it so that the wafer is facing you.

(q) Switch OFF the electrostatic clamp

(r) Take the wafer off the heating plate.

Do not touch the wafer holder; it may be contaminated with HF. Use soft tweezers which do not scratch the dielectric layer isolating the electrodes of the electrostatic chuck! Rinse the tweezers after usage.

(s) Close the valve (tap horizontal) after the HF acid has flown into the reservoir

(t) Close the reaction chamber by placing the lid onto the reaction chamber

Heat the wafer holder to 60C (30 min) before you switch the equipment off. This helps that the rest gases of the HF evaporate.

(u) Switch OFF the controller box

(v) You need to refer to IR Microscope to make sure that etch setting you used is optimal and all the moving structures are fully released. You will also have to make sure that the anchors are not released or over-released. The anchors provide the structure for the wirebonder to bond a wire.

HF acid has to be exchanged once in a while. Usually HF can be reused for more than a month (1-6).

Appendix D

List of Vendors

Allied High Tech Products, Inc.

Location: Rancho Dominguez, CA, USA

Phone: (800) 675-1118

E-mail: orderalliedhightech.com

Multiprep Polishing System from Allied High Tech Products, Inc. was used primarily for back lapping of 4" wafers with copper electroplated vias. The diamond lapping films were also bought from Allied High Tech Products Inc.

BayArea Circuits, Inc.

Location: Fremont, CA, USA

Phone: (510) 933-9010

E-mail: bcadao@bacircuits.com

Several of the front-end PCBs used in this dissertation were fabricated by BayArea Circuits, Inc.

Disco Hi-Tech America, Inc.

Location: Santa Clara, CA, USA

Phone: (408) 987-3776

E-mail: richard_b@discousa.com

Stealth dicing technology from Disco Hi-Tec America was used to dice in-house fabricated silicon-on-insulator gyroscopes developed as part of this dissertation. Stealth laser dicing eliminates process dust and need for the associated cleaning that typically happens after dicing.

dSPACE, Inc.

Location: Wixon, MI, USA

Phone: (248) 295-4700

E-mail: cpasque@dspaceinc.com

dSpace compact rapid control prototyping (RCP) system-Microlab Box with Xilinx Kintex-7 FPGA was used to implement the control loops for the gyroscopes. The system provides rapid control system development by integrating Simulink environment with a powerful DSP based controller and FPGA.

Gamma Vacuum

Location: Shakopee, MN, USA

Phone: (952) 445-4841

E-mail: orders@gammavacuum.com

A small TiTan ion pump from Gamma Vacuum was used as a part of a vacuum chamber assembly to substitute for the turbo pump during the gyroscopes noise characterization. In addition, a macro-scale Non-evaporable Getter (NEG) pump from Gamma Vacuum was integrated into a vacuum chamber assembly for gyroscope characterization.

Idonus Sarl

Location: Hauterive/Neuchatel, Switzerland

Phone: +41 32 724 44 40

E-mail: patrick.schoeneich@idonus.com, christian.spoerl@idonus.com

Hydrofluoric acid Vapor Phase Etcher (HF VPE) from Idonus was used for stiction-free vapor HF release of SOI devices developed as part of this dissertation.

JH Technologies, INC.

Location: Irvine, CA, USA

Phone: (408)436-6336 x371

E-mail: ddavis@jhtechnologies.com

Leica DM4 microscope with a motorized stage was bought from JH Technologies, INC. distributor. The microscope was used for inspection and imaging of the devices presented in this dissertation.

Kurt J. Lesker

Location: Livermore, CA, USA

Phone: (925) 449-0104

E-mail: salesus@lesker.com

Vacuum chamber components and the vacuum gauges were purchased from Kurt J. Lesker.

PCB and Stencils Unlimited, Inc.

Location: Tualatin, OR, USA

Phone: (503) 639-7601

E-mail: support@pcbunlimited.com

The stainless steel SMT stencils for PCB in-house assembly were fabricated by PCB and Stencils Unlimited.

Photosciences, Inc.

Location: Torrance, CA, USA

Phone: (310) 634-1500

E-mail: fasttrack@photo-sciences.com

Photomasks used throughout this dissertation were fabricated by Photosciences, Inc.

Rigol Technologies, Inc.

Location: Oakwood Village, OH, USA

Phone: (440) 232-4488 x110

E-mail: chris_armstrong@rigol.com

Oscilloscopes and function generators from Rigol Technologies, Inc. were used for characterization of devices and testing of front-end PCBs.

Sierra Circuits, Inc.

Location: Sunnyvale, CA, USA

Phone: 408-735-7137 x9838

E-mail: webpcb@protoexpress.com

Majority of the front-end PCBs used in this dissertation were fabricated by Sierra Circuits, Inc. Part of the PCBs were also assembled by Sierra Circuits, whereas the rest was assembled in house.

Stanford Research Systems

Location: Sunnyvale, CA, USA

Phone: (408) 744-9040

E-mail: info@thinksrs.com

Analog filters, scaling amplifiers and precision voltage sources from Stanford Research Systems were used for characterization of MEMS gyroscopes presented in this dissertation.

Ultrasil Corporation

Location: Hayward, CA, USA

Phone: (510) 266-3700

E-mail: rduque@ultrasil.com

Silicon and SOI wafers used thought this dissertation were purchased from Ultrasil Corporation.

Westbond, Inc.

Location: Anaheim, CA, USA

Phone: (714) 978-1551 x206

E-mail: sales@westbond.com

Westbond Wire Bonder was used for wire bonding of devices developed as part of this dissertation.

Xilinx, Inc.

Location: San Jose, CA, USA

Phone: (408) 559-7778

E-mail: -

Xilinx Vivado Design Suite (System Edition with the System Generator) was used to graphically model in Simulink the FPGA application for the dSpace Microlab Box.